NASA CR-134954
MDC-J7708

EFFECT OF FORWARD MOTION ON ENGINE NOISE

By G. L. Blankenship, J. K. C. Low, J. A. Watkins, and J. E. Merriman

Douglas Aircraft Company
McDonnell Douglas Corporation
Long Beach, California 90846

Prepared for

NASA

National Aeronautics and Space Administration

NASA Lewis Research Center

Contract NAS 3-20031

October 1977

1. Report No.	2. Government Accession No.	3. Recipient's Catalog No.
NASA CR-134954		

4. Title and Subtitle	5. Report Date
EFFECTS OF FORWARD MOTION ON ENGINE NOISE	October 1977
	6. Performing Organization Code

7. Author(s)	8. Performing Organization Report No.
G. L. Blankenship, J.K.C. Low, J. A. Watkins, and J. E. Merriman	MDC-J7708
	10. Work Unit No.

9. Performing Organization Name and Address	11. Contract or Grant No.
Douglas Aircraft Company McDonnell Douglas Corporation 3855 Lakewood Boulevard Long Beach, California 90846	NAS 3-20031
	13. Type of Report and Period Covered

12. Sponsoring Agency Name and Address	14. Sponsoring Agency Code
National Aeronautics and Space Administration Washington, D.C. 20456	Contractor Report

15. Supplementary Notes

Project Manager, Eugene A. Krejsa, V/STOL and Noise Division, NASA
Lewis Research Center, Cleveland, Ohio

16. Abstract

A study was conducted to determine a procedure for correcting static engine data for the effects of forward motion. Data were analyzed from airplane flyover and static-engine tests with a JT8D-109 low-bypass-ratio turbofan engine installed on a DC-9-30, with a CF6-6D high-bypass-ratio turbofan engine installed on a DC-10-10, and with a JT9D-59A high-bypass-ratio turbofan engine installed on a DC-10-40. The observed differences between the static and the flyover data bases are discussed in terms of noise generation, convective amplification, atmospheric propagation, and engine installation. The results indicate that each noise source must be adjusted separately for forward-motion and installation effects and then projected to flight conditions as a function of source-path angle, directivity angle, and acoustic range relative to the microphones on the ground.

17. Key Words (Suggested by Author(s))		18. Distribution Statement
Jet noise	Forward Motion	
Core noise	Engine installation	
Fan noise	Excess attenuation	
Turbine noise	Noise generation	
Nonpropulsive noise	Inlet distortion	
	Convective amplification	

19. Security Classif. (of this report)	20. Security Classif. (of this page)	21. No. of Pages	22. Price*
Unclassified	Unclassified	198	

* For sale by the National Technical Information Service, Springfield, Virginia 22151

CONTENTS

CONTENTS - (Concluded)

1. SUMMARY

A study was conducted to determine a procedure for correcting static-engine data for the effects of forward motion. Data were analyzed from airplane-flyover and static-engine tests with a JT8D-109 low-bypass-ratio turbofan engine installed on a DC-9-30, with a CF6-6D high-bypass-ratio turbofan engine installed on a DC-10-10, and with a JT9D-59A high-bypass-ratio turbofan engine installed on a DC-10-40. The observed differences between the static and the flyover data bases are discussed in terms of noise generation, convective amplification, atmospheric propagation, and engine installation. The results indicate that each noise source must be adjusted separately for forward-motion and installation effects and then projected to flight conditions as a function of source-path angle, directivity angle, and acoustic range relative to the microphones on the ground. In order to investigate the effect of forward motion on jet noise, other low-frequency sources such as core noise, nonpropulsive noise (airframe-generated noise), and jet-flap-interaction noise must be considered. High-frequency noise measured on the static-test stand and projected to flight must be adjusted for an additional source of atmospheric absorption, excess attenuation. The level and the directivity of the fan tone at blade-passing frequency generated under static conditions must be corrected for the reduced level of turbulence in flight and for the change in the modal constituents of the source. At frequencies equal to and greater than the fan-blade-passing frequency, the increased flight levels of turbine noise must be considered.

2. INTRODUCTION

The accurate prediction of airplane flyover noise levels has become important in the evaluation of noise-reduction features for both present and future aircraft designs. Engine noise can be reduced by using aero-acoustic design features to reduce the intensity of generated noise at the source and by using acoustic treatment to reduce the intensity of noise propagating through the engine ducts. With the many possible tradeoffs for meeting specified in-flight noise goals, each noise-reduction feature must be evaluated against the potential penalties in weight, performance, and cost that it would impose on the engine/airframe system. An accurate definition of the engine noise sources (jet, core, fan inlet, fan discharge, and turbine) relative to the total engine and airframe flyover noise levels is therefore essential in order to properly assess noise-reduction features and requirements.

An important consideration now is the effects of forward flight and engine installation (on the airplane) on flyover noise, and whether flyover noise can be predicted accurately by using static-noise measurements or wind-tunnel-simulated flight-noise measurements. It is now widely recognized that forward motion and engine installation alter the mechanisms of noise generation and propagation (refs. 1 through 14). Contradictory results have been noted for the effects of forward motion on the low-frequency jet noise levels (refs. 1 through 6). The lower flight levels in the aft quadrant were consistent with predicted relative-velocity effects, but small decreases and even increases in the inlet quadrant were not. The changes were not constant with angle (directivity angle relative to the inlet centerline), as had been assumed in earlier prediction methods. The increased levels in the inlet quadrant were neither observed in model-jet flight simulation (refs. 15 through 19) nor predicted on the basis of classical jet-noise theories. References 6 and 20 have shown that the discrepancy can be reconciled by taking into consideration the contributions from other low-frequency noise sources, such as core noise and shock-cell noise. Comparisons of fan noise levels (refs. 6 through 14) have shown that the high-frequency levels are significantly reduced during flight compared with the noise generated statically. The difference was due to the lower level of the fan fundamental tone

in the flight spectra and to the lower level of the flight fan spectra relative to the static-projected fan spectra for frequencies greater than the fundamental blade-passing frequency. However, turbine noise levels were shown to be lower under static conditions. The results suggested (1) that the mechanism of fan-noise generation and the resultant modal structure of the sound field propagating in engine ducts was different under static and under flight conditions, (2) the method that had been used to project static engine data to flight conditions did not properly account for the propagation of high-frequency noise through the atmosphere, and (3) the mechanisms of turbine noise propagation was different under static conditions. As a result, the evaluation of noise-reduction features that uses static-engine data projected to flight conditions may be inaccurate unless the static-to-flight differences (differences required to correct static-projected levels to the flyover noise levels) and correction procedures are known. The prediction method therefore depends on (1) proper identification of static-engine noise source levels, spectra, and directivity and (2) adjustment on a noise-source basis of the data for the effects of engine installation, propagation, and forward motion.

This report discusses the procedures used to identify, separate, and correlate static-engine and flyover noise sources. Comparisons of static-engine and airplane flyover noise are based on results of test programs with a JT8D-109 low-bypass-ratio turbofan engine installed on a DC-9-30, with a CF6-6D high-bypass-ratio turbofan engine installed on a DC-10-10, and with a JT9D-59A high-bypass-ratio turbofan engine installed on a DC-10-40. The observed differences between static and flyover data bases are discussed in terms of noise generation, convective amplification, atmospheric propagation, and engine installation. The objectives of this study are (1) to define the effects of forward motion on static-engine noise levels and (2) to develop methods of adjusting the static-engine data for the effects of forward motion and engine installation.

This study was conducted by the Douglas Aircraft Company, a division of the McDonnell Douglas Corporation, under contract to the NASA-Lewis Research Center (NAS-20031).

3. TECHNICAL APPROACH

This section of the report describes the selection of the static- and the flyover-noise data bases to be used in the noise-source analysis. The specific tasks were (1) to define and to separate engine-noise sources (jet, core, fan inlet, fan exhaust, and turbine) in both static and flyover data bases, (2) to define the differences between the two data bases, (3) to account for the static-to-flight differences in terms of the effects of engine installation, propagation, and forward motion, and (4) to account for the remaining differences empirically as effects of forward motion on static-engine noise levels.

3.1 TEST CONFIGURATIONS AND PROGRAMS

The flyover-noise data used in the analyses were derived from test programs that used a DC-9-30 (fig. 1) powered by two Pratt and Whitney refanned JT8D-109 low-bypass-ratio turbofan engines, a DC-10-10 (fig. 2) powered by three General Electric CF6-6D high-bypass-ratio turbofan engines, and a DC-10-40 (fig. 3) powered by three Pratt and Whitney JT9D-59A high-bypass-ratio turbofan engines. The DC-9 program was conducted under NASA contract number NAS3-17841 (ref. 21). The others were funded by McDonnell Douglas. All the tests were conducted at the Douglas Test Facility in Yuma, Arizona. Flyover noise data were measured with ground- and tripod-mounted microphones. Microphones mounted flush with the ground beneath the airplane flight path were used in order to minimize ground-reflection effects on the low- to mid-frequency regions of the spectra. In addition, microphones were mounted in both inlet and fan discharge ducts of the CF6-6D and in inlet, fan duct, and tailpipe of the JT8D-109. References 9 and 21 describe the locations of internally mounted microphones in the CF6-6D and the JT8D-109, respectively. The instrumentation and the procedures used to measure and to reduce acoustical data, engine and airplane performance data, weather data, and airplane space-positioning data are discussed in references 14 and 21. The flyover noise data presented were averaged over several runs with approximately the same power setting. Table 1 summarizes the flyover noise runs used in the flight data base. The static-noise data obtained from Pratt and Whitney for the refanned JT8D-109 and for the JT9D-59A engines were measured with 4.88m-pole microphones

(10° to 150° from the inlet) and flush-mounted ground microphones (90° to 160° from the inlet) located on a 45.7m radius. In the inlet quadrant, for which flush data were not available, the static-noise data measured with a 4.88m-pole microphone were corrected to the levels of ground-microphone measurements by using empirical correction factors developed from 4.88m-pole- and ground-microphone noise data measured in the aft quadrant. Static-noise data obtained from General Electric for the CF6-6D engine were measured with 12.2m-pole microphones on a 45.7m-radius. The static engine noise runs to be used in comparison with the flight data base are given in table 2.

Figure 1(b) shows the JT8D-109 engine and nacelle. Acoustically absorptive materials were used to suppress fan noise in inlet and discharge ducts and fan and turbine noise in the primary nozzle. Figures 2(b) and 3(b) show the CF6-6D and JT9D-59A wing-engine nacelles, respectively. The production nacelle for the CF6-6D and JT9D-59A uses acoustically absorptive materials to suppress fan noise in the inlet and fan discharge ducts. The primary nozzle of the JT9D-59A is treated to suppress turbine noise.

3.2 PROCEDURES FOR SEPARATING ENGINE NOISE SOURCES

In the following analyses, the procedures are discussed that were used to identify, to separate, and to correlate the engine noise sources from static and flyover noise levels. In order to use the noise-source separation procedures for static and flyover noise, the flyover noise data were corrected to a polar-arc radius of 45.7 meters, to be consistent with the measured-static engine data. The steps used in the correction procedure are as follows:

1. Adjust measured flyover noise to reference weather conditions using reference 22 and layered atmosphere corrections (sound-path weather at 100 ft. intervals).

2. Determine the acoustic range and the directivity angle from the lead engine inlet centerline at each point in the flyover-flight-path profile.

3. Convert the flyover SPLs to 45.7m-polar noise levels by using spherical divergence and atmospheric absorption derived in reference 22.

4. Estimates of airplane nonpropulsive noise levels at a 45.7 meter radius derived from measurements of the DC-10 idle flyover noise, described in reference 23, were subtracted on an energy basis from the flyover data.

The noise-source definition had to account for the separate contributions of discrete-frequency and broadband noise from fan, compressor, and turbine stages, as well as the broadband low-frequency noise due to the combustion process and to externally generated jet noise. In addition, it was required that the sum of the separated static and flyover noise sources be equivalent to the measured levels.

3.2.1 Separation of Low-Frequency Noise Components from Measured Data

In order to eliminate the masking effects due to ground reflections, static- and flyover-noise data measured with flush-mounted microphones were used to identify and to separate the low-frequency noise components from the measured data. By using the procedures outlined above, the flyover noise data were projected back to a polar-arc radius consistent with the static-engine noise data. No corrections were made for the effect of jet-noise source distribution, since the adjustments would not have been applicable to flyover and static data at jet velocities less than takeoff velocity, where core noise becomes more prominent. The low-frequency (50 to 1000 Hz) parts of the measured static and flyover adjusted spectra were assumed to be due to contributions from jet-plus-core noise. The high-frequency (1250 to 10,000 Hz) parts of the jet-plus-core spectra were determined by using an assumed "roll-off" rate based on inspection of measured data at each inlet angle (see fig. 4). Roll-off rates were found to vary from 4 to 6 per octave, depending on the inlet angle (table 3). The remaining high-frequency portion of the measured spectra was assumed to be due to turbomachinery-noise components.

3.2.2 Comparisons of Static and Flight Low-Frequency Noise

Figure 5 presents a typical comparison of flight and static low-frequency-noise OASPLs for the DC-9-30/JT8D-109 measured at a primary jet velocity of 221 m/sec. The figure shows little or no difference between static and flight OASPLs in the inlet quadrant. In the exhaust quadrant, the flight levels are

lower than the static levels. Comparison of static and flight spectra at an inlet angle of 50° (fig. 6) shows nearly equal peak SPLs in the 315- to 1250-Hz frequency range, which are responsible for the equal static and flight OASPLs in the inlet quadrant of figure 5. At a primary jet velocity of 392 m/sec (fig. 7), the flight low-frequency OASPLs are lower than the static OASPLs at all angles, with the largest reductions in the exhaust quadrant.

Figure 8 shows a comparison of flight and static low-frequency OASPLs for the DC-10-40/JT9D-59A at a typical approach power setting (primary jet velocity of 268 m/sec). The flight levels are higher for inlet angles up to 120°. Comparisons of static and flight spectra at an inlet angle of 50° in figure 9 show flight SPLs higher than static SPLs, in contrast to the relative levels for the DC-9-30/JT8D-109 (fig. 6). Another low-frequency noise source related to the impingement of the fan-jet exhaust on the deflected flaps under approach flight condition is thought to be responsible for the higher flight noise levels in the inlet angles in figure 9. At a higher jet velocity (436 m/sec) corresponding to takeoff power (fig. 10), the flight low-frequency OASPLs are lower than the static OASPLs at all angles. That trend is similar to the trend observed in the DC-9-30/JT8D-109 at takeoff power. All of the comparisons indicate the need to identify and to separate the jet and core noise components from the measured low-frequency noise.

3.2.3 Separation of Static Jet- and Core-Noise Components

The first step is to identify the individual jet and core noise spectral components from the measured low-frequency SPL spectra. The assumptions used are summarized below and are illustrated in figure 11.

1. At high power settings (jet velocities above 305 m/sec), the measured jet-plus-core noise spectra are dominated by jet noise.

2. At low power settings (jet velocities below 200 m/sec), core noise dominates.

3. At intermediate power settings, the contributions of jet and of core noise are about equal.

In general, pure-jet-noise spectra normalized in terms of 1/3-octave-band SPLs relative to OASPLs have been shown to correlate with the nondimensional Strouhal parameter, fD/V_{jp}. An example of the correlation is shown in figure 12 for model-scale static jet noise at 120° from the inlet. In contrast, core noise, which is of higher frequency, does not correlate with Strouhal number. It has been shown in reference 24 that for a given engine the peak frequency and the normalized spectral shape are independent of power settings (i.e., primary-jet velocities). Plotting the static JT8D-109 low-frequency noise spectra versus Strouhal number (e.g., fig. 13) shows the data for high-jet-velocity collapsed to a single spectrum identical to the model-scale jet noise spectrum at the same angle. The data for lower jet velocities have shifted progressively to higher Strouhal numbers; that is, they do not correlate with Strouhal numbers. The peak frequencies of those spectra are approximately 400 to 500 Hz over a wide range of jet velocities and angles (fig. 14). The low-frequency noise spectra for the very low jet velocities were normalized as functions of the peak frequency and SPL, which was suggested in reference 24. The resulting spectra are shown in figure 15 for inlet angles of 50°, 90°, 120°, and 140°. The spectra are the same for all angles, and they are therefore considered to be individual core-noise spectra.

The corresponding normalized spectra for jet and core noise identified from the static JT9D-59A low-frequency SPL spectra are shown in figures 16 and 17 for angles 50°, 90°, 120°, and 140°. Again, the normalized spectral shapes for core noise are the same for all angles, and they are nearly identical to the spectral shapes derived for the static JT8D-109 core-noise component. The core-noise peak frequencies (fig. 18) for the static JT9D-59A engine are lower than the corresponding core frequencies for the JT8D-109 engine.

With the jet- and core-spectrum shapes that had been determined, the second step in the analyses was to determine the relative levels of jet and core noise in the measured low-frequency spectra. A curve-fit technique was required to provide the best combination of the jet and core normalized spectra to fit the measured data as illustrated in figure 19. Initial estimates of the individual jet and core noise SPLs were combined to give an

estimated jet-plus-core noise SPL spectrum. Beginning with the 1/3-octave-band center frequency at 50 Hz and continuing to successive bands at higher frequencies, the estimated SPLs were subtracted from the measured SPLs, giving the sum of the differences between the measured and the estimated SPL spectra for the 24 frequency bands as

$$\sigma^2 = \sum_{i=1}^{24} [SPL(i)_{measured} - SPL(i)_{estimated}]^2$$

The quantity σ^2 (variance) is used to find out how close the estimated SPL spectrum is to the actual spectrum. The estimates of individual jet and core noise levels were then incremented independently to create a matrix of σ^2-values. Curve-fit techniques were then used to determine the set of jet and core levels that would give the best fit to the measured SPL data. The OASPLs for the individual jet and core components were then calculated.

The measured low-frequency OASPLs and jet and core OASPLs derived by that method are shown in figure 20 for the JT8D-109 and in figure 21 for the JT9D-59A static data at 120°. For simplicity, both jet and core OASPLs are correlated on the basis of the primary jet velocity. In the JT8D-109, the measured low-frequency noise levels are dominated by core noise at jet velocities below 192 m/sec and by jet noise at jet velocities above 340 m/sec. Similarly, the total low-frequency noise levels for the JT9D-59A are dominated by core noise at jet velocities below 120 m/sec and by jet noise at jet velocities above 240 m/sec. Tables 4 and 5 present correlations of static jet- and core-noise levels for the JT8D-109 and the JT9D-59A, respectively, for angles from 50° to 150°.

3.2.4 Separation of Flight Jet- and Core-Noise Components

The procedures previously described for the separation of static jet- and core-noise components were used to identify and to separate the individual spectra and levels of jet- and core-noise components for the DC-9-30/JT8D-109 and the DC-10-40/JT9D-59A flyover noise data. The normalized jet-noise-component spectra derived from the DC-9-30/JT8D-109 flyover data are presented in figure 22 for angles of 50°, 90°, and 120°. The relative jet velocity,

$V_{jp} - V_a$, was used in the Strouhal parameter instead of the primary jet velocity, V_{jp}. The corresponding in-flight spectra for the DC-10-40/JT9D-59A are presented in figure 23. The normalized spectral shapes for core-noise components for the DC-9-30/JT8D-109 are presented in figure 24. The core spectral shapes were identical for all angles. The in-flight core peak frequencies, f_{peak}, were higher than the peak frequencies observed statically (fig. 25). The corresponding normalized spectral shapes for core noise of the DC-10-40/JT9D-59A are shown in figure 26. The core peak frequencies of the JT9D-59A were also higher in flight (fig. 27).

Examples of correlations of the individual levels of jet- and core-noise components and the combined level for the two components are given in figures 28 and 29 for the DC-9-30/JT8D-109 and the DC-10-40/JT9D-59A flyover data at 120°, respectively. For the purpose of comparison, the individual levels and the combined total levels were correlated on the basis of primary-jet velocity.

3.2.5 Separation of Turbomachinery Noise from Static-Engine Data

In the inlet quadrant, high-frequency noise consists primarily of fan-inlet noise; in the exhaust quadrant it consists primarily of fan discharge and turbine noise. Fan noise is composed of discrete tones at blade-passing frequency and of harmonics at multiples of the blade-passing frequency superimposed on a broadband-noise spectrum. At supersonic fan tip speeds multiple-pure-tone (MPT) noise is generated by the fan rotor and is propagated out the inlet. Turbine noise is composed of discrete tones and a broadband noise spectrum generated by the stages of the low-pressure turbine. For the spectral comparisons that follow, tones generated by the fan rotor and by the booster stage are designated by F and B, respectively, and the numbers 1 through 5. Fundamental tones generated by the last three stages of the low-pressure turbine stages are designated by T and by the numbers 2, 3, and 4 for the JT8D-109, by 3, 4, and 5 for the CF6-6D, and by 4, 5, and 6 for the JT9D-59A engines. The following sections discuss the component-noise separation based on static-engine data for the refanned JT8D-109. Similar results were obtained for the CF6-6D and the JT9D-59A.

3.2.5.1 Removal of low-frequency noise from measured data. - Before turbomachinery noise sources could be separated into components, low-frequency noise sources (jet-plus-core noise) were removed from the measured data. Correlations of jet and core noise described in section 3.2.1 were used to define the jet-plus-core-noise spectra and levels. Table 3 presents the roll-off rates used to extrapolate the low-frequency jet-plus-core noise to the high frequencies. Beginning with the 10 kHz band and continuing to successively lower bands, the jet-plus-core noise levels were subtracted on an energy basis from the total measured levels to get the total turbomachinery noise levels. The subtraction procedure continued band by band until the jet plus-core-noise spectrum was within 1 dB of the total measured data. The high-frequency turbomachinery noise was then extrapolated to lower frequencies (fig. 30) by using roll-off rates consistent with fan/compressor test-stand data previously obtained from engine manufacturers (table 3).

3.2.5.2 Separation of data into discrete tones and broadband noise. - The procedures for predicting turbomachinery noise required the determination of the relative contributions of tones and broadband noise to a given spectrum. The following criteria for separating broadband and discrete tone noise were used:

1. The tones considered were those of the fan-blade-passing frequency (BPF), the second through the fifth harmonics, fan booster (BPF of the first stage of the low-pressure compressor), and the BPF tones from the last three low-pressure turbine stages.

2. If more than one tone from the same noise source (e.g., turbine BPFs) occurred in the same 1/3-octave band, they were assumed to have equal strength.

3. If more than one tone from different sources (e.g., one or more turbine BPFs and a fan harmonic) occurred in the same 1/3-octave band, narrowband data were used to determine the relative levels. Details of the procedure will be described in more detail in section 3.2.5.4.

4. The broadband noise spectrum was assumed to be piecewise linear with 1/3-octave-band number. The broadband level in the band containing the BPF tone was determined by interpolating between adjacent frequency bands

composed of essentially broadband noise only.

The sound pressure level (SPL) of the tone(s) in a band was obtained by subtracting the mean-square broadband pressure from the total mean-square turbomachinery sound pressure. The total mean-square sound pressure of the tone(s) was then distributed equally among the tones present in the band for the same source and finally converted to a sound pressure level.

3.2.5.3 Separation of inlet and aft turbomachinery noise. - In order to separate inlet from aft turbomachinery noise levels, procedures developed under the NASA Refan Program (ref. 21) were used to define the directivity of the exhaust noise in the inlet quadrant and that of the inlet noise in the aft quadrant. Table 3 presents the roll-off rates for all frequencies determined for the contribution of inlet and aft levels in their opposing noise quadrants. Figure 31 illustrates the results of the separation procedure as applied to the JT8D-109. Similar results were obtained for the CF6-6D and JT9D-59A static-noise levels.

3.2.5.4 Separation of fan-exhaust and turbine noise. - At power settings below takeoff, noise generated by the last three stages of the low-pressure turbine could in most cases be identified from narrowband data. Figure 32 shows the prominent features of JT8D-109 and JT9D-59A turbine noise as tones with a haystacking of broadband noise around the blade-passing frequencies of the low-pressure turbine stages. For those power settings, narrowband data were used to separate the peak turbine (broadband plus discrete) from the fan 1/3-octave-band levels for a given fan rotor speed and angle as given in figure 33. That procedure was used to define turbine levels for a wide range of angles at each fan rotor speed at which turbine noise could be identified. The turbine directivity derived from the source-separation analyses was found to be approximately constant with power setting. It is given in figure 34, together with similar results derived in references 25, 26, and 27 and in a Douglas analysis of the JT9D-20 data. In addition, the turbine broadband-spectrum shape was found to be approximately constant with power setting and angle, as is shown by the solid line in figure 35. The derived spectrum shape compares well with the results of reference 25 and Douglas analysis of the JT9D-20 data, but reference 26 shows a more broad spectrum shape at frequencies below the peak frequency.

Those procedures were used to define turbine noise spectra, levels, and directivities. With the spectra defined, the turbine noise levels could be subtracted from the total-aft-turbomachinery spectral levels on an energy basis to obtain the fan-exhaust noise levels shown in figure 36 for the JT8D-109 static-noise levels. Again, similar results were obtained for the CF6-6D and the JT9D-59A engines. The spectral levels were then normalized with respect to engine airflow rates and correlated with physical- and corrected-fan rotor speed and angle.

3.2.6 Separation of Turbomachinery Noise from Flyover-Noise Data

To provide a comparative flight data base, the high-frequency levels were corrected to a 45.7-meter radius and separated from the measured flyover-noise levels by a procedure similar to that used in the static-noise analysis. Before the turbomachinery components could be identified and separated the high-frequency noise levels had to be corrected back to the source for the effects of Doppler frequency shift on the broadband and the discrete-tone components. In addition, all spectra were inspected for completeness, or for data dropouts. Data dropouts generally occurred at the very high frequencies when the airplane was at such large distances from the microphone that the sound generated was not distinguishable from the background noise. In those cases, extrapolated values were supplied. Once the corrections were applied, the flyover spectrum was then separated into the jet plus core, inlet turbomachinery, and aft turbomachinery noise components (figs. 37 and 38) as described previously in section 3.2.5 for static noise data. To derive turbine noise levels in the flight data, the derived static levels were modified to account for the effects of jet exhaust sound scattering (described in section 3.4.1.4). The modified turbine levels were then subtracted from the aft turbomachinery levels to yield the fan-exhaust noise levels (fig. 39). As with the static-turbomachinery source levels, the separated source levels were normalized with respect to airflow rates and correlated with physical- and corrected-fan rotor speed and angle.

3.3 DEFINITION OF STATIC-TO-FLIGHT DIFFERENCES

To identify the effects of forward motion on the engine noise sources, the static-engine and the flyover noise levels were compared and the areas of disagreement discussed in terms of the mechanisms that alter the generation and the propagation of the noise under forward motion. To compare the static-engine and the flyover noise data, the separated noise sources that had been determined were projected to flight conditions, with the same adjustments applied to the flyover noise data (section 3.2). Flyover and static-projected noise components were added, to give the original flight levels and the total static-projected levels. In the following analysis, comparisons of flyover and static-projected noise levels are presented and the areas of disagreement are noted.

3.3.1 Jet and Core Noise

Comparisons of static and flight total low-frequency noise were presented in figures 5 - 10. In general, the flight levels were shown to be lower than those measured during static operation at all angles. For low jet velocities comparisons of DC-9 flyover and JT8D-109 static data show that the flight data are only slightly less than the static levels, whereas, the DC-10 flyover levels are slightly higher than the JT9D-59A static levels in the inlet quadrant. Separation of the total measured data into its jet and core noise components (figs. 20 and 21) have shown that core noise is the dominant source at low jet velocities while the jet noise dominates at high jet velocities.

3.3.2 Turbomachinery Noise

Figure 40 shows comparison of flight- and static-projected tone-corrected perceived noise levels (PNLT) plotted versus inlet angle for the DC-9-30/JT8D-109 airplane configuration. At approach power (fig. 4a), the flight data are lower than the static data in both the inlet quadrant and, to a lesser degree, in the exhaust quadrant. Conversely, for a takeoff power setting (fig. 40b), the flight data are higher than the static. Figure 41 shows comparisons of the flight- and the static-projected 1/3-octave-band spectra at approach power, at particular angles of interest in the flight-path profile. The higher static

PNLTs are due to increases in the high frequencies at and above the fan blade-passing frequency. The differences are less pronounced at aft angles. At takeoff power, measured flyover and static spectra are dominated by low-frequency jet noise sources. There is little contribution from turbomachinery noise.

Figure 42 shows comparisons of flyover and predicted PNLTs for the DC-10-10/CF6-6D airplane configuration. The static-predicted levels are again higher than the flight in the inlet quadrant at approach power (fig. 42a), but the flight levels are higher than the static levels at the peak aft-noise angles. Figure 42b shows that at takeoff power the flight data are higher than the static at the peak inlet-noise angles and that the static data are higher than the flight at the peak exhaust angles. Figures 43 and 44 show the flight- and the static-spectra comparisons for approach and for takeoff power settings, respectively. Figure 43 shows that the increased static PNLTs at approach power are due to increased levels at the fan fundamental frequency and the frequencies of the fan harmonics and turbine blade passing. For aft quadrant angles, the level of the static fan fundamental is higher than in flight, and the increased flight levels are due to higher levels at the turbine blade-passing frequencies. Figure 44 shows that increased flight levels in the inlet quadrant at takeoff power setting are due to the propagation of multiple-pure-tone noise (MPT) at multiple frequencies of the fan speed. In addition, the high-frequency static data at the fan fundamental and harmonics are higher than the flight data, the differences becoming greater with increasing frequency.

Figure 45 shows static and flyover PNLT comparisons for the DC-10-40/JT9D-59A. As with the DC-10-10/CF6-6D, the static data for approach power are higher in the inlet quadrant and lower in the aft quadrant than the flight data. But at takeoff power the static data are higher than the flight at all angles in the flyover-noise history. Spectral comparisons at approach power (fig. 46) show that the increased static levels in the inlet are due to the higher levels of the fan fundamental and harmonics. At angles farther aft, the flight data are higher for frequencies at and near the 1/3-octave band containing the turbine discrete tones. At takeoff power (fig. 47), the spectra are dominated to a large extent by jet noise, but the contribution of turbomachinery noise is still evident.

3.4 CORRECTIONS FOR THE EFFECTS OF ENGINE INSTALLATION AND ATMOSPHERIC PROPAGATION

To identify the effects of forward motion on engine noise sources, it is necessary to adjust the static-engine data for engine installation and propagation effects. The effects of engine installation include (1) effects of relative engine location (axial separation between engines), (2) effects of fuselage and wing shielding of the fan-inlet noise, (3) effects of sound scattering of fan and turbine noise by the wing-flap-wheel wake, (4) effects of jet-exhaust sound scattering of turbine noise, and (5) effects of inlet contour on fan-inlet noise. Nonpropulsive noise, which is described in reference 23 and which is defined as the noise generated in flight by sources other than the engines (fuselage, wing-flap system, landing-gear struts, and wheel wells), must also be included in the category of installation effects. The effects of wing shielding and of sound scattering by the wing-flap-wheel wake will be discussed for the DC-9-30/JT9D-109 airplane configuration, and the effects of jet-exhaust sound scattering will be discussed for the exhaust-nozzle configuration for the CF6-6D and for JT9D-59A high-bypass-ratio engines. Propagation effects, in particular, the effects of excess attenuation, will be discussed for both a DC-9 and a DC-10 airplane in section 3.4.2.

3.4.1 Engine-Installation Effects

3.4.1.1 Engine location. - Figure 48 shows the location of the engines on the DC-10-10. Two engines are mounted under the wings, and a third is mounted in the vertical tail 68 feet aft of the wing engines. For low-altitude flyovers, the engine noise cannot be considered to come from a point source, with three engines at the same axial location. Static levels for each engine must therefore be adjusted for spherical divergence, atmospheric absorption, Doppler shift, etc., as functions of the source-path angle (angle between the observer and the flight path), the directivity angle (the angle between the observer and the inlet centerline), and the acoustic range relative to the ground microphone.

Figure 49 shows the effect of the DC-10-10 tail-engine location on directivity angles during a level-flight flyover at an altitude of 152.4 m. When the airplane is directly overhead, the propagation angle from the inlet of the wing-mounted engines is approximately 10° greater than that of the tail engine. As the airplane approaches and passes overhead, the differences in directivity angle and in acoustic range make the noise levels lower than they would be if the engines had no axial separation. The effect is the opposite for the noise levels in the aft quadrant. The effects of Doppler shift and, to a lesser degree, of atmospheric absorption will also be affected.

3.4.1.2 Fuselage shielding. - With the third DC-10 engine mounted above the fuselage in the vertical tail, fan-inlet noise is shielded by the fuselage from microphones located directly beneath the flight path, which further reduces the inlet flyover-noise levels from those of the static case.

3.4.1.3 Wing shielding and wake sound scattering. - Comparisons of static and flight narrowband spectra (ref. 14), which were measured by microphones mounted in the inlet of the JT8D-109-powered DC-9-30 airplane, showed that the levels of the random broadband noise and tones at discrete frequencies did not change significantly in flight at approach power settings. Similar trends were observed for static and flight narrowband spectra measured in the fan duct and in the tailpipe, which suggested that the static-to-flight differences observed in figure 40 were due to factors affecting the propagation rather than the generation of fan noise. Specifically, it was suggested that the location of the fuselage-mounted engines relative to the wing affected the propagation of fan noise. Figure 50 shows the location of the JT8D-109 engine relative to the wing-flap configuration of the DC-9-30 airplane. Fan-inlet noise propagating at shallow angles is shielded from microphones under the flight path by the wing-flap system. In addition, fan-inlet, fan-exhaust, and turbine noise must propagate through the turbulent wake from the wing-flap-landing-gear system during forward motion. A detailed description of the analyses performed to account for those effects is reported in reference 21.

The approach used to predict the attenuation due to wing shielding was adapted from the barrier theory described by Beranek in reference 28. The barrier theory, which is based on optical-diffraction (Fresnel) theory, assumed that

only the incident wavefield close to the top edge of the barrier contributed to the wavefield diffracted over the barrier. The barrier was modeled by the wing-flap system, and the noise generated by the fan was assumed to come from a point source.

To account for the differences between static-projected and flyover noise data in the regions outside the shadow zone, it was suggested that the wake generated by the wings, flaps, and landing gear altered the propagation of turbomachinery noise sources. An analysis was therefore performed by applying Rudd's concept of sound scattering by turbulence (ref. 29). Rudd's treatment of the scattering of sound by turbulent jets was modified to represent the similar spreading rates and velocity distributions of the wing-flap-wheel wake.

3.4.1.4 Jet-exhaust sound scattering. - Figure 51 compares the turbine-noise suppression during static and flyover operation measured with and without the acoustically treated turbine reverser installed in the CF6-6D. It shows that more noise reduction was measured in flight than in static operation. On the basis of Rudd's results and an experimental program described in reference 30, which was conducted to investigate shielding and scattering by a jet flow, it was shown that the thickness of the jet was very effective in reducing aft-radiated noise. Comparison of the difference in the fan/ambient shear layer between static and flight operation of the CF6-6D in figure 52 suggested that the increased level of turbine noise in flight is primarily due to the decreased sound scattering through the fan ambient shear layer to the far field during forward motion. To investigate those effects, the sound-scattering theory of Rudd was applied to the CF6-6D and JT9D-59A turbine-static noise levels. The thickness of the JT8D-109 shear layer was estimated to be smaller due to the long duct nozzle configuration. As a result, the effects of sound scattering on JT8D-109 turbine noise were considered to be negligible.

It should be noted that because jet-exhaust sound scattering affects the relative levels of turbine and fan noise in the same 1/3-octave-bands, the source-separation procedures had to be modified. The separation of fan exhaust and turbine noise from flyover noise data, which was based on the

relative turbine noise levels determined from static narrowband data, was modified to increase the turbine noise levels relative to the fan levels in accordance with the decreased scattering effect through the fan ambient shear layer (section 3.2.6).

3.4.1.5 Inlet contour. Figure 53 compares the inlet quadrant spectra for a flight inlet with that of a bellmouth inlet during static operation of the JT9D-20 at static takeoff power. The noise levels with the bellmouth inlet are higher, particularly in the inlet quadrant. Potential-flow studies show that with the production nacelle operated statically the ambient air is drawn in from all directions as in a classical "sink" flow with a stagnation point on the nacelle lip, as in figure 54. The result is that the flow accelerates around the lip, producing regions of high Mach numbers on the inlet walls. During forward motion, flow is ingested along lines nearly parallel to the inlet centerline. As a result, the inlet stagnation point moves inside the nacelle lip (fig. 55), and the high-velocity flow regions are reduced.

That phenomenon is most important in the attenuation of multiple-pure-tone (MPT) noise generated by shock waves from the rotors operating at sonic and supersonic tip speeds. In static operation, MPT noise propagating in the nacelle suffers significant attenuation in traversing the high Mach number regions. During forward motion, MPT noise propagates out of the inlet without appreciable attenuation. Because MPTs occur at frequencies that are integral multiples of the fan shaft speed, the increased noise levels in flight can occur at any point in the spectrum, although they occur typically in the low to middle frequencies. In addition, the increased flows during static operation are typically higher than the optimum flow for the design acoustic-liner impedance, which can affect the attenuation of the propagated discrete tones at the fundamental and the harmonics of blade-passing frequency.

3.4.1.6 Nonpropulsive noise. - The noise generated by the airframe in flight provides a noise floor from which potential engine-noise reductions must be evaluated. At lower fan speeds and with more effective acoustic liners in fan nacelles and discharge ducts, nonpropulsive noise becomes dominant in flight. Figure 56 illustrates the various nonpropulsive noise sources on a

DC-10 airplane configuration. Fluctuating lift forces on the wing-flap system, fuselage, empennage, and open wheel wells during approach result in a lift-dipole source of noise. Drag dipoles are generated by fluctuating drag forces on those components and on the landing-gear structures. The procedures used for defining nonpropulsive noise sources are reviewed in reference 23.

3.4.2 Propagation Effects - Excess Attenuation

Comparison of flyover noise and static-engine noise projected to flight conditions has consistently shown static-projected spectra higher than flight spectra at frequencies greater than blade passage (refs. 6, 7, 9, 11). Since the high-frequency reduction was independent of engine type and observation angle and since no reduction was indicated by microphone measurements in inlet and fan ducts, it is believed to be due to increased atmospheric attenuation over propagation distances usually larger than those for static measurements. Specifically, it is thought that the high-frequency spectral differences are due to excess attenuation, which is defined in reference 31 as the attenuation over and above the attenuation obtained by using current procedures to predict molecular and classical absorption. (ref. 22).

3.4.2.1 Description of problem. - Comparison of CF6-6D static-engine 1/3-octave-band spectra projected to flight conditions and DC-10-10 flyover-noise data (fig. 57) showed that at frequencies greater than blade passage the static spectra were higher than the flight spectra. At the 8000-Hz band, differences of from 10 to 20 dB were common. Observation of narrow-band spectra measured by microphones mounted internally in inlet and fan discharge ducts of the CF6-6D during static and flight operation showed changes in the high-frequency region of the spectra of the order of 2 dB (fig. 58). That result indicated that static and flight high-frequency sound sources were substantially the same. In order to evaluate and to eliminate, if possible, the procedure used for correcting test-day spectra to reference weather conditions as a potential source of the high-frequency error, DC-10-10 flyover noise spectra measured during approach at an altitude of 121 meters for three different weather conditions were compared. The sound-path weather conditions for each run are shown in figure 59; the test-day spectra are shown in figure 60. Comparisons of the spectra and of the weather conditions aloft showed

that two of the spectra were nearly equal and that the weather conditions were similar. However, the high-frequency region of the third spectrum was considerably lower than those of the other two, which was similar to the results in figure 57. Although the temperature profiles were all similar, the humidity profile of the third was considerably lower, which indicated a higher level of atmospheric absorption. Correcting the measured spectra to reference weather conditions by using sound-path weather collapsed the data to approximately the same reference spectrum (fig. 61). That result indicated that the use of ARP 866 to correct measured data to a given set of reference weather conditions on a layered-weather basis was adequate and that it was not the cause of the high-frequency differences in figure 57.

The high-frequency differences observed in figure 57 therefore appeared to be due to increased atmospheric attenuation over propagation distances usually larger than those for static-engine measurements - excess attenuation. The primary cause of excess attenuation was believed to have been sound scattering due to atmospheric turbulence. Secondary causes, such as sound refraction due to temperature and wind gradients and to variations in ground absorption, were shown to have small effects.

3.4.2.2 Test configurations and programs. - The data base for the analysis consisted of measured flight spectra obtained from the DC-9-30 airplane powered by JT8D-109 refan engine (fig. 1) and from the DC-10-40 airplane powered by JT9D-59A engines (fig. 3). For the DC-9-30 flyovers, three microphone locations were used, with a maximum total spacing of approximately 3.2 km. A summary of the DC-9-30/JT8D-109 test data is shown in table 6. For the DC-10-40, two microphone locations were used, with a maximum total spacing of approximately 2.2 km. A summary of the DC-10-40/JT9D-59A test data used is shown in Table 7. The data were recorded during the following types of flyover noise runs with microphones directly beneath the flight path:

1. Approach-altitude flyover at a constant glideslope (table 6a)

2. Level flight at approach altitude with climbout to takeoff altitude at a constant climb angle (table 6b).

3. Takeoff-altitude flyover at a constant climb angle (tables 6a and 7).

In all runs, noise data were measured when there were no temperature inversions, and the weather variations were limited to temperature between 7°C and 17°C and humidities between 30 and 75 percent.

3.4.2.3 Method of analysis. - In order to account for high-frequency differences between static-projected levels and flyover-noise levels, an additional source of atmospheric absorption had to be included, together with the classical and the molecular absorption coefficients defined in reference 22. The additional attenuation is defined as excess attenuation.

High-frequency spectral differences were analyzed by comparing flyover-noise data measured beneath the flight path of a selected airplane configuration at a given power setting. Each flyover-noise spectrum measured at one microphone location was corrected to reference weather conditions by using the sound-path weather measured at incremental heights above the microphone. In order to correct the spectrum to a common altitude (defined as the minimum height over the microphone) and common flight-path profile, reference 22 and spherical divergence were applied to the measured data at each microphone location (fig. 62). That approach had two advantages: The airplane acted as a constant noise source with a uniform pattern of noise emission during each run, and it minimized the effects of changes in weather, in wind speed, and in wind direction that might occur between runs. Also, comparing flight data with flight data made it unnecessary to apply any correction for the effects of forward motion and of the engine installation that would be required for making valid comparisons of static and flight data. But that approach could introduce into the analysis two other variables as potential sources of error -- differences in ground reflection and absorption at different microphone locations and use of two different microphones. In order to eliminate those variables, data from a DC-9 level flight run at takeoff power were compared. The data had been measured overhead at two microphone locations at nearly equal altitudes. Figure 63 shows the resulting comparison of spectra measured at altitudes of 138 m and 149 m and adjusted to the common altitude of 131 m. The spectra are essentially equal at all frequencies, which eliminated microphone and microphone location as possible sources of error in the subsequent analysis.

Figure 64(a) presents a spectral comparison of DC-9-30/JT8D-109 flyover noise measured during one approach run at the close-in altitudes of 262 meters and 113 meters. As was to be expected, the spectrum measured at 262 meters was lower at all frequencies than that measured at 113 meters, because of additional absorption and spherical divergence over a greater distance. The comparison of the two spectra adjusted to the common altitude of 121 meters is shown in figure 64(b). Using the present projection methods of reference 22 and spherical divergence should theoretically have collapsed the two adjusted spectra to a single reference spectrum. However, as is shown by figure 64(b), the high-frequency region of the spectrum from 262 meters is lower, which indicates an additional source of atmospheric attenuation. The discrepancies in the low-frequency range may be considered to be due to ground dip and therefore neglected.

A comparison of DC-9-30/JT8D-109 spectra measured at takeoff power and large distances from the microphones is shown in figure 65. The same kind of comparison for the DC-10-40/JT9D-59A is shown in figure 66. Although the results were similar to those obtained from comparisons at approach altitude, the high-frequency differences measured at the higher takeoff altitudes were smaller, even though the spectra were projected over greater distances. The fact that the high-frequency differences observed at approach altitudes were larger than those observed at takeoff altitudes indicated that excess attenuation was greater closer to the surface of the earth.

3.4.2.4 Variation with altitude. - It is reported in references 31 through 38 that excess attenuation is greater near the earth's surface than at higher altitudes. Specifically, it was shown that there was much excess attenuation below altitudes of approximately 250 meters and little or none above that altitude.

In order to investigate the variation of excess attenuation with altitude, spectral differences derived from approach and takeoff flyover runs of the DC-9-30/JT8D-109 were plotted versus difference in overhead altitude for 1/3-octave-band frequencies greater than 1000 Hz. Because of contamination by background noise, it was not possible to define spectral differences for frequencies greater than 4000 Hz at takeoff. At approach, there was some

contamination at frequencies greater than 6300 Hz. Figure 67 shows the high-frequency spectral differences for flyover-noise runs at approach and takeoff altitudes. At the lower approach altitudes, the spectral differences increased rapidly with distance and frequency. Since the takeoff spectra were projected over greater distances than the approach spectra, it was to be expected that the increased effect of excess attenuation would appear as larger high-frequency differences. However, the rate of increase for the higher takeoff altitudes was not as great as that for lower approach altitudes. That result confirms the findings in references 31 through 38, which indicate that excess attenuation is more pronounced at altitudes less than approximately 250 meters.

3.4.2.5 Variation with frequency. - Two equations for excess attenuation were derived in reference 31. The first assumes an ideal atmosphere, for which sound scattering may be treated as a Bragg diffraction phenomenon. The excess-attenuation coefficient, α_s, is a function of frequency squared. The second assumes a real atmosphere for which, because of the nonhomogeneous and non-isotropic nature of the atmosphere, Bragg diffraction is only an approximation. The excess-attenuation coefficient is then a function of the one-third power of frequency.

In order to investigate the variation of excess attenuation with frequency, the excess-attenuation coefficients per 330 meters were calculated as functions of ΔSPL and ΔAlt, where ΔSPL is defined as the difference in sound pressure level between the measured and the projected spectra and ΔAlt is the distance over which the spectrum was projected. Excess-attenuation coefficients calculated at approach for the DC-9-30 are shown in figure 68. In the curve of figure 68, excess attenuation is a function of the 1.3 power of the frequency, which lies between frequency squared for a homogeneous atmosphere and the one-third power of the frequency for a nonhomogeneous atmosphere described in reference 31. Figure 69 shows excess-attenuation coefficients at takeoff for the DC-9-30 and the DC-10-40. Because of the smaller effect of excess attenuation at the higher takeoff altitudes, the absorption coefficients for takeoff are smaller. An empirical formula for excess attenuation at takeoff is not presented, since, because of background-noise contamination, the spectral differences could not be defined clearly at frequencies greater than 4000 Hz. The averages of the excess-attenuation coefficients for approach

and takeoff altitudes are shown in figures 70 and 71, respectively. From empirical correlations of DC-9-30 and DC-10-40 flyover noise, the effects of excess attenuation in the atmosphere were derived. The correlations show significant data scatter in the spectral differences at high frequencies. In order to more clearly define the mechanisms of excess attenuation and to develop more accurate and reliable prediction methods more work is required. In order to reduce the scatter, data would have to have been recorded under strictly controlled conditions. To obtain the necessary conditions in an actual atmospheric environment would have been very difficult, if not impossible, since the properties and the conditions of the air (temperature, humidity, velocity, turbulence, composition, etc.) in the atmosphere vary constantly in time and space.

4. DISCUSSION OF RESULTS

4.1 EFFECTS OF FORWARD MOTION AND OF ENGINE INSTALLATION ON JET- AND CORE-NOISE

Comparisons of individual static and flight jet- and core-noise levels and normalized spectra for the DC-9-30/JT8D-109 and DC-10-40/JT9D-59A are presented in this section. The differences between static and flight spectra and between OASPLs are discussed in terms of the effects of forward motion and of engine installation.

4.1.1 Static-to-Flight Comparisons of JT8D-109 Data

Comparisons of static and flight total low-frequency noise and individual jet and core noise components for the JT8D-109, correlated by using primary-jet velocity as the abscissa, are presented in figures 72, 73 and 74 for angles of 50°, 90°, and 140°, respectively. At 50° to the inlet centerline (fig. 72), the low-frequency noise levels measured in flight crossed over the corresponding static levels for jet velocities less than 200 m/sec, because the core-noise levels generated in flight are higher than the levels generated statically. The corresponding jet-noise levels generated in flight are lower than those generated statically. At 90° (fig. 73), flight and static core noise are nearly equal, but the difference between flight and static jet noise levels has increased relative to the difference shown in figure 72. At 140° (fig. 74), the measured low-frequency noise and the individual jet and core noise components are all lower in flight.

In flight, core-noise levels are higher in the inlet quadrant (fig. 72), equal at 90° (fig. 73), and lower in the exhaust quadrant (fig. 74) than the corresponding static data, which suggested that convective amplification could be important. The differences between flight and static core OASPLs were therefore plotted versus inlet angle for six different jet velocities with approximately the same airplane velocity (V_a = 76.2 $\pm$ 9.0 m/sec) and compared with the convective amplification predicted theoretically for a moving point source. Specifically, the changes in noise levels caused by the relative

motion of a point source with respect to an observer is given by

$$\Delta OASPL = 40 \log_{10} (1 - M_a \cos \theta \ ) \qquad (1)$$

where M_a is the airplane Mach number and θ is the angle between the inlet centerline and the observer (refs. 20, 39, and 40). Figure 75 shows good agreement between the data and the predicted results for convective amplification of core noise.

Comparison of figures 15 and 24 showed no significant differences between static and flight core-noise spectral shapes. But the peak frequency appeared to be Doppler-shifted, as is suggested by figure 76, in which the ratio of the flight-to-static core peak frequencies is plotted versus inlet angle for five jet velocities, all with the same airplane velocity.

To investigate the differences in jet-noise levels between flight and static conditions resulting from the combined effect of relative velocity and convective amplification (ref. 16), a velocity exponent m was calculated and plotted versus inlet angle for seven jet velocities (fig. 77). The expression used to define m is given by

$$m = \frac{\Delta OASPL - 10 \log_{10} (1 - M_a \cos \ )^{-1}}{10 \log_{10} (V_{rel}/V_{jp})} \qquad (2)$$

The results indicated that at inlet angles less than or equal to 90° the value of m is approximately equal to 3.7. At inlet angles greater than 90°, m increases with increasing angle. To define the separate contributions of relative velocity and convective amplification to jet noise will require further analyses.

Figure 78 compares static and flight normalized jet-noise spectra for angles of 50°, 90°, and 140°. In flight, the normalized jet spectral shapes are broader, with higher levels for all angles than the static spectra at low Strouhal numbers. It is not possible to reconcile the differences by considering Doppler effect alone. Again, to fully understand the jet spectral

differences will require further analyses.

4.1.2 Static-to-Flight Comparisons of JT9D-59A Data

Comparisons of static and flight total low-frequency noise and the individual jet and core noise components for the JT9D-59A are presented in figures 79, 80, and 81 for angles of 50°, 90°, and 120°, respectively. At 50° (fig. 79) and jet velocities above 305 m/sec (jet velocities corresponding to takeoff power), the flight jet-noise levels are lower than the corresponding static levels even though the core-noise levels measured in flight are higher. At lower jet velocities corresponding to approach power, the flight jet-noise and total-noise levels are higher than the corresponding static levels by as much as 5 dB. At 90° (fig. 80) and in flight, the core-noise levels are about equal and the jet-noise levels are lower. At 140° (fig. 81), both core- and jet-noise levels are lower in flight. However, at very low jet velocity (V_{jp} < 216 m/sec), the decrease in jet noise is considerably less than the decrease observed at higher jet velocities. The lessened decrease in jet noise at low jet velocities is attributed to low frequency noise generated by the impingement of the fan jet flow on the trailing flaps of the DC-10 during approach operation. It should be noted that the primary-jet velocity may not be the proper criterion to use for comparing static-projected jet-noise levels with flyover-noise levels for high-bypass-ratio turbofan engines at very low power setting, where the noise from the fan jet can be more important than the noise from the primary jet.

The higher core noise levels in the inlet quadrant (fig. 79), the equal levels at 90°, (fig. 80), and the lower levels in the exhaust quadrant (fig. 81), show good agreement with the predicted results for convective amplification (fig. 82). As with the JT8D-109, there are also no significant differences between static and flight core-noise spectral shapes. Again, the core peak frequencies appeared to be Doppler-shifted in flight (fig. 83).

Figure 84 shows the correlation of the flight-effect velocity, m, versus inlet angle for eight jet velocities representing data from takeoff and approach flyover-noise runs. The negative values of m for angles less than

90° correspond to the approach cases. The velocity exponents for the takeoff data are positive for all inlet angles and are very similar to those for the DC-9-30/JT8D-109. The velocity exponents for the approach data showed a different trend: The exponents are positive in the exhaust quadrant and are generally lower than the exponents in the takeoff data. It is believed that another low-frequency noise source, unique to airplane configurations with engines under the wing such as those of the DC-10, is responsible for the trend observed in the velocity exponent obtained from approach data.

4.1.2.1 Masking effect of jet-flap interaction noise. - Figure 3 shows the location of the engines on the DC-10-40 airplane. Two engines are mounted under the wings, and a third is mounted in the vertical tail 68 feet aft of the wing engines. During approach (see fig. 85), parts of the flaps are extended out and deflected downward, making a flap angle between 35° and 50°. A small central portion of the flap was left unchanged, to allow the hot jet exhaust from the primary nozzle of the engine under the wing to pass through. It is believed that the bigger diameter of the fan jet exhaust caused the flow to impinge on part of the deflected flaps and generated a low-frequency noise (jet-flap-interaction noise). To investigate that effect, flyover noise from a DC-10-10 airplane powered by General Electric CF6-6D engines was analyzed for conditions where the airplane was flown at constant airspeed and power setting but with different flap-deflection angles.

Figure 86 shows a comparison of the flyover-noise levels for the airplane flown at low power settings with the same airspeed but with different flap-deflection angles (0° and 15°). At all inlet angles there are no significant differences in low-frequency noise between the two sets of flyover noise. At a higher power setting there are significant increases in the low-frequency (50 to 250 Hz) region of the spectrum for flap deflections greater than 30°. The increase in low-frequency noise is maximum at inlet angles from 50° to 60°, smaller at 90°, and zero for angles greater than 120° (fig. 87). Those results indicated that for the DC-10 airplane with engines under the wing and with flap deflection greater than 30°, the interaction of the fan jet with the flap increases the levels of the low-frequency part of the spectrum by as much as 5 dB.

Jet-flap-interaction noise has peak frequencies and spectral shapes very similar to those of jet noise, and it is difficult to distinguish between their spectra. But since jet-flap interaction noise has a frequency range between 50 and 250 Hz, it does not affect the separation of core noise levels and spectra from the measured low-frequency noise at power setting corresponding to the approach flight conditions.

On the basis of those results, it was concluded that at high jet velocities and small flap deflection corresponding to takeoff conditions the jet noise levels were not affected by jet-flap-interaction noise. At low jet velocities and large flap deflections corresponding to approach conditions, the core-noise levels were not affected, but the corresponding jet-noise levels were contaminated by jet-flap-interaction noise.

4.1.3 Comparison With Proposes ANOPP Method

The individual jet- and core-noise components separated from DC-9-30/JT8D-109 and DC-10-40/JT9D-59A static-engine and flyover noise provide an excellent data base for comparing, on a noise-source basis, the prediction of jet- and core-noise flight effects calculated by the proposed ANOPP method (ref. 20). As are shown in figures 75 and 82, the DC-9-30/JT8D-109 and the DC-10-40/JT9D-59A data agreed quite well with the $-40 \log_{10} (1 - M_a \cos \theta)$ expression given for the effect of convective amplification on core-noise levels in flight. The same expression is used in reference 20 to correct core-noise levels for convective amplification. Comparison of the predicted and the measured spectral shapes of core noise (fig. 88) shows that the ANOPP core spectral shape is more broad than those derived for the DC-9-30/JT8D-109 and the DC-10-40/JT9D-59A. Also, as shown in figures 76 and 83, the core-noise peak frequencies for those data appeared to be Doppler-shifted in flight, as the ANOPP method predicts.

Figures 89 and 90 compare the predicted and the measured jet-noise reductions due to the combined effects of relative velocity and convective amplification for the DC-9-30/JT8D-109 and the DC-10-40/JT9D-59A, respectively. The figures show good agreement between measured and predicted noise reductions for angles up to and including 130°. For angles greater than 130°, the

predicted noise reductions were consistently less than the measured values. Predicted and the measured spectral shapes for the jet-noise component for the DC-9-30/JT8D-109 and DC-10-40/JT9D-59A in flight are shown in figures 91 and 92, respectively. Comparisons of the jet-noise spectral shapes for angles of 50° to 120° show that the predicted levels for both DC-9-30/JT8D-109 and DC-10-40/JT9D-59A are lower at the high Strouhal numbers and higher at the low Strouhal numbers than the corresponding spectra predicted by the ANOPP method. At the peak Strouhal number, the predicted levels show good agreement.

4.2 EFFECTS OF FORWARD MOTION, PROPAGATION, AND ENGINE INSTALLATION ON TURBOMACHINERY NOISE

4.2.1 Engine-Installation and Propagation Effects

To identify the effects of forward motion on fan and turbine noise sources, the static-projected data in figures 41, 43, and 46 were first adjusted on a source basis for the effects of engine installation. Figure 93 shows comparisons of DC-9-30 flyover noise levels and JT8D-109 static-projected noise levels at approach power, corrected for wing shielding at an angle of 30° (fig. 93a) and for sound scattering in the wing-flap-wheel wake at 90° and 120° (figs. 93b and c), respectively. In addition, DC-9-30 nonpropulsive noise levels, which affects the static spectra primarily below blade passing frequency were included. Although the agreement between the spectra was improved, applications of the barrier and of the sound-scattering theories did not entirely account for the static-to-flight differences. The remaining high-frequency differences could be due to conservative modeling techniques in the application of those theories, but it was thought that the remaining high-frequency differences were due to the effects of excess attenuation in the atmosphere.

Figure 94 shows JT8D-109 static-noise levels at approach power corrected for engine installation and for excess attenuation in the atmosphere (sect. 3.4.2) and compared with DC-9-30 flyover-noise levels. The data show that excess attenuation adequately accounts for the remaining high-frequency differences shown in figure 93. As a result, it can be seen that the static-to-flight differences for the DC-9-30/JT8D-109 airplane configuration are

due primarily to installation and propagation effects, as opposed to the effects of forward motion on turbomachinery-noise generation.

Figures 95 and 96 show DC-10-10 and DC-10-40 flyover spectra compared with CF6-6D and JT9D-59A static-projected spectra, respectively, at approach power settings, corrected for relative engine location, fuselage shielding, jet-exhaust-sound scattering, and nonpropulsive noise. In the inlet quadrant (fig. 95a) and at overhead angles (fig. 95b) the engine-installation effects reduce the CF6-6D static-projected levels and improve the static-to-flight agreement by a small amount for frequencies at and above blade-passing frequency. In the aft quadrant (fig. 95c), the corrections increase the static-to-flight differences. For frequencies below blade passing, the inclusion of DC-10-10 nonpropulsive noise levels improves the agreement at the inlet and the overhead angles. Figure 96 shows similar results for the JT9D-59A static-projected levels corrected for engine installation. Although the agreement between static and flyover noise levels was improved by incorporating installation effects in the CF6-6D and JT9D-59A static-engine noise levels, significant differences remain at frequencies equal to and greater than blade passage frequency.

In section 3.4.2 it was shown that when noise data are projected over large differences in acoustic range, significant high-frequency differences due to excess attenuation in the atmosphere are found. Figure 97 shows a comparison of CF6-6D static-projected noise levels corrected for excess attenuation and compared with DC-10-10 flyover noise levels. In the inlet quadrant (fig. 97a), the static-to-flight agreement is improved for frequencies equal to and higher than blade passing. At overhead (fig. 97b), and in the aft quadrant (fig. 97c), the correction for excess attenuation improved the agreement above 6300 Hz, where the static-projected levels were higher At the frequencies where fan harmonics and turbine tones occur in the same 1/3-octave band, the agreement was not improved. Figure 98(a) shows similar results in the inlet quadrant for the JT9D-59A static-projected levels corrected for excess attenuation and compared with DC-10-40 flyover-noise levels. At overhead (fig. 98b), and in the aft quadrant (fig. 98c), where the flight-noise levels were higher than the static-projected levels, less agreement was

obtained for all frequencies above blade passing. Although the static-to-flight agreement was improved, significant high-frequency differences remain in the levels of the fan fundamental tone and in the increased flight levels at the frequency bands containing both fan harmonics and turbine tones.

To determine the source characteristics at those frequencies, narrowband data were analyzed. Inlet and fan discharge duct measurements with flush-mounted Kulite microphones (ref. 9 and fig. 58) have shown that in flight the levels of the fan fundamental are lower below cutoff and approximately equal above cutoff, but that the levels of the fan harmonics and of broadband noise remained essentially unchanged. As a result, it was thought that the mechanisms of noise generation for the fan fundamental tone during forward motion are different from those under static conditions. In addition, the high-frequency differences at overhead and at aft quadrant angles are the result of forward-motion effects on the propagation of turbine noise and not on fan noise (sect. 4.2.4).

4.2.2 Effects of Forward Motion

4.2.2.1 Convective amplification. - In order to investigate the effects of forward motion on the dynamic, or convective amplification (refs. 39 and 41) of turbomachinery-noise sources, static-to-flight differences in the fan-broadband noise levels at the blade passing frequency of the fan were plotted as functions of inlet angle in figure 99 for the DC-10-40/JT9D-59A and DC-10-10/CF6-6D. The fan broadband levels derived in section 3.2.5.2, were used rather than discrete tone levels, because (1) the effect of convection on tone levels is masked by differences between static and flyover noise generation and (2) narrowband data measured in the inlet duct (ref. 9 and fig. 58) show that the broadband noise levels remain essentially constant with forward motion. For flight Mach numbers equal to 0.282 and 0.296, which are typical for high-approach or takeoff flight speeds, the data follow the predicted effects for the motion of a point source discussed for core noise in section 4.1.1. For low flight speeds (M = 0.227 and 0.220) the trends are similar in the inlet quadrant, but, in the aft quadrant the flyover and static levels are nearly equal for the peak-aft noise angles. In the aft quadrant, the increased flight levels relative to the predicted convection effects are similar to the

trends noted earlier in section 4.2.1 for the high frequency spectra. As a result, the discrepancies at the fan-blade passing could be due to increased turbine-broadband levels generated in flight at the low power settings.

The 40 log relationship, discussed above, was assumed to hold for all fan speeds for both fan and turbine noise sources. Correcting the JT8D-109 static-projected spectra (fig. 94) for convection will improve the static-to-flight agreement as shown in figure 100. Correcting the static-projected spectra in figures 97 and 98 for the CF6-6D and JT9D-59A, respectively, will not, however, account for the remaining differences which were assumed to be due to forward motion effects on source noise generation.

4.2.2.2 Noise generation. - In the following discussions, the effects of fan-noise generation and of the interaction of the fan harmonics and turbine tones will be presented. As a result of trends noted in narrowband spectra (fig. 58), the effects of fan-noise generation will be restricted to the blade-passing-frequency tone.

The increased level of the fan fundamental tone under static conditions was assumed to be due to differences between the mechanisms of noise generation in static and in flight environments. Specifically, under static conditions, there is sufficient inflow distortion to cause the generation of a strong blade-passing-frequency tone (rotor-turbulence interaction) for approach power settings (refs. 42 through 44). The absence or the reduced level of the fan fundamental tone during forward motion indicates that the inlet flow is sufficiently clean and free of disturbances to enable the cut-off conditions for which the CF6-6D and JT9D-59A engines were designed to be realized at approach power settings. Since it is a difficult task to predict the theoretical change in tone levels due to inflow distortion, an empirical approach was used.

The empirical approach required determination of the strength and the directivity characteristics of the fan fundamental tone from the static and flight spectra. The broadband levels at the blade-passing frequency derived in section 3.2.5.2 were therefore used to define the strength of the fan fundamental tone in terms of the relative level of the total fan noise to the

fan broadband noise (i.e., a comparison similar to a signal-to-noise comparison) at the blade-passing frequency. The relative levels were obtained for a wide range of angles and power setting; they are shown in figures 101 and 102 for the DC-10-10/CF6-6D and DC-10-40/JT9D-59A airplanes, respectively. The data show the increased level of the static tone relative to the flight tone and the corresponding broad directivity pattern at all fan speeds. At supersonic tip speeds ($N_1/\sqrt{\theta} \geq 3063$ RPM for the CF6-6D and $N_1/\sqrt{\theta} \geq 3212$ RPM for the JT9D-59A), the flyover data show a lobed directivity pattern, in contrast to a relatively broad shape for subsonic tip speeds. At higher tip speeds, static and flight directivity collapse in good agreement.

4.2.3 Interpretation of Static-to-Flight Differences

4.2.3.1 Spinning-mode theory. - Interpretation of the differences between the static levels and the flight levels of the fan fundamental tone requires identification of the three sources of noise at blade-passing frequency - the rotor-alone sound field, the rotor-stator-interaction sound field, and the sound field generated by the interaction of the fan rotor with unsteady or distorted inflow. Tyler-Sofrin theory (ref. 45) pointed out the cutoff phenomena associated with the spinning modes of rotor-alone and rotor-stator-interaction noise. At the blade-passing frequency of the fan fundamental for a rotor with B blades and V stator vanes, a criterion was established for determining whether the spinning mode pattern of order m would propagate or decay in a cylindrical hardwalled duct with uniform axial flow. The criterion was given by the cutoff ratio ξ_m as

$$\xi_m = \frac{M_m}{M_m * \sqrt{1 - M_x^2}} \tag{3}$$

The tip Mach number of the patterns is given by

$$M_m = \frac{BM_t}{B + kV} \tag{4}$$

Those equations apply for the first radial mode for a spinning mode of order m, given by the denominator of equation (4). Propagation of the pattern occurs if ξ_m is greater than unity; decay occurs if ξ_m is less than unity. For propagating modes, it was shown that the spinning-mode pattern traverses

the duct in a spiral angle of propagation expressed as a function of the circumferential Mach number of the pattern.

Homicz and Lordi (ref. 46) have shown that the far-field directivity pattern of the duct acoustic modes can be predicted by using simple cylindrical duct theory. They showed that the location of the principal lobe from an m-order spinning mode can be approximated by the spiral angle, ψ_p, at which the pattern propagates in the duct. As a result, propagating modes with cutoff ratios much greater than unity will propagate at angles of slight inclination to the inlet centerline and modes with $\xi_m \approx 1$ will propagate at right angles to the inlet centerline. If the inlet flow is sufficiently clear and free of distortion, it should be possible to identify the modes generated by rotor-alone noise and by rotor-stator-interaction noise by comparing calculated and measured directivity.

4.2.3.2 Sound fields of rotor-alone and rotor-stator interaction. - Figure 103 shows the cutoff ratios for the first three fan harmonics of the rotor-stator interaction (rotor wake interaction with bypass-outlet guide vanes) and the first two fan harmonics of the rotor-alone as functions of fan rotor speed for the CF6-6D engine. Tyler-Sofrin theory was used to generate the data, for which a hardwall cylindrical duct with uniform axial flow (refs. 45 and 47) was assumed. The effects of inlet length, inlet contour, and acoustic treatment were not included in the analysis. The cutoff ratios were calculated for the first propagating spinning mode and for the first radial mode. The figure shows that the fan fundamental tone due to rotor-stator interaction (m =-42) is above cutoff for fan rotor speeds greater than 3100 RPM. The fan fundamental tone due to the rotor-alone sound field (m = 38) is above cutoff for fan speeds greater than 2900 RPM. At approach power settings, the fan fundamental tone due to rotor-alone or rotor-stator interaction should therefore decay. Similar results were obtained for the cutoff ratios for JT9D-59A rotor alone (m = 46) and for rotor-stator interaction (m =-50) at the fan-blade-passing frequency above fan speeds of 2800 and 3100 RPM, respectively.

The static-to-flight comparisons in figures 101 and 102 can now be interpreted in terms of the modal constituents in the radiated sound field. Figure

101 shows that for fan speeds above a cutoff ratio of unity ($N_1/\sqrt{\theta} = 3063$), the directivity of the DC-10-10 flight data shows distinct lobes at angles of above 50° and 80° to the inlet centerline. At the higher corrected fan speed of 3384 RPM, the flight data again show lobes at angles of 50° and 80° and a broad aft lobe around 120°. According to the approximations in reference 46, the first three radial modes above cutoff for an m = 38 rotor-alone spinning mode should propagate at angles of 50°, 61°, and 78° to the inlet, respectively. At 3384 RPM, the first four radial modes should propagate at angles of 42°, 52°, 63°, and 76°, respectively, and the first two radial modes for the rotor-stator interaction mode (m = -42) should propagate at angles of 121° and 108°, respectively. According to Tyler-Sofrin theory the m = -42 rotor-stator interaction mode spins in a direction opposite to that of the fan rotor (contra-rotating). As the contra-rotating mode propagates forward, it is significantly attenuated as a result of blade-row transmission loss, and the mode therefore propagates to the far field only from the fan discharge ducts. Because 10° intervals were used to reduce the flyover noise data, the individual radial modes are not clearly distinguishable. In spite of that, the flyover directivity pattern for fan speeds above cutoff is in good agreement with the predicted directivity for the principal spinning modes of rotor alone and rotor-stator interaction. The corresponding broad directivity pattern for the static-projected levels can now be interpreted as the result of a large number of modes propagating out of the duct associated with the interaction of the rotor and inflow distortion. The strength of the rotor-distortion tone relative to the broadband noise is essentially constant with increasing fan speed and approximately equal to the flight levels above cutoff at the locations of the principal propagating modes.

Figure 102 shows similar results for the DC-10-40 flyover and JT9D-59A static-engine noise levels. Tyler-Sofrin theory predicts the propagation of an m = 46 rotor-alone spinning mode and the propagation of an m =-50 spinning mode due to rotor-stator interaction at the corrected fan-rotor speeds of 3212 and 3364 RPM. The approximations in reference 46 indicate that at a corrected fan speed of 3212 RPM the first three radial modes of the m = 46 spinning mode should propagate at angles of 55°, 66°, and 77°, respectively, relative to the inlet centerline. At 3364 RPM, the first five radial modes are above

cutoff and propagate at angles of approximately 30°, 41°, 52°, 63°, and 69° respectively. In addition, the m = -50 rotor-stator interaction mode should propagate out the fan discharge ducts at angles of 105° and 120° for the first two radials at 3212 RPM and 104°, 115°, and 124° for the first three radials at 3364 RPM. Again, the predicted and measured flyover directivity are in good agreement.

Figure 104 shows the measured flyover directivity for the DC-9-30 at approach power in comparison with the measured JT8D-109 static directivity for the fan fundamental tone. Tyler-Sofrin theory and reference 46 were again used to predict the principal lobe locations for the cuton rotor-IGV (inlet guide vane) interactions m = 11 and -12, which propagate at angles of small inclination to the inlet centerline out of the inlet and fan discharge ducts, respectively.

For fan speeds below cutoff, references 45 and 46 show that the lobed directivity patterns should be replaced by a broad directivity pattern and that the blade-passing-frequency tone should not propagate. Wind-tunnel testing of various engines (refs. 13 and 48) has demonstrated that for cutoff fan speeds the 1/3-octave band containing the blade-passing-frequency tone is predominantly broadband noise. But figures 101 and 102 show that the flyover directivity patterns show tones propagating in the inlet quadrant at cutoff fan speeds. Figure 101 shows that the DC-10-10 flyover noise has increasing tone strength in a broad directivity pattern for increasing fan speeds up to the cutoff point, where the lobed directivity pattern discussed previously dominates at 3063 RPM. The tone levels in the far field below cutoff appear to be essentially the result of inlet radiated noise. In comparison, the static levels are correspondingly broad in directivity and of increased magnitude at all angles. The broad static directivity is indicative of rotor-turbulence interaction, which results in increased static levels of the fan fundamental tone. Figure 102 shows similar results for the DC-10-40 flyover and the JT9D-59A static noise levels. For fan speeds below cutoff, the flight data show that the relative levels of the propagating tones are nearly constant with increasing fan speed. The levels appear again to be the result of inlet-radiated noise.

There are several possible explanations suggested for the absence of complete tone cutoff in engines so designed. Reference 49 has shown that inlet obstructions such as a protruding temperature probe can disturb the steady inlet flow, resulting in a mechanism of noise generation by induced periodic lift fluctuations on the fan-rotor blades. The mechanism produces a rotor-distortion tone at the blade-passing frequency. The characteristics of the rotor-distortion tone can be modeled by the interaction of the rotor with the wake from a single-upstream stator vane, which, according to Tyler-Sofrin theory (ref. 45), results in a large number of propagating modes at the blade-passing frequency. Like rotor-turbulence interaction under static conditions, the multiple propagating modes are characterized by a broad directivity pattern in the far field. In addition, the interaction of the rotor wakes with the core-stator vanes could be cut-on and could dominate the fan sound field when the rotor-OD OGV (outer-diameter-outlet guide vane) interaction was cutoff. Reference 8 has also suggested that boundary-layer noise could contribute significantly below cutoff to the rotor sound field.

The propagating sound fields for the DC-10-40/JT9D-59A and DC-10-10/CF6-6D were further examined, in an attempt to find out if the noise mechanisms could be contributing to the fan levels below cutoff. The core-stator stage for the JT9D-59A engine had the same number of blades as the outlet-bypass guide vanes, which, according to reference 45, results in a cutoff rotor-stator interaction mode at the lower fan speeds being considered. The JT9D-59A inlet does have an inlet temperature probe several rotor chords upstream of the fan-rotor face. It was therefore suggested that the rotor-probe interaction could be responsible for the cutoff tone strength at the blade-passing frequency for the DC-10-40/JT9D-59A fan-inlet levels (fig.102). But the CF6-6D inlet was free of inlet obstructions, and the rotor/core-stator interaction was also predicted to be cutoff. Wind-tunnel tests of scale-model fans at cutoff fan speeds (refs. 13 and 48) have shown complete absence of tones at the blade-passing frequency, which would tend to eliminate the boundary-layer noise as a principal source below cutoff. Since the directivity of flyover levels below cutoff is similar to that of the static levels (fig. 101), the flyover-tone levels in the inlet quadrant were attributed to residual inflow turbulence in the flight environment. The phenomenon of complete tone cutoff

in wind-tunnel tests may be the result of levels of turbulence in the test section too low to simulate the actual flight environment. The effects of inflow turbulence on the DC-10-40/JT9D-59A flight levels may be masked by the more efficient rotor-probe noise mechanisms. One consequence is that the use of wind-tunnel testing without regard to in-flight turbulence levels may underpredict the flight levels at the fan-fundamental-tone frequency.

4.2.3.3 Fan-fundamental tone correction. - The procedures used to correct the static-to-flight differences at the blade passing frequency of the fan fundamental tone for the effects of noise generation are described below. The corrections account for the static-to-flight differences as functions of directivity angle, fan-rotor-tip Mach number, and circumferential mode number, m. As a first step, the broadband noise contribution to the relative levels of figures 101 and 102 was removed, to yield the absolute tone levels as functions of fan-rotor-tip Mach number. For fan speeds below cutoff an average level of the static and flyover fan-fundamental tones was obtained in inlet and aft quadrants. Above cutoff, the lobes in the flyover directivity pattern were removed, temporarily, to give a broad directivity pattern from which an average inlet and aft-quadrant tone level could be derived and compared with the average levels derived from the static directivity. The increased flight levels at the principal lobe locations were accounted for by a directivity correction described later. The modified directivity above cutoff allows an average inlet and aft quadrant tone level to be derived. Figure 105(a) shows the effect of fan-rotor tip Mach number on the level of the fan fundamental tone in flight and the turbulence-generated tone under static conditions for the DC-10-10/CF6-6D airplane. At the fan speeds examined the levels of the statically generated tone were uniformly higher than the corresponding flight levels. Again, above cutoff the static-to-flight differences reflect average differences without the contribution from propagating duct acoustic modes. In the inlet quadrant, the levels increase with tip Mach number until sonic tip speeds exist where the levels decrease with increasing tip Mach number. In the exhaust quadrnat, the static levels are higher than the flight and increase with tip Mach number except that above cutoff the levels continue to increase with tip Mach number. Similar results for the inlet and exhaust quadrants are shown in figure 105(b) for the DC-10-40/JT9D-59A. The inlet static levels are

again higher than the flight levels for subsonic tip speeds and are equal to the flight levels for supersonic tip speeds. In the aft quadrant, however, the absolute levels for supersonic tip speeds decrease, in contrast to the trends for the DC-10-10/CF6-6D (fig. 105(a)).

The static and flight levels shown in figure 105 were used to determine the static-to-flight correction shown in figure 106. Figure 106(a) shows that in the inlet quadrant the static-to-flight differences for the DC-10 airplanes are consistent. The figure shows that the relative levels for the DC-10-10/CF6-6D and DC-10-40/JT9D-59A are consistent and decrease uniformly with increasing tip Mach number. In the exhaust quadrant (fig. 106(b)), the relative levels are again consistent, remaining constant until approximately sonic tip speeds, where the relative levels decrease uniformly with increasing tip speeds. To correct for forward motion, the static levels of the fan fundamental tone were therefore reduced in the inlet quadrant by the levels in figure 106(a) for angles up to 70° and in the aft quadrant by the levels in figure 106(b) for angles greater than 100°. For overhead angles, an average of the two curves was used. To account for the shape of the flight directivity, the approximations in reference 46 were used to determine the angles of principal-lobe location. At those angles, the static and flight levels are approximately equal (figs. 101 and 102). The correction methods were therefore not applied for the angles of propagating modes. With the directivity and the level correction, the static levels can be corrected at all angles and power settings to approximate the measured flight levels.

The results of including the corrections to those of fan fundamental tone for noise-generation effects and for convective amplification, with the corrections for engine installation and propagation, are shown in figures 107 and 108 for the DC-10-10/CF6-6D and DC-10-40/JT9D-59A, respectively. Figure 107(a) shows that significant improvement is achieved by correcting the CF6-6D-static tone levels at the blade-passing frequency for noise-generation effects. Figure 107(a) shows that below blade passing frequency, inclusion of the effects of convective amplification improves the static-to-flight agreement. In the aft quadrant (fig. 107(c)) there is better agreement for frequencies greater than 5000 Hz, but at the blade passing frequencies of the turbine and fan harmonics there are less agreement. Similarly, figure 108

shows that inclusion of the effects of noise generation on the blade-passing frequency tone improves the JT9D-59A static-to-flight agreement. In the inlet quadrant (fig. 108(a)), the inclusion of convection effects improves the agreement at the broadband frequencies between the fan first and second harmonics and at the high frequencies above 6300 Hz. In the aft quadrant (fig. 108(c)), there is less agreement seen at all frequencies except at the blade-passing frequency.

Figures 109 and 110 show that, in general, the remaining differences are the higher static levels in the inlet quadrant and the lower static levels in the aft quadrant at approach power settings. At takeoff power settings, the DC-10-10/CF6-6D comparisons show higher static levels in the inlet quadrant, except at 50° from the inlet, with otherwise good agreement. The DC-10-40/JT9D-59A comparisons show higher static levels in both inlet and aft quadrants. In figure 107, the higher CF6-6D static levels in the inlet quadrant are due to differences at frequencies greater than 3150 Hz. The static-to-flight differences in the aft quadrant are due to the reduced static levels at the fan-harmonics/turbine-blade-passing frequencies. In figure 108 the agreement is relatively good in the inlet quadrant, but less agreement is found at the fan-harmonic/turbine-blade-passing frequencies. Figure 111 shows that at takeoff power the static-to-flight differences for the DC-10-10/CF6-6D are due to the propagation of MPT noise in flight and the higher static levels above 2500 Hz. Figure 112 shows that for the DC-10-40/JT9D-59A the propagation of MPT noise is not a factor and that the static-to-flight differences are due to the higher static levels for the fan harmonics.

The corrections to the fan fundamental tone for forward motion effects were not applied to the JT8D-109 fan levels as comparisons of far field data did not exhibit appreciable differences at the blade passing frequency after inclusion of engine installation, propagation and convection effects. Figure 113 shows that the remaining static-to-flight differences in PNLT are negligible in comparison to those for the DC-10-10/CF6-6D and DC-10-40/JT9D-59A.

4.2.4 High-Frequency Spectral Differences

In summary, the prominent static-to-flight differences in turbomachinery noise levels are at takeoff power, where, in flight, MPTs propagate out the inlet at frequencies below blade passing, and at approach power, where turbine and fan discrete tones occur in the same 1/3-octave band. To account for the propagation of MPTs in flight, more work will be required to account for the effects of inlet contour on the inlet wall velocities during static and flight operation. At approach power settings, the flight levels were higher than those measured statically at the fan/turbine-blade-passing frequencies. To account for the differences, the static and flight source characteristics had to be examined.

In section 4.2.2.1, the predicted effects of convective amplification were found to differ from the measured data in the aft quadrant at approach power settings. Figure 114 shows typical comparisons of noise data from Kulite (flush-mounted) microphones in the CF6-6D fan-discharge ducts during static and flyover operation. The levels of the fan harmonics and broadband noise remain essentially unchanged. Figure 51 compared the turbine noise suppression during static and flight operation measured with and without an acoustically treated turbine reverser installed in the CF6-6D. More noise reduction was measured in flight, which suggests that turbine noise increases during forward motion (figs. 107 and 108).

To investigate the differences further, the directivity of the tone levels at the 1/3-octave bands containing both fan and turbine noise were examined in a manner similar to that described in section 4.2.2.2. Figure 115 presents a comparison of DC-10-10 flyover and CF6-6D static-corrected levels and directivity for the 1/3-octave band containing the fan second harmonic, which is also shared by one or more turbine tones. At takeoff power settings the relative tone strengths are equal. At approach power settings, however, the flight data are higher at overhead and aft quadrant angles. The static and the flyover directivities appear to cross. The effects of source generation or inflow turbulence would tend to make the static levels higher, which is contrary to the aft-quadrant results. In addition, since the fan harmonics are well cuton, the rotor-stator-interaction modes should propagate at angles

of shallow inclination to the inlet centerline, which suggests that modal constituents are not the cause of the observed differences. Similar results are shown in figure 116 for the DC-10-40/JT9D-59A at the third harmonic frequency.

It was thought that a scattering phenomenon similar to that described in reference 29, occurring in the CF6-6D and JT9D-59A fan ambient shear layers was responsible for the apparent attenuation of turbine noise in the aft quadrant under static conditions. It has been shown that the fan ambient shear layer is thicker statically than the flight shear layer (fig. 52). The application of the effects of jet-exhaust sound scattering to the levels described in section 4.2.1 did not, however, account for the static-to-flight differences. As a result, it was suggested that the turbine levels, spectra, and directivities, which were derived from static data, are insufficient and that more work would be required to define the static levels and the effects of forward motion on turbine-noise propagation.

5. STATIC-TO-FLIGHT CORRECTION

The use of static engine noise data to predict airplane/engine flyover noise requires the separation of the total measured levels into the principal noise sources which include:

1. Jet Noise
2. Core Noise
3. Fan Inlet Noise
4. Fan Exhaust Noise
5. Turbine Noise

Based on the desired flight path profile, each engine noise-source levels must be extrapolated to the far field using the engine directivity angle and acoustic range unique to each engine on the airplane. The source levels are then corrected for spherical divergence and atmospheric absorption using standard techniques.

In addition, each engine noise source must be corrected for the effects of engine installation, atmospheric propagation, and forward motion.

JET NOISE	-	Excess Attenuation Relative Velocity Exponent - m (or ANOPP method)
CORE NOISE	-	Excess Attenuation Doppler Shift Convective Amplification
FAN INLET	-	Wing/Flap Shielding Wing/Flap/Wheel Wake Sound Scattering Fuselage Shielding Inlet Contour Excess Attenuation Doppler Shift Convective Amplification Noise Generation - Rotor - Turbulence Interaction
FAN EXHAUST	-	Wing/Flap/Wheel Sound Scattering Excess Attenuation Doppler Shift Convective Amplification Noise Generation
TURBINE	-	Wing/Flap/Wheel Wake Sound Scattering Jet Exhaust Sound Scattering Excess Attenuation Doppler Shift Convective Amplification

In addition, sources of airframe or nonpropulsive noise and jet/flap interaction noise must be included in the flyover noise prediction.

6. CONCLUSIONS

The effects of forward motion on airplane-engine noise were investigated by comparing separated engine-noise sources from static-engine and flyover noise data for DC-9-30/JT8D-109, DC-10-10/CF6-6D, and DC-10-40/JT9D-59A airplane configurations. The results are summarized below.

1. Static-engine data should be adjusted, on a noise source basis, for the effects of forward motion, engine installation, and propagation and then projected to flight conditions, for each engine as functions of source path-angle, directivity angle, and acoustic range relative to the ground microphone.

2. The effect of convective amplification on core-noise and turbo-machinery noise levels caused by the motion of the engines with respect to an observer agreed with the theoretical relationship, $-40 \log (1 - M_a \cos \theta)$, derived for a moving point source.

3. The shift in core noise peak frequency agreed with Doppler shift effects, $(1 - M_a \cos \theta)$.

4. At all angles of inclination from the inlet centerline, the levels of jet noise generated in flight were lower than those generated statically. The largest differences occurred in the exhaust quadrant. The lower levels measured in flight are due to the combined effects of relative velocity and convective amplification. Further analyses and tests are required to determine the separate contributions of those effects on jet noise.

5. In flight, the normalized jet spectral shapes were broader, with higher levels at low Strouhal numbers than those of the static spectra. Those spectral differences had been observed at all angles. It was not possible to reconcile the differences by considering Doppler effect alone and to understand them will require further analyses.

6. For the DC-10 airplane with engines under the wing and flaps with flap deflection greater than 30°, the jet-flap-interaction noise generated by the impingement of the fan-jet exhaust on the deflected flaps, was responsible for higher low-frequency noise levels in flight during approach conditions.

In the inlet, the effect can be as much as 5 dB. It was significantly less for the exhaust.

7. The differences between static and flight jet noise levels were correlated in terms of a relative velocity exponent as a function of directivity angle. The corresponding exponents for the DC-9-30/JT8D-109 and the DC-10-40/JT9D-59A followed similar curves.

8. Comparisons of measured and ANOPP-predicted jet noise reductions for the DC-9-30/JT8D-109 showed good agreement for angles of 40 degrees to 130 degrees. The predicted jet noise and core noise spectral shapes show good agreement at the peak frequencies for both the DC-9-30/JT8D-109 and DC-10-40/JT9D-59A. At the higher frequencies ANOPP overpredicts both DC-9-30/JT8D-109 and DC-10-40/JT9D-59A levels. At the lower frequencies ANOPP overpredicts DC-9 levels and underpredicts the DC-10 levels. The jet noise reductions predicted by ANOPP for the DC-10-40/JT9D-59A are in good agreement with those measured at higher jet exit velocities, however, the levels at the low to mid velocities are overpredicted.

9. The static-to-flight differences (the differences between static-projected and flyover-noise levels) for the DC-9-30/JT8D-109 airplanes were found to be due to wing shielding, wake sound scattering, and convective amplification.

10. For approach power settings the effects of engine location and of fuselage shielding on DC-10 flyover noise are canceled by the effects of convective amplification. The improved agreement in the mid-frequency range is obtained by including DC-10 nonpropulsive noise in the static-projected noise levels.

11. The high-frequency static-to-flight differences were shown to be smaller if excess attenuation in the atmosphere was taken into account. Further analyses are required to more accurately determine the absorption coefficients as functions of altitude and frequency.

12. Acoustic measurements with far-field microphones indicate that the static-to-flight differences in fan noise are due primarily to differences in noise generation at the fan-blade-passing frequency. Static data are

characterized by a broad directivity pattern with increased levels due to inflow distortion that must be corrected to the lobed directivity in flight, which is due to the propagation of spinning and radial modes for rotor-alone and rotor-stator interaction tones above cutoff.

13. The presence of propagating fan tones in flyover-noise measurements at cutoff fan speeds was attributed to residual inflow distortion during forward motion. Further analysis will be required to isolate the particular noise mechanisms that generate the blade-passing-frequency tone.

14. More work will be required to define the effects of inlet contour on the propagation of multiple-pure-tone noise at supersonic fan tip speeds.

15. The remaining static-to-flight differences are characterized by the increased flight levels at the 1/3-octave bands containing both fan harmonics and turbine tones. Measurements have suggested that the fan harmonics and broadband noise are the same in static and in flight conditions, which suggest that turbine noise becomes more prominent in flight. It is thought that a scattering phenomenon is responsible for reduced static levels of turbine noise in the aft quadrant. More work is required to define the turbine spectrum and the directivity shapes under static and under flight conditions and the effects of forward motion on turbine-noise propagation.

The results show the importance of properly identifying static and flight engine noise source levels, spectra, and directivities and of adjusting the static noise levels for forward motion on a noise source basis.

7. SYMBOLS

A_p	primary nozzle area, m^2
B	number of fan rotor blades
BPF	blade passing frequency, Hz
Bl	fan booster stage BPF, Hz
dB	Decibel
D, D_p	diameter of primary nozzle, m
f	1/3-octave-band center frequency, Hz
f_{peak}	core noise peak frequency, Hz
F	fan BPF, Hz
Hz	Hertz
m	flight-effect velocity exponent
m	circumferential mode number
M, M_a	airplane flight Mach number
M_m	tip Mach number of spinning mode pattern
M_m^*	cutoff tip Mach number of spinning mode pattern
M_t	fan-rotor tip Mach number
M_x	axial Mach number of inlet flow
MPT	multiple pure tone
N	static core-noise OASPL versus jet velocity correlation slope
OASPL	overall sound pressure level, dB
PNLT	tone-corrected perceived noise level, dB
SPL	sound pressure level, dB
T	turbine BPF, Hz
V	number of fan stator vanes

V_a	airplane flight speed, m/sec
V_{jp}	primary jet velocity, m/sec
V_{rel}	relative jet velocity, $V_{jp}-V_a$, m/sec
α_s	excess attenuation coefficients, dB/330 m
ΔOASPL	difference between static and flight OASPL, dB
ΔSPL	difference between static and flight SPL, dB
ΔAlt	difference in slant range for projection on one spectrum to another, m
ϵ_m	cutoff ratio of mth circumferential mode
θ	angle between inlet centerline and observer, deg
σ^2	variance defined as the sum of the square of the differences between measured and estimated SPLs for 1/3-octave-band center frequency to to 10,000 Hz
ψ_p	principal lobe location for a particular circumferential and radial mode number, deg

REFERENCES

1. Anon., "Jet Noise Prediction", Society of Automotive Engineers, AIR 876, 1965.
2. Colos, G. M., "Estimating Jet Noise", Aeronautical Quarterly, Vol. 14, 1963.
3. Ffowcs Williams, J. E., "The Noise from Turbulence Convected at High Speed", Philosophical Transactions of the Royal Society, Vol. A255, 1963, pp. 469-503.
4. Bushell, K. W., "Measurement and Prediction of Jet Noise in Flight", AIAA Preprint No. 75-461, Hampton, Virginia, 1975.
5. Munoz, L. J., "727/JT8D Jet and Fan Noise Flight Effects, FAA-D-76-110, August 1976.
6. Merriman, J. E. et. al., "Forward Motion and Installation Effects on Engine Noise", AIAA preprint No. 76-584, Palo Alto, California, 1976.
7. Feiler, C. E., and Merriman, J. E., "Effects of Forward Velocity and Acoustic Treatment on Inlet Fan Noise", AIAA Preprint No. 74-946, Los Angeles, California.
8. Cumpsty, N. A., and Lowrie, B. W., "The Cause of Tone Generation by Aeroengine Fans at High Subsonic Tip Speeds and the Effect of Forward Speed", ASME Preprint No. 73-WA1GT-4, Detroit, Michigan, 1973.
9. Merriman, J. E., and Good, R. C., "Effect of Forward Motion on Fan Noise", AIAA Preprint No. 75-464, Hampton, Virginia, 1975.
10. Plucinksy, J. C., "Quiet Aspects of the Pratt and Whitney Aircraft JT15 Turbofan", SAE Business Aircraft Meeting, Preprint 730289, 1973, Wichita, Kansas.
11. Roundhill, J. P., and Schaut, L. A., "Model and Full Scale Test Results Relating to Fan Noise in Flight Effects", AIAA Preprint No. 75-465, Hampton, Virginia, 1975.
12. Lowrie, B. W., "Simulation of Flight Effects on Aero Engine Fan Noise", AIAA Preprint No. 75-463, Hampton, Virginia, 1975.
13. Heidmann, M. F., and Dietrich, D. A., "Simulation of Flight-Type Engine Fan Noise in the NASA-Lewis 9 x 15 Anechoic Wind Tunnel" NASA TMX-73450, 1976.

14. Zwieback, E. L., "Flyover Noise Testing of Commercial Jet Airplanes", AIAA Journal of Aircraft, Vol. 10, No. 9, 1973, pp. 538-542.
15. Packman, A. B., Ng, K. W. and Paterson, R. W., "Effect of Simulated Forward Flight on Subsonic Jet Exhaust Noise", AIAA Preprint No. 75-869, Hampton, Virginia, 1975.
16. Cocking, B. J. and Bryce, W. D., "Subsonic Jet Noise in Flight Based on Some Recent Wind-Tunnel Results", AIAA Preprint No. 75-462, Hampton, Virginia, 1975.
17. Cocking, B. J., "The Effect of Flight on Subsonic Jet Noise", AIAA Preprint No. 76-555, Palo Alto, California, 1976.
18. Tanna, H. K. and Morris, P. J., "Inflight Simulation Experiments on Turbulent Jet Mixing Noise", AIAA Preprint No. 76-554, Palo Alto., California, 1976.
19. DeBelleval, J. F., Chen, C. Y. and Perulli, M., "Investigation of Inflight Jet Noise Based on Measurements in an Anechoic Wind Tunnel", Paper presented at the 6th International Congress on Instrumentation in Aerospace Simulation Facilities, Ottawa, September 1975.
20. Stone, J. R., "Flight Effects on Exhaust Noise for Turbojet and Turbofan Engines - Comparison of Experimental Data with Prediction". NASA TMX-73552, 1976.
21. "DC-9 Flight Demonstration with Refanned JT8D Engines - Final Report, Volume IV, Flyover Noise", NASA CR-134860, Douglas Aircraft Company, 1975.
22. "Standard Values of Atmospheric Absorption as a Function of Temperature and Humidity for Use in Evaluating Aircraft Flyover Noise", SAE ARP 866, August 31, 1964.
23. Munson, A. G., "A Modeling Approach to Nonpropulsive Noise", AIAA Preprint No. 76-525, Palo Alto, California, 1976.
24. Mathews, D. C., Rekos, N. F., "Direct Combustion Generated Noise in Turbopropulsion Systems - Prediction and Measurement", AIAA Preprint No. 76-579, Palo Alto, California, 1976.
25. "Final Report on Phase II Program for Refan JT8D Engine Design, Fabrication and Test", NASA CR-134876, Pratt and Whitney Aircraft Company, 1975.
26. "Core Engine Noise Control Program - Volume III - Prediction Methods", FAA-RD-74-12, III, Aircraft Engine Group - General Electric Company, 1974.

27. Krejsa, E. A., and Valerino, M. F., "Interim Prediction Method for Turbine Noise", NASA TMX-73566, 1976.
28. Beranek, L. L., "Noise and Vibration Control", McGraw-Hill Book Co. (1971) pp. 174-178.
29. Rudd, M. J., "Note on the Scattering of Sound in Jets and the Wind", Journal of Sound and Vibration, Vol. 26, No. 4 (1973), pp 551-560.
30. Candel, S. M. and Julienne, A., "Shielding and Scattering by a Jet Flow", AIAA Preprint No. 76-545, Palo Alto, California, 1976.
31. DeLoach, R., "On the Excess Attenuation of Sound in the Atmosphere", NASA TND-7823, March 1975.
32. Beran, D. W., Reynolds, R. M. and Gething, J. T., "Sound Attenuation in the Free Atmosphere", Publication No. 17, Project EAR, Report No. V, Meteorological Department, University of Melbourne, December 1970.
33. Beran, Donald W., "Turbulence Detection", Ph.D. Thesis, University of Melbourne, July 1970.
34. Benson, R. W.. and Karplus, H. B., "Sound Propagation Near the Earth's Surface as Influenced by Weather Conditions", WADC Technical Report 57-353, Part I, U.S. Air Force, March 1958. (Available from DDC as AD 130 793.)
35. Burkland, M. D., Karplus, H. B. and Sabine, J. J., "Sound Propagation Near the Earth's Surface as Influenced by Weather Conditions", WADC Technical Report 57-353, Part II, U.S. Air Force, December 1960.
36. Sabine, H. J., Raelson, V. J. and Burkland, M. D., "Sound Propagation Near the Earth's Surface as Influenced by Weather Conditions", WADC Technical Report 57-353, Part III, U.S. Air Force, January 1961.
37. Sabine, H. J., "Sound Propagation Near the Earth's Surface and Influenced by Weather Conditions", WADC Technical Report 57-353, Part IV, U.S. Air Force, January 1961.
38. Beran, D. W. and Gething, J. T., "Use of a Sailplane in Measuring Acoustic Attenuation in the Atmosphere", Aero-Revue, Issue 2, February 1972, pp. 93-95.
39. Lighthill, M. J., "Sound Generated Aerodynamically", The Bakerian Lecture 1961. Proc. Roy. Soc. (London), Vol. 267A, 1972, pp. 147-182.
40. Lowson, M. V., "The Sound Field for Singularities in Motion", Proc. Roy. Soc. (London), Vol. 286A, 1965, pp. 559-572.

41. Crighton, D. G., "Scattering and Diffraction of Sound by Moving Bodies", Journal of Fluid Mechanics, Vol. 72, Part 2, 1975, pp. 209-227.
42. Mani, R., "Noise Due to Interaction of Inlet Turbulence with Isolated Stators and Rotors", Journal of Sound and Vibration, Vol. 17, No. 2, July 1971, pp. 251-260.
43. Pickett, G. F., "Effects of Non-Uniform Inflow on Fan Noise", Paper B5 presented at the 87th meeting of the Acoustical Society of America, New York, New York, April 1974, also J. Acoust. Soc. Am., 55, S3(A), Spring 1974.
44. Clark, B. J., Heidmann, M. F., and Kreim, W. J., "Microscopic Study of Time Unsteady Noise of an Aircraft Engine During Static Tests", NASA TMX-73556, 1976.
45. Tyler, J. M. and Sofrin, T. G., "Axial Flow-Compressor Noise Studies", Transactions of the SAE, Vol. 70, 1962, pp. 309-332.
46. Homicz, G. F., and Loudi, J. A., "A Note on the Radiation Directivity Patterns of Duct Acoustic Modes", Journal of Sound and Vibration, Vol. 41, 1975, pp. 283-290.
47. Sofrin, T. G., and McCann, J. C., "Pratt and Whitney Aircraft Experience in Compressor Noise Reduction", Paper 2D2 presented at the 72nd meeting of the Acoustical Society of America, Los Angeles, California, November 1966; also J. Acoust. Soc. Am., 40, 1248(A), No. 5, 1966.
48. Dietrich, D. A. and Heidmann, M. F., "Acoustic Signatures of a Model Fan in the NASA-Lewis Anechoic Wind Tunnel", NASA TMX-73560, 1977.
49. Hodder, B. K., "Further Studies of Static to Flight Effects on Fan Tone Noise Using Inlet Distortion Control for Source Identification", NASA TMX-73183, 1976.

TABLE 1

SUMMARY OF AIRPLANE FLIGHT TEST PROGRAMS USED IN FLYOVER NOISE ANALYSIS

AIRPLANE/ENGINE	FLIGHT CONDITION(S)	MICROPHONE LOCATION(S)	POWER SETTINGS	ALTITUDES (m)	NUMBER OF RUNS
DC-9-30/JT8D-109	APPROACH AND TAKEOFF	FLUSH, 1.2 METER, NACELLE	APPROACH THROUGH TAKEOFF	112.8 TO 640.0	16
DC-10-10/CF6-6D	LEVEL FLIGHT	1.2 METER AND NACELLE	APPROACH THROUGH TAKEOFF	152.4	17
DC-10-40/JT9D-59A	APPROACH AND TAKEOFF	FLUSH AND 1.2 METER	APPROACH THROUGH TAKEOFF	112.8 TO 762.0	17

TABLE 2

SUMMARY OF STATIC ENGINE TEST PROGRAMS USED IN STATIC NOISE ANALYSIS

ENGINE	MICROPHONE LOCATIONS	NUMBER OF POWER SETTINGS
JT8D-109	FLUSH, TRIPOD, NACELLE	24 (IDLE TO TAKEOFF)
CF6-6D	12.2-m TRIPOD AND NACELLE	30 (IDLE TO TAKEOFF)
JT9D-59A	FLUSH AND4.3-m TRIPOD	24 (IDLE TO TAKEOFF)

TABLE 3

SUMMARY OF ROLL-OFF RATES FOR TURBOMACHINERY SOURCE SEPARATION PROCEDURES

ROLL-OFF RATES FOR SOURCE SEPARATION PROCEDURES

JET AND CORE HIGH FREQUENCY NOISE (dB/1/3 OCTAVE)

ANGLE FROM INLET CENTERLINE	30	40	50	60	70	80	90	100	110	120	130	140	150
JT8D-109	1.67	1.67	1.67	1.67	1.67	1.67	2.0	2.0	2.0	2.0	2.33	2.5	2.5
CF6-6D	1.9	1.9	1.9	1.9	1.9	1.9	2.0	2.0	2.0	2.0	2.33	2.5	2.5
JT9D-59A	1.9	1.9	1.9	1.9	1.9	1.9	2.0	2.0	2.0	2.0	2.33	2.5	2.5

FAN AND TURBINE NOISE

SPECTRA

- FAN LOW FREQUENCY BROADBAND –3 dB/OCTAVE
- TURBINE BROADBAND –30 dB/OCTAVE

DIRECTIVITY

- INLET TURBOMACHINERY IN AFT –2.5 dB/10 DEG
- AFT TURBOMACHINERY IN INLET –2.5 dB/10 DEG

TABLE 4.

JET AND CORE NOISE COMPONENT OASPL CORRELATIONS FOR THE JT8D-109 STATIC ENGINE AT 45.7-METER RADIUS*

JET NOISE $OASPL_{jet} = M\ 10\ Log_{10}\ V_{jp} - 10\ Log_{10}\ A_p + C_1$

INLET ANGLES DEGREES	50	60	70	80	90	100	110	120	130	140	150
M	5.57	5.61	5.69	5.87	6.20	6.43	6.63	7.03	7.20	7.97	8.50
C_1	-33.7	-34.6	-35.6	-39.3	-48.9	-50.4	-53.8	-62.0	-63.6	-80.9	-93.4

CORE NOISE $OASPL_{Core} = N\ 10\ Log_{10}\ V_{jp} + 10\ Log_{10}\ A_p + C_2$

INLET ANGLES DEGREES	50	60	70	80	90	100	110	120	130	140	150
N	2.63	2.65	3.10	3.37	3.53	3.28	3.39	2.83	2.20	1.96	2.04
C_2	34.2	34.8	23.8	18.2	17.5	25.2	19.2	39.2	52.0	54.5	51.6

*GROUND MICROPHONE DATA, SINGLE ENGINE

TABLE 5.

JET AND CORE NOISE COMPONENT OASPL CORRELATIONS FOR THE JT9D-59A STATIC ENGINE AT 45.7-METER RADIUS*

JET NOISE $\quad OASPL_{jet} = M\ 10\ Log_{10}\ V_{jp} + 10\ Log_{10}\ A_p + C_1$

INLET ANGLES (DEGREES)	50	60	70	80	90	100	110	120	130	140	150
M	5.22	5.25	5.24	5.14	5.18	5.30	5.32	5.86	6.34	6.96	7.60
C_1	-28.9	-28.9	-27.7	-24.4	-24.1	-25.8	-24.4	-36.3	-46.3	-60.4	-75.2

CORE NOISE $\quad OASPL_{Core} = N\ 10\ Log_{10}\ V_{jp} + 10\ Log_{10}\ A_p + C_2$

INLET ANGLES (DEGREES)	50	60	70	80	90	100	110	120	130	140	150
N	3.24	3.40	3.20	3.20	3.00	3.00	3.00	3.00	3.00	3.26	3.86
C_2	14.7	11.4	16.8	18.2	24.2	25.2	26.2	27.2	27.0	19.2	3.1

*GROUND MICROPHONE DATA, SINGLE ENGINE

TABLE 6(a). SUMMARY OF DC-9-31/JT8D-109 TEST DATA USED FOR EXCESS ATTENUATION ANALYSIS

AIRCRAFT	ENGINE	FLIGHT	RUN	MIC NO.	MIC LOC.	$N_1/\sqrt{\theta}$ RPM	ALTITUDE, (m)	AIRSPEED KNOTS
DC-9-31	JT8D-109	19	27	1	C6	5487.9	263	138.2
			27	6	C10	5461.5	113	136.0
			28	1	C6	5339.0	264	138.5
			28	6	C10	5317.4	95	135.2
			29	1	C6	5359.3	260	129.1
			29	6	C10	5334.7	116	125.2
			30	1	C6	5507.5	276	140.9
			30	6	C10	5487.8	121	---
			31	1	C6	5376.0	277	138.1
			31	6	C10	5355.1	120	134.5
			32	1	C6	5488.7	281	132.3
		19	32	6	C10	5464.5	125	137.1
		21	53	1	C6	7557.2	677	180.6
			53	3	C11	7529.4	102	177.8
			54	1	C6	7508.6	695	179.7
			54	3	C11	7493.3	110	182.1
			55	1	C6	7503.0	725	113.9
		21	55	3	C11	7483.3	141	179.9
		22	65	3	C11	7553.0	192	172.4
		22	65	6	C10	7580.4	347	174.6
		23	84	6	C10	7570.5	334	174.9
			84	3	C11	7531.0	182	172.9

TABLE 6(b). SUMMARY OF DC-9-31/JT8D-109 TEST DATA USED FOR EXCESS ATTENUATION ANALYSIS

AIRCRAFT	ENGINE	FLIGHT	RUN	MIC. NO.	MIC. LOC.	$N_1/\sqrt{\theta}$ RPM	ALTITUDE, (m)	AIRSPEED KNOTS
DC-9-31	JT8D-109	23	85	1	C6	7439.0	264	174.6
			85	6	C10	7424.1	149	171.4
			85	3	C11	7430.1	138	160.5
			86	1	C6	7472.2	244	173.9
			86	6	C10	7456.4	151	167.7
DC-9-31	JT8D-109	23	86	3	C11	7451.0	121	159.5
DC-9-31	JT8D-109	23	87	1	C6	6573.7	204	176.8
			87	6	C10	6563.5	137	187.7
			87	3	C11	6568.5	121	184.6
			90	1	C6	6545.5	166	175.4
			90	6	C10	6546.1	134	174.1
			90	3	C11	6536.9	135	172.7
			91	1	C6	6561.1	187	176.4
			91	6	C10	6562.8	154	175.0
DC-9-31	JT8D-109	23	91	3	C11	6554.9	141	166.5

TABLE 7. SUMMARY OF DC-10-40/JT9D-59A TEST DATA USED FOR EXCESS ATTENUATION ANALYSIS

AIRCRAFT	ENGINE	FLIGHT	RUN	MIC NO.	MIC LOC.	N_1/√θ RPM	ALTITUDE (m)	AIRSPEED KNOTS
DC-10-40	JT8D-59A	212	44	1	C6	3450.6	466	182.0
			44	7	C73	2470.6	824	184.2
			45	1	C6	3459.3	477	180.4
			45	7	C73	3479.7	939	182.3
			46	1	C6	3452.4	483	177.6
DC-10-40	JT9D-59A	212	46	7	C73	3476.0	880	176.6

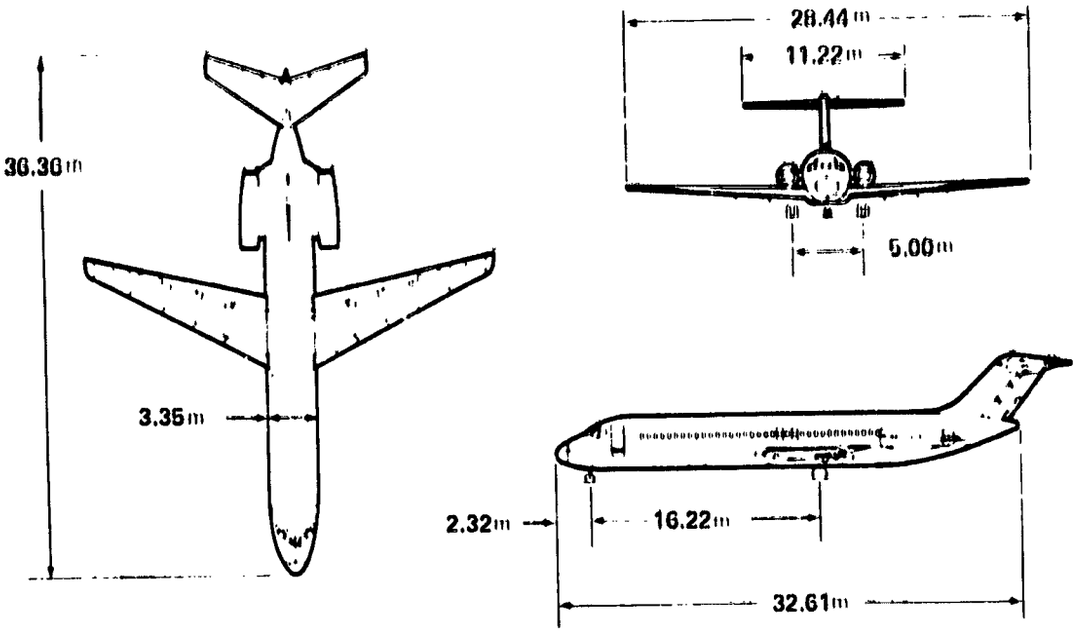

(a) DC-9-30 AIRPLANE GEOMETRY

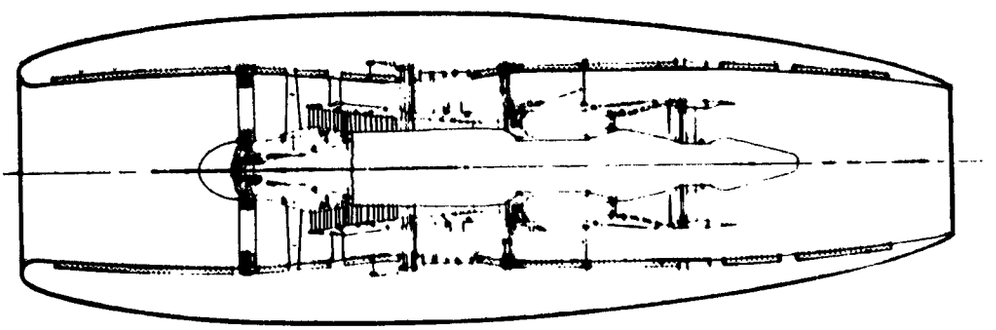

(b) JT8D-109 ENGINE/NACELLE

FIGURE 1. DC-9-30/JT8D-109 AIRPLANE CONFIGURATION

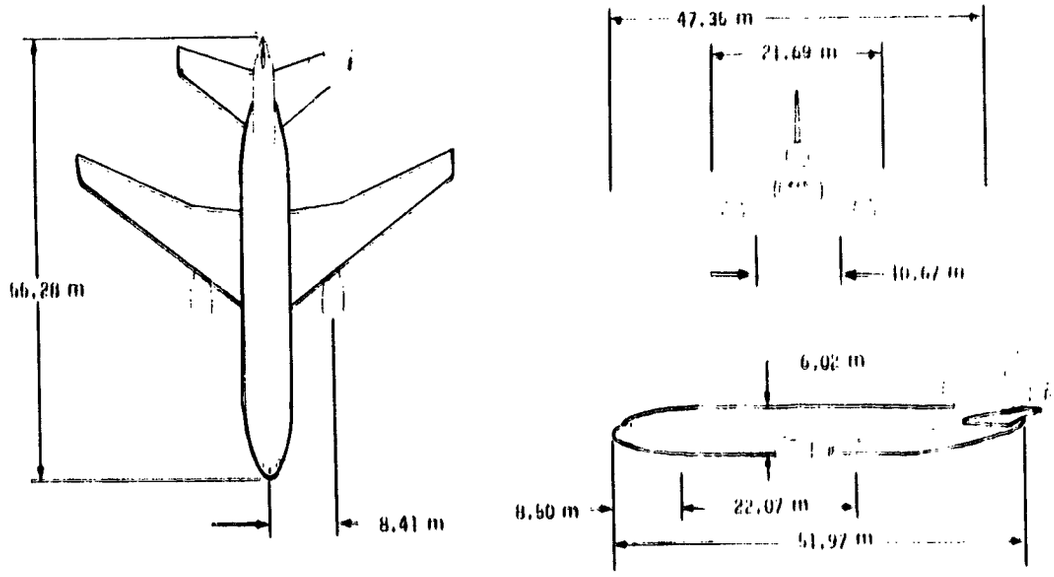

(a) DC-10-10 AIRPLANE GEOMETRY

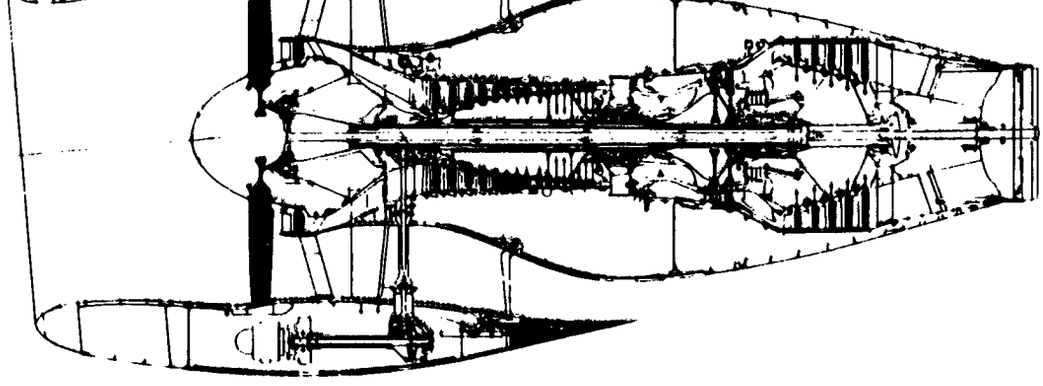

(b) CF6-6D WING ENGINE/NACELLE

FIGURE 2. DC-10-10/CF6-6D AIRPLANE CONFIGURATION

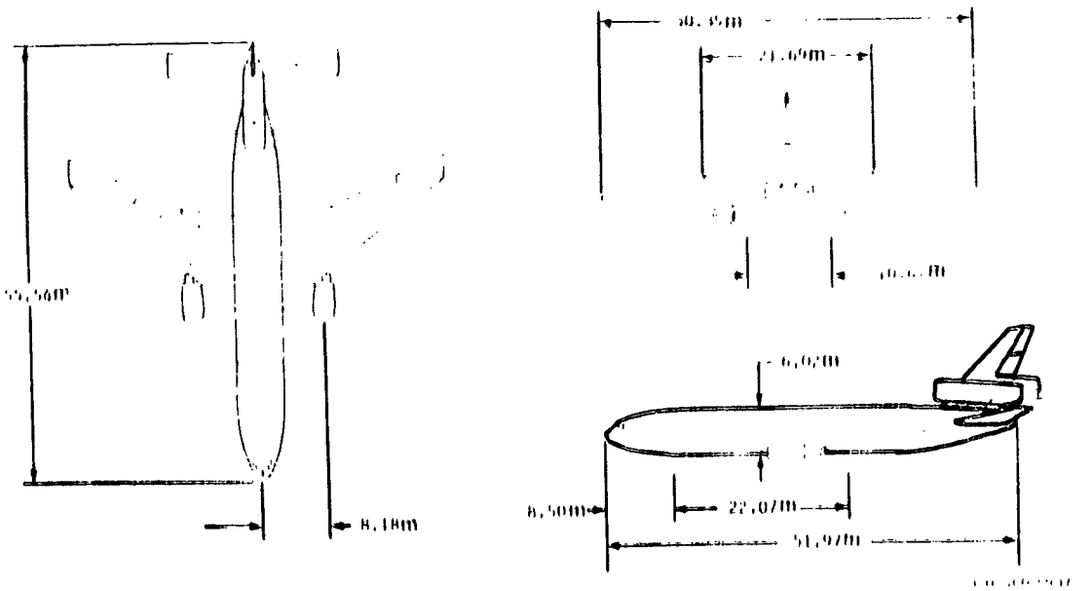

(a) DC-10-40 AIRPLANE GEOMETRY

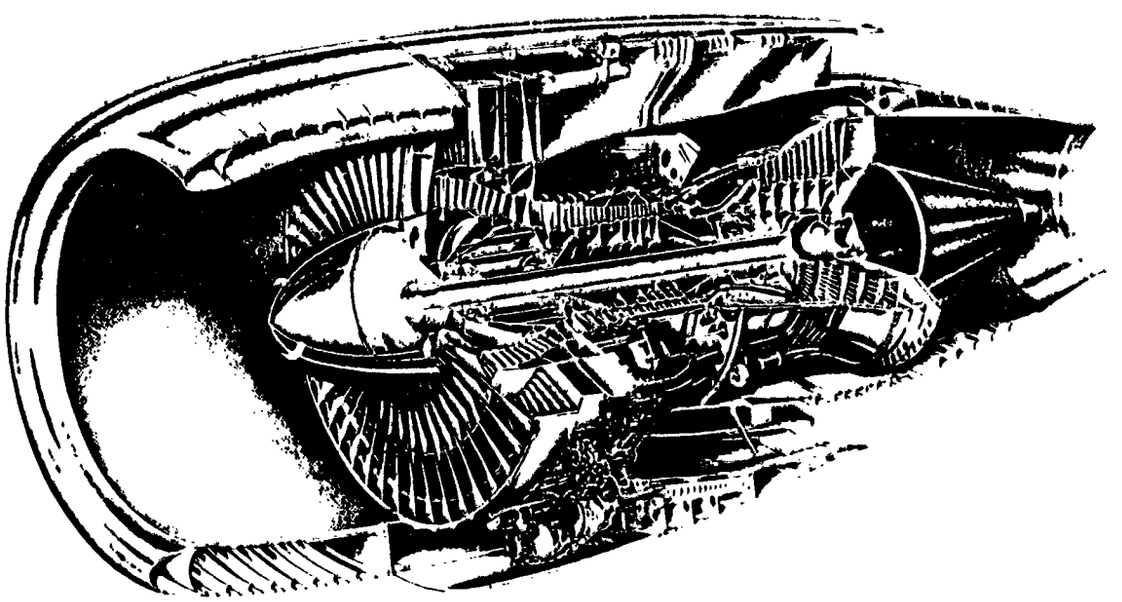

(b) JT9D-59A WING ENGINE/NACELLE

FIGURE 3. DC-10-40/JT9D-59A AIRPLANE CONFIGURATION

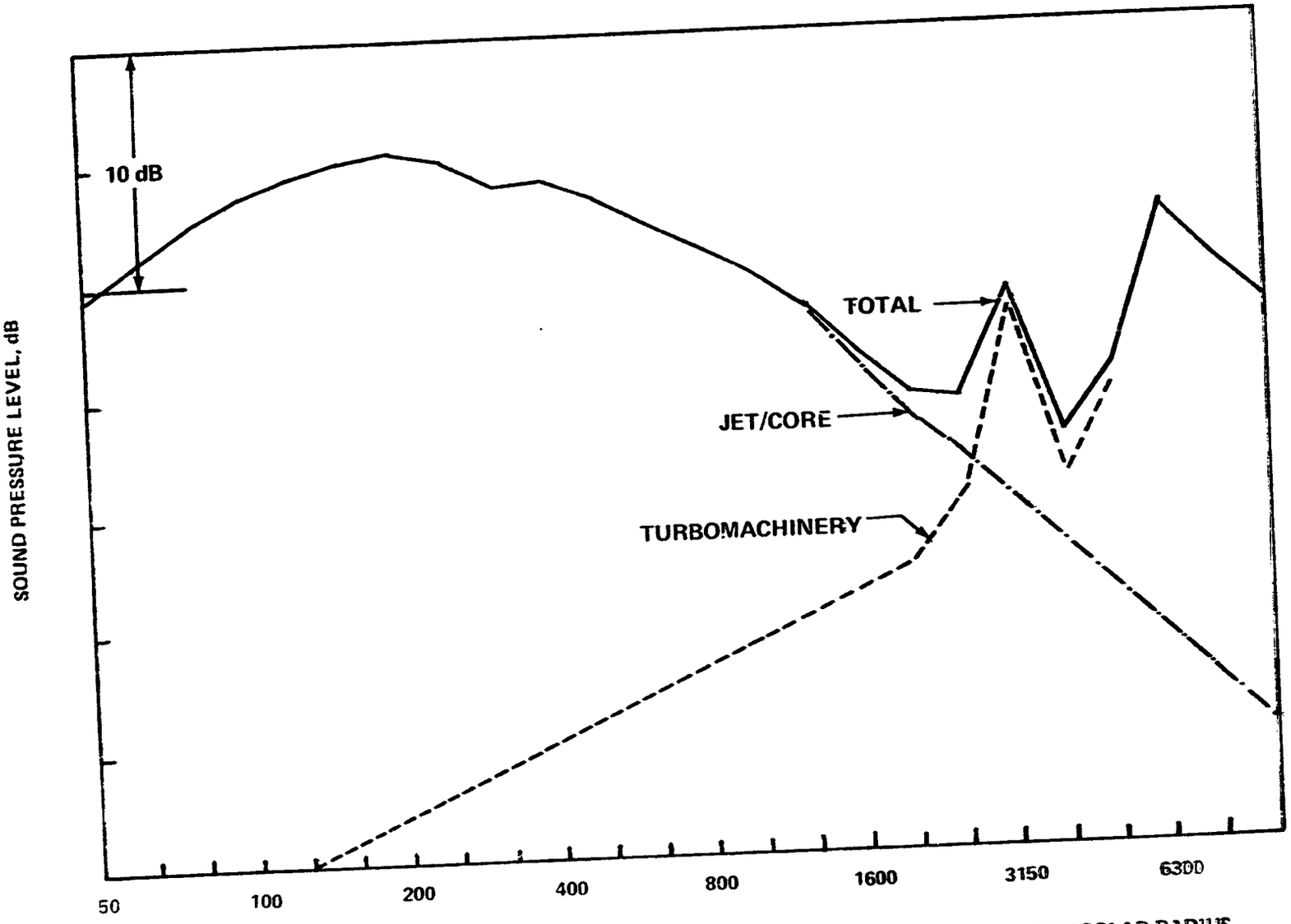

FIGURE 4. SEPARATION OF TURBOMACHINERY AND JET-PLUS-CORE NOISE FROM MEASURED DATA, 45.7M POLAR RADIUS

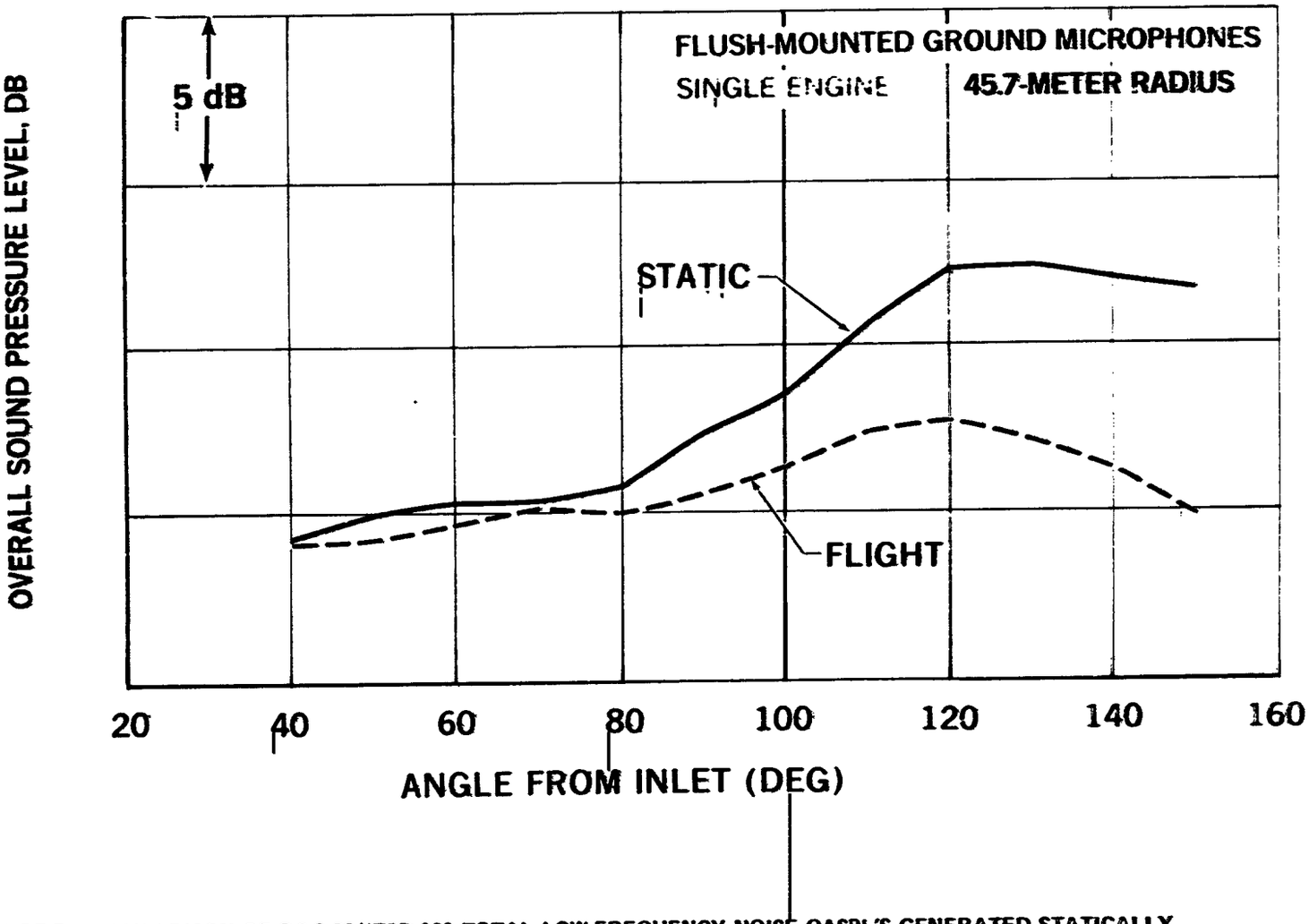

FIGURE 5. COMPARISON OF DC-9-30/JT8D-109 TOTAL LOW-FREQUENCY NOISE OASPL'S GENERATED STATICALLY AND IN FLIGHT. V_{jp} = 221 M/SEC AND V_a = 72 M/SEC

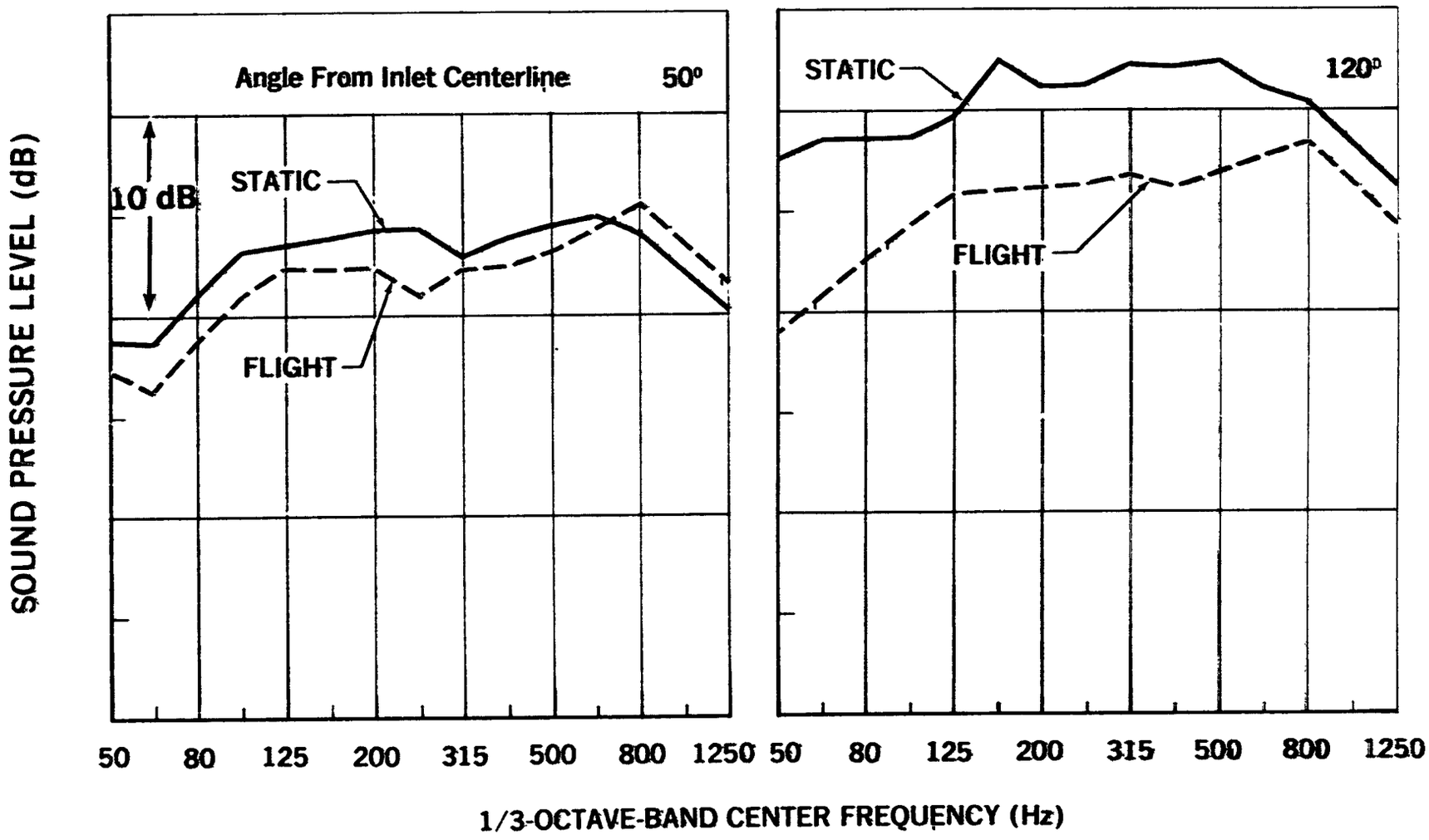

FIGURE 6. COMPARISON OF DC-9-30/JT8D-109 TOTAL LOW-FREQUENCY NOISE SPECTRA GENERATED STATICALLY AND IN FLIGHT. V_{jp} = 221 M/SEC AND V_a = 72 M/SEC

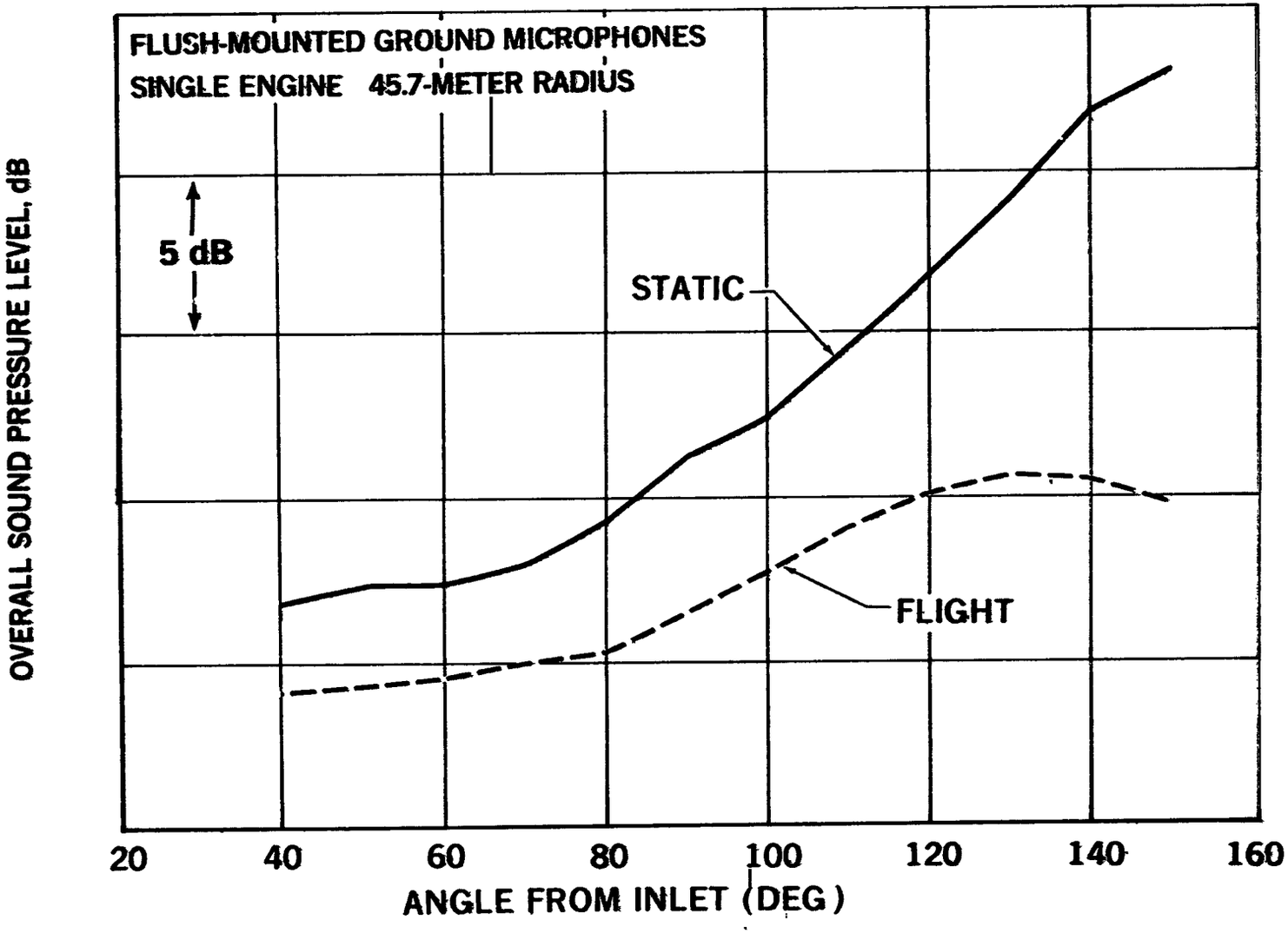

FIGURE 7. COMPARISON OF DC-9-30/JT8D-109 TOTAL LOW-FREQUENCY NOISE OASPL'S GENERATED STATICALLY AND IN FLIGHT. V_{jp} = 392 M/SEC AND V_a = 90 M/SEC

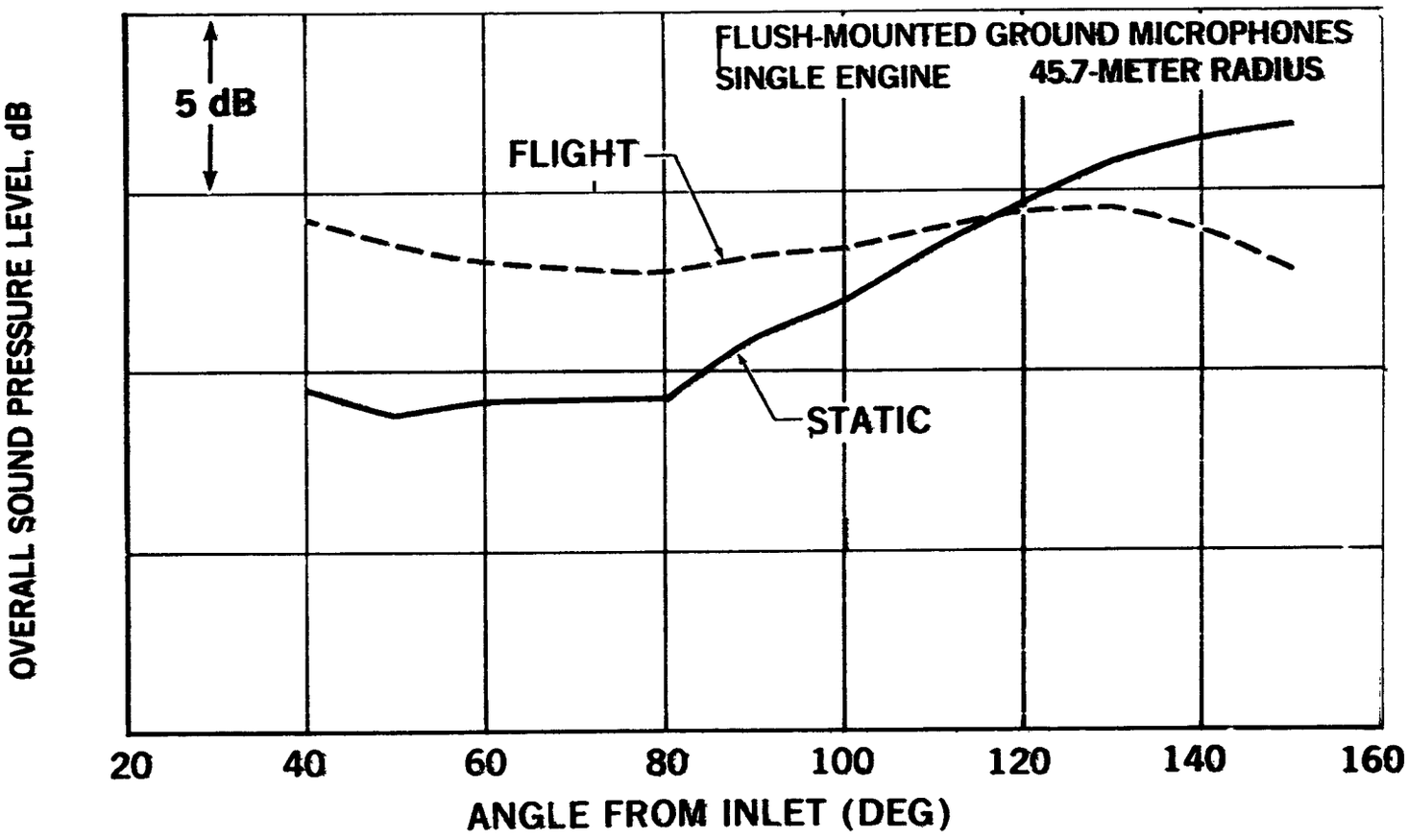

FIGURE 8. COMPARISON OF DC-10-40/JT9D-59A TOTAL LOW-FREQUENCY NOISE OASPL'S GENERATED STATICALLY AND IN FLIGHT. V_{jp} = 268 M/SEC AND V_a = 78 M/SEC

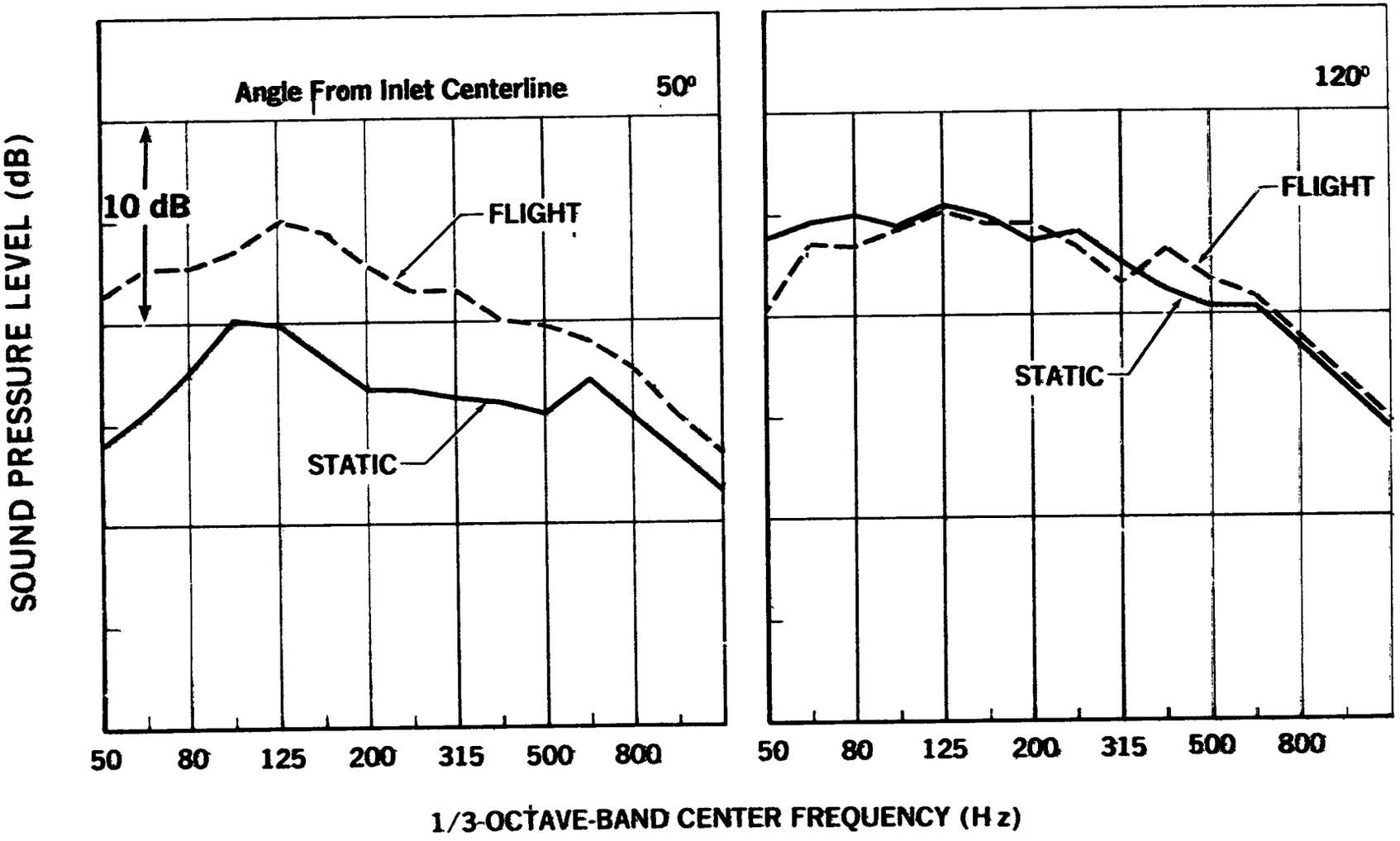

FIGURE 9. COMPARISON OF DC-10-40/JT9D-59A TOTAL LOW-FREQUENCY NOISE SPECTRA GENERATED STATICALLY AND IN FLIGHT. V_{jp} = 268 M/SEC AND V_a = 78 M/SEC

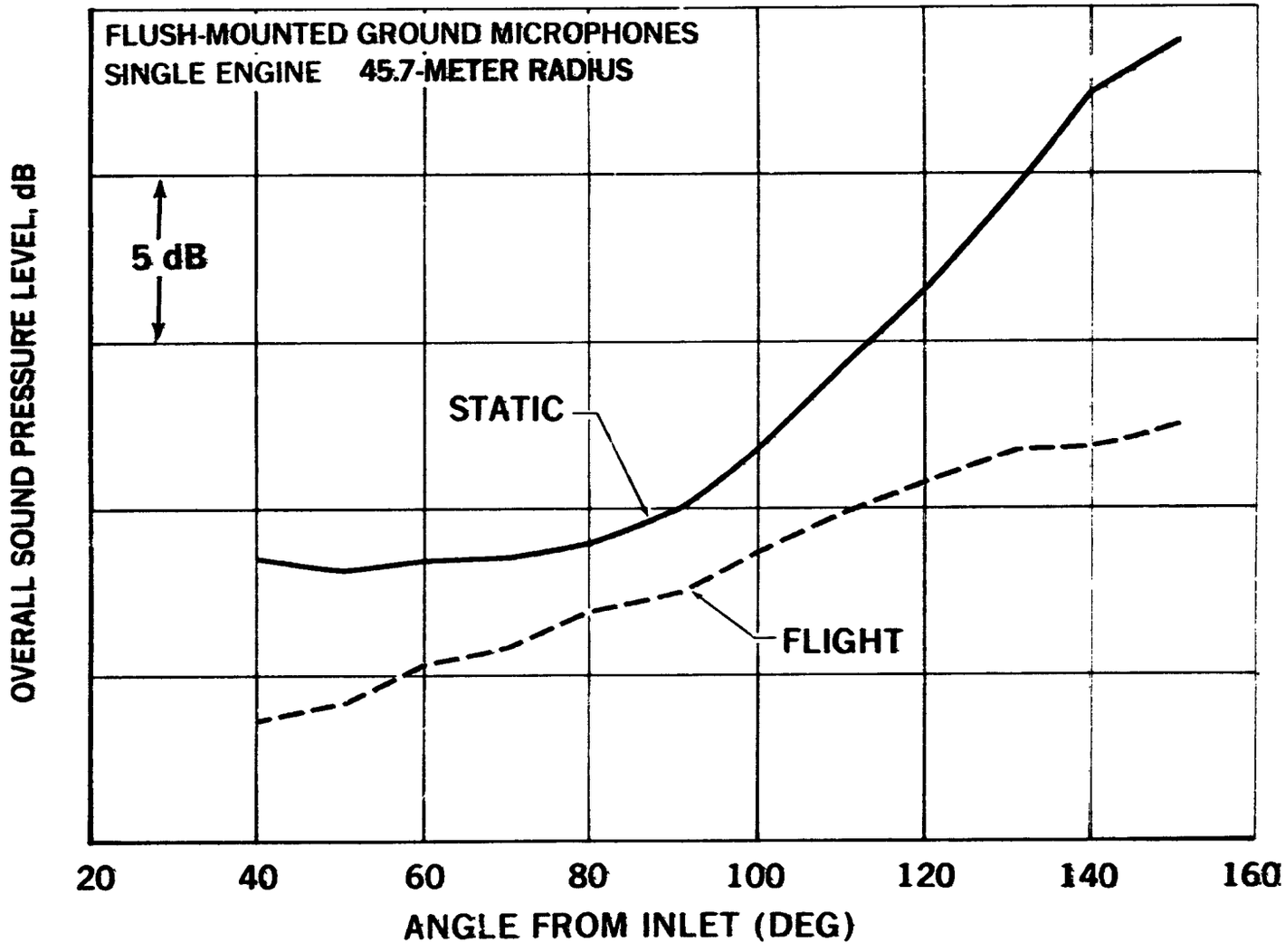

FIGURE 10. COMPARISON OF DC-10-40/JT9D-59A TOTAL LOW-FREQUENCY NOISE OASPL'S GENERATED STATICALLY AND IN FLIGHT. V_{jp} = 436 M/SEC AND V_a = 97 M/SEC

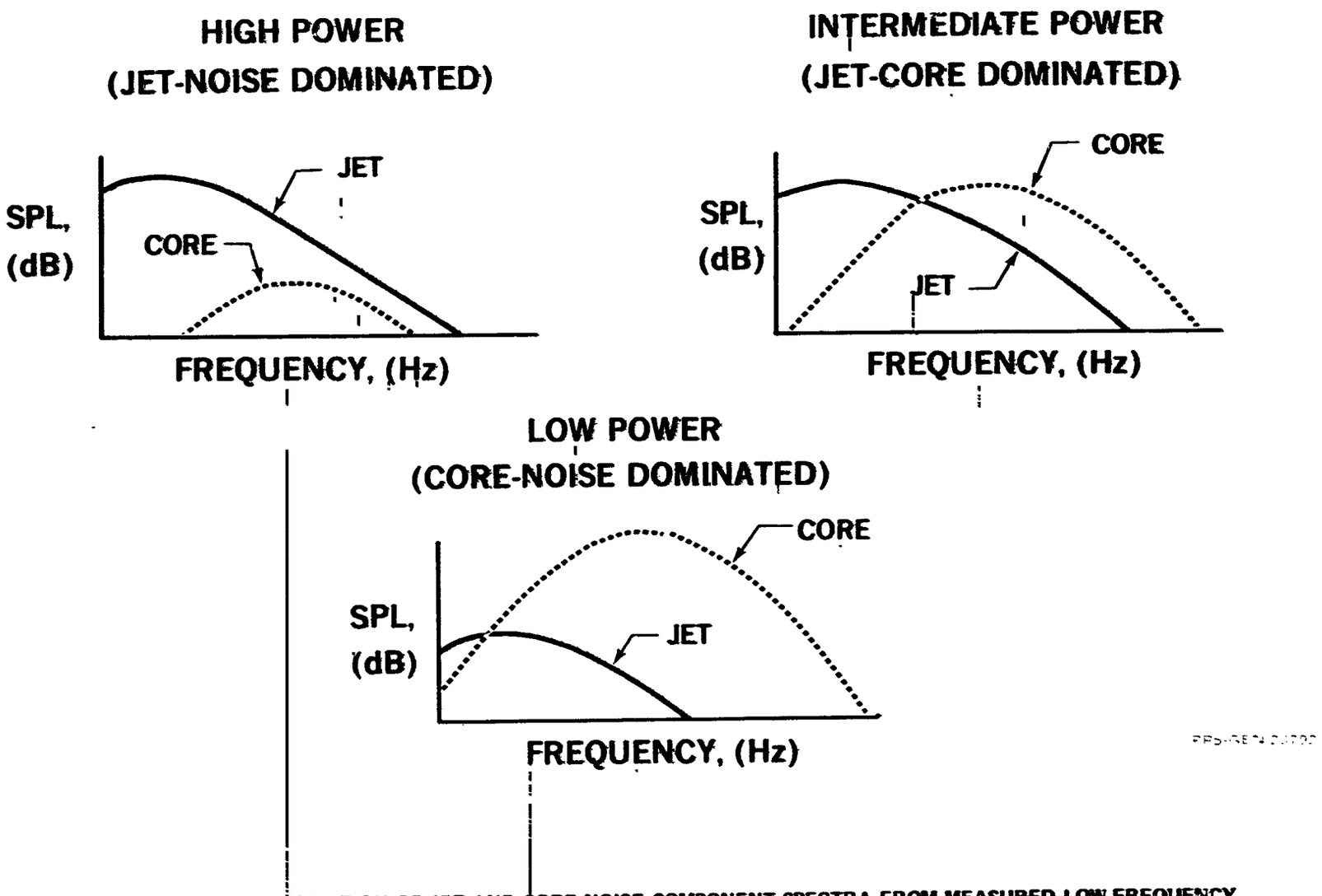

FIGURE 11. DETERMINATION OF JET AND CORE NOISE COMPONENT SPECTRA FROM MEASURED LOW-FREQUENCY NOISE SPECTRA

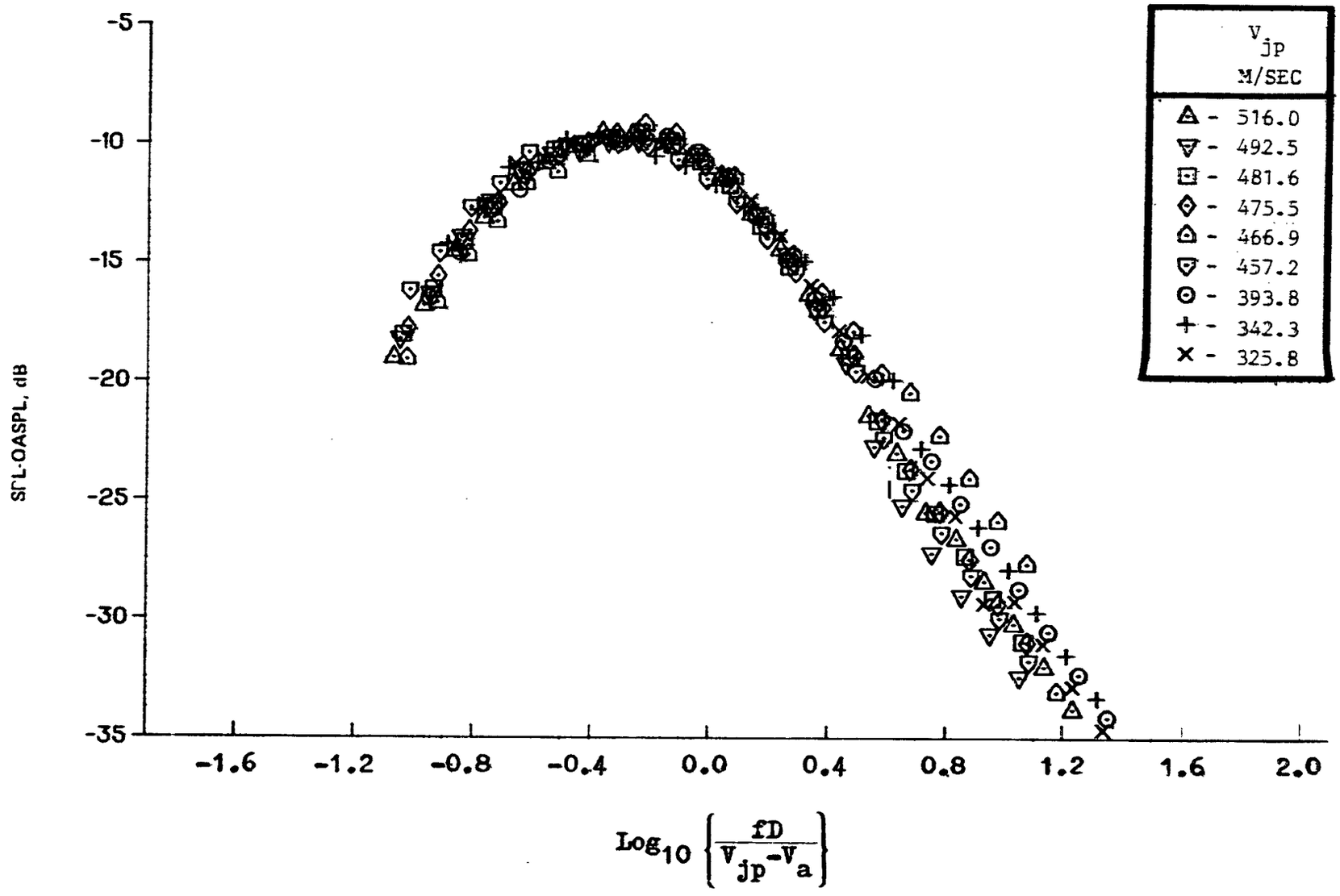

FIGURE 12. NORMALIZED SPECTRA OF MODEL-SCALE STATIC JET NOISE AT 45.7-METER RADIUS AND 120° FROM INLET. V_a = 0 M/SEC

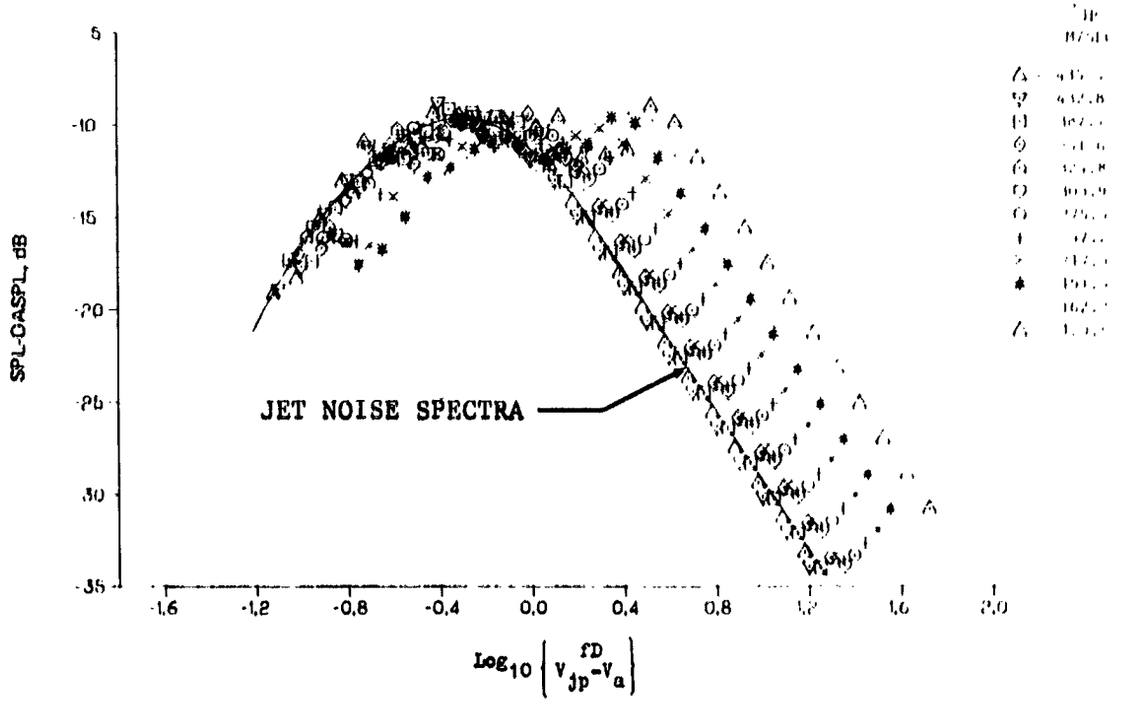

(a) 50° FROM INLET CENTERLINE

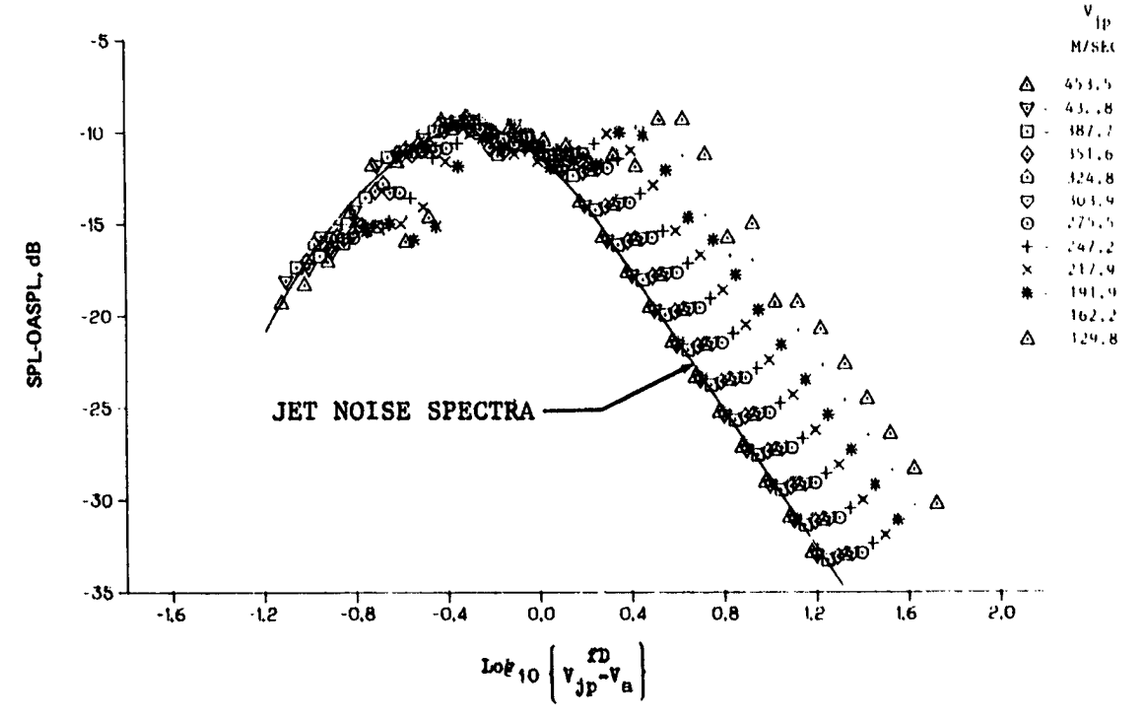

(b) 90° FROM INLET CENTERLINE

FIGURE 13. NORMALIZED SPECTRA OF JT8D-109 STATIC JET-PLUS-CORE NOISE AT 45.7-METER RADIUS. V_a = 0 M/SEC

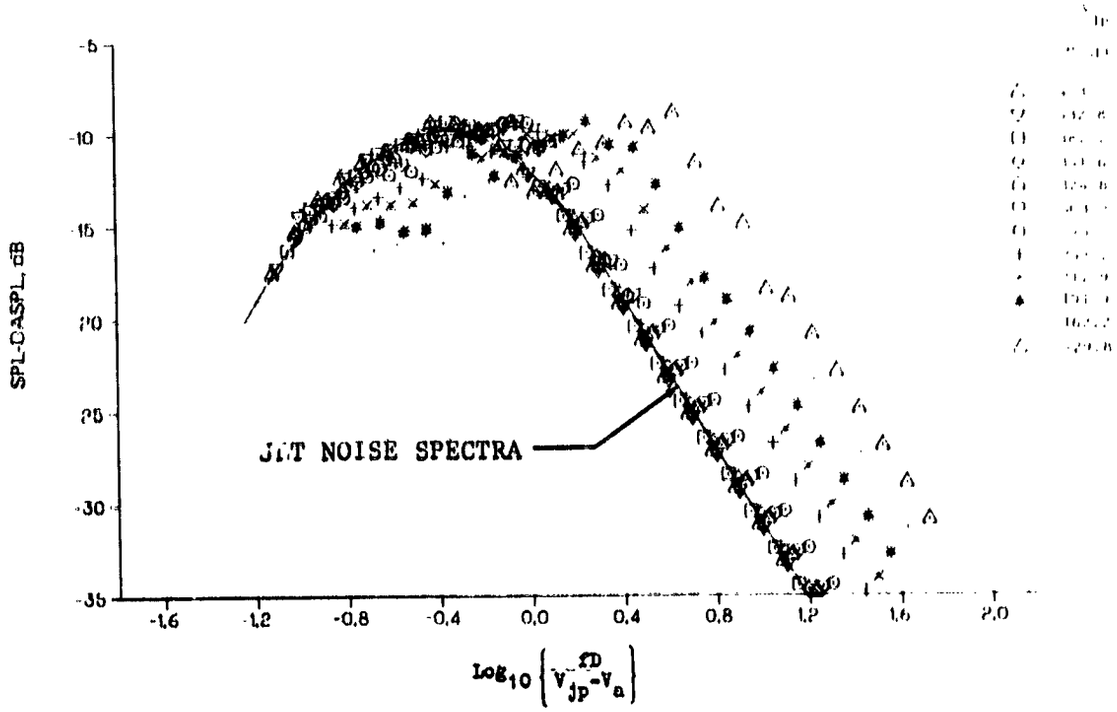

(c) 120° FROM INLET CENTERLINE

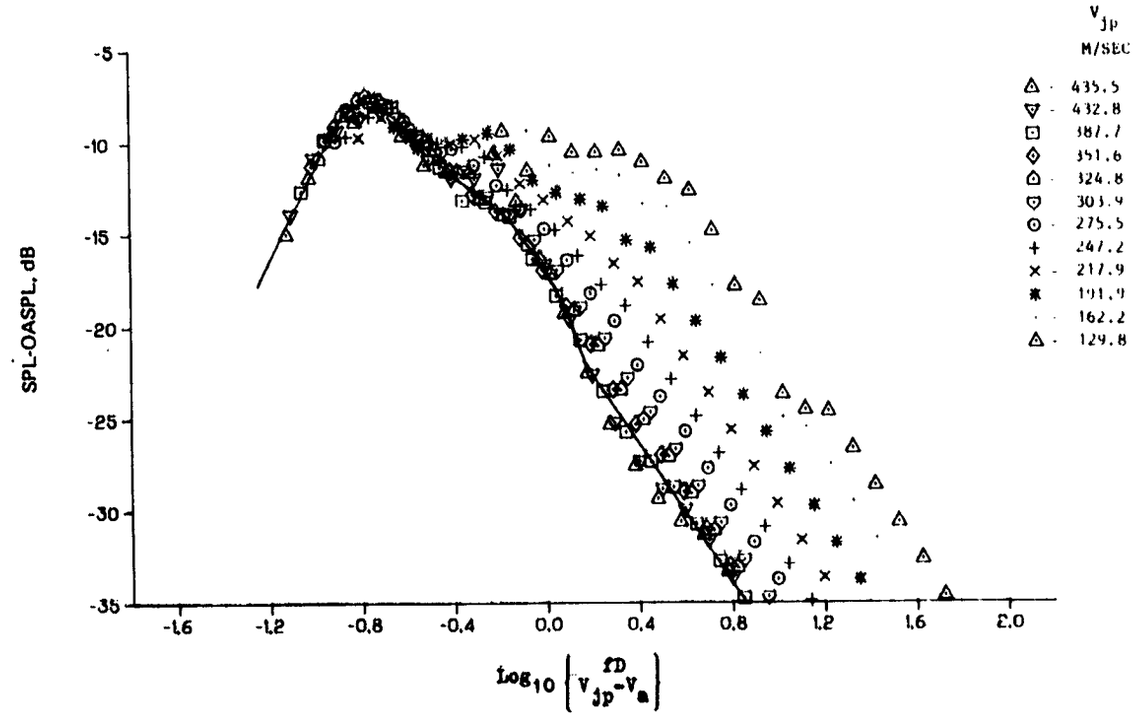

(d) 140° FROM INLET CENTERLINE

FIGURE 13 NORMALIZED SPECTRA OF JT8D-109 STATIC JET-PLUS-CORE NOISE AT 45.7-METER RADIUS. V_a = 0 M/SEC

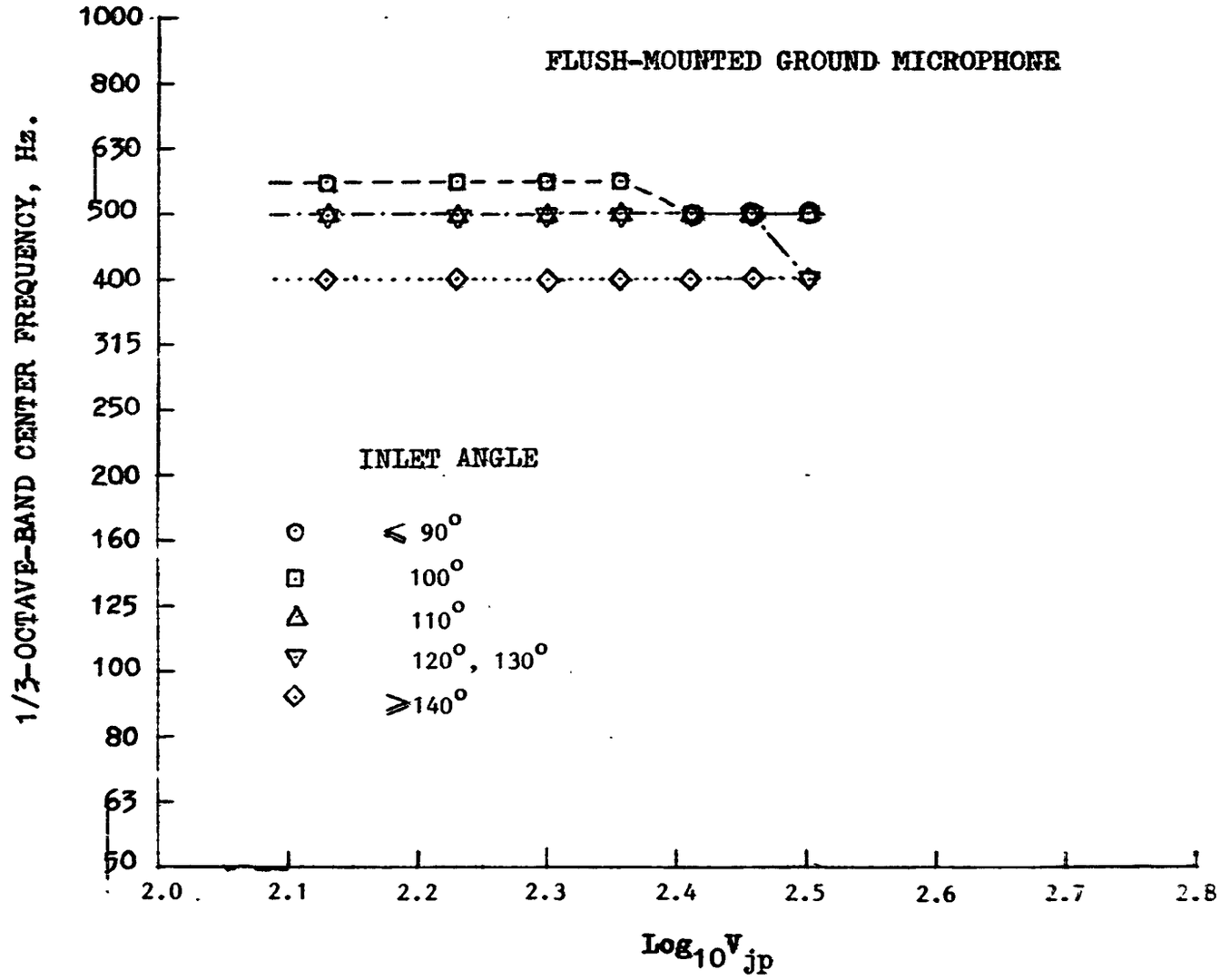

FIGURE 14. CORRELATION OF CORE NOISE PEAK FREQUENCY FOR STATIC JT8D-109 ENGINE AT 45.7-METER RADIUS

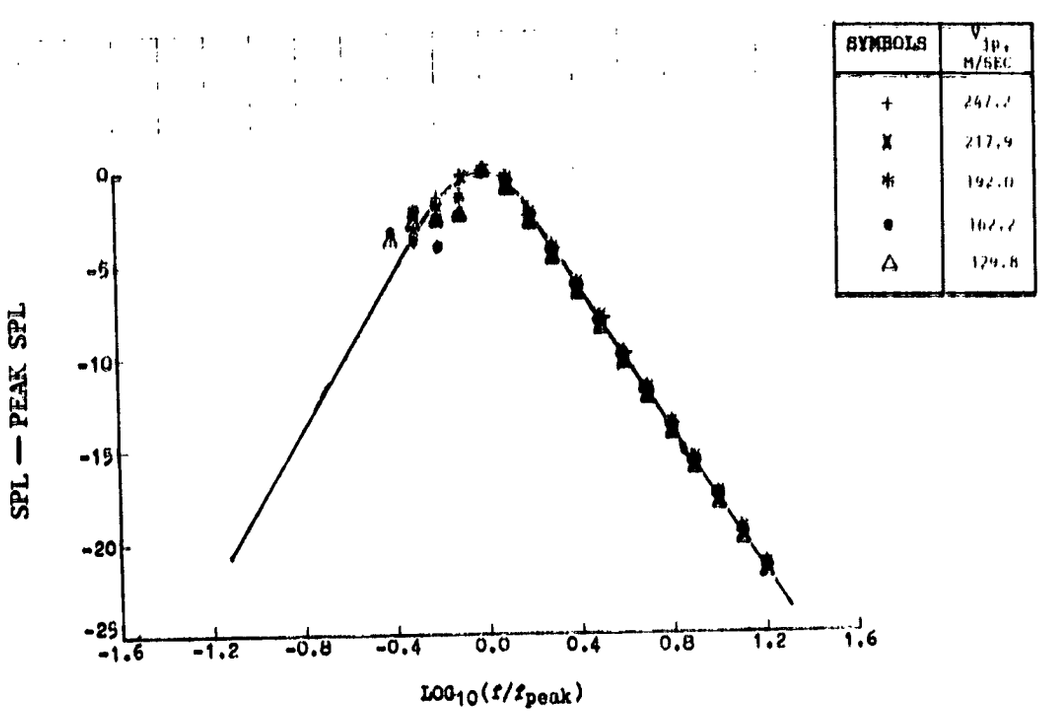

(a) 50° FROM INLET CENTERLINE

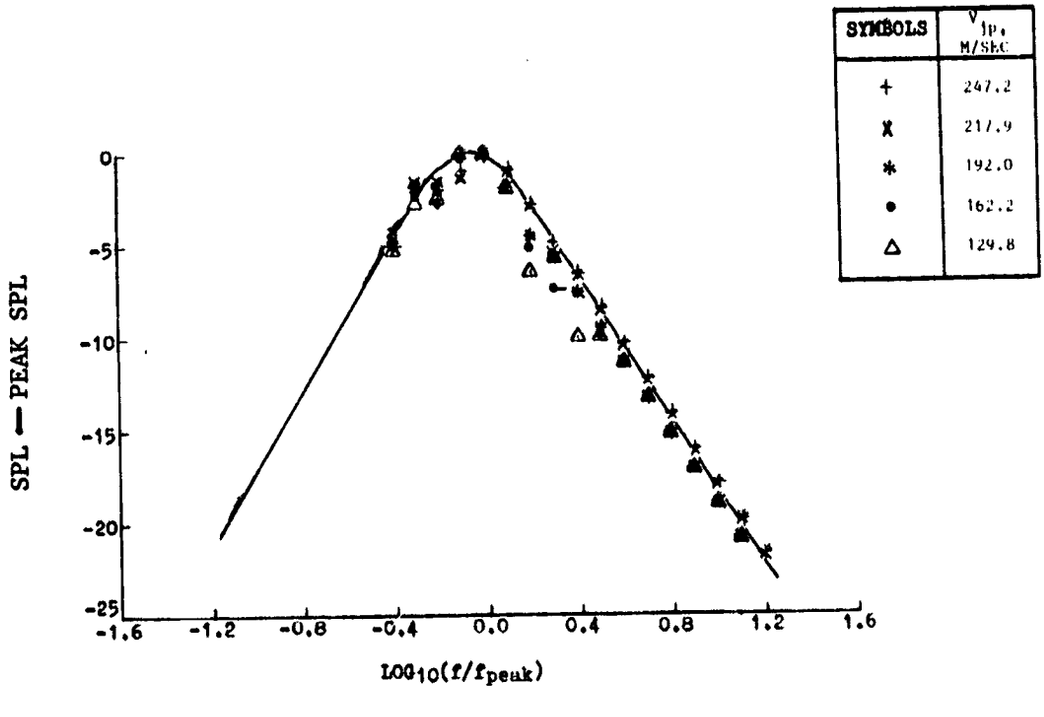

(b) 90° FROM INLET CENTERLINE

FIGURE 15. NORMALIZED SPECTRA OF JT8D-109 STATIC CORE AT 45.7-METER RADIUS

PRECEDING PAGE BLANK NOT FILMED

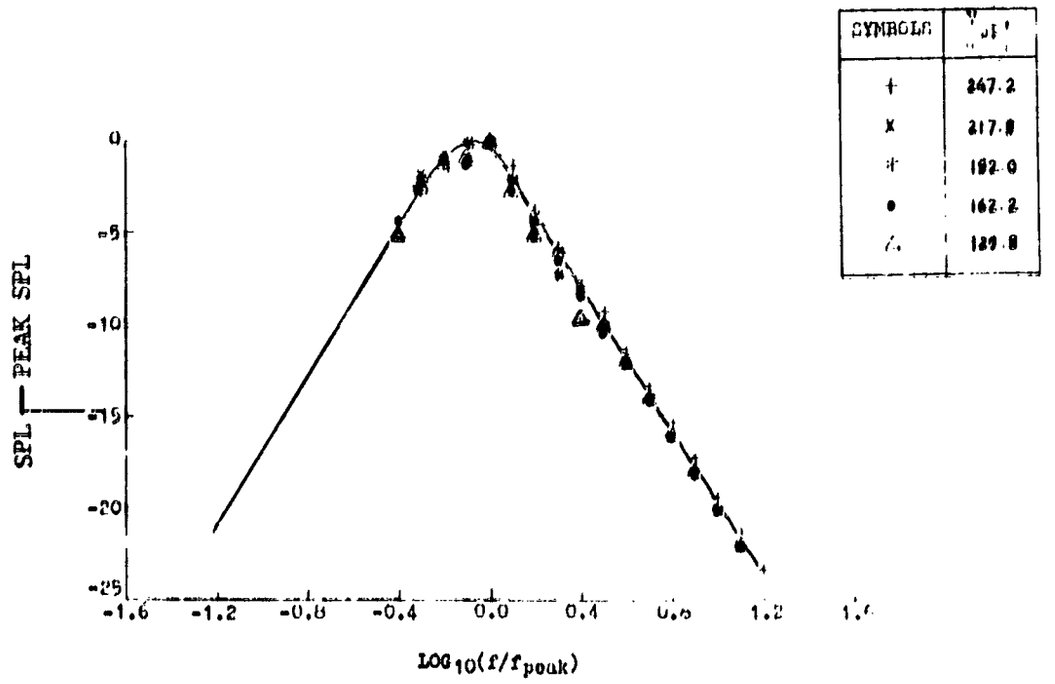

(c) 120° FROM INLET CENTERLINE

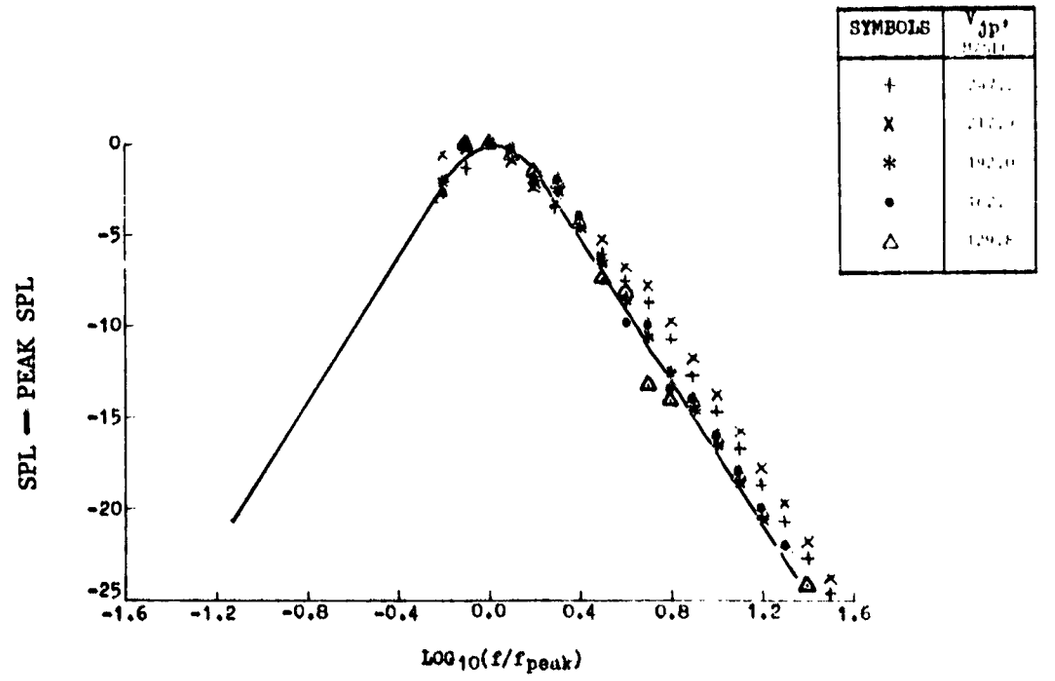

(d) 140° FROM INLET CENTERLINE

FIGURE 15 NORMALIZED SPECTRA OF JT8D-109 STATIC CORE AT 45.7-METER RADIUS (CONTINUED)

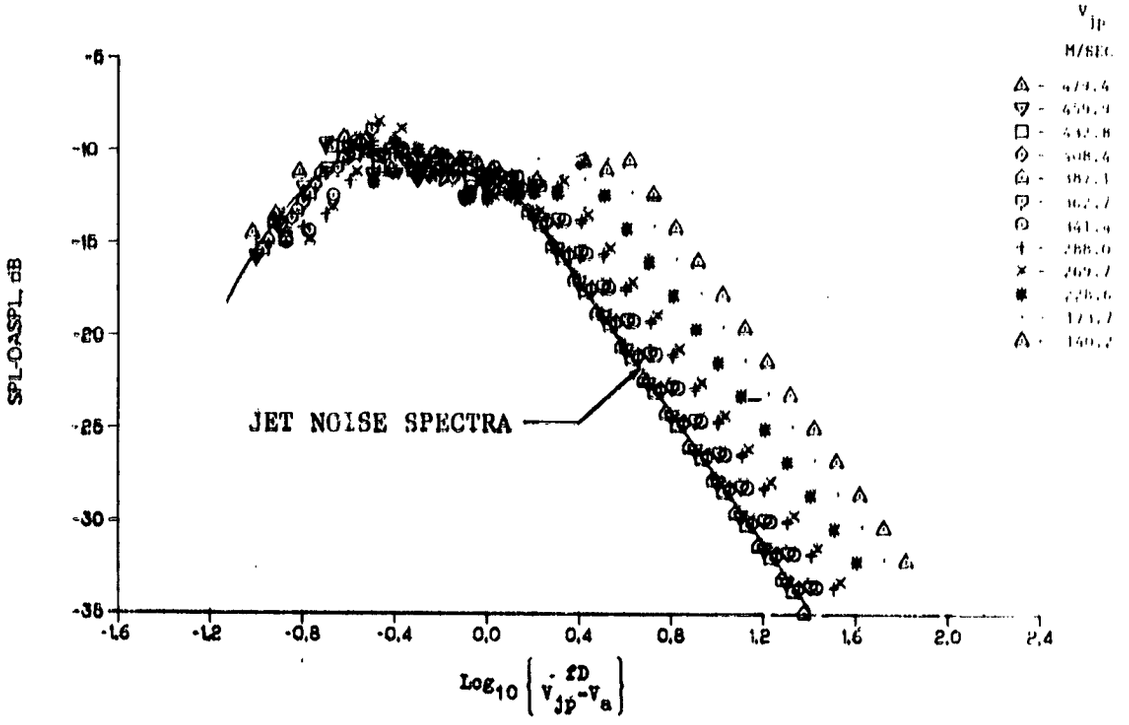

(a) 50° FROM INLET CENTERLINE

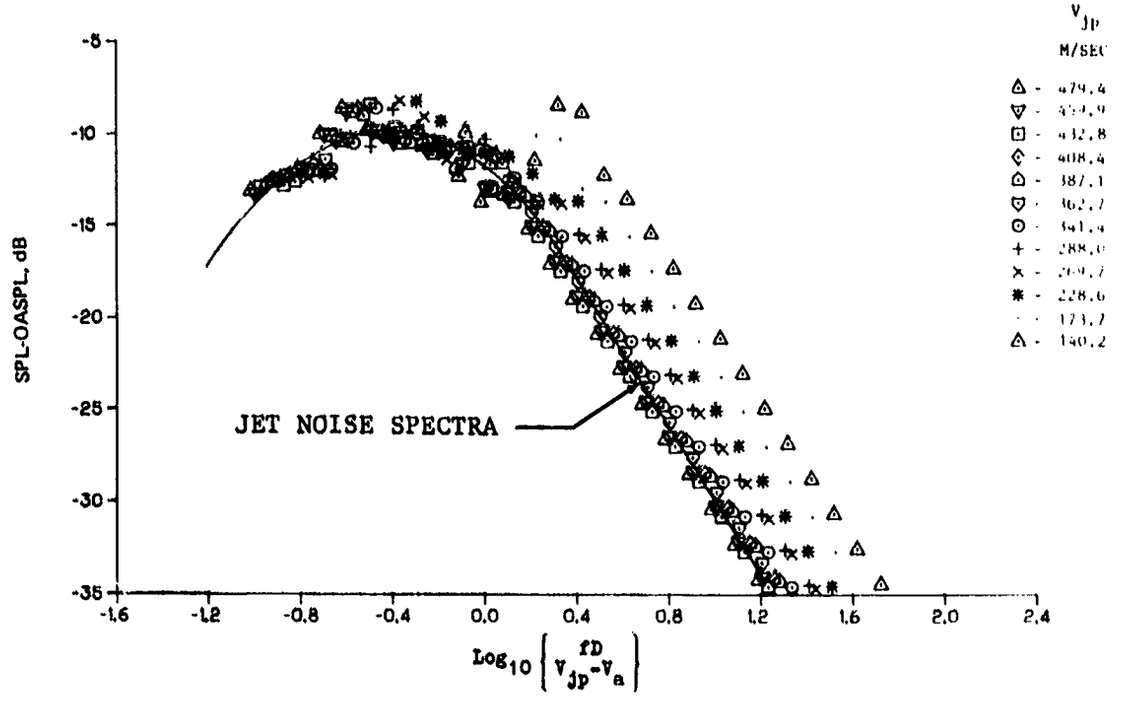

(b) 90° FROM INLET CENTERLINE

FIGURE 16. NORMALIZED SPECTRA OF JT9D-59A STATIC JET-PLUS-CORE NOISE AT 45.7-METER RADIUS. V_a = 0 M/SEC

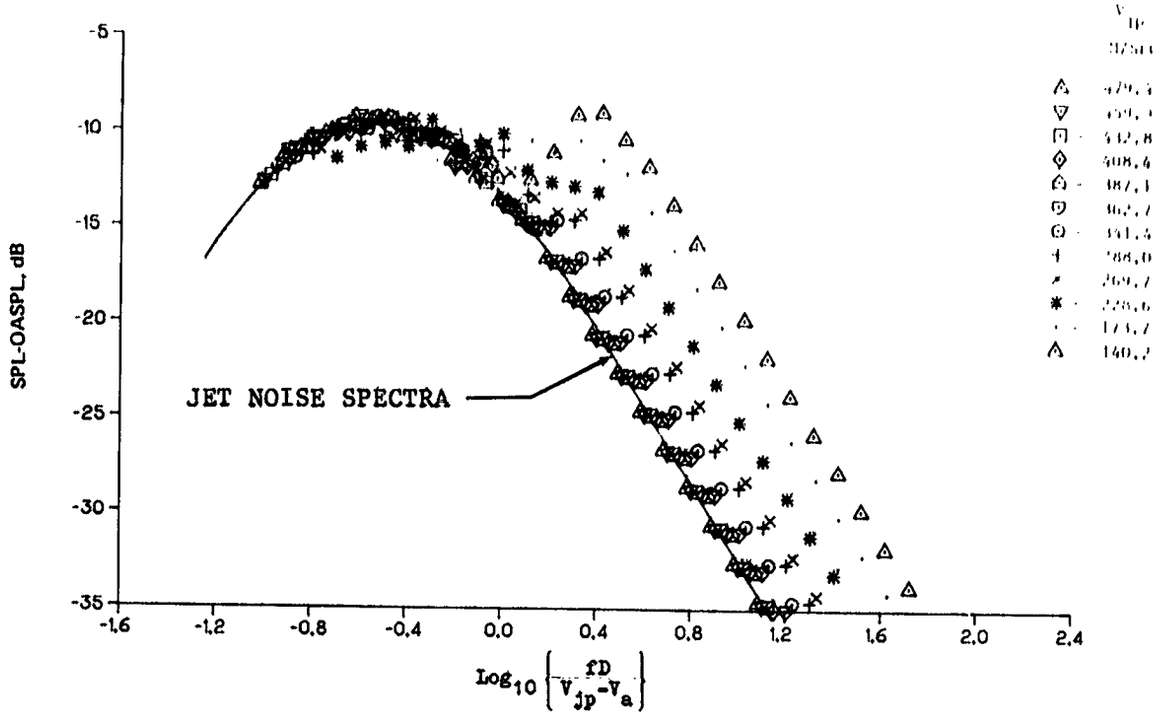

(c) 120° FROM INLET CENTERLINE

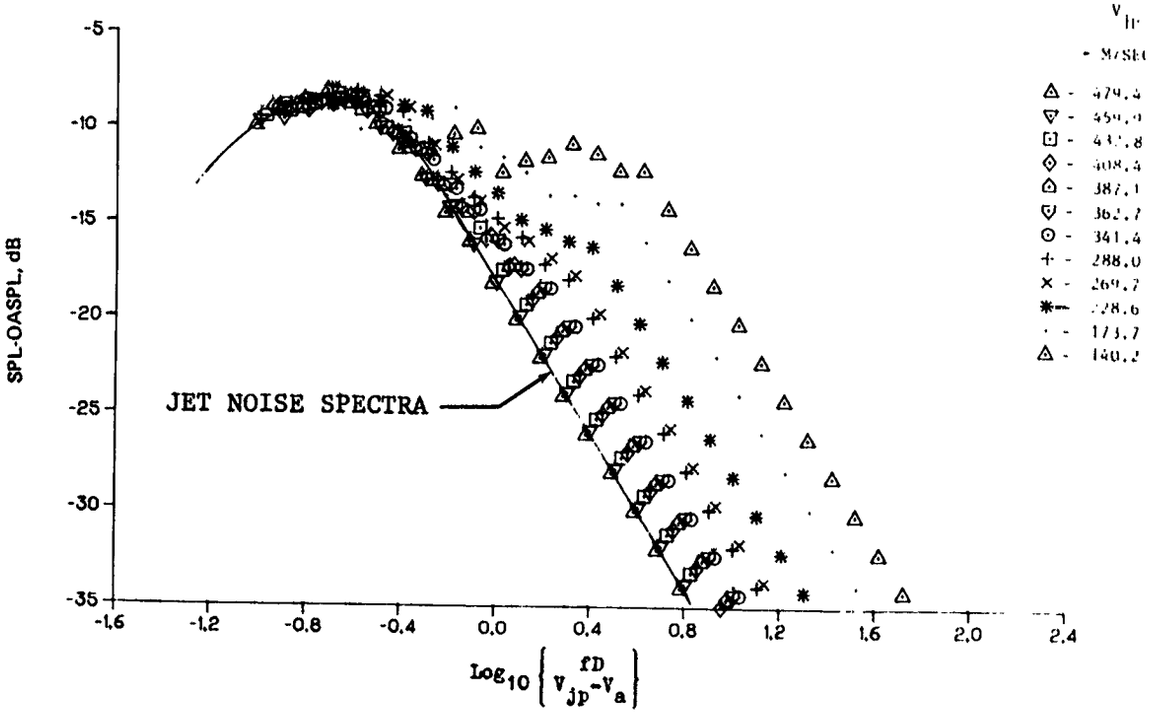

(d) 140° FROM INLET CENTERLINE

FIGURE 16 NORMALIZED SPECTRA OF JT9D-59A STATIC JET-PLUS-CORE NOISE AT 45.7-METER RADIUS. V_a = 0 M/SEC (CONTINUED)

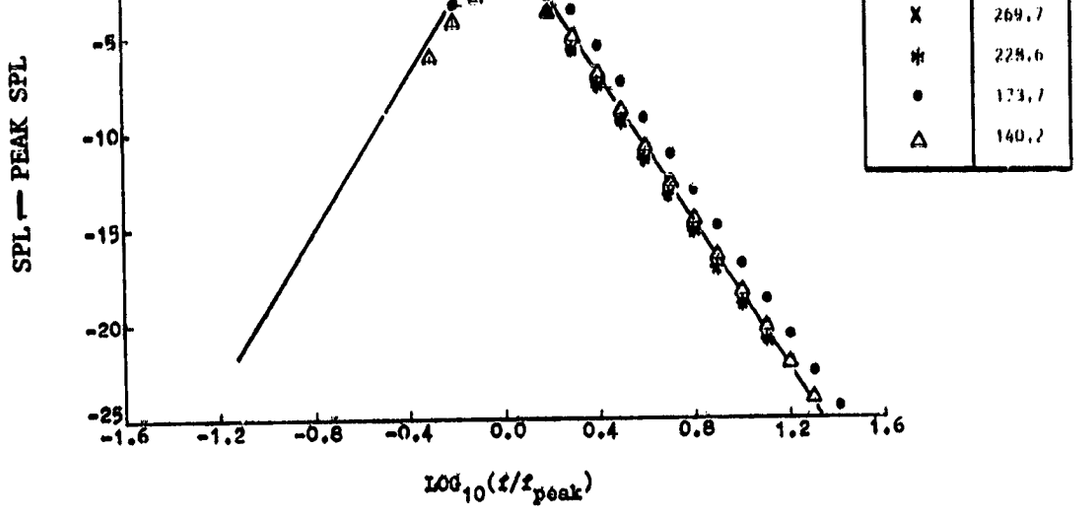

(a) 50° FROM INLET CENTERLINE

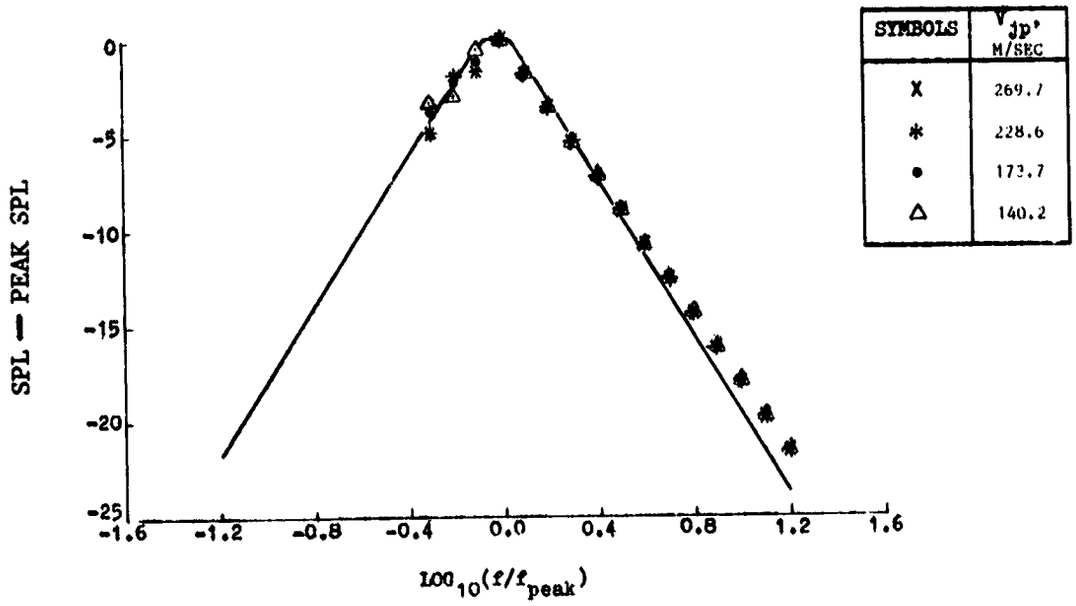

(b) 90° FROM INLET CENTERLINE

FIGURE 17. NORMALIZED SPECTRA OF JT9D-59A STATIC CORE NOISE AT 45.7-METER RADIUS

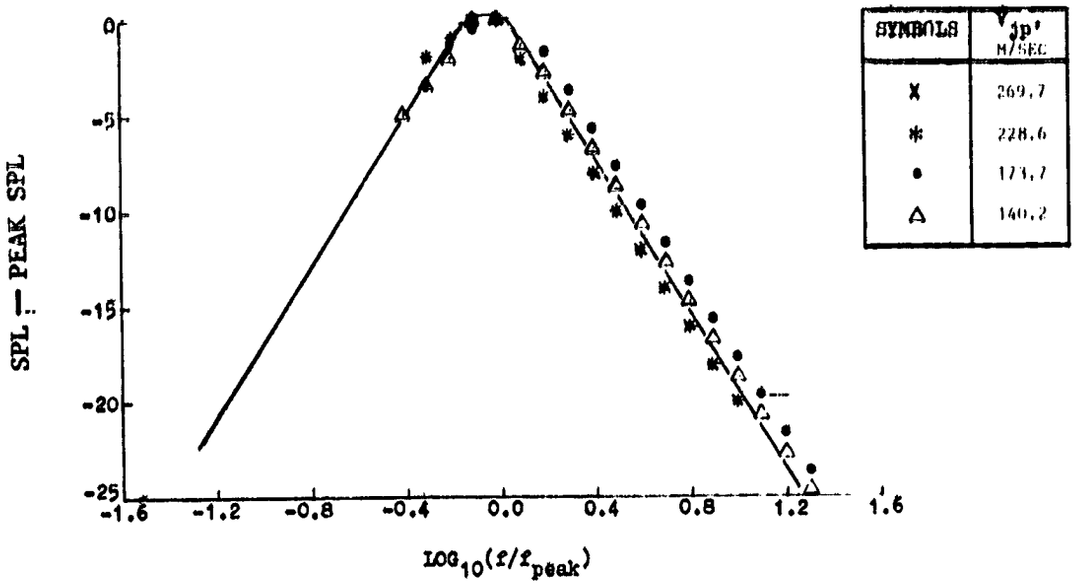

(c) 120° FROM INLET CENTERLINE

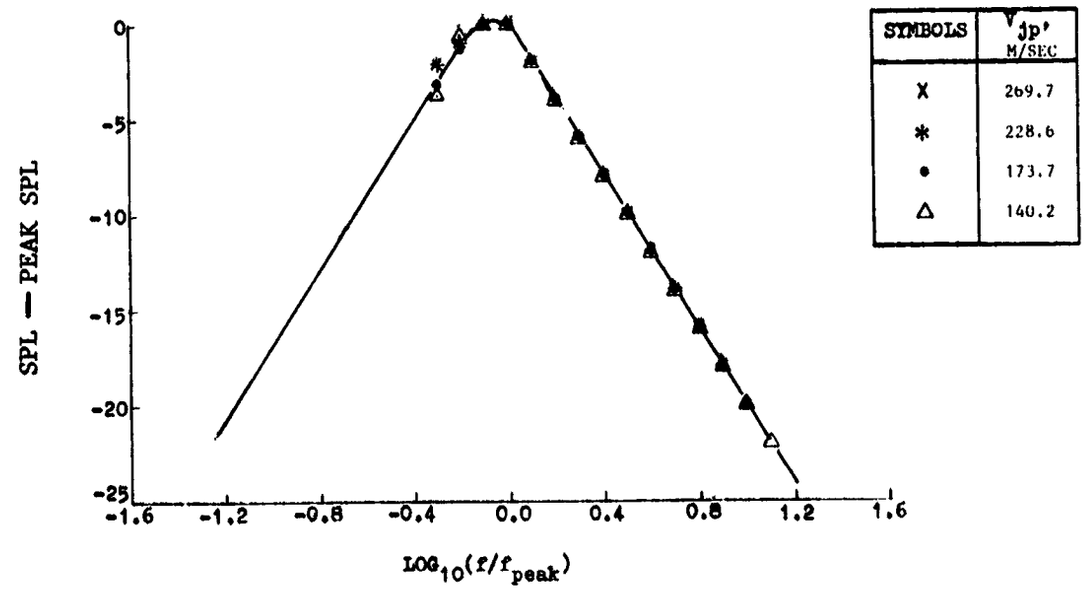

(d) 140° FROM INLET CENTERLINE

FIGURE 17 NORMALIZED SPECTRA OF JT9D-59A STATIC CORE NOISE AT 45.7-METER RADIUS (CONTINUED)

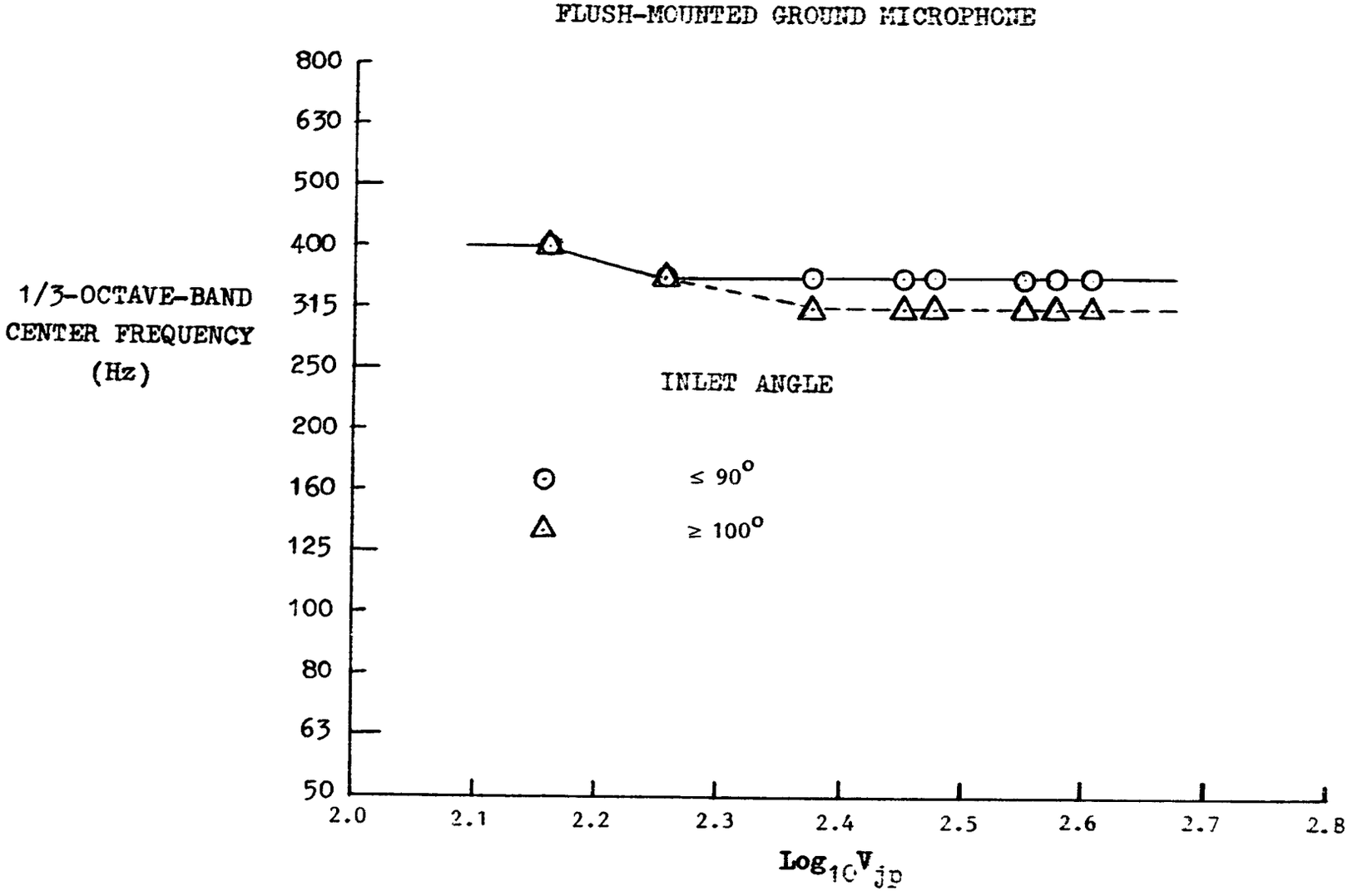

FIGURE 18. CORRELATION OF CORE-NOISE PEAK FREQUENCY FOR STATIC JT9D-59A ENGINE AT 45.7-METER RADIUS

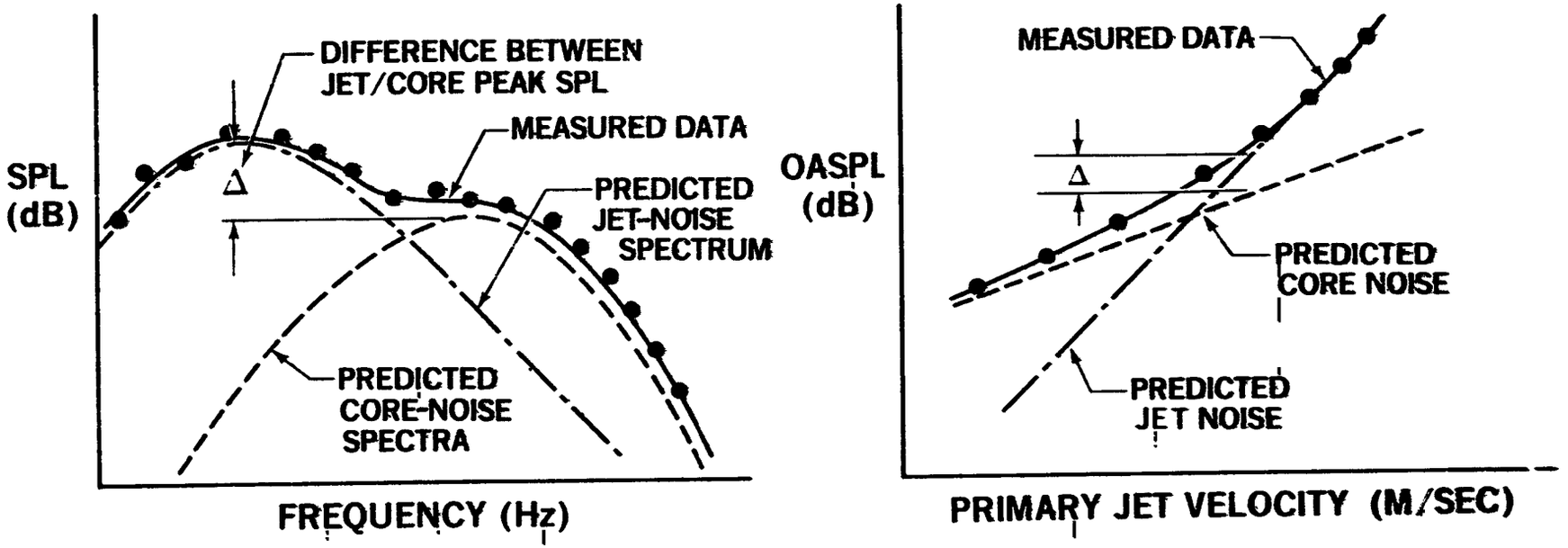

FIGURE 19. DETERMINATION OF RELATIVE JET AND CORE NOISE SOURCE LEVELS FROM MEASURED LOW-FREQUENCY NOISE SPECTRA (CURVED-FIT TECHNIQUE)

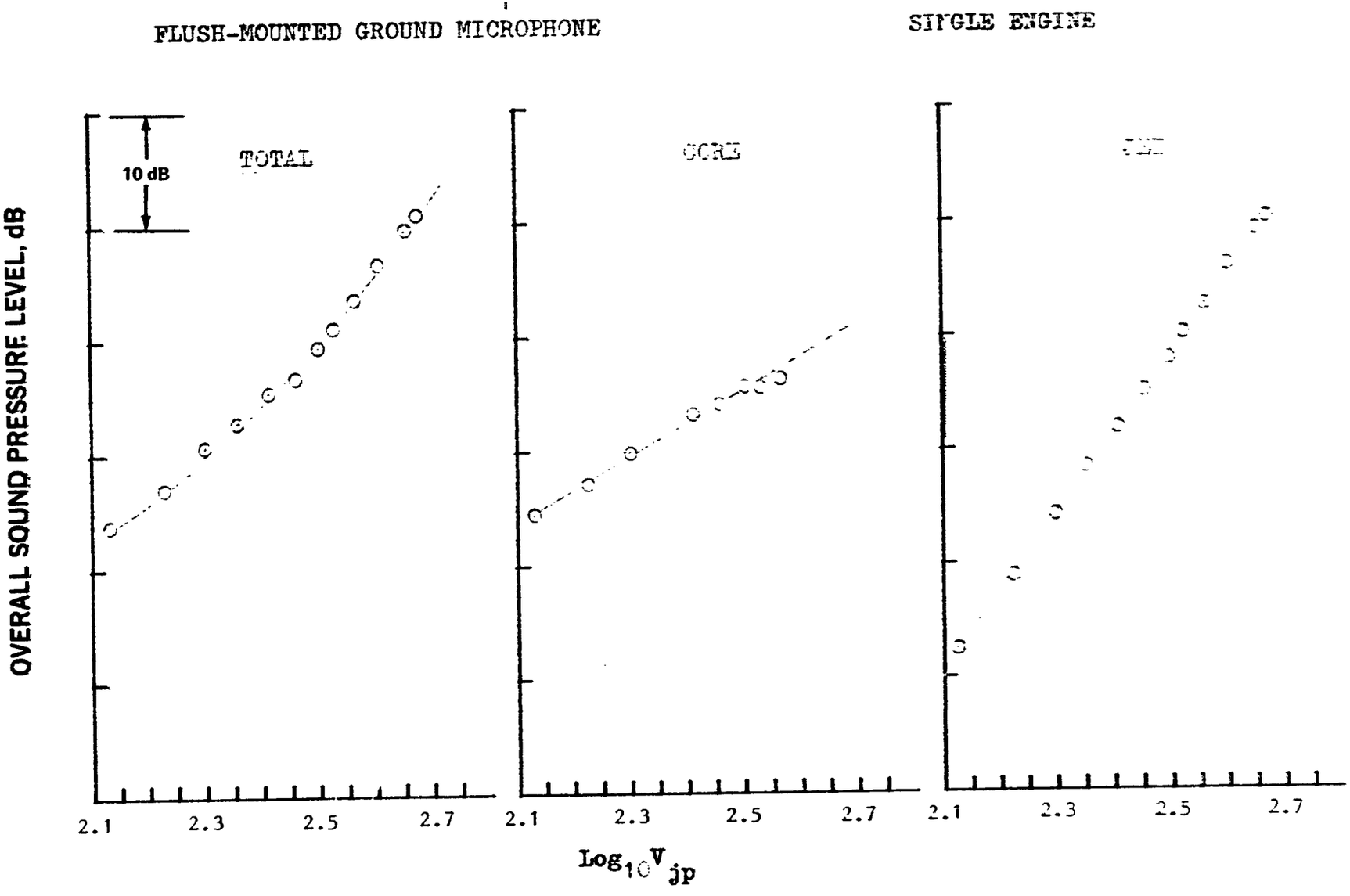

FIGURE 20. CORRELATIONS OF OASPL'S OF TOTAL, JET, AND CORE NOISE COMPONENTS FOR JT8D-109 STATIC ENGINE AT 45.7-METER RADIUS AND 120° FROM INLET CENTERLINE

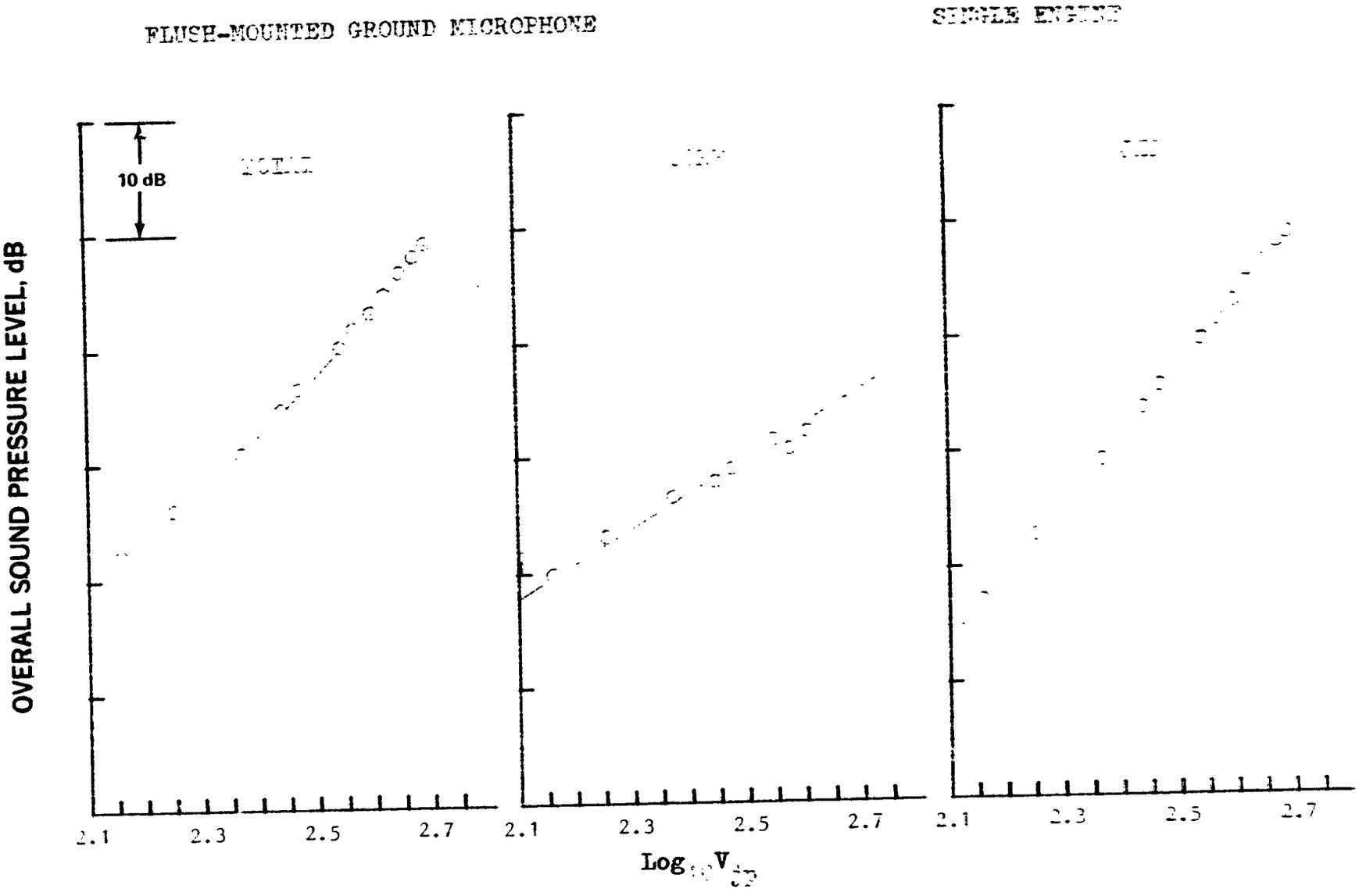

FIGURE 21. CORRELATIONS OF OASPL'S OF TOTAL, JET, AND CORE NOISE COMPONENTS FOR JT9D-59A STATIC ENGINE AT 45.7-METER RADIUS AND 120° FROM INLET

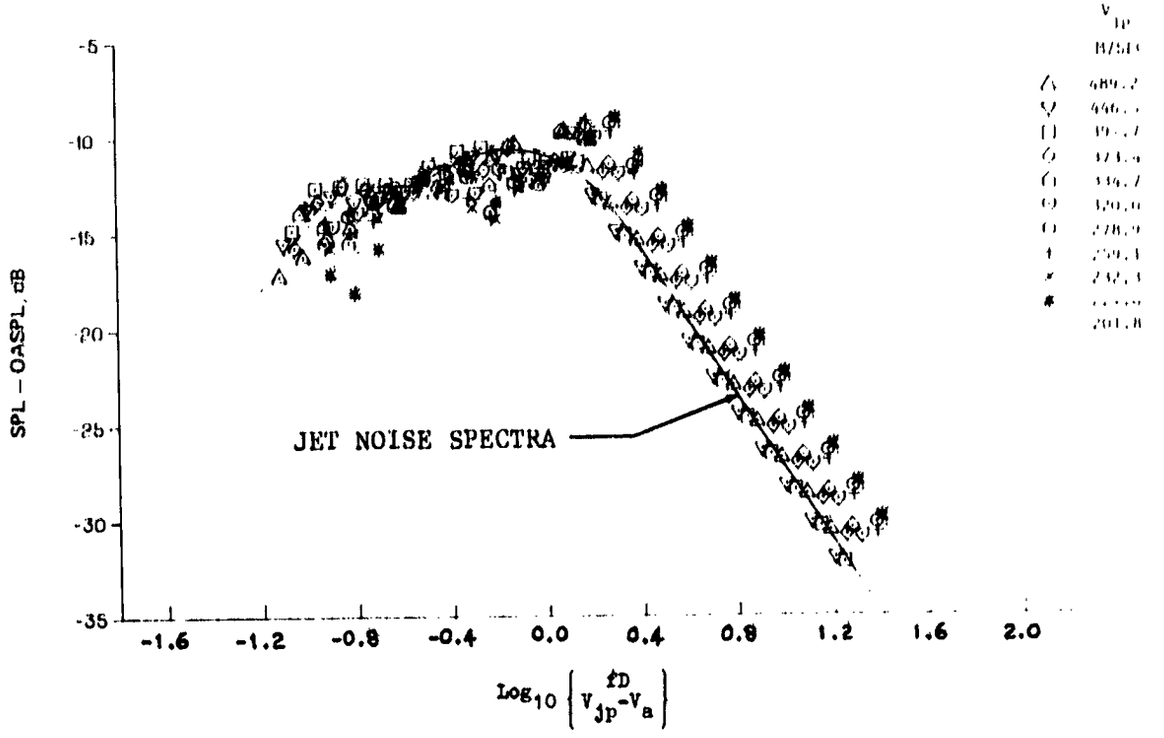

(a) 50° FROM INLET CENTERLINE

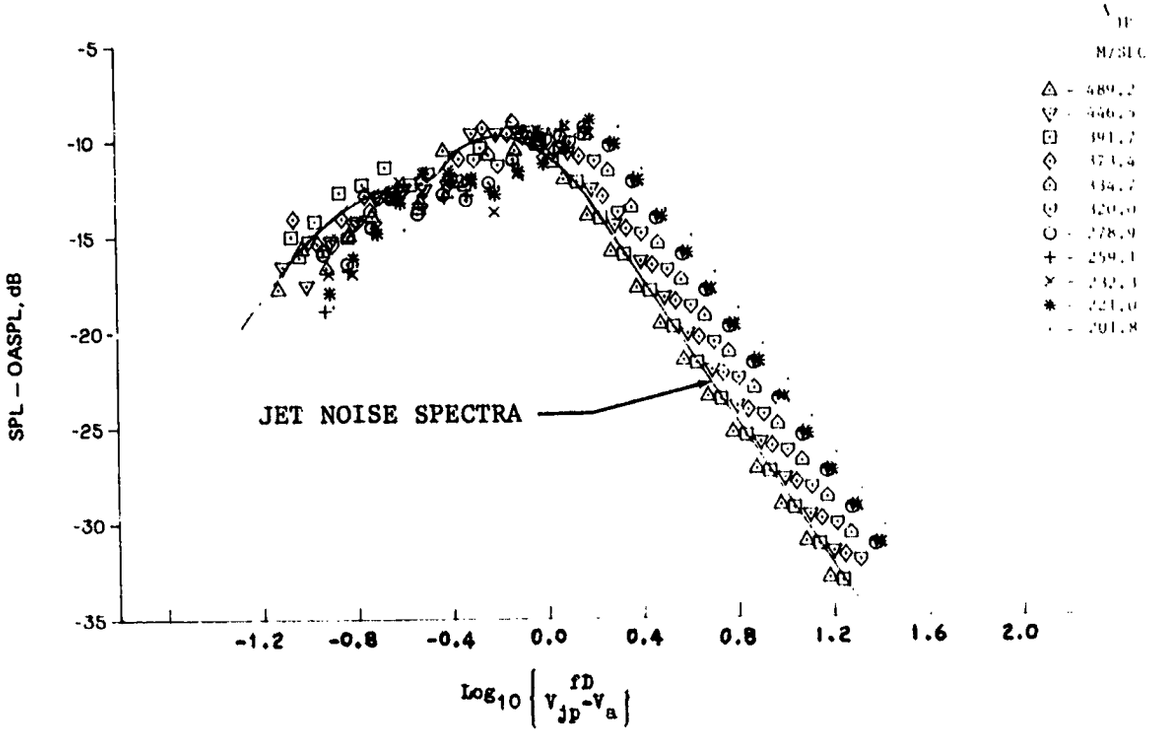

(b) 90° FROM INLET CENTERLINE

FIGURE 22. NORMALIZED SPECTRA OF DC-9-30/JT8D-109 INFLIGHT JET-PLUS-CORE NOISE AT 45.7-METER RADIUS

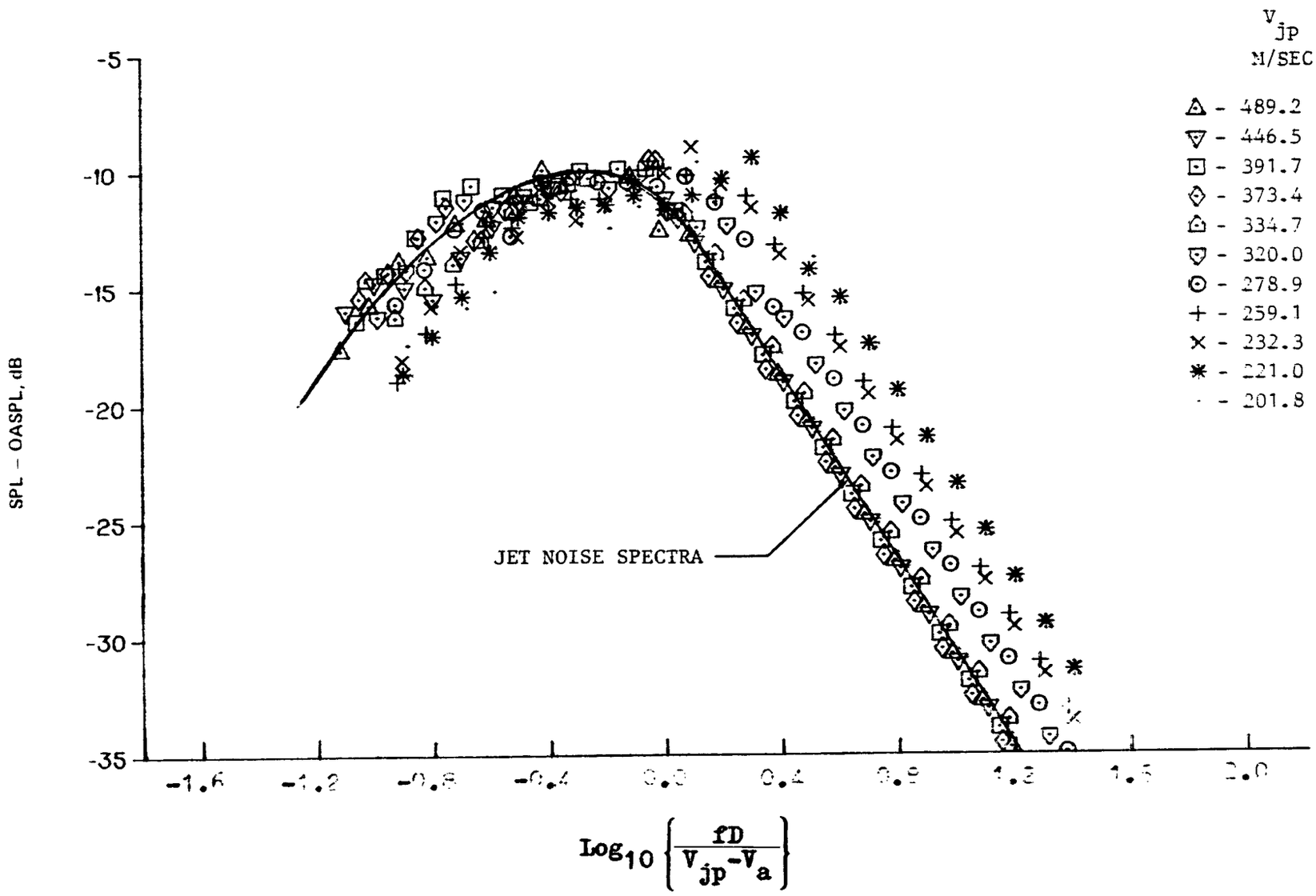

(c) 120° FROM INLET CENTERLINE

FIGURE 22 NORMALIZED SPECTRA OF DC-9-30/JT8D-109 INFLIGHT JET-PLUS-CORE NOISE AT 45.7-METER RADIUS (CONTINUED)

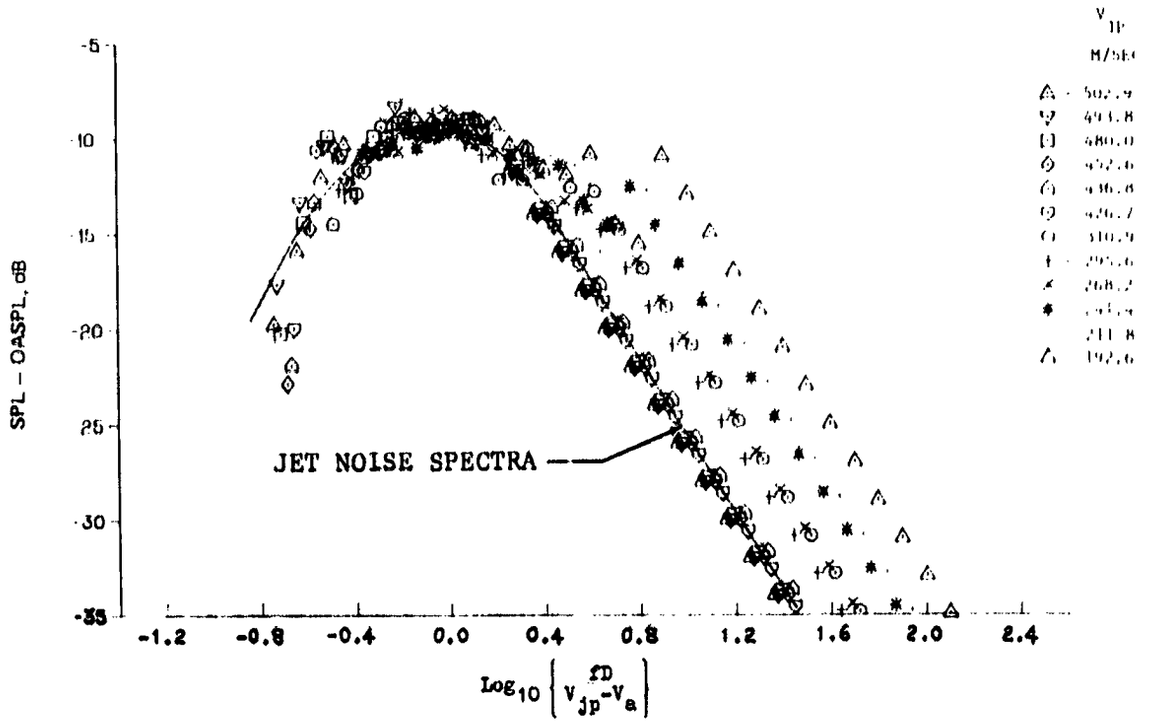

(a) 50° FROM INLET CENTERLINE

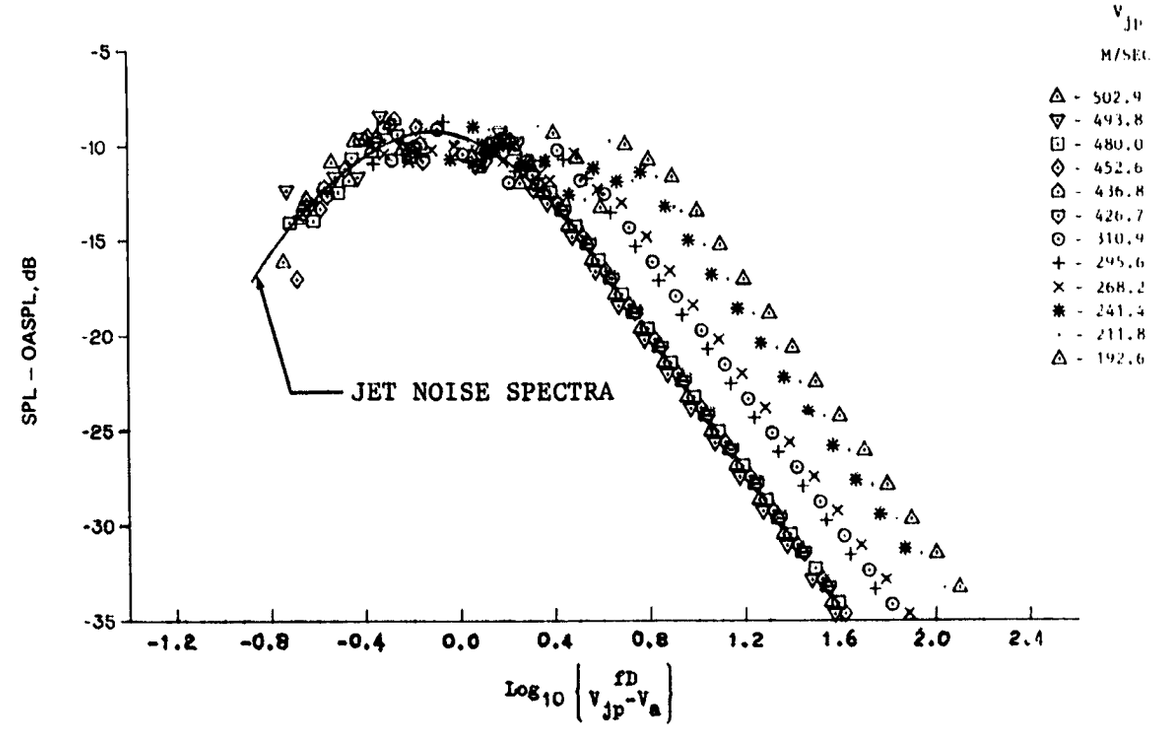

(b) 90° FROM INLET CENTERLINE

FIGURE 23. NORMALIZED SPECTRA OF DC-10-40/JT9D-59A INFLIGHT JET-PLUS-CORE NOISE AT 45.7-METER RADIUS

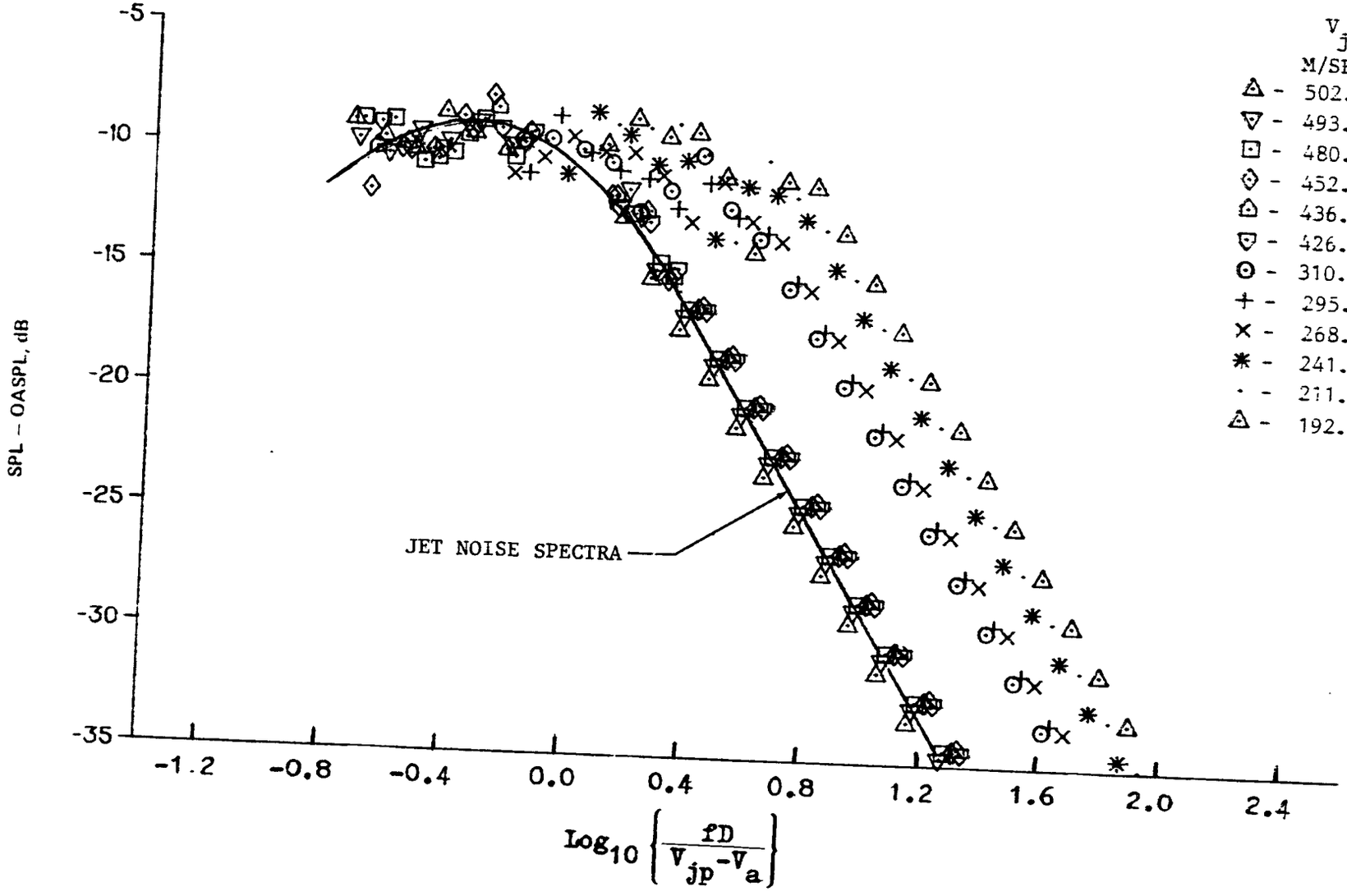

(c) 120° FROM INLET CENTERLINE

FIGURE 23 NORMALIZED SPECTRA OF DC-10-40/JT9D-59A INFLIGHT JET-PLUS-CORE NOISE AT 45.7-METER RADIUS (CONTINUED)

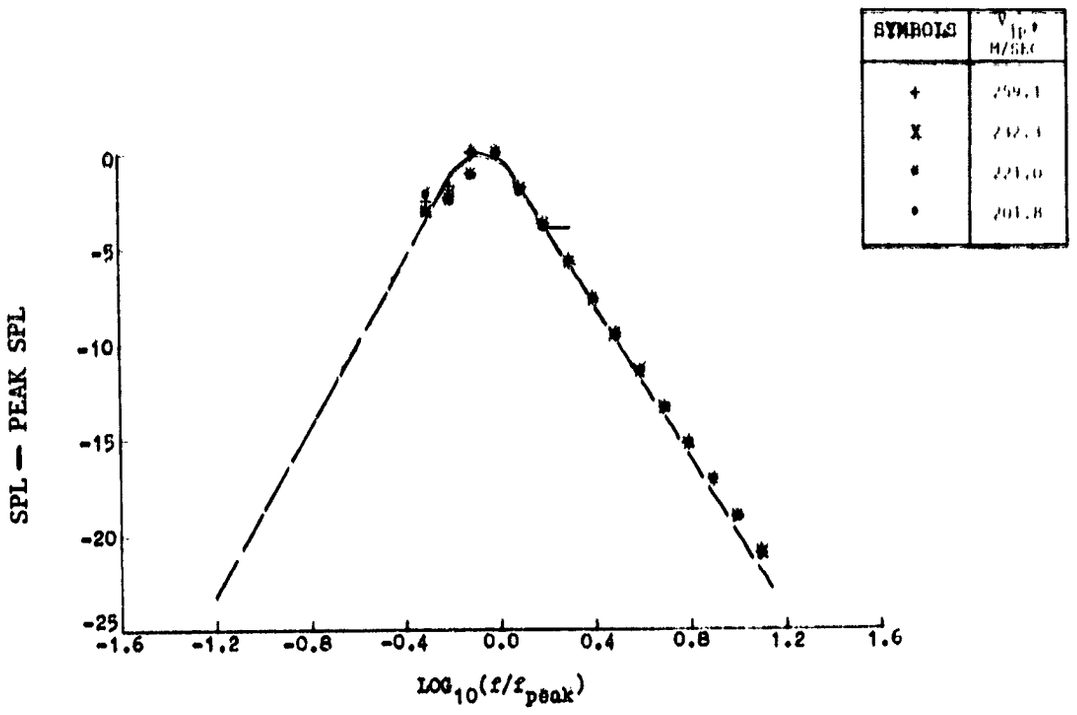

(a) 50° FROM INLET CENTERLINE

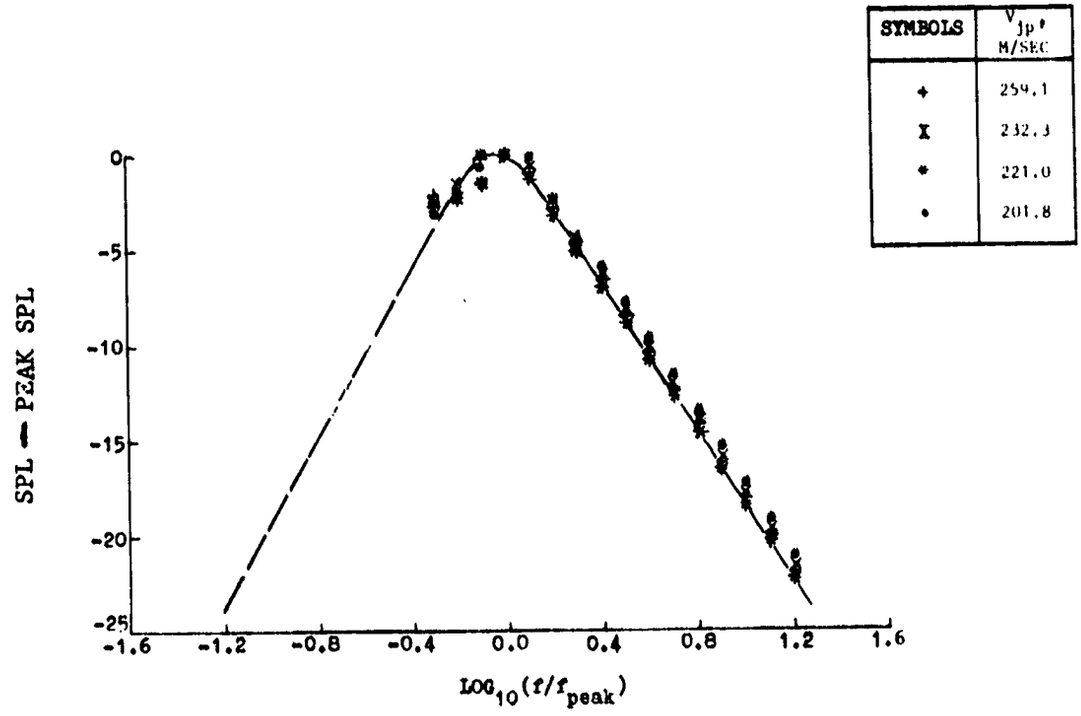

(b) 90° FROM INLET CENTERLINE

FIGURE 24. NORMALIZED SPECTRA OF DC-9-30/JT8D-109 INFLIGHT CORE NOISE AT 45.7-METER RADIUS

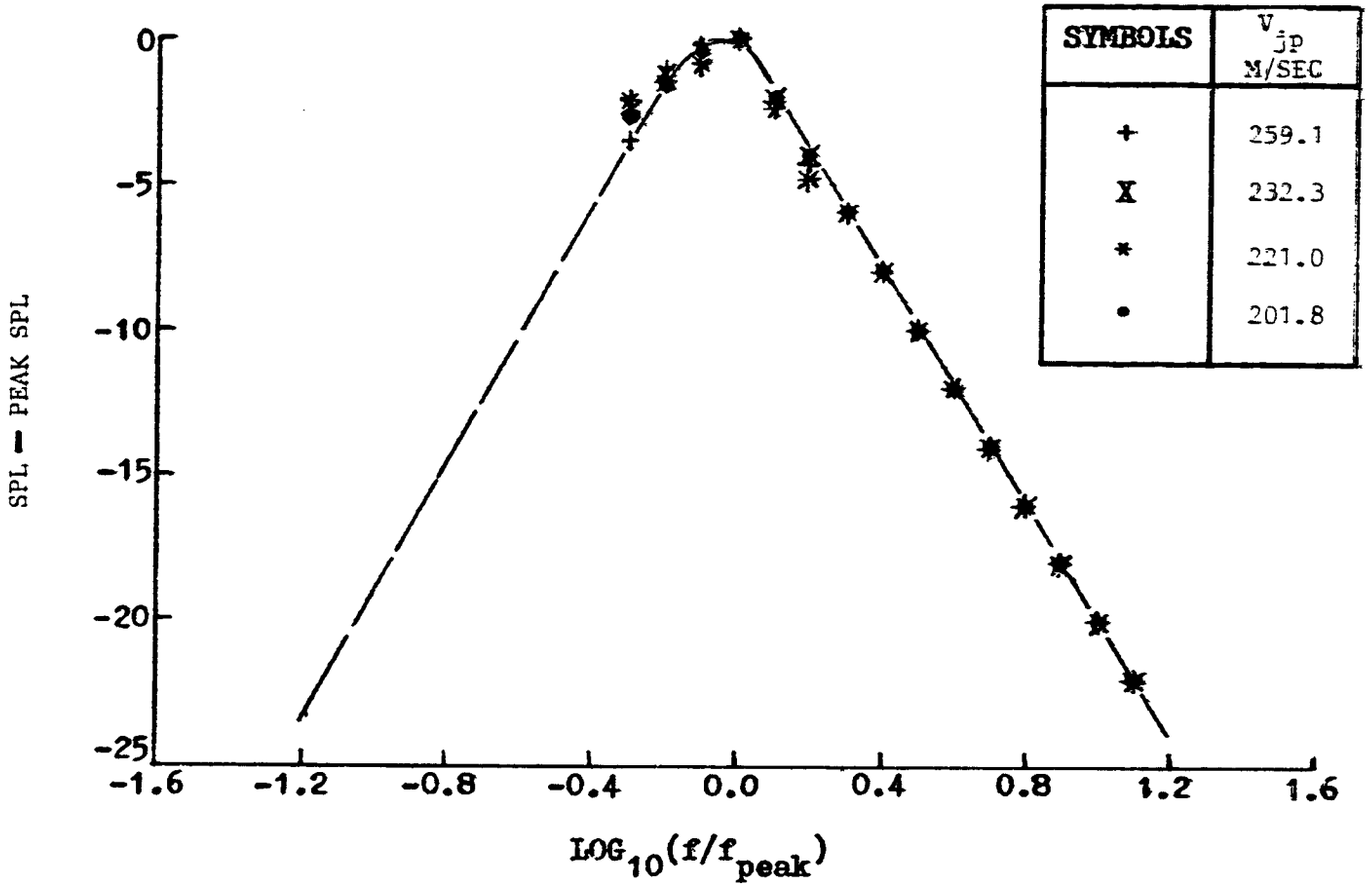

(c) 120° FROM INLET CENTERLINE

FIGURE 24 NORMALIZED SPECTRA OF DC-9-30/JT8D-109 INFLIGHT CORE NOISE AT 45.7-METER RADIUS (CONTINUED)

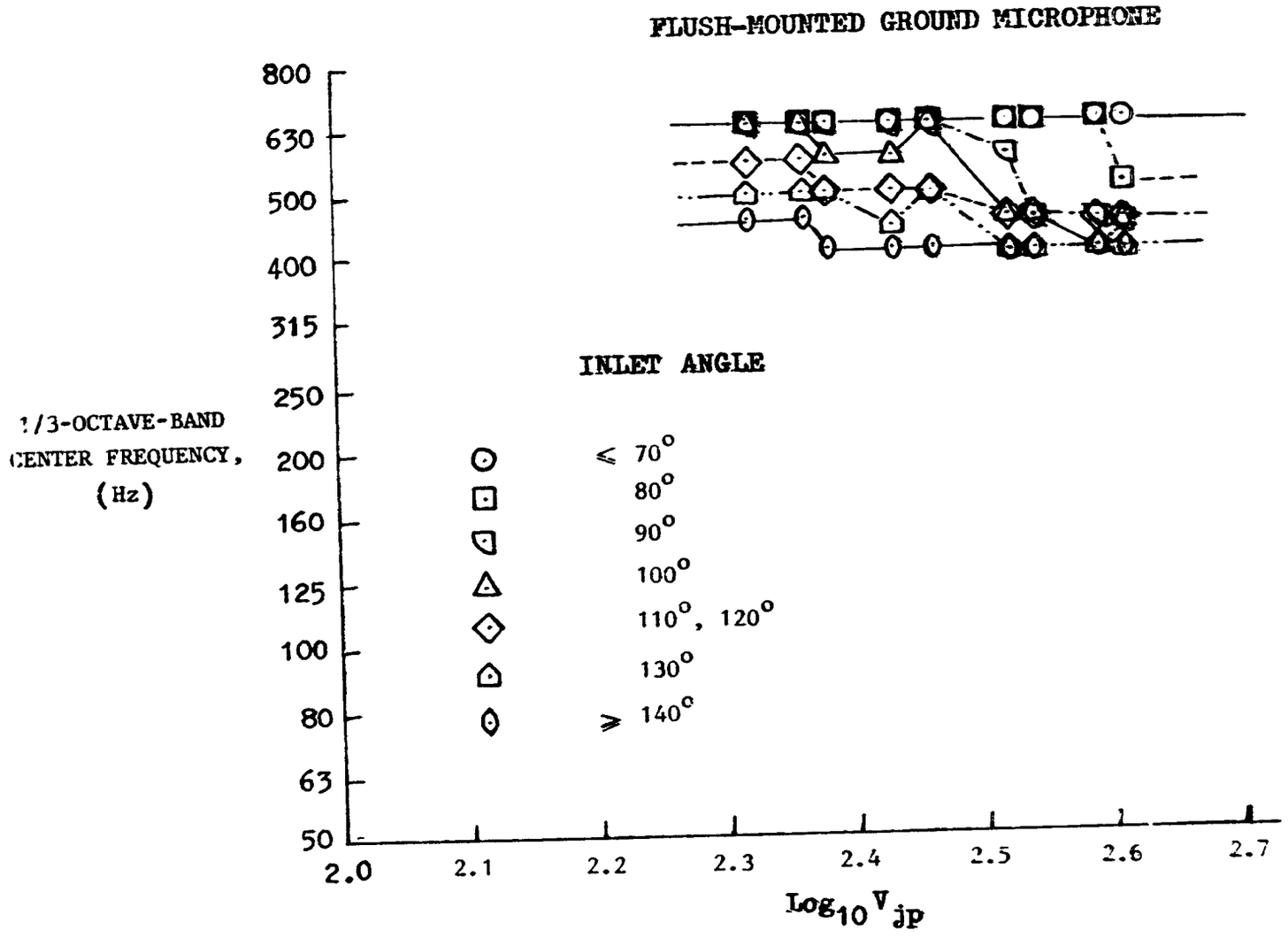

FIGURE 25. CORRELATION OF INFLIGHT CORE-NOISE PEAK FREQUENCY OF DC-9-30/JT8D-109 AT 45.7-METER RADIUS

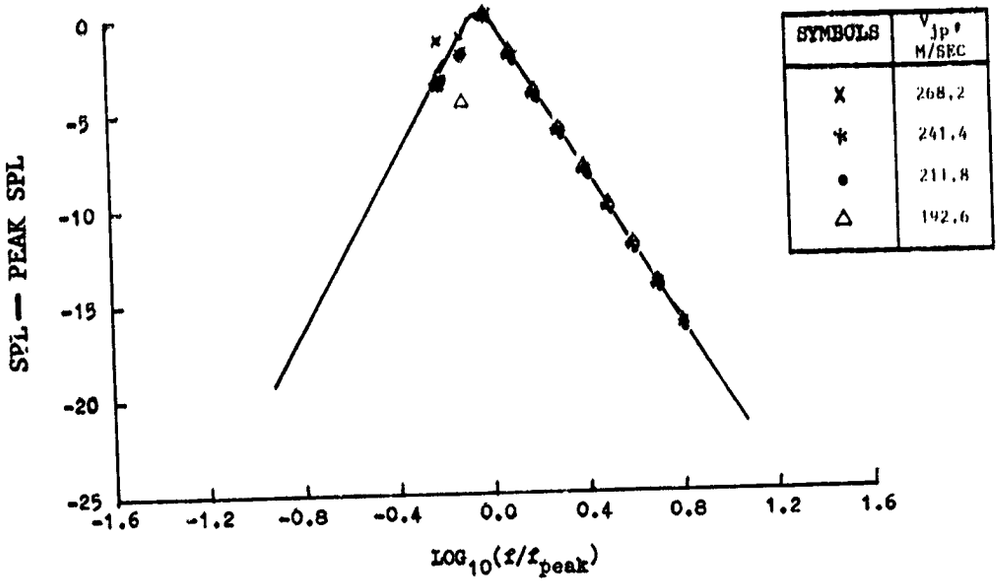

(a) 50^{o} FROM INLET CENTERLINE

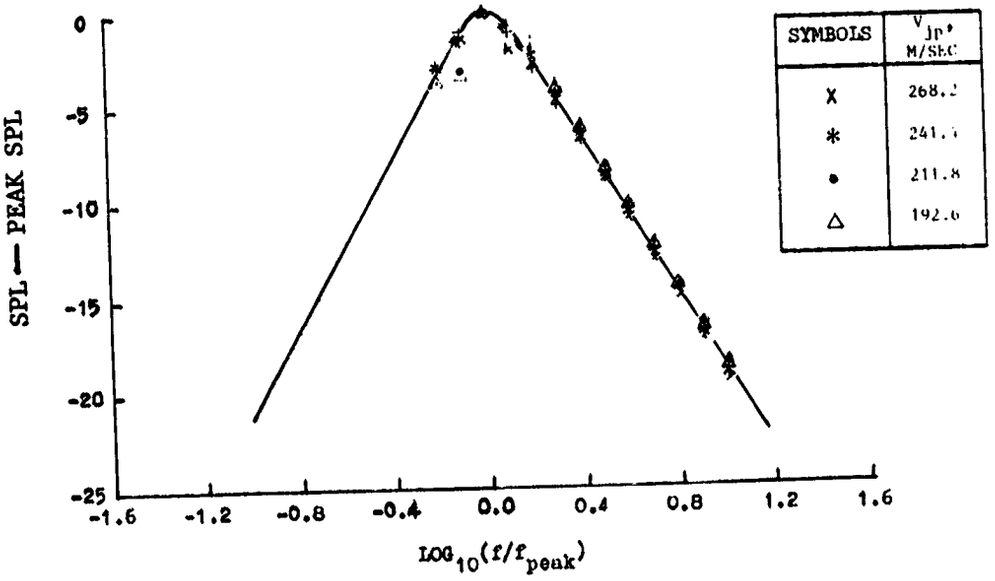

(b) 90^{o} FROM INLET CENTERLINE

FIGURE 26. NORMALIZED SPECTRA OF DC-10-40/JT9D-59A INFLIGHT CORE NOISE AT 45.7-METER RADIUS

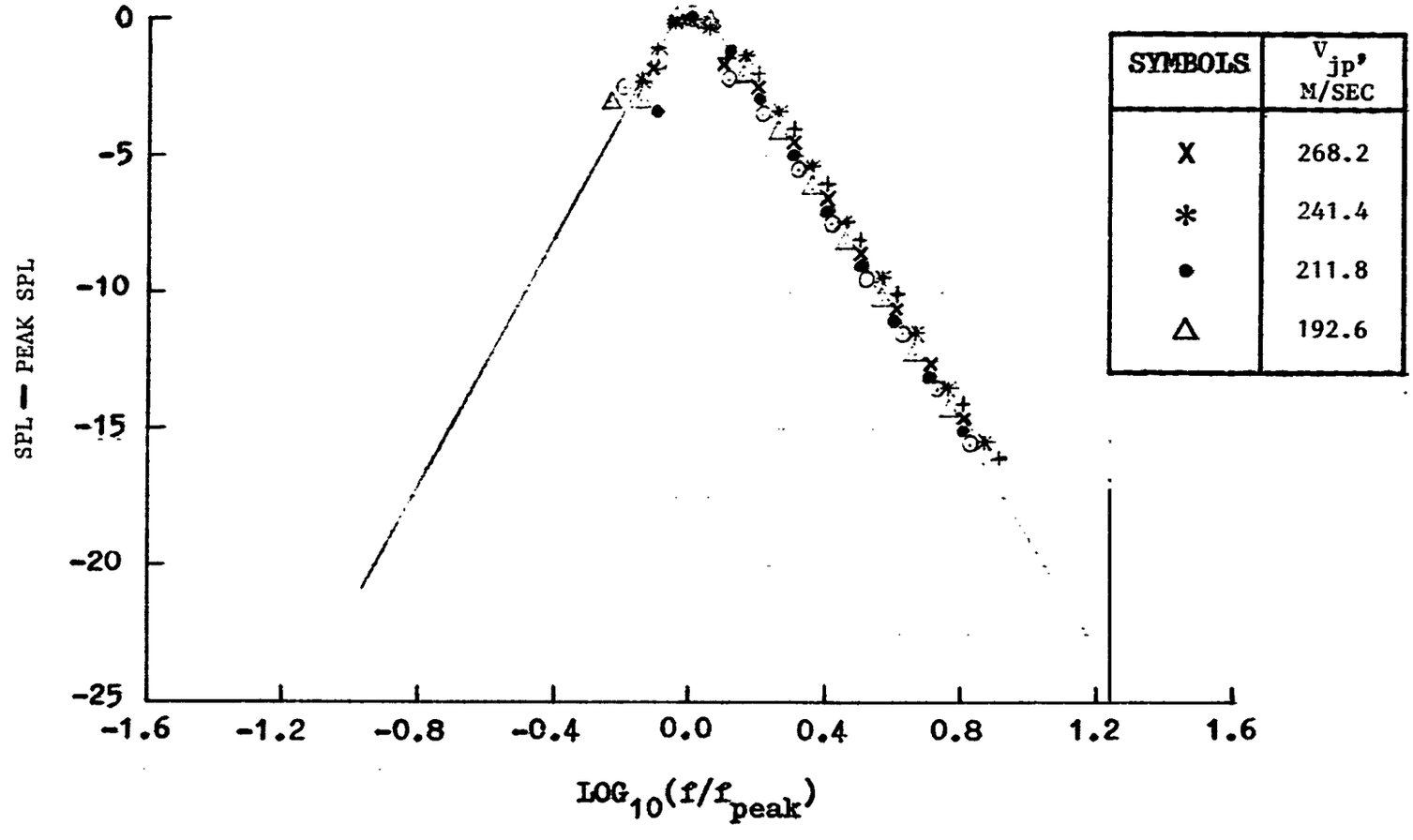

(c) 120° FROM INLET CENTERLINE

FIGURE 26 NORMALIZED SPECTRA OF DC-10-40/JT9D-59A INFLIGHT CORE NOISE AT 45.7-METER RADIUS (CONTINUED)

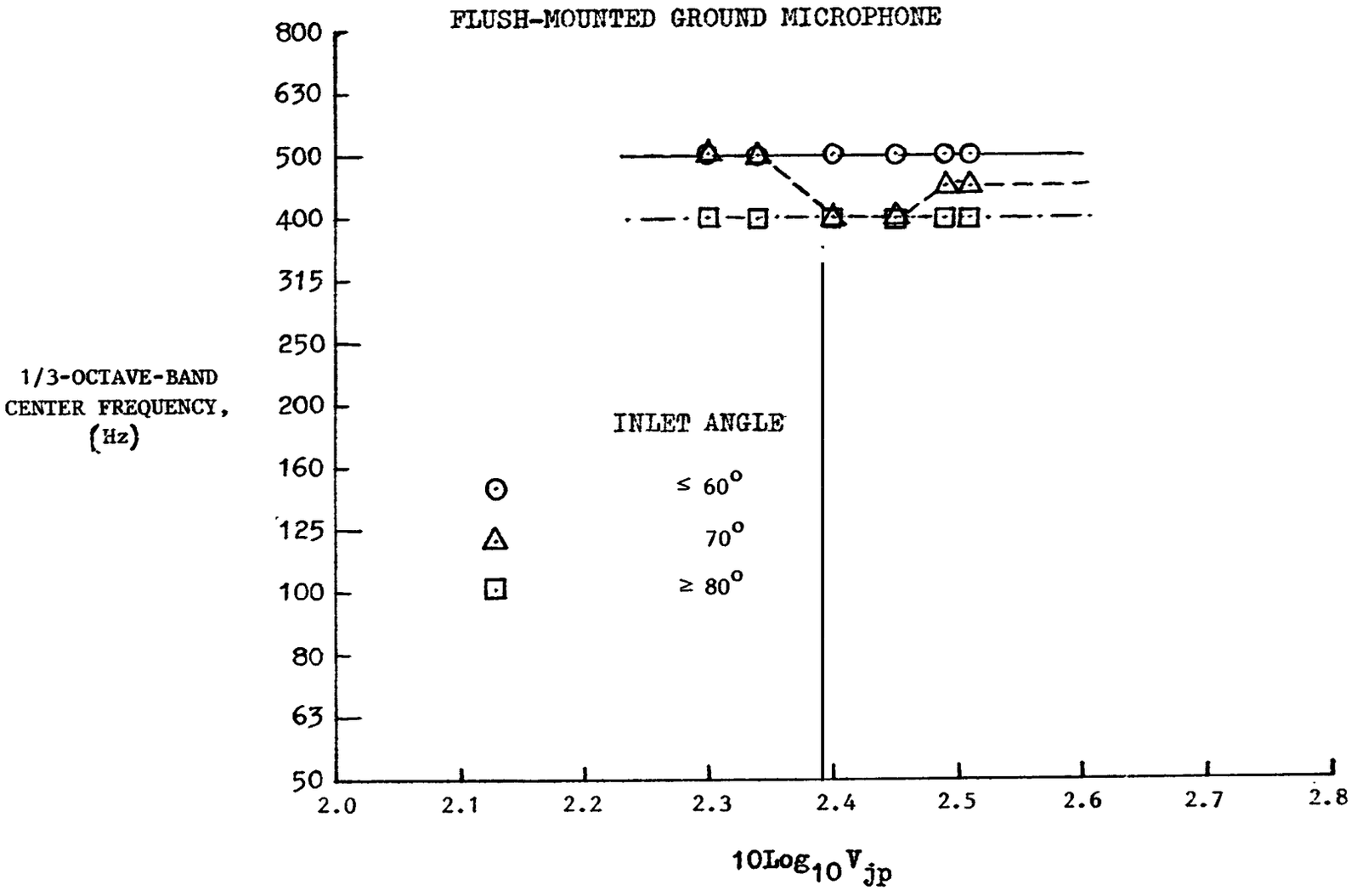

FIGURE 27. CORRELATION OF INFLIGHT CORE-NOISE PEAK FREQUENCY OF DC-10-40/JT9D-59A AT 45.7-METER RADIUS

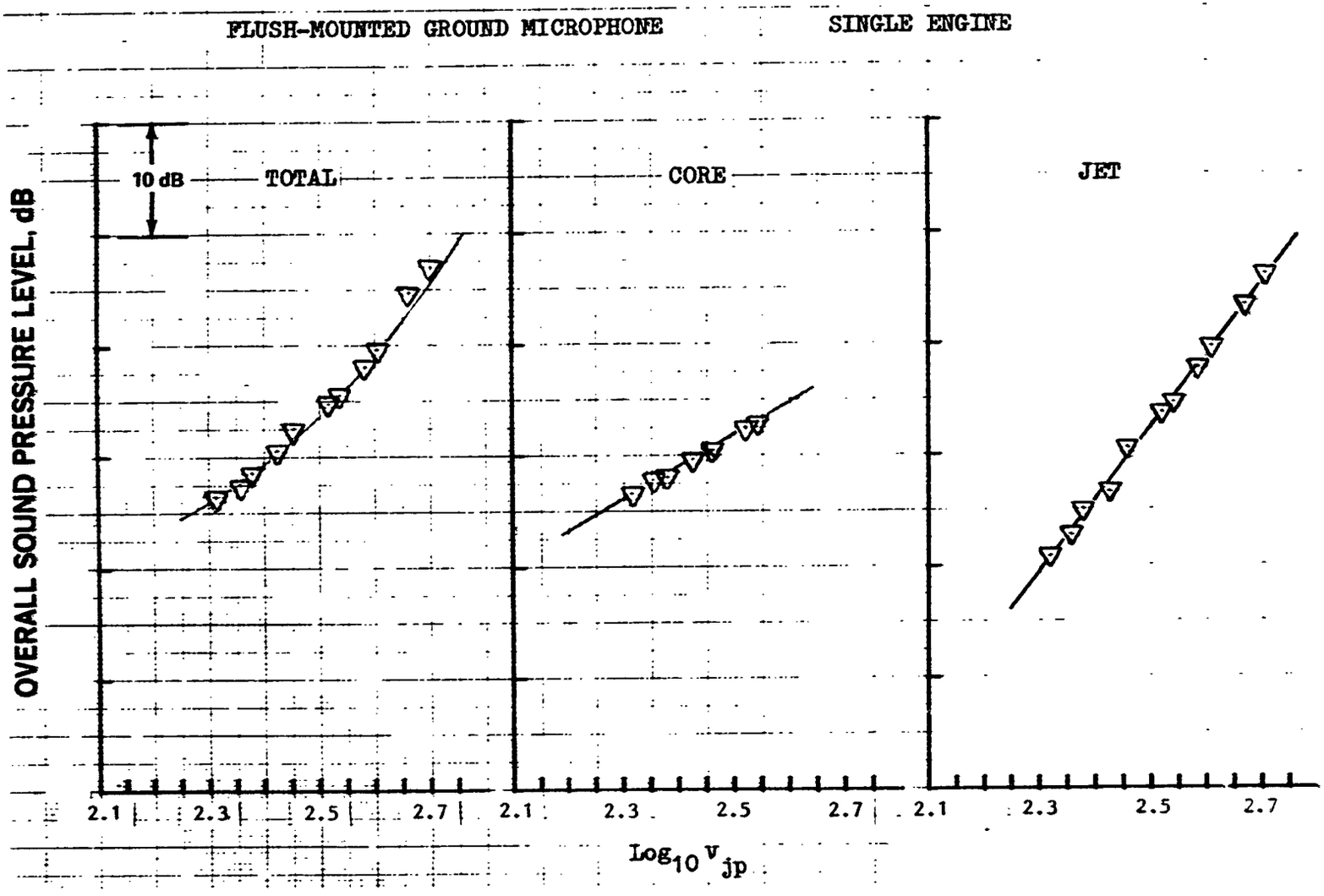

FIGURE 28. CORRELATIONS OF OASPL'S OF TOTAL, JET, AND CORE NOISE COMPONENTS FOR DC-9-30/JT8D-109 AT 45.7-METER RADIUS AND 120° FROM INLET CENTERLINE

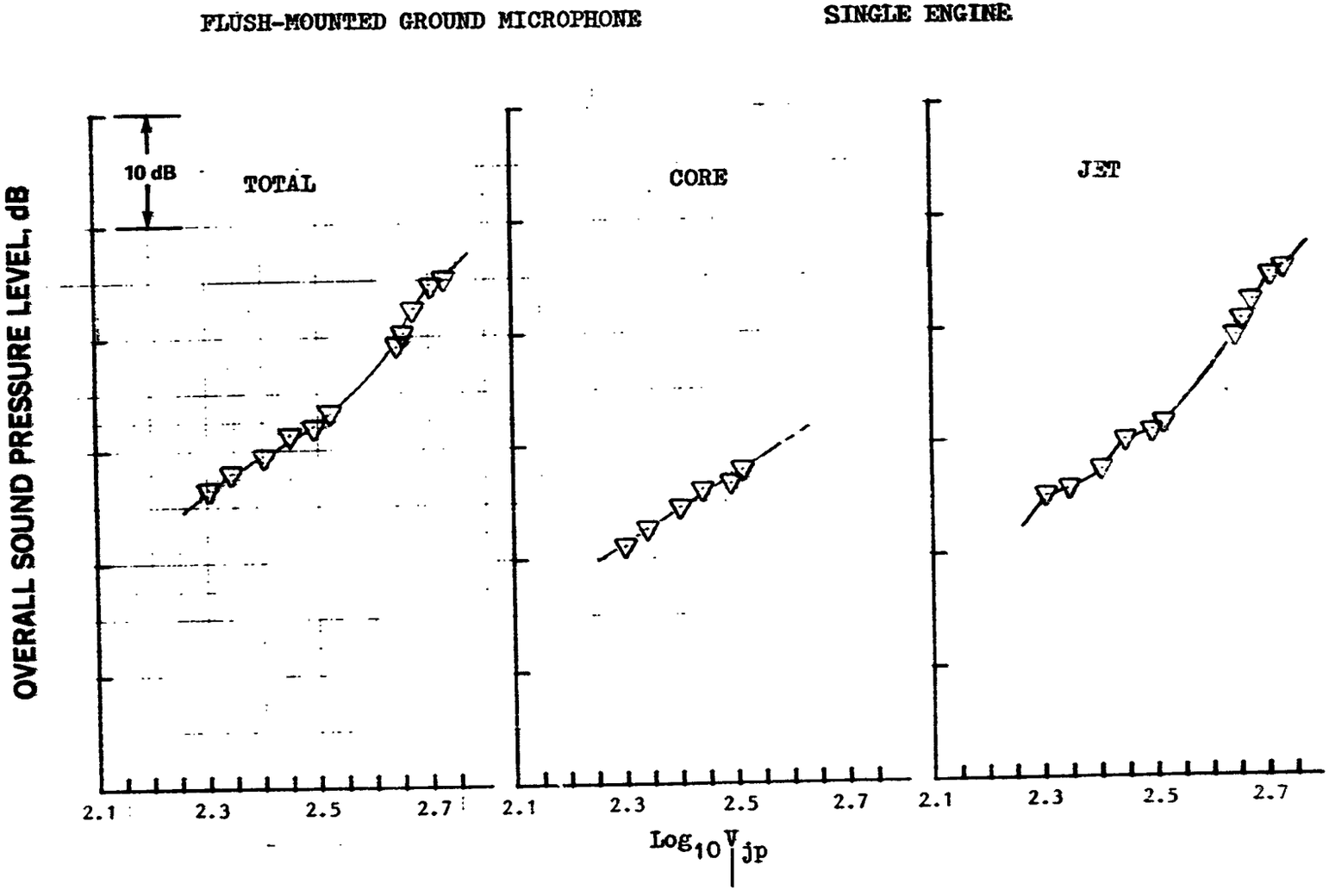

FIGURE 29. CORRELATIONS OF OASPL'S OF TOTAL, JET, AND CORE NOISE COMPONENTS FOR DC-10-40/JT9D-59A AT 45.7-METER RADIUS AND 120° FROM INLET CENTERLINE

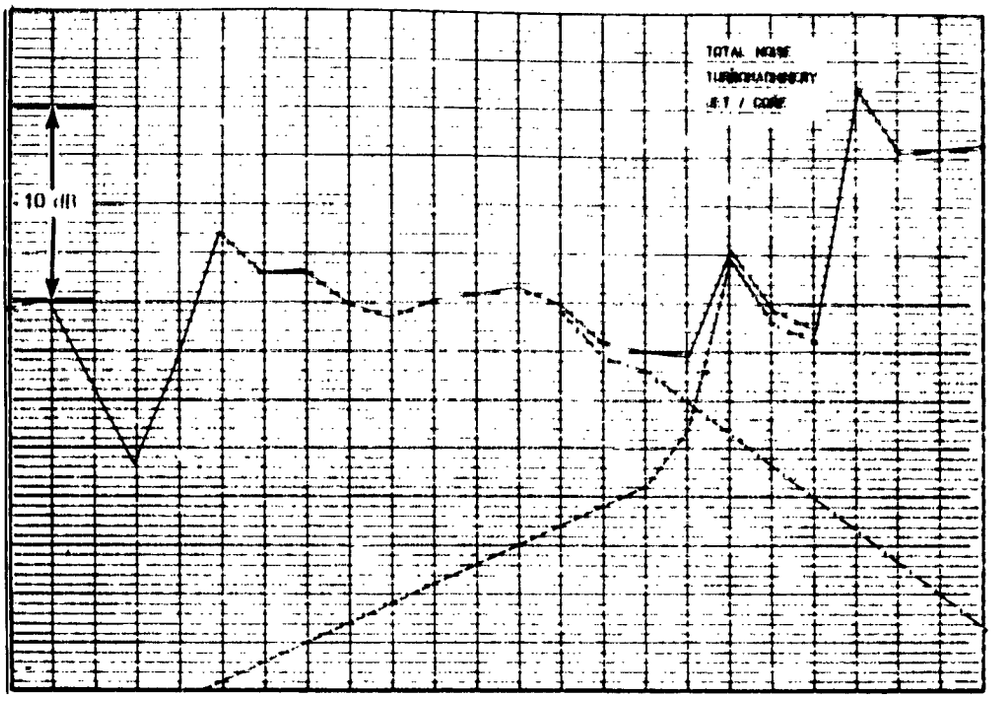

(a) $N1/\sqrt{\theta}$ = 4297.0 RPM

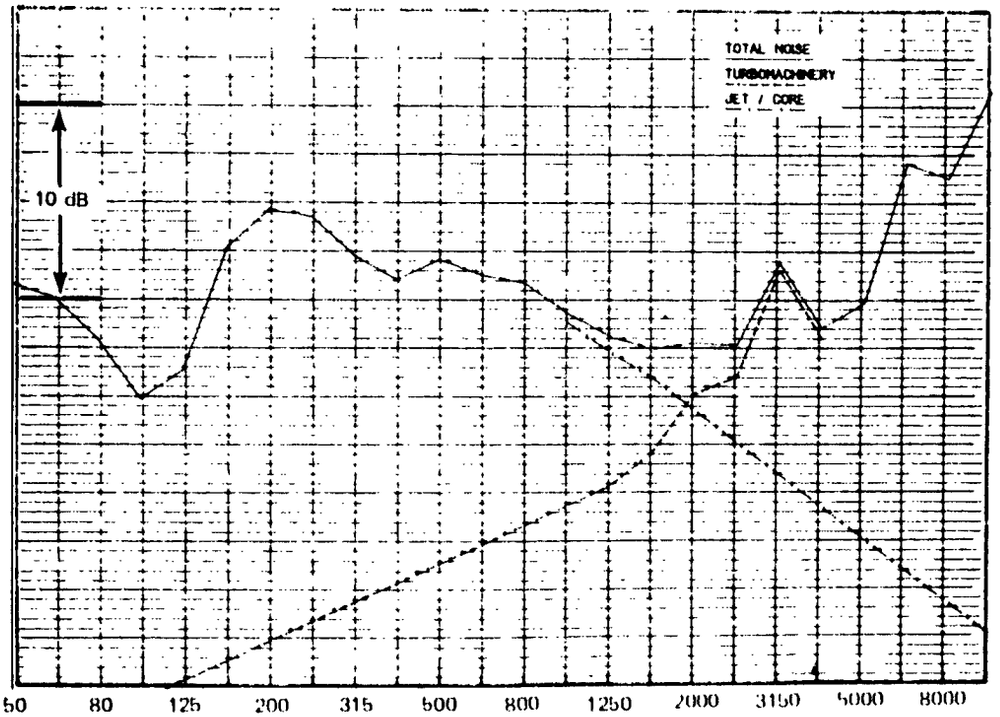

SOUND PRESSURE LEVEL, dB

50 80 125 200 315 500 800 1250 2000 3150 5000 8000

1/3 OCTAVE-BAND CENTER FREQUENCY (HZ)

(b) $N1/\sqrt{\theta}$ = 5497.0 RPM

FIGURE 30. JET/CORE AND TURBOMACHINERY STATIC NOISE SEPARATION FOR THE JT8D-109, AT 70 DEGREES, 45.7-M POLAR RADIUS

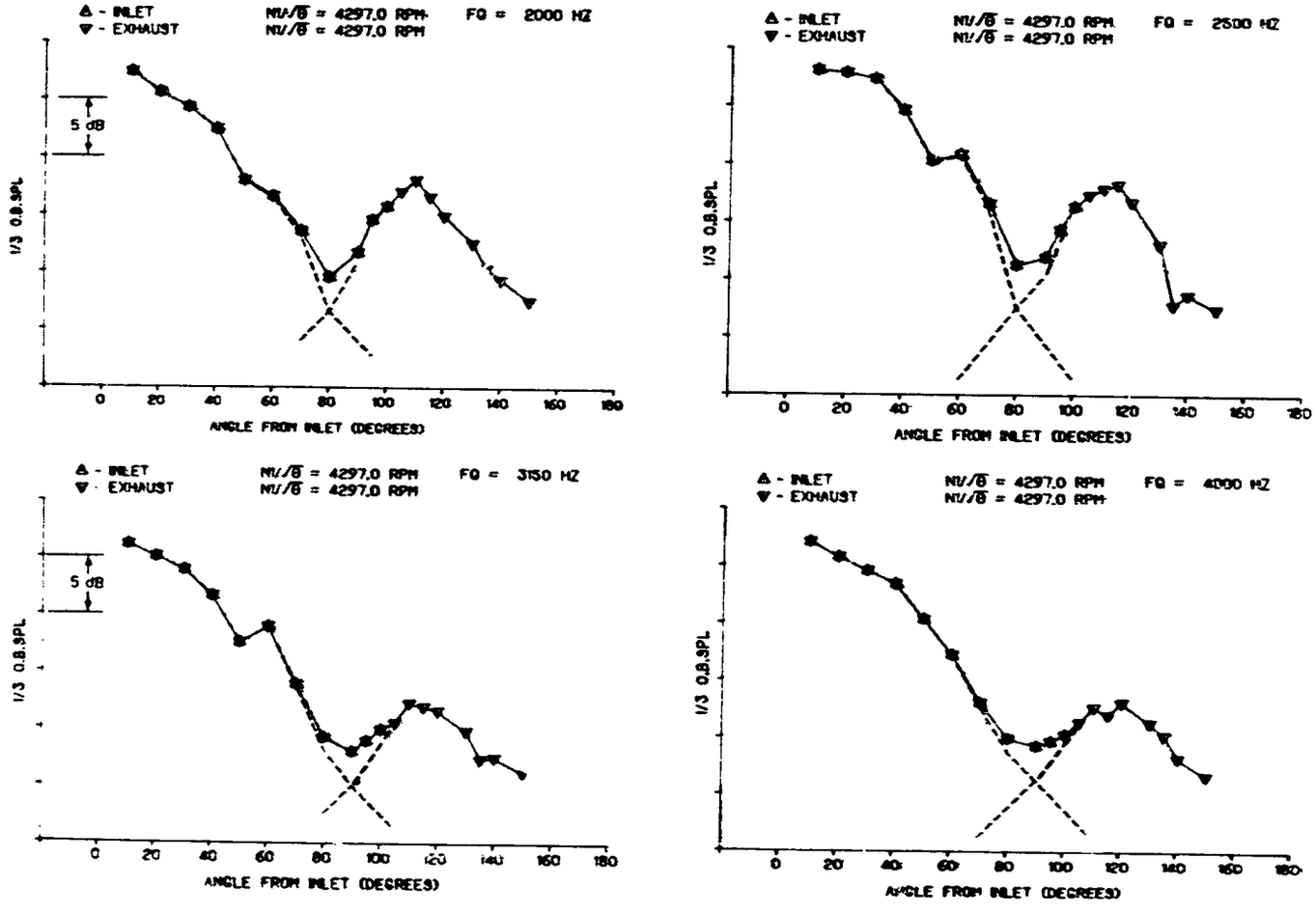

FIGURE 31. INLET AND AFT TURBOMACHINERY STATIC NOISE SEPARATION FOR THE JT8D-209, AT 2.0 TO 4.0 KHz AND N1$_{\sqrt{\theta}}$ = 4297.0 RPM, 45.7M POLAR RADIUS

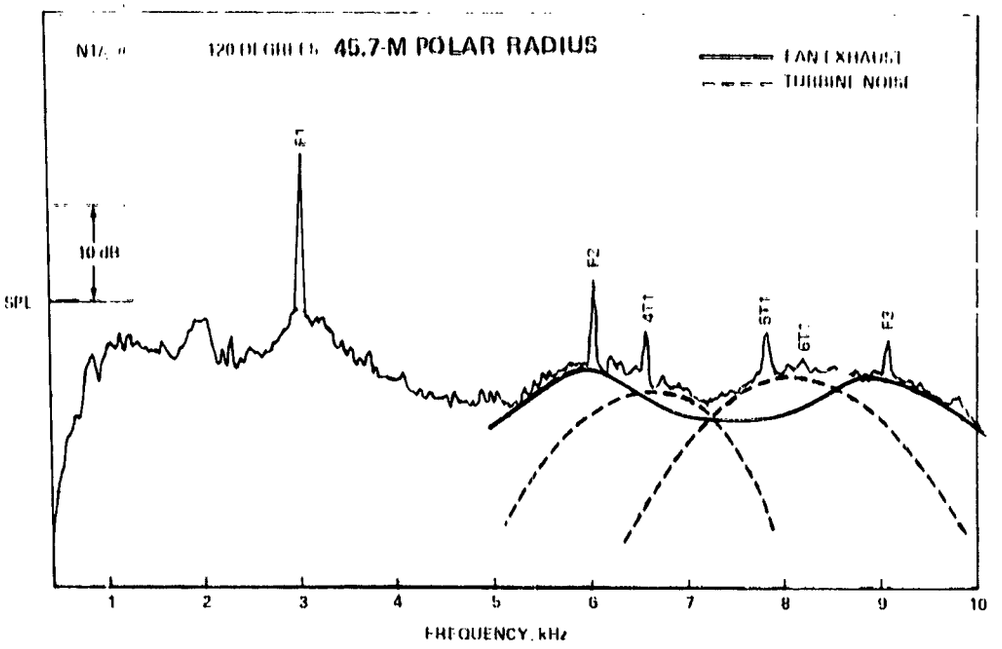

(a) JT8D-109 FREQUENCY SPECTRUM

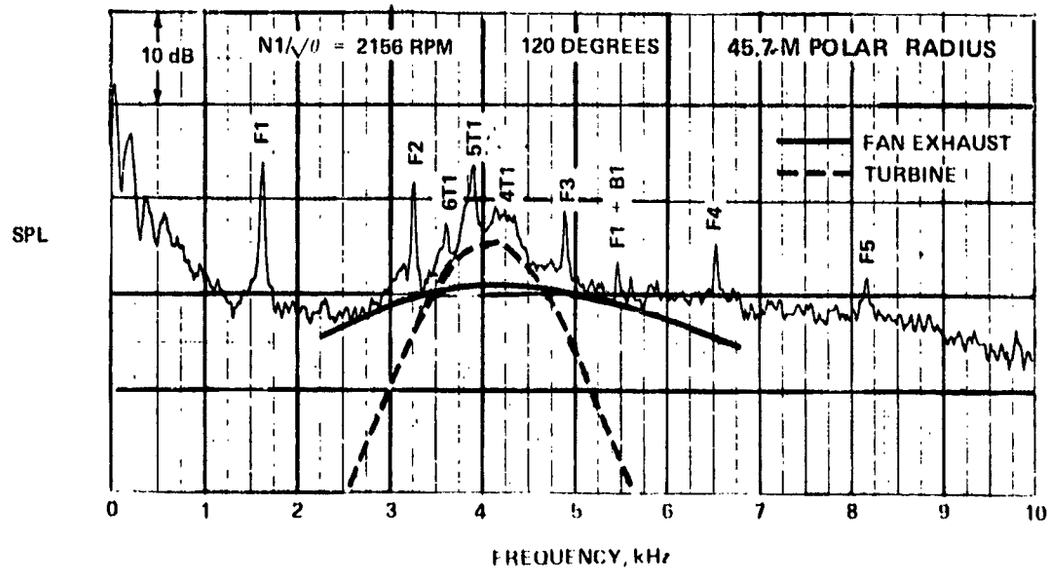

(b) JT9D-59A FREQUENCY SPECTRUM

FIGURE 32. IDENTIFICATION OF TURBINE NOISE IN STATIC TURBOMACHINERY NOISE LEVELS

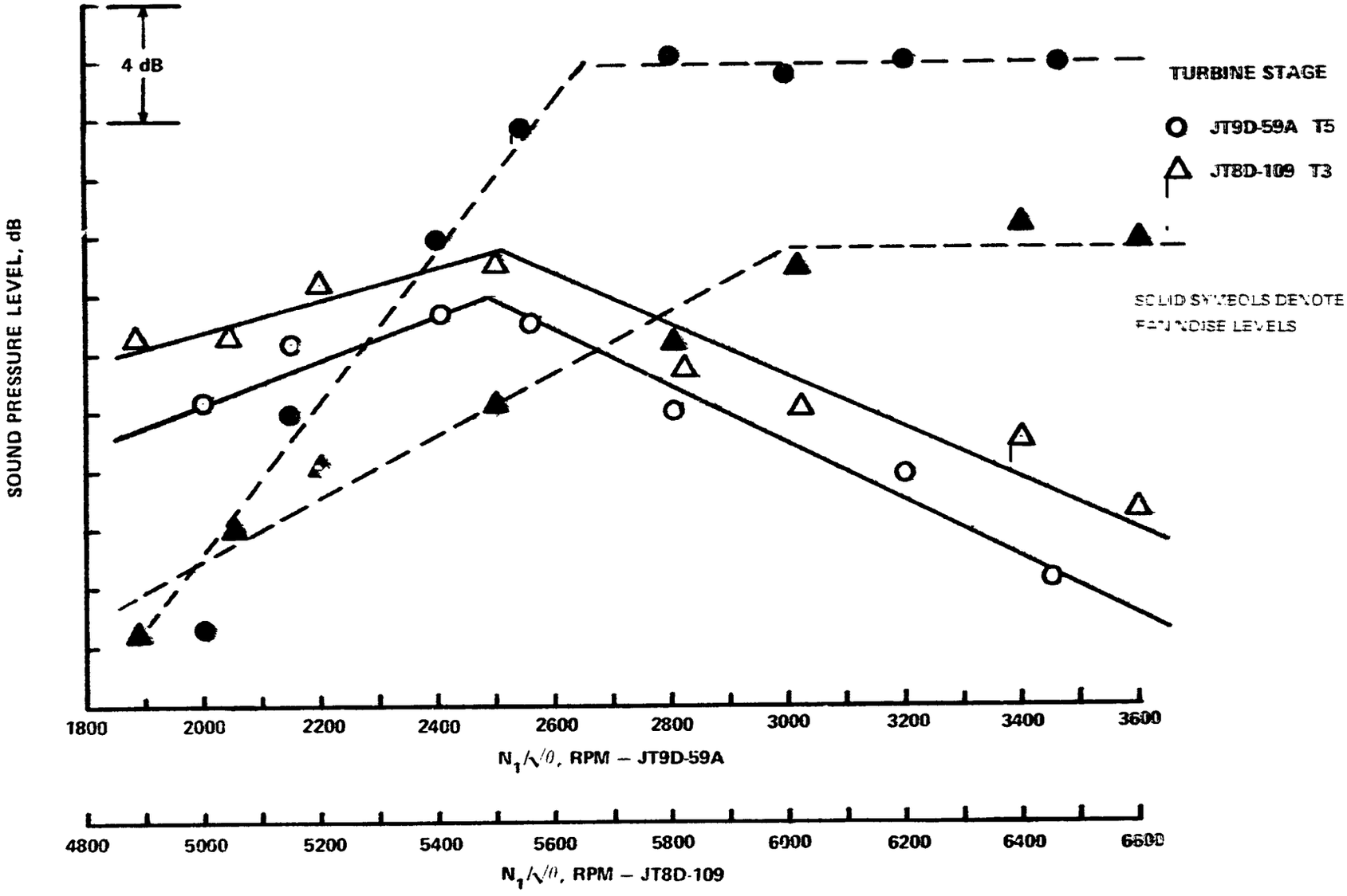

FIGURE 33. TURBINE NOISE LEVELS DERIVED FROM STATIC NARROWBAND DATA AT PEAK AFT ANGLE
PEAK AFT NOISE ANGLE ≈ 120° 45.7-METER RADIUS

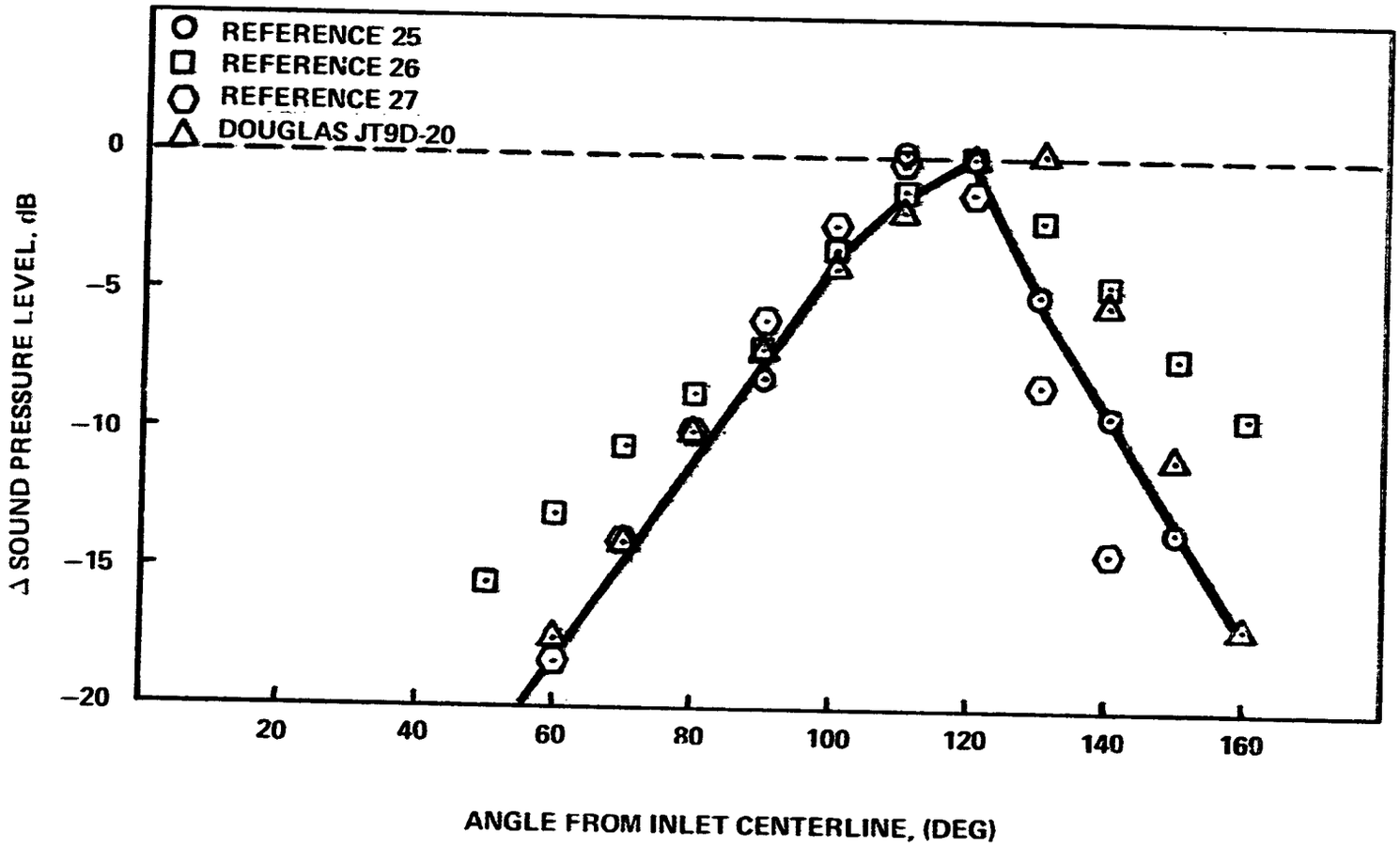

FIGURE 34. DERIVATION OF GENERALIZED TURBINE DIRECTIVITY USED IN TURBOMACHINERY NOISE SOURCE SEPARATION PROCEDURES

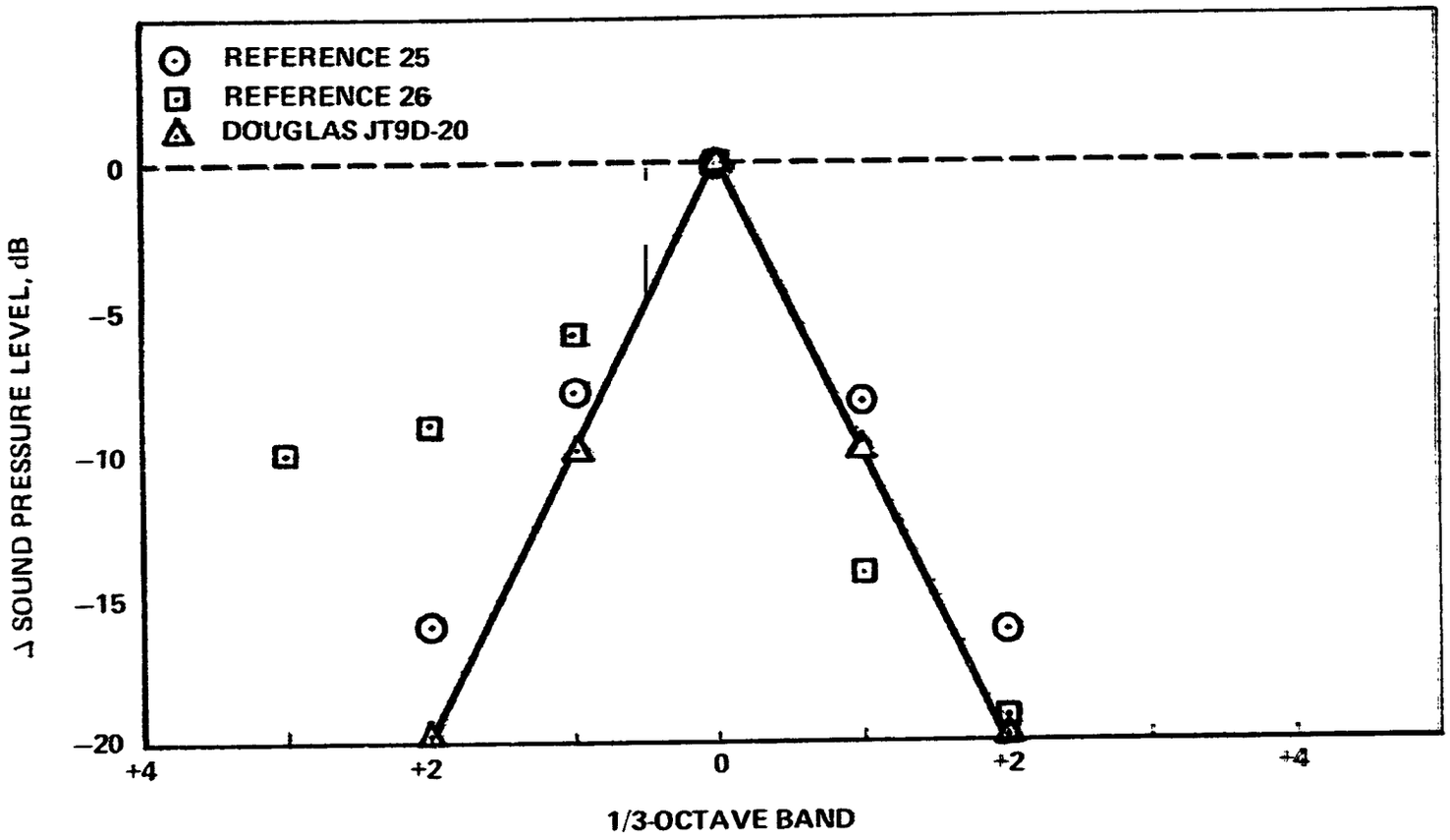

FIGURE 35. DERIVATION OF GENERALIZED TURBINE NOISE SPECTRUM SHAPE USED IN TURBOMACHINERY NOISE SOURCE SEPARATION PROCEDURES

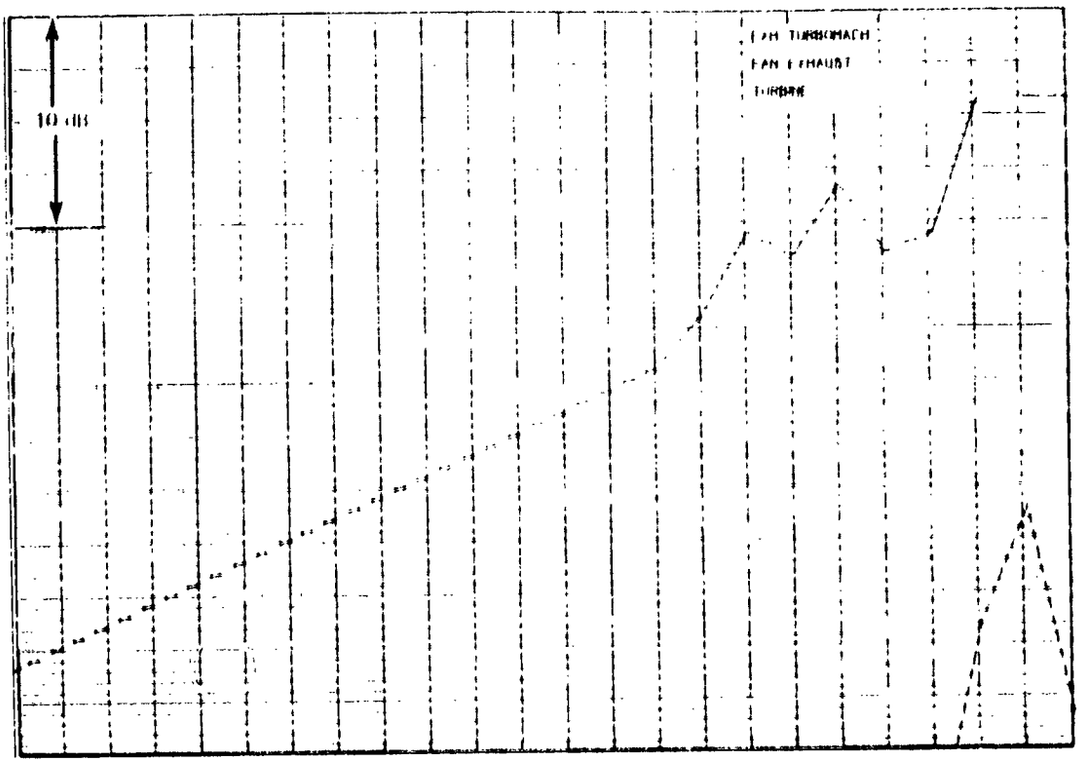

(a) $N1/\sqrt{\theta}$ = 4297.0 RPM

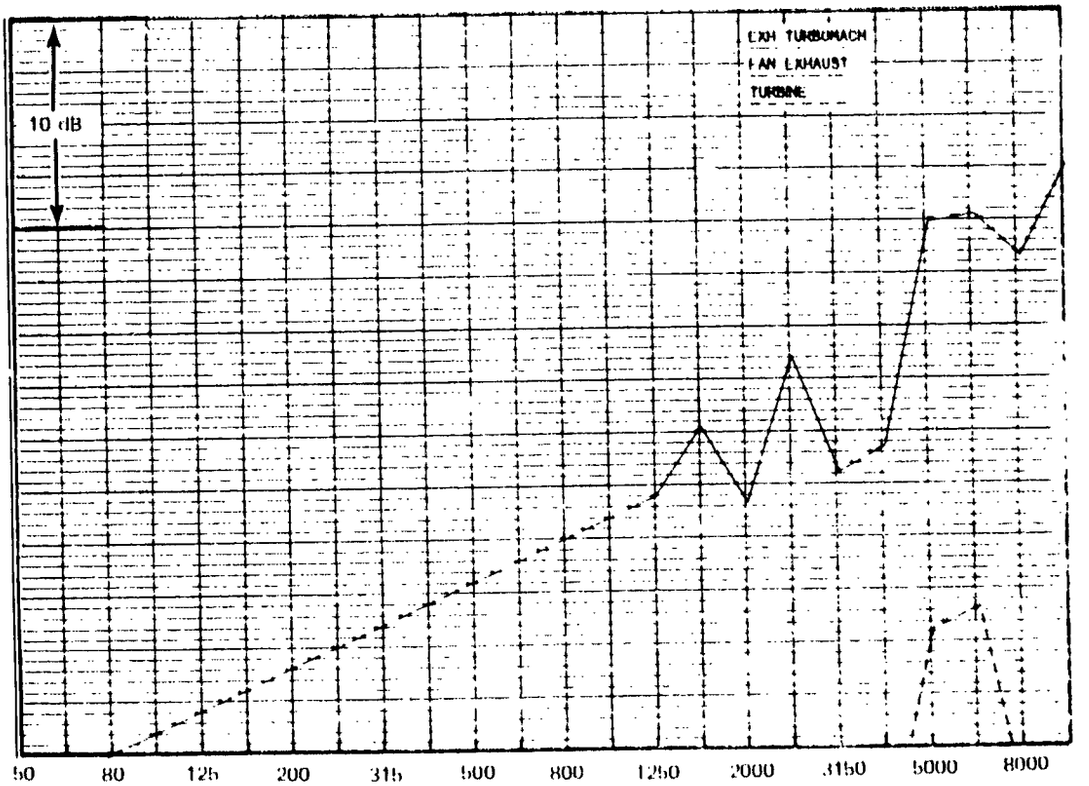

SOUND PRESSURE LEVEL, dB

(b) $N1/\sqrt{\theta}$ = 5497.0 RPM

FIGURE 36. FAN EXHAUST AND TURBINE STATIC NOISE SEPARATION FOR THE JT8D-109 AT 130 DEGREES AND 45.7-M POLAR RADIUS

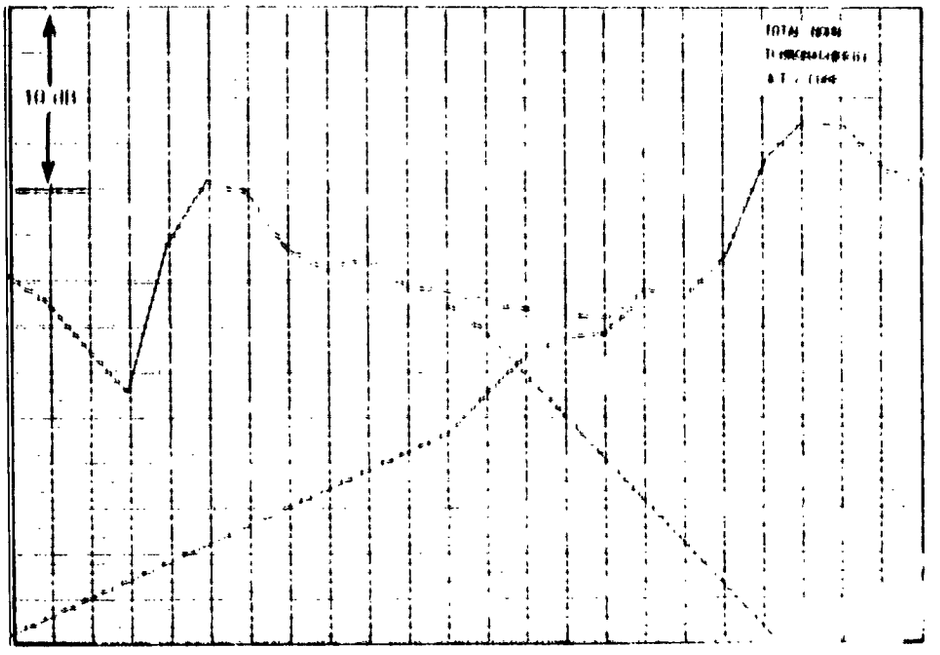

(a) N1/√θ 2507.0 RPM

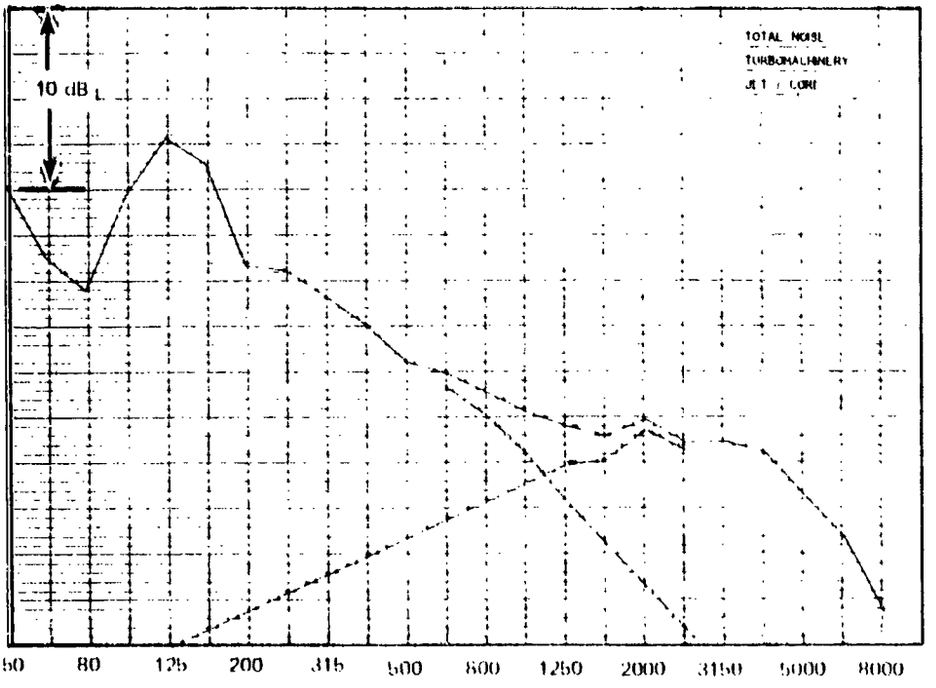

(b) N1/√θ 3440.0 RPM

SOUND PRESSURE LEVEL, dB

FIGURE 37. JET/CORE AND TURBOMACHINERY FLYOVER NOISE SEPARATION FOR THE DC-10-40/JT9D-59A, AT 130 DEGREES, 45.7-M POLAR RADIUS

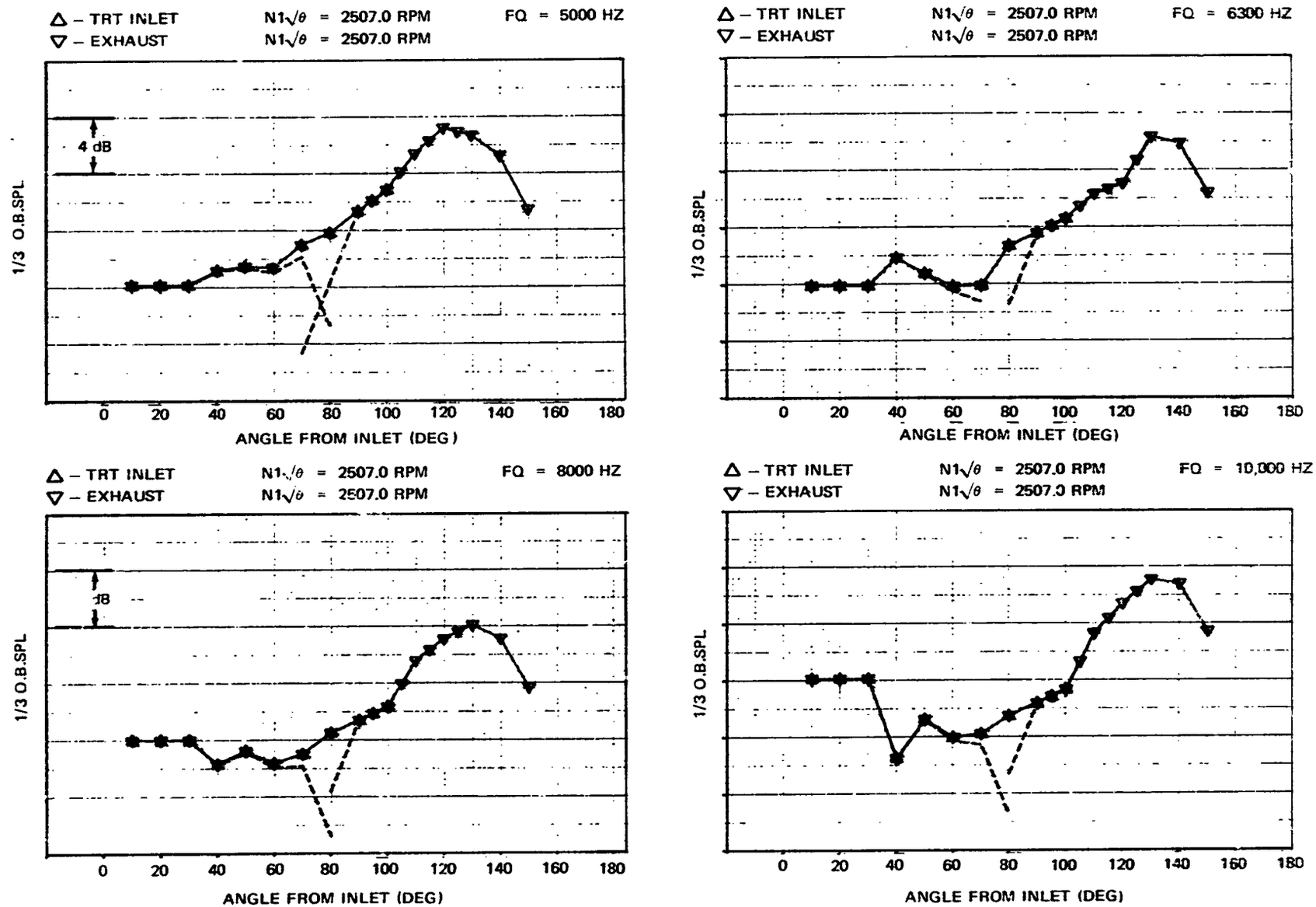

FIGURE 38. INLET AND AFT TURBOMACHINERY FLYOVER NOISE SEPARATION FOR THE DC-10-40/JT9D-59A, AT 5.0 TO 10.0 kHz AND N1/$\sqrt{\theta}$ = 2507.0 RPM, 45.7-M POLAR RADIUS

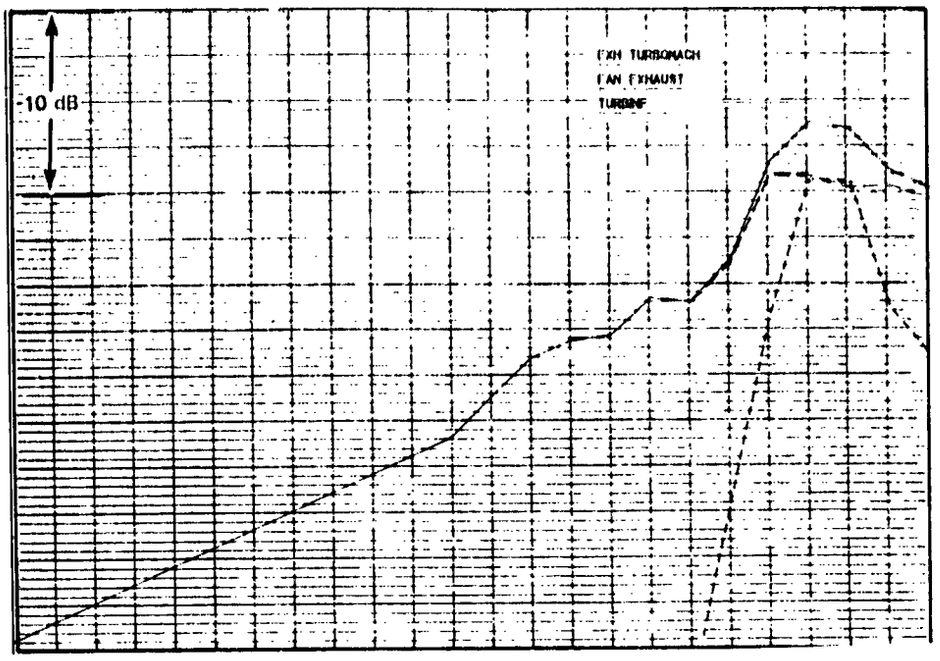

(a) $N1/\sqrt{\theta}$ = 2507.0 RPM

SOUND PRESSURE LEVEL, dB

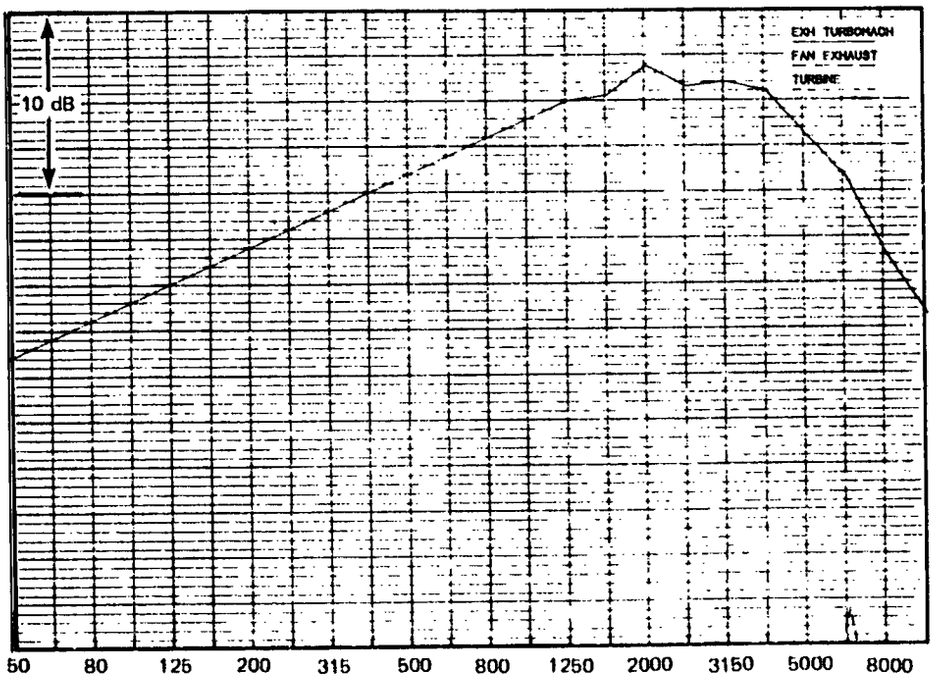

1/3 OCTAVE-BAND CENTER FREQUENCY (Hz)

(B) $N1/\sqrt{\theta}$ 3440.0 RPM

FIGURE 39. FAN EXHAUST AND TURBINE FLYOVER NOISE SEPARATION FOR THE DC-10-40/JT9D-59A, AT 130 DEGREES, 45.7-M POLAR RADIUS

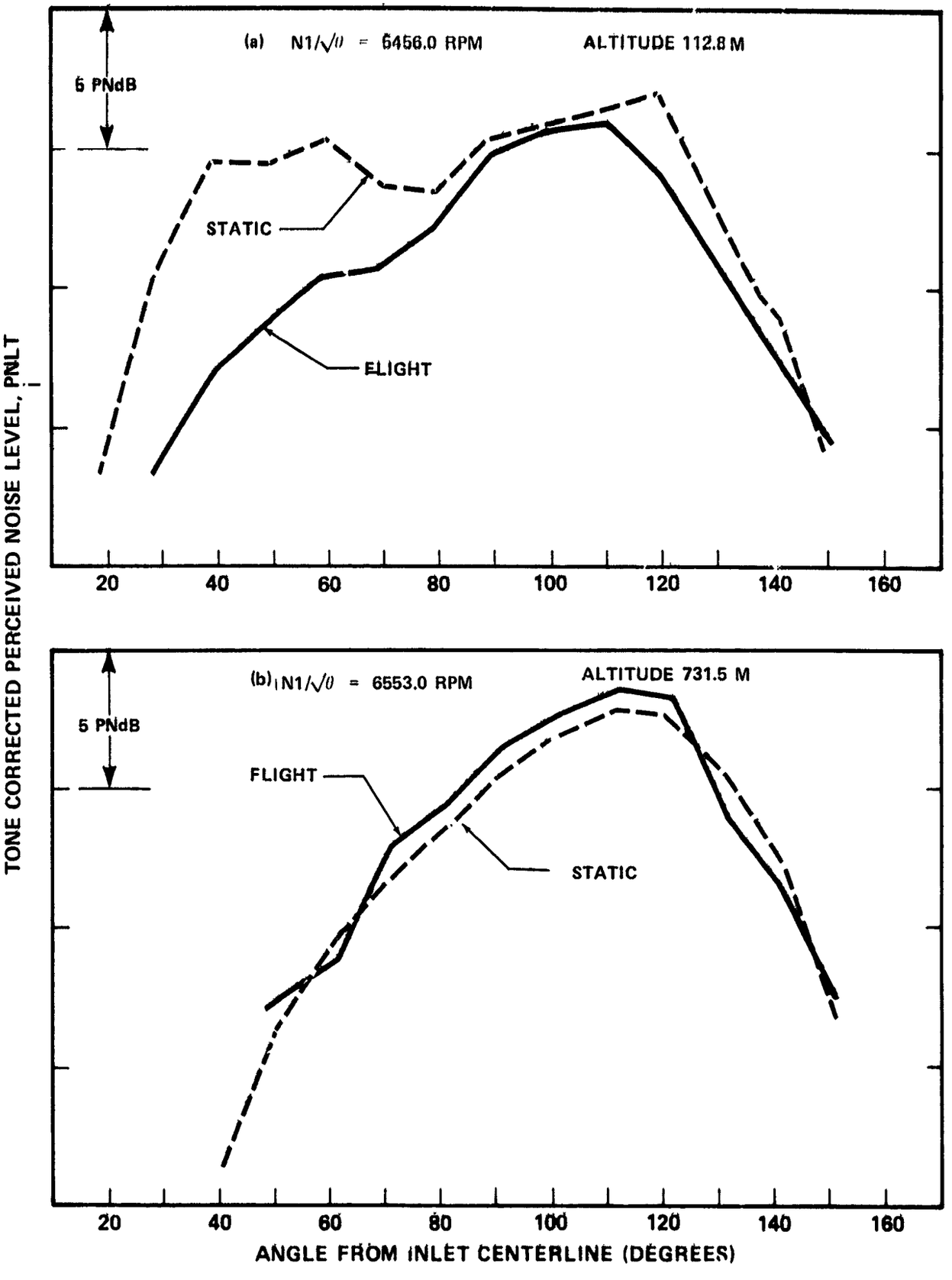

FIGURE 40. COMPARISON OF FLIGHT AND STATIC-PROJECTED PNLTS FOR THE DC-9-30/JT8D-109

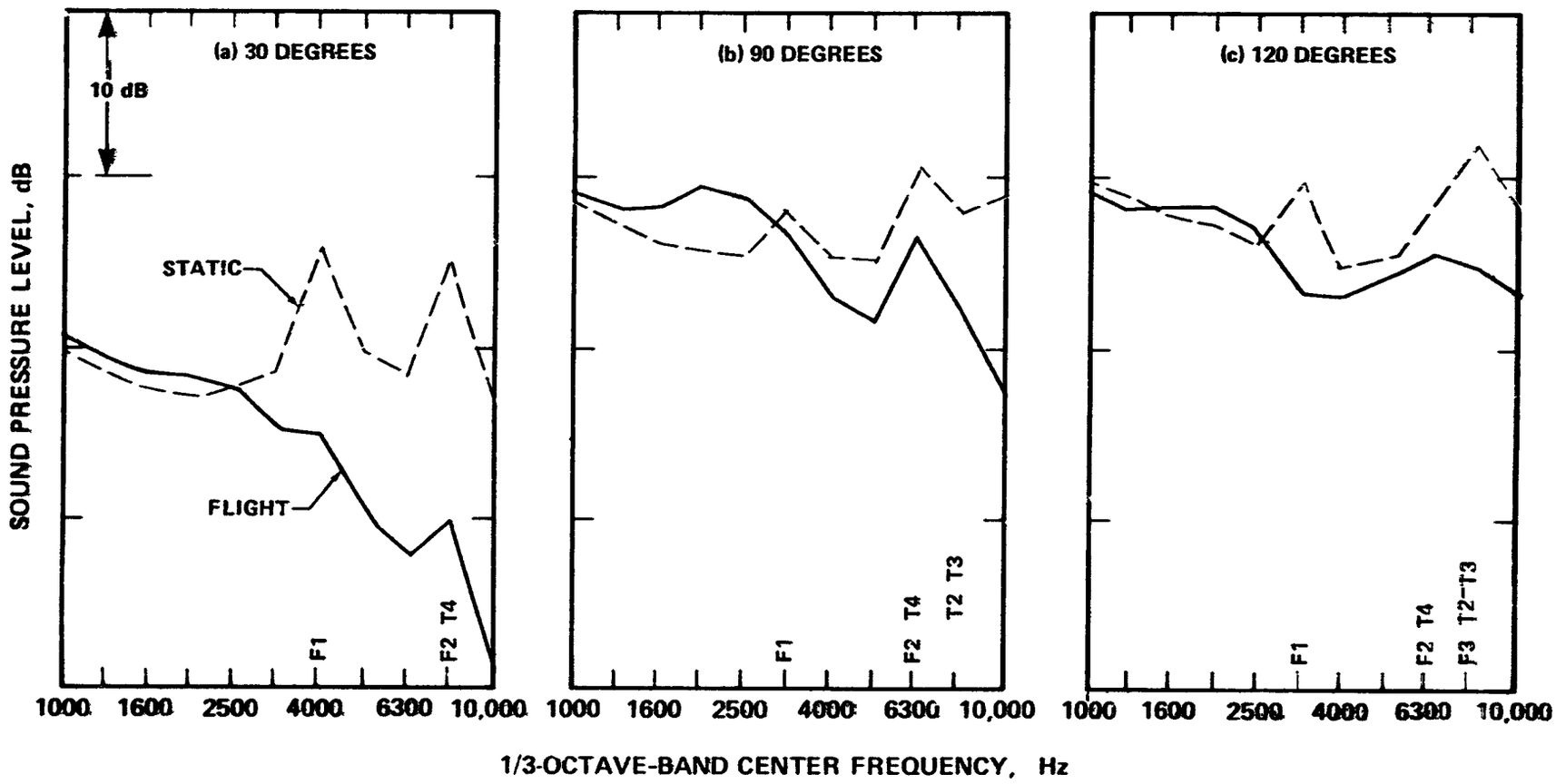

FIGURE 41. COMPARISON OF FLIGHT AND STATIC-PROJECTED SPL SPECTRA FOR THE DC-9-30/JT8D-109 DURING A 112.8-METER (370-FOOT) FLYOVER. CORRECTED FAN ROTOR SPEED = 5456.0 RPM

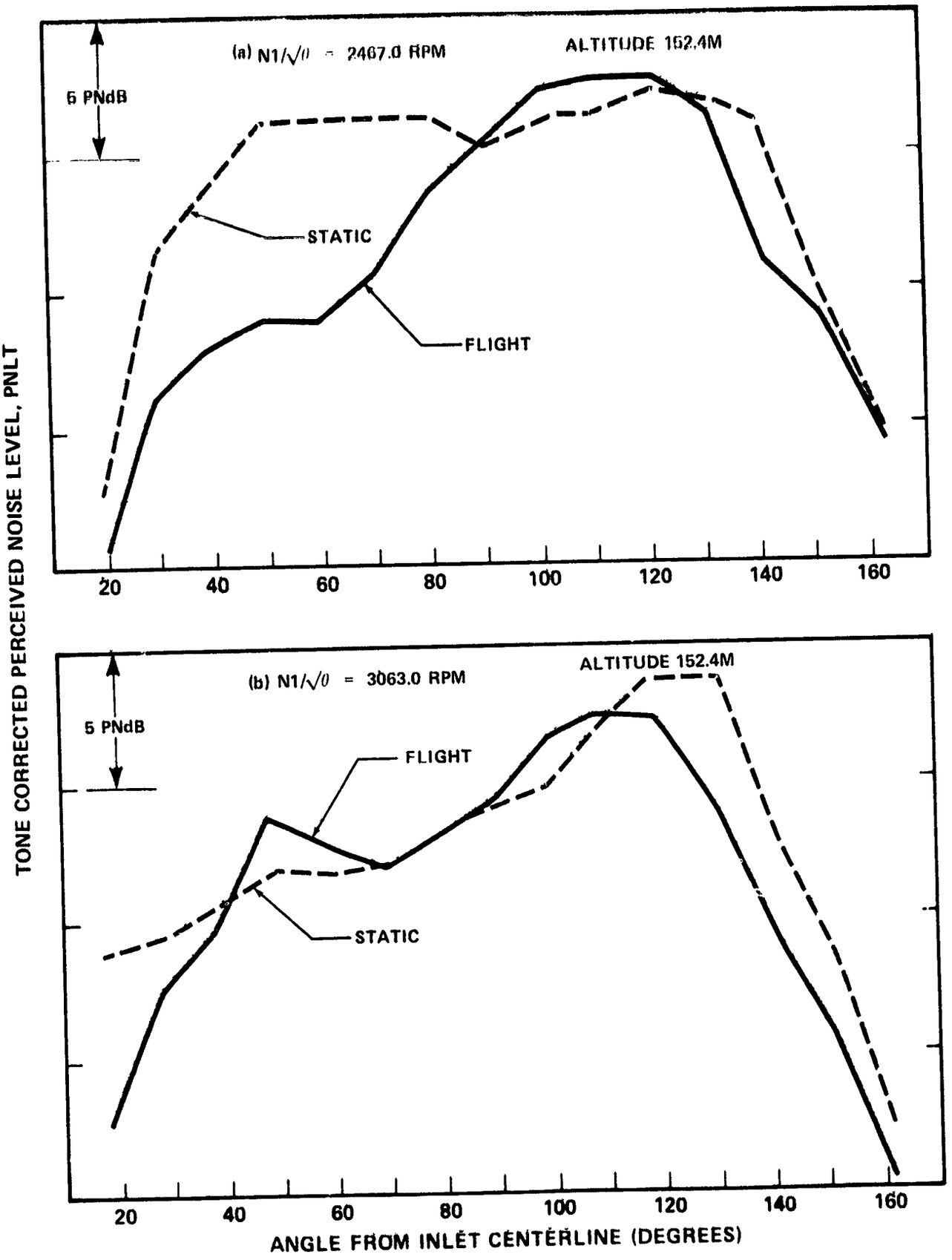

FIGURE 42. COMPARISON OF FLIGHT AND STATIC-CORRECTED PNLTS FOR THE DC-10-10/CF6-6D

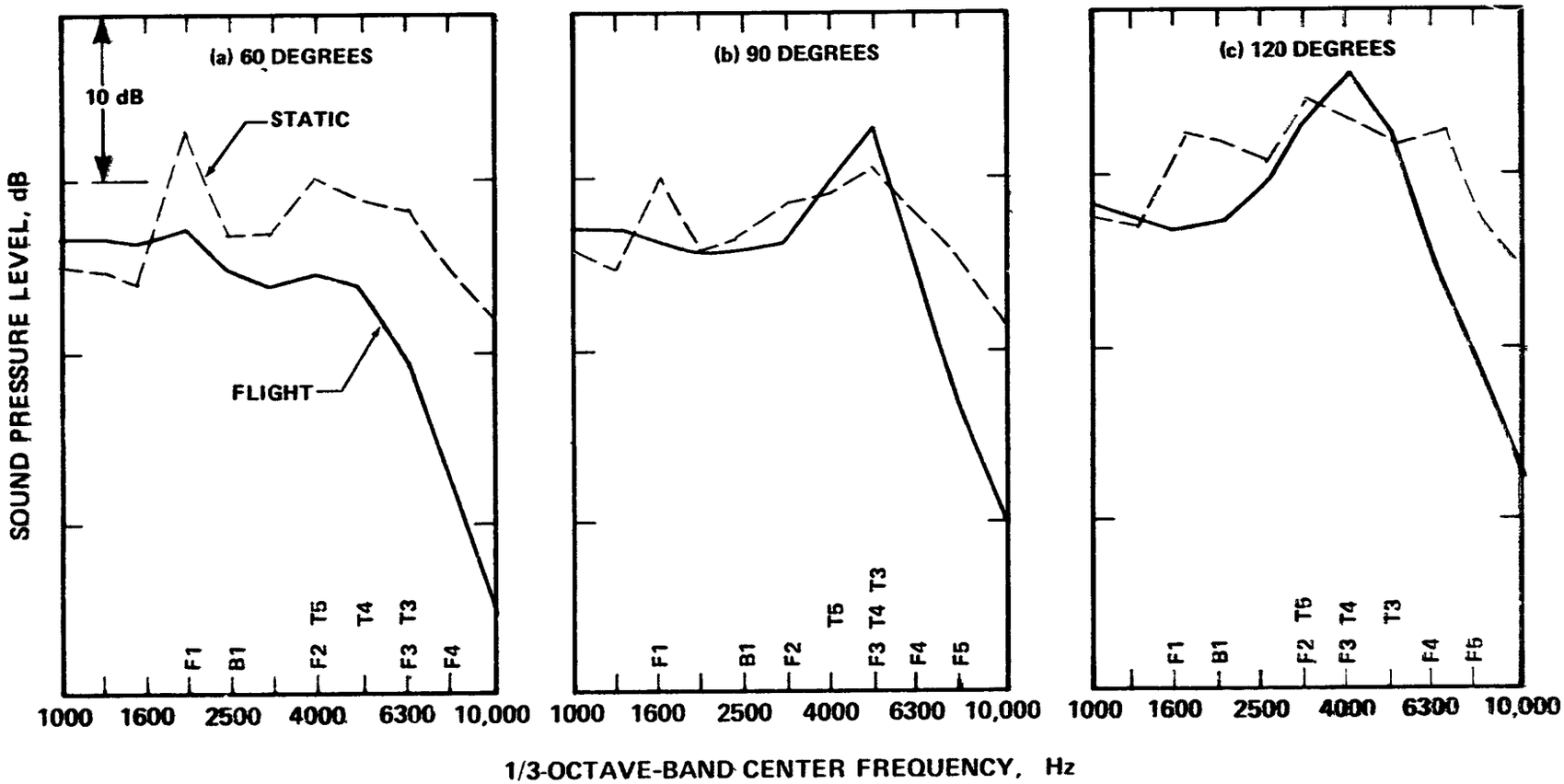

FIGURE 43. COMPARISON OF FLIGHT AND STATIC-PROJECTED SPL SPECTRA FOR THE DC-10-10/CF6-6D DURING A 152.4-METER (500-FOOT) LEVEL FLYOVER. CORRECTED FAN ROTOR SPEED = 2467.0 RPM.

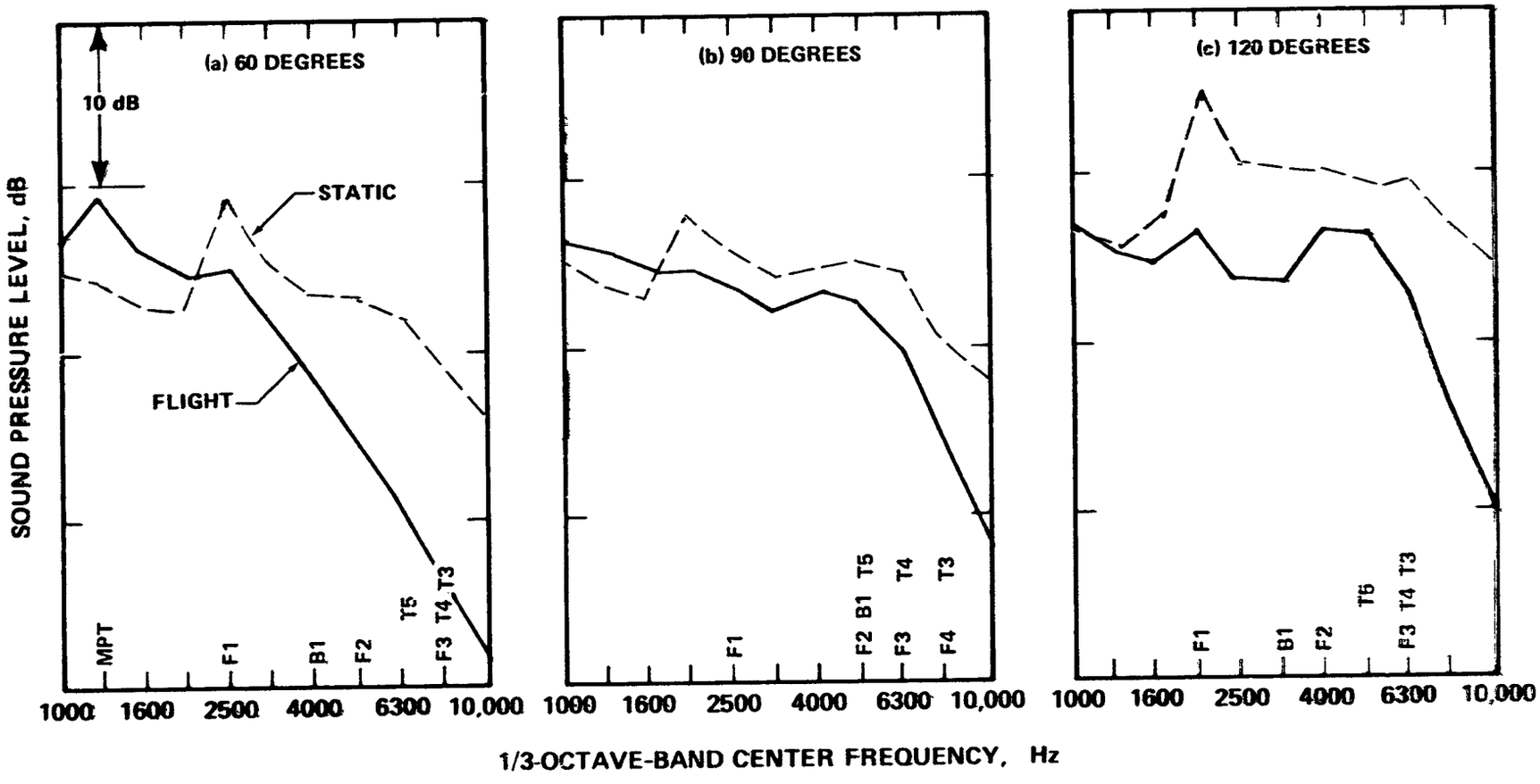

FIGURE 44. COMPARISON OF FLIGHT AND STATIC-PROJECTED SPL SPECTRA FOR THE DC-10-10/CF6-6D DURING A 152.4-METER (500-FOOT) LEVEL FLYOVER. CORRECTED FAN ROTOR SPEED = 3063.0 RPM.

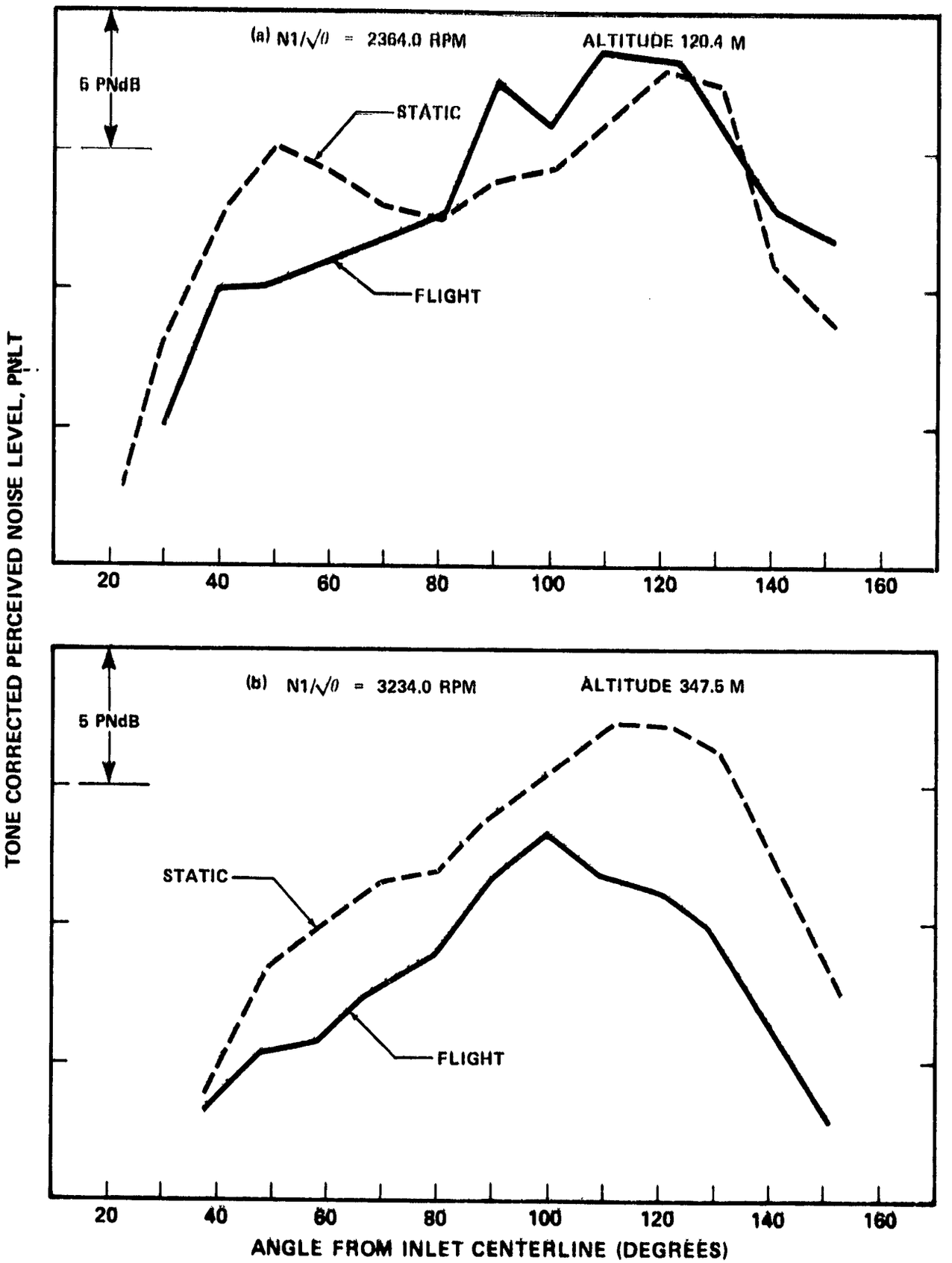

FIGURE 45. COMPARISON OF FLIGHT AND STATIC-CORRECTED PNLTS FOR THE DC-10-40/JT9D-59A.

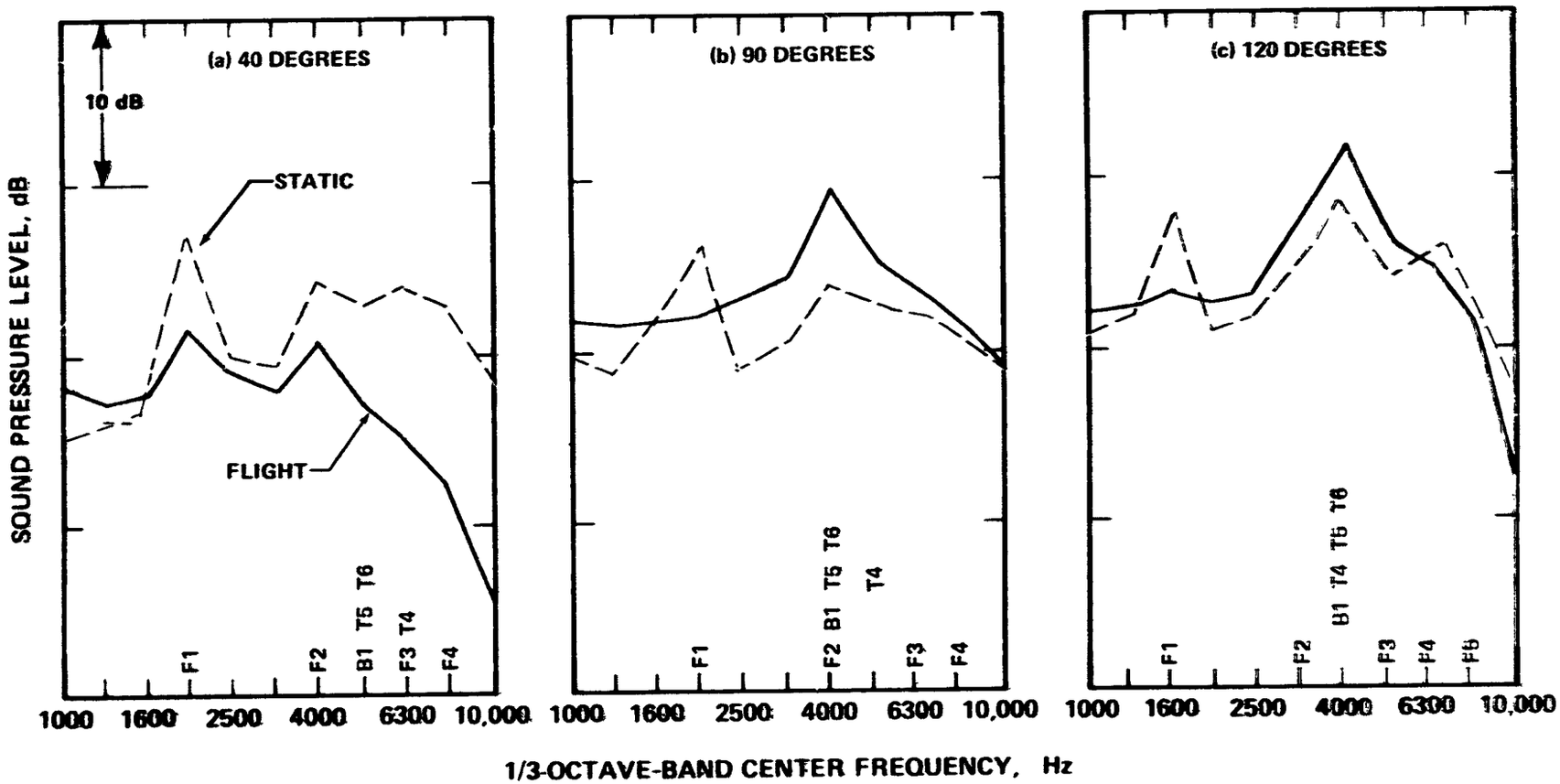

FIGURE 46. COMPARISON OF FLIGHT AND STATIC-PROJECTED SPL SPECTRA FOR THE DC-10-40/JT9D-59A DURING A 120.4-METER (395-FOOT) FLYOVER. CORRECTED FAN ROTOR SPEED = 2364.0 RPM.

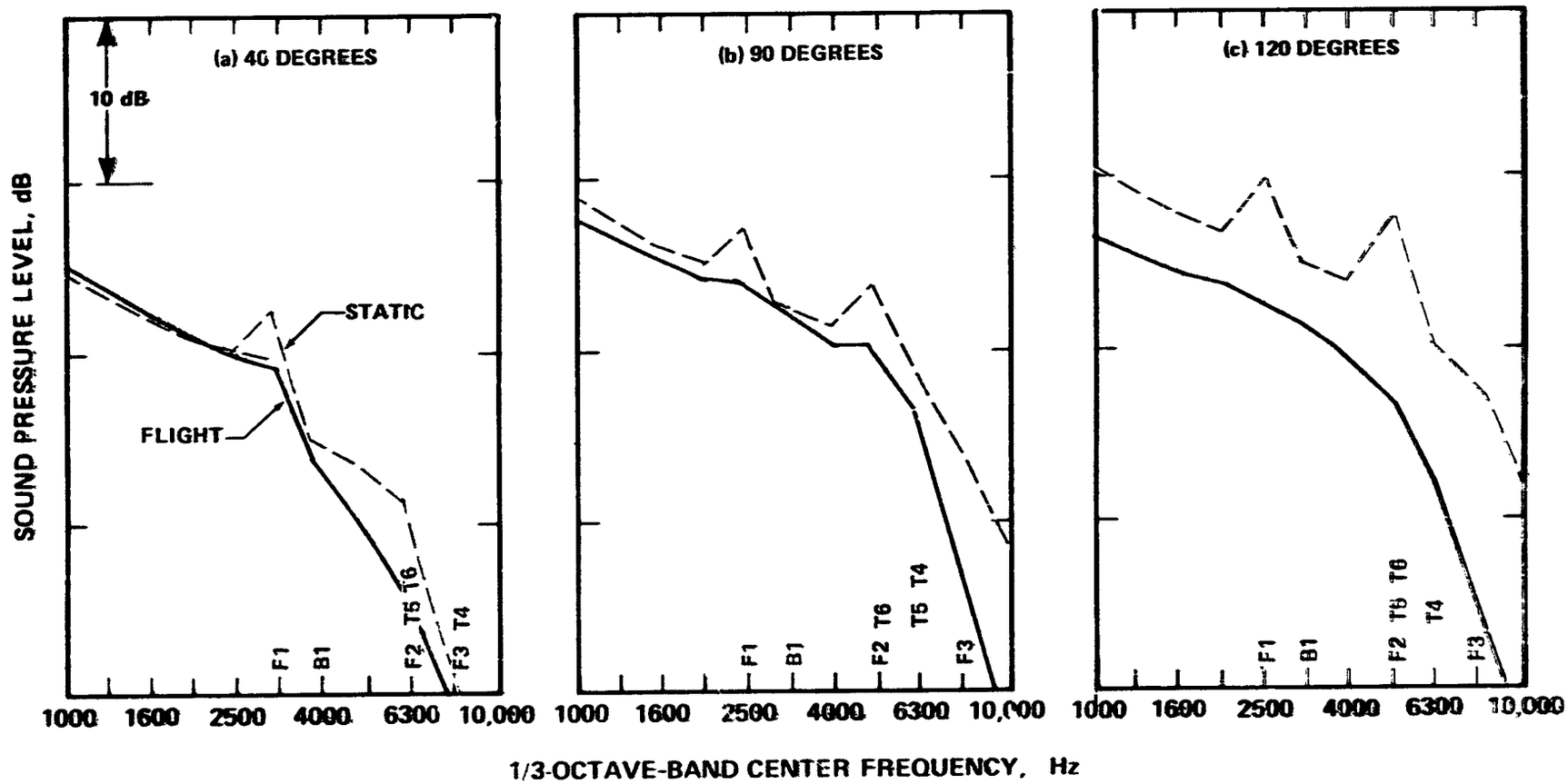

FIGURE 47. COMPARISON OF FLIGHT AND STATIC-PROJECTED SPL SPECTRA FOR THE DC-10-40/JT9D-59A DURING A 347.5-METER (1140-FOOT) FLYOVER. CORRECTED FAN ROTOR SPEED = 3234.0 RPM

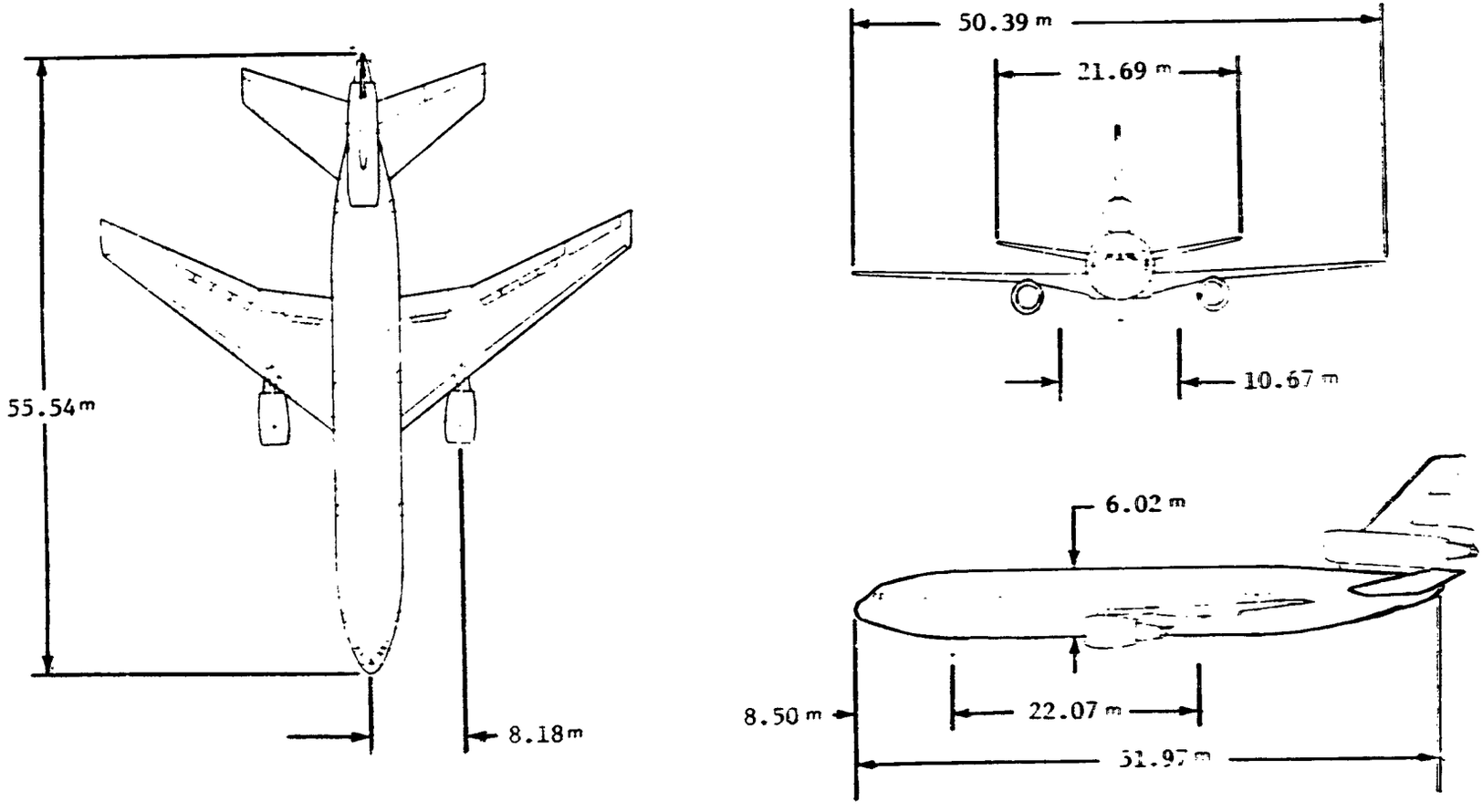

FIGURE 48. RELATIVE ENGINE LOCATION ON DC-10 AIRPLANE

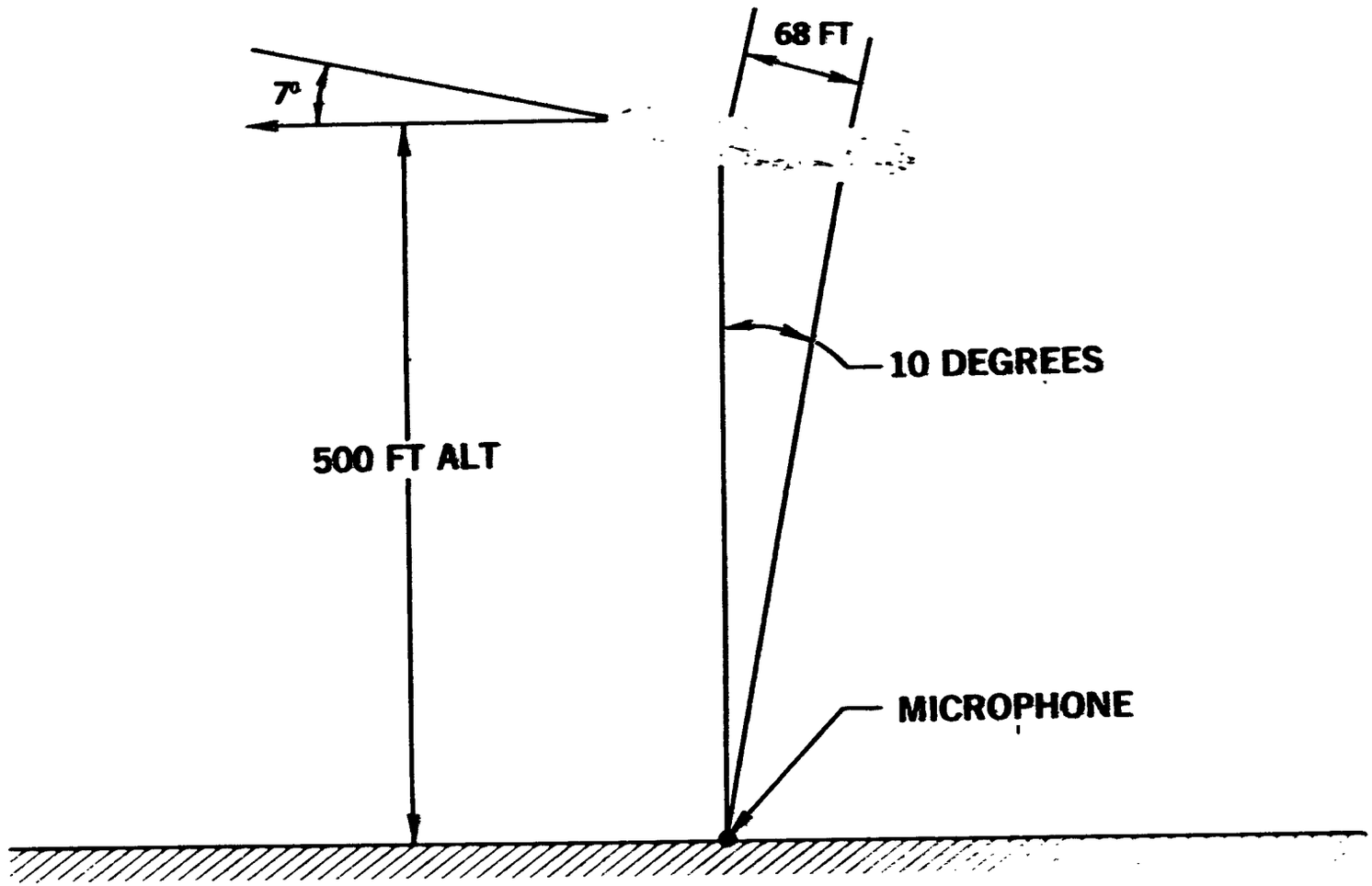

FIGURE 49. EFFECT OF ENGINE LOCATION ON DC-10-10 FLYOVER NOISE DIRECTIVITY

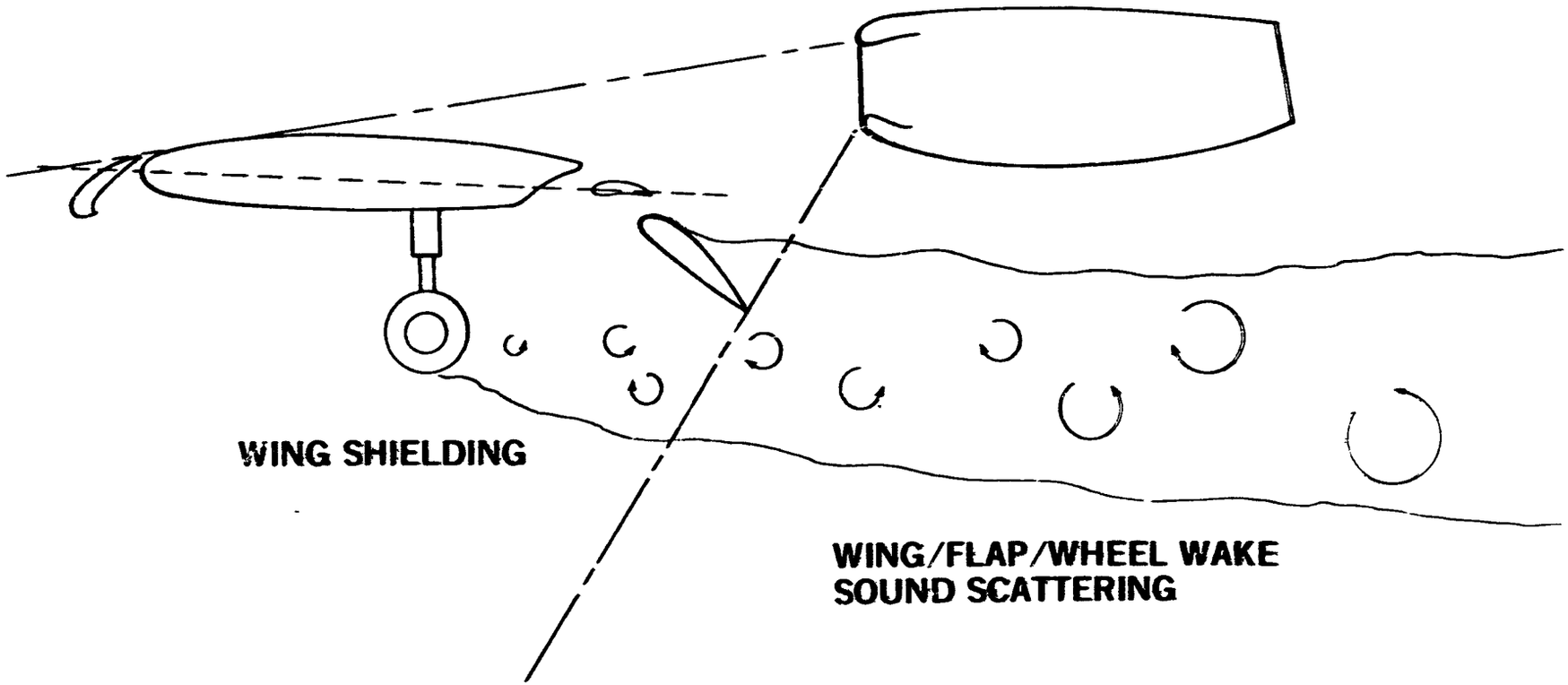

FIGURE 50. DC-9-30 INSTALLATION EFFECTS WHICH ALTER THE PROPAGATION OF FAN NOISE

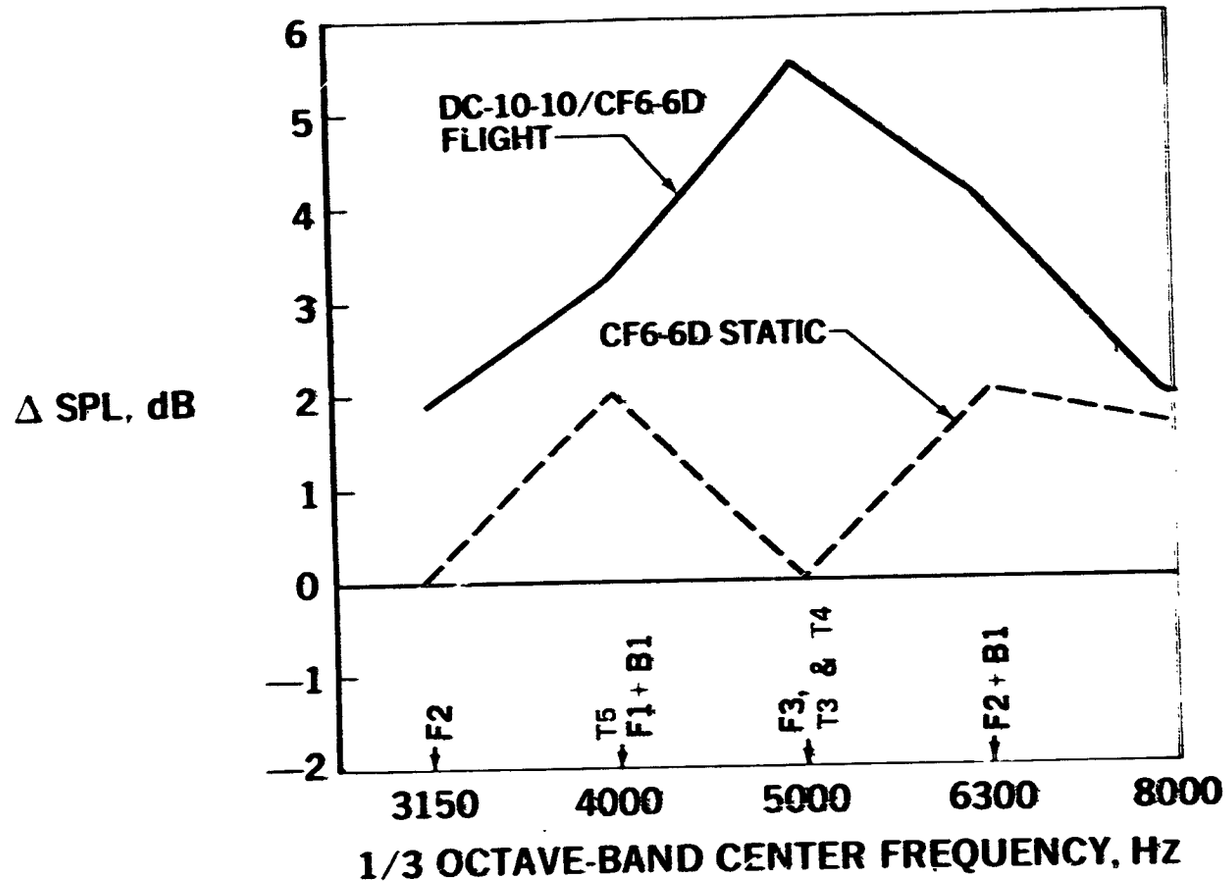

FIGURE 51. EFFECT OF ACOUSTIC TREATMENT AND FORWARD MOTION ON CF6-6D TURBINE NOISE SUPPRESSION AT 120 DEGREES FROM THE INLET. CORRECTED FAN ROTOR SPEED = 2600 RPM

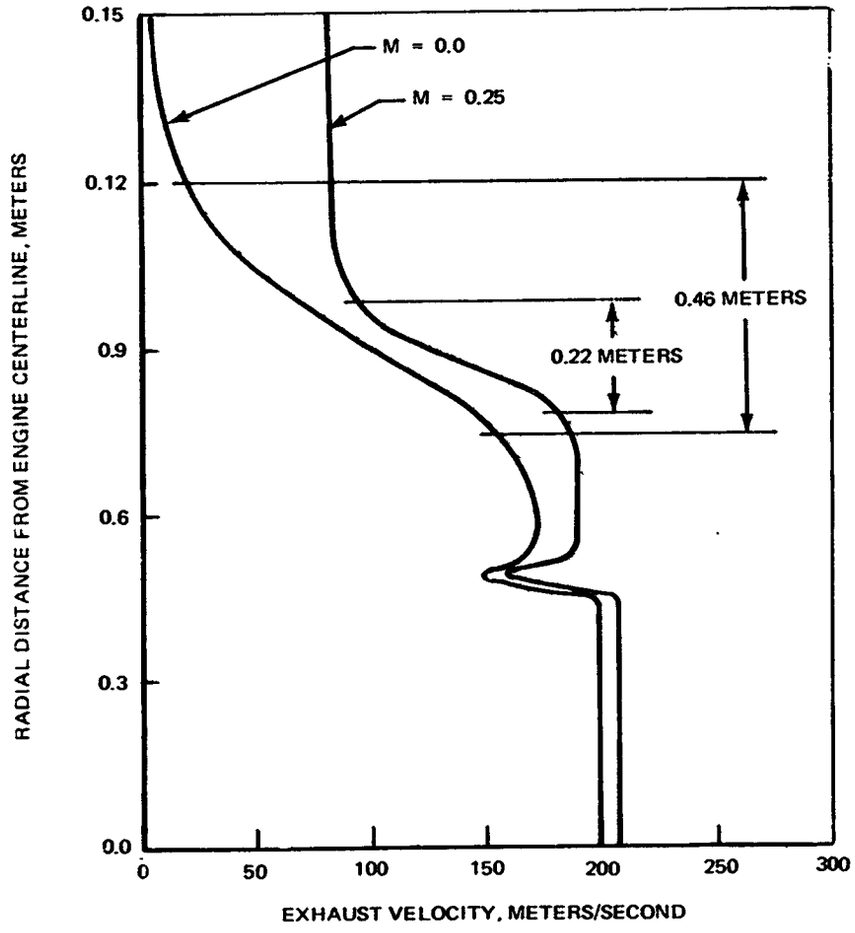

FIGURE 52. ESTIMATED CF6-6D EXHAUST WAKE VELOCITY PROFILES 0.92 METERS FROM NOZZLE EXIT AT APPROACH POWER

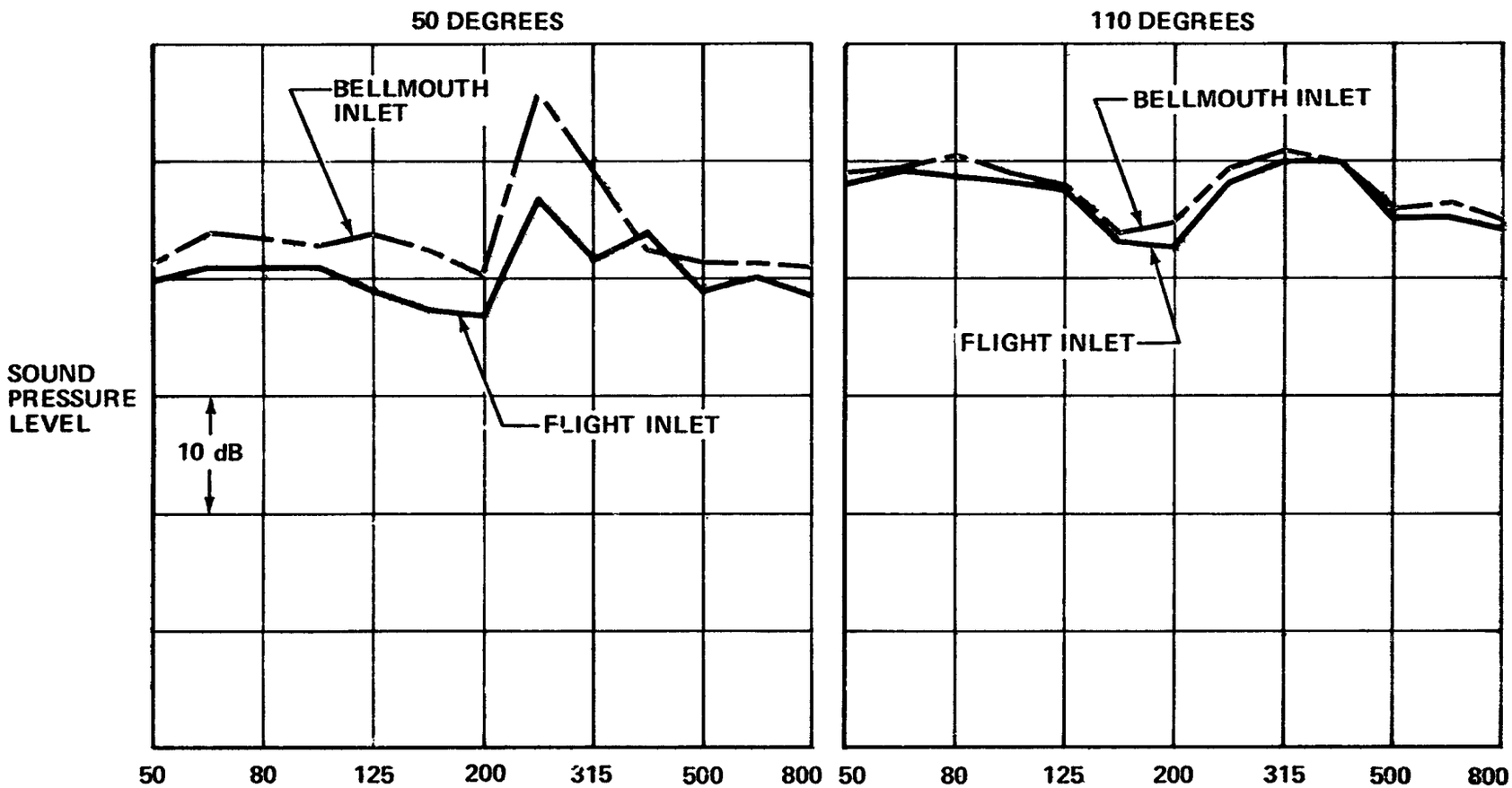

FIGURE 53. EFFECT OF INLET CONTOUR ON STATIC ENGINE SPL'S JT9D-20/TREATED NACELLE/TAKEOFF

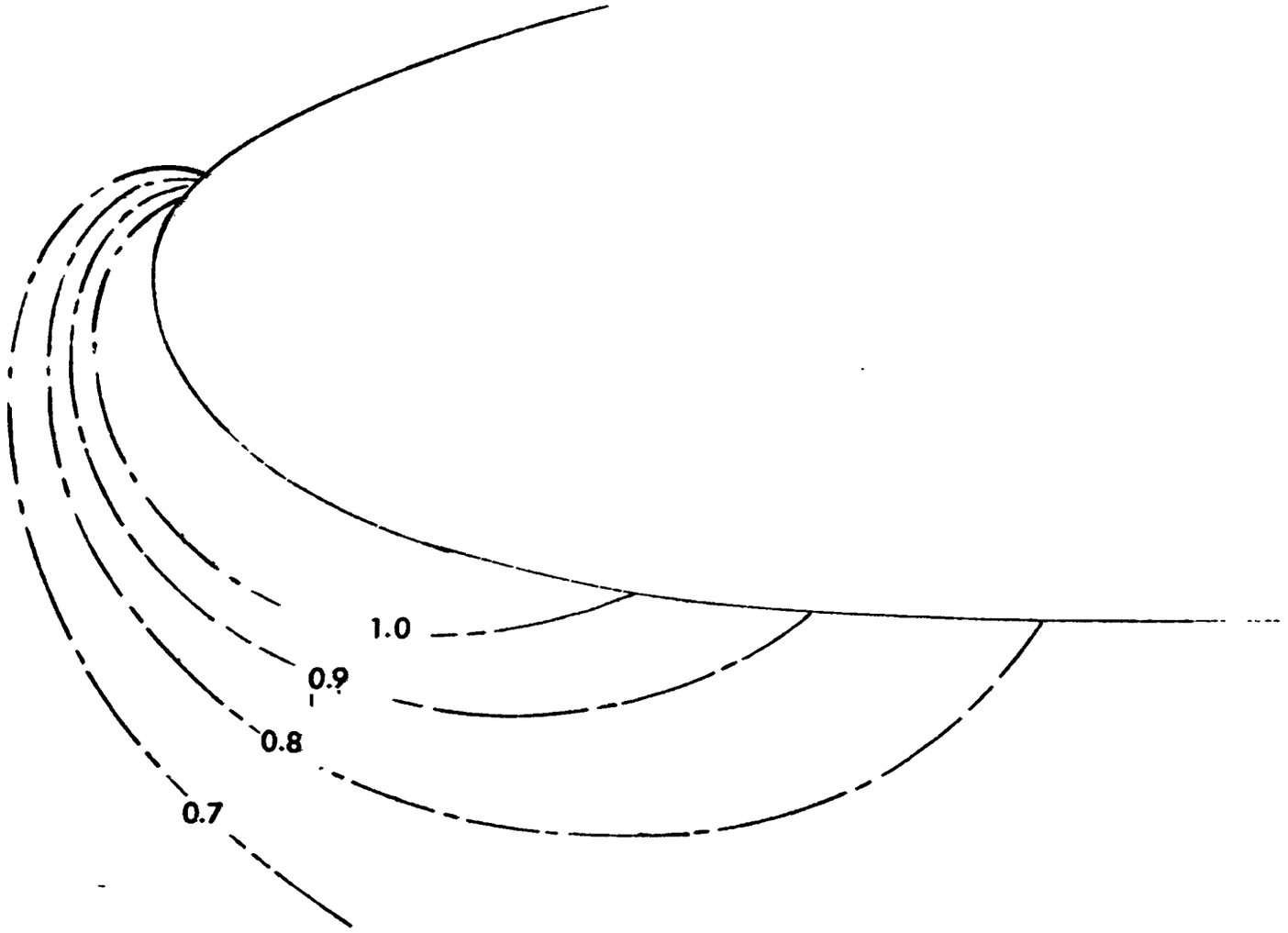

FIGURE 54. LOCAL MACH NUMBER DISTRIBUTIONS ON DC-10-40/JT9D-20 WING INLET AT STATIC-SEA-LEVEL TAKEOFF POWER

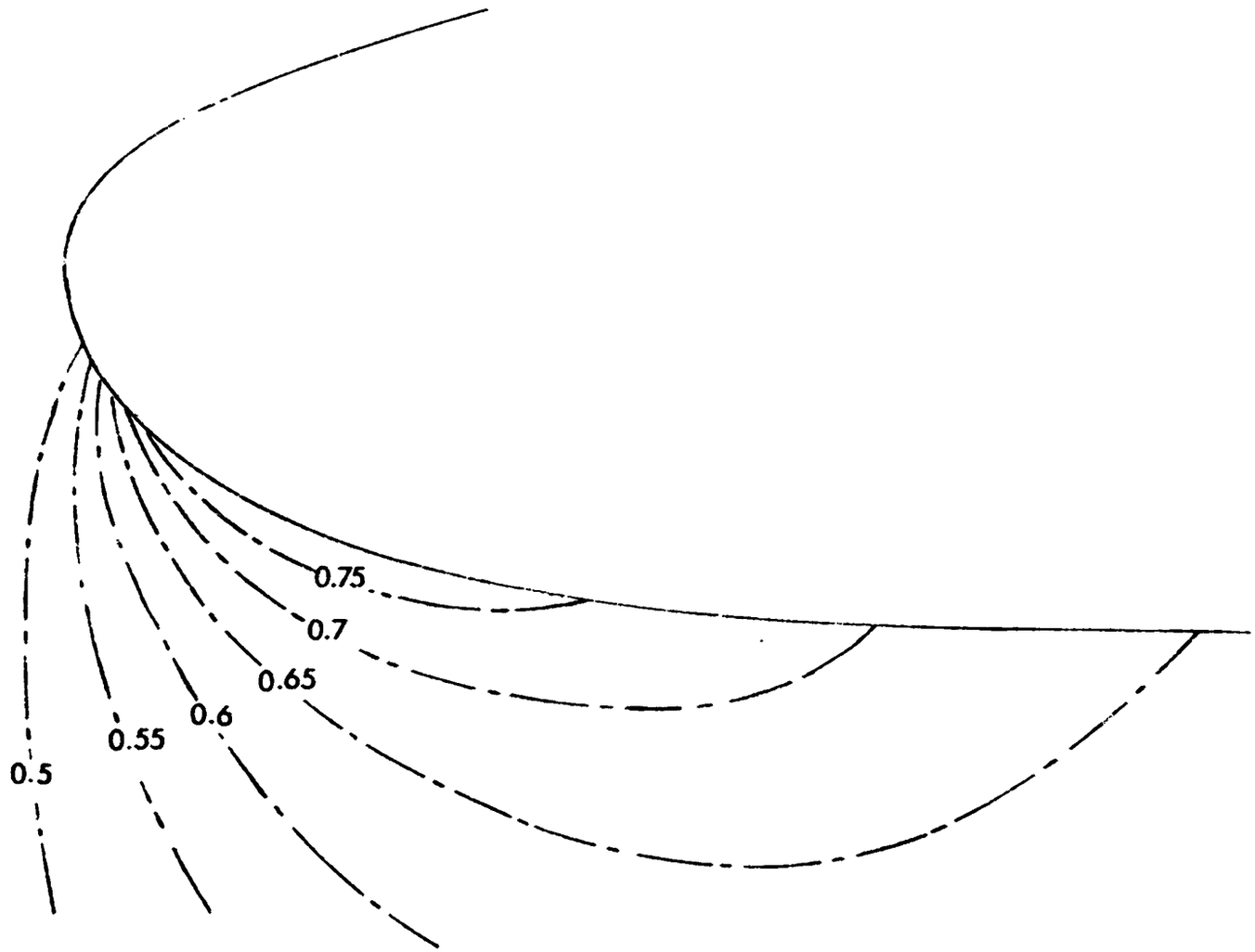

FIGURE 55. LOCAL MACH NUMBER DISTRIBUTIONS ON DC-10-40/JT9D-20 WING INLET IN FLIGHT AT MAX CLIMB POWER

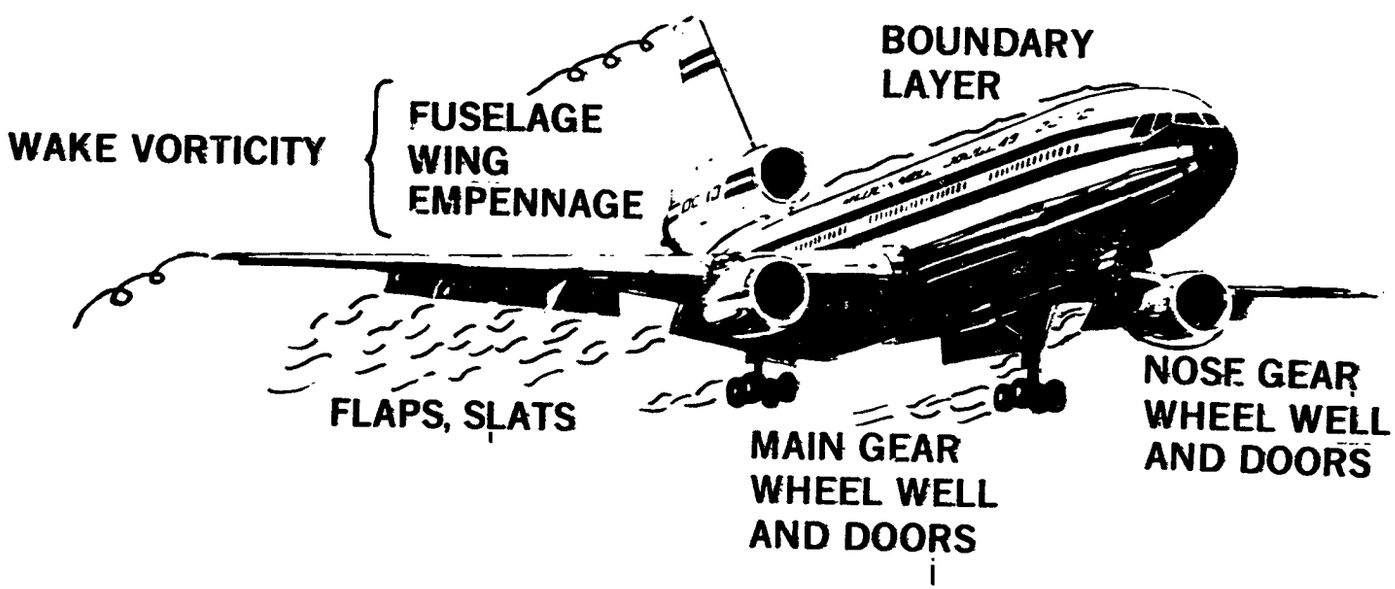

FIGURE 56. NONPROPULSIVE NOISE SOURCES

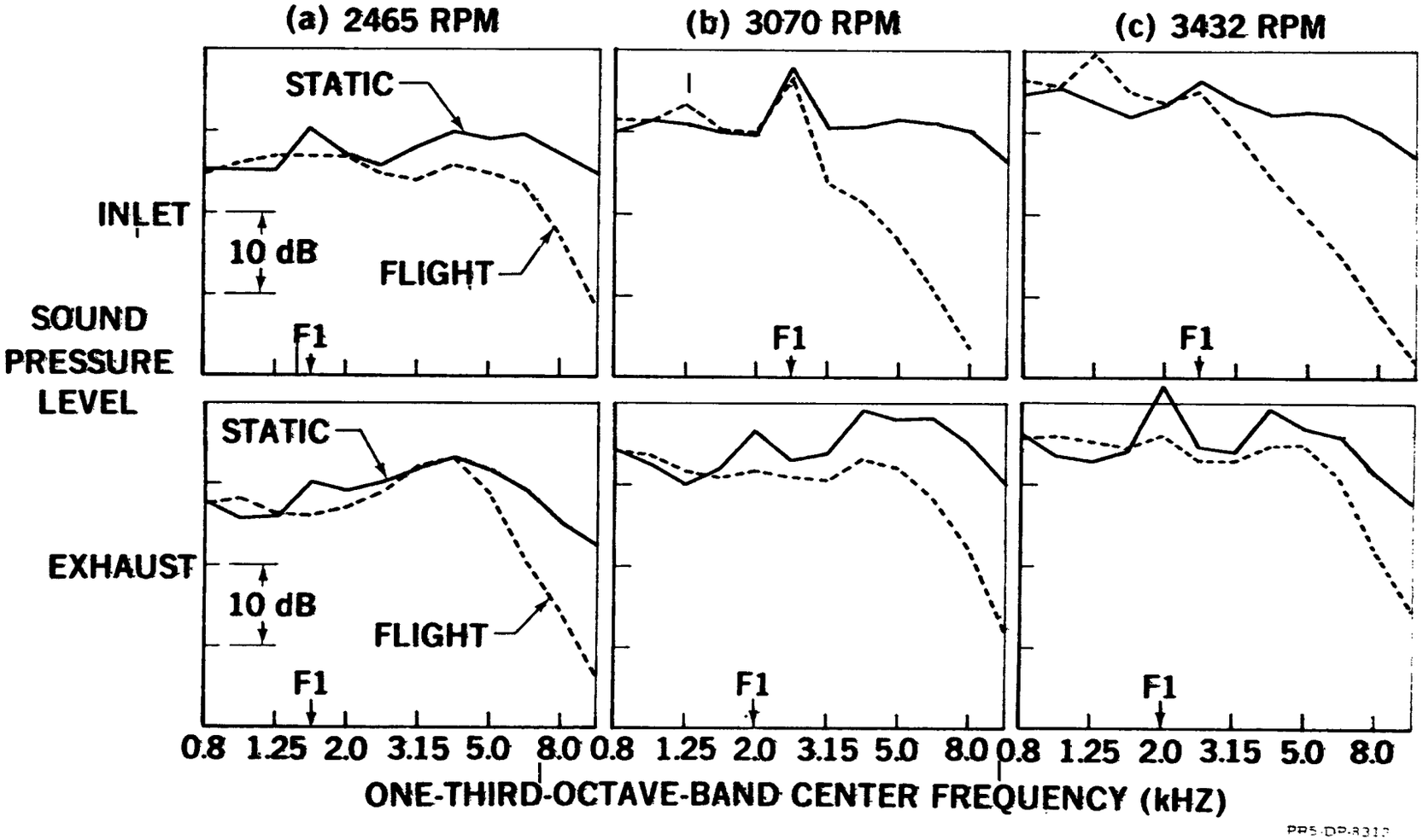

FIGURE 57. COMPARISON OF FLIGHT AND STATIC-PROJECTED SPECTRA FOR DC-10-10/CF6-6 – 152.4-METERS

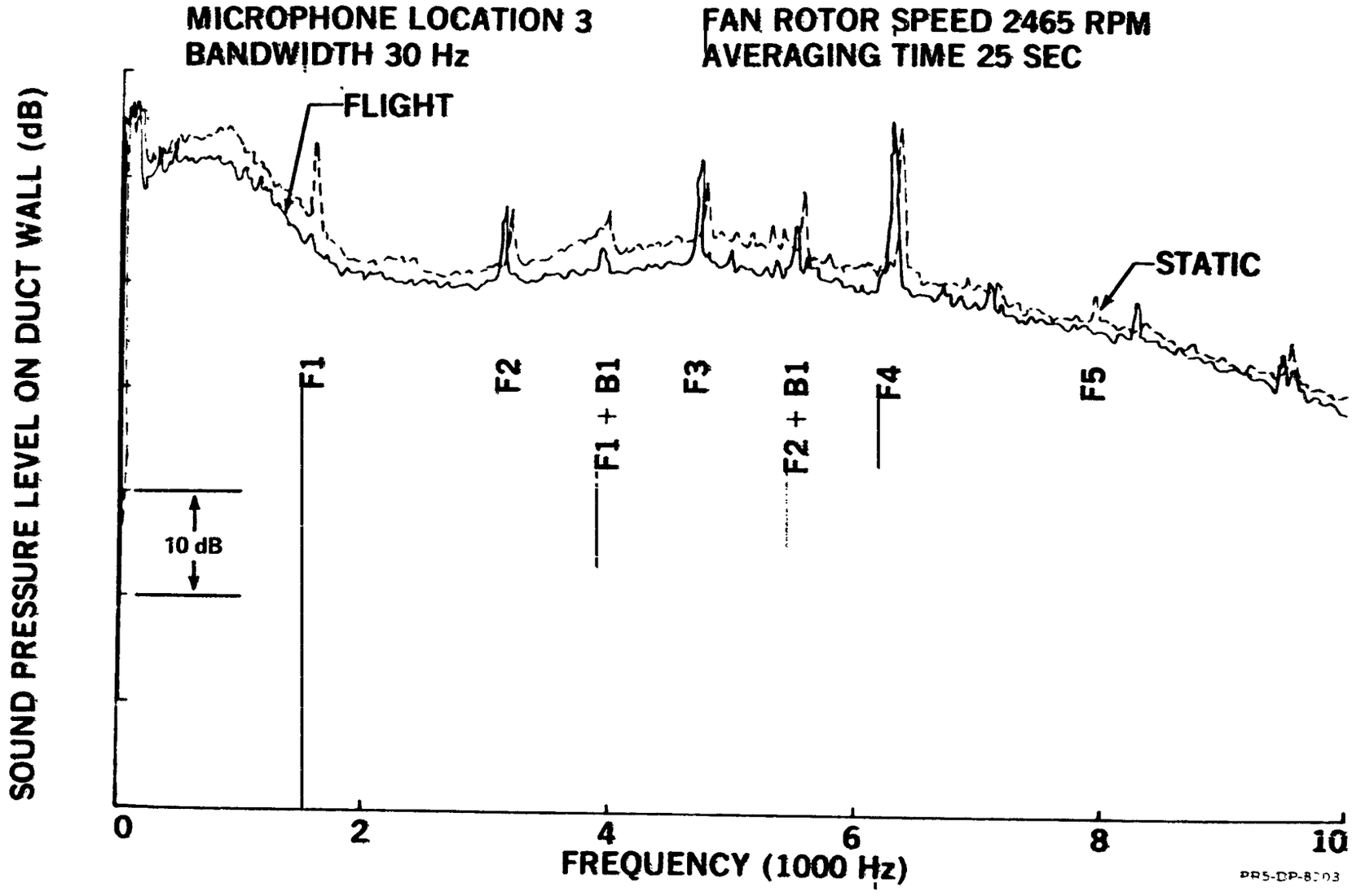

FIGURE 58. COMPARISON OF FLIGHT AND STATIC NARROW-BAND SPECTRA MEASURED ON THE INLET WALL OF THE CF6-6 ENGINE

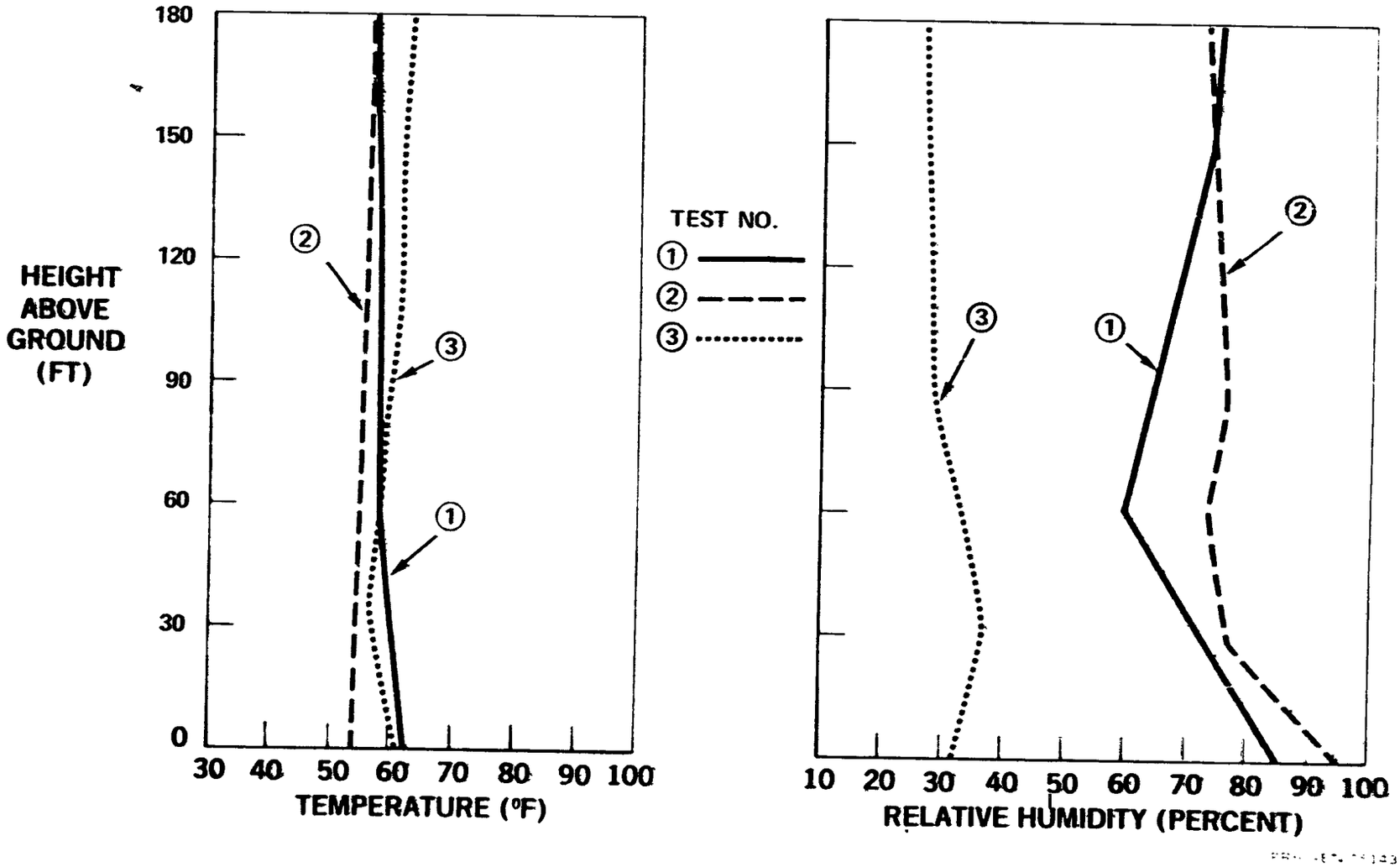

FIGURE 59. SOUND PATH WEATHER FOR DC-10-10/CF6-6D AT APPROACH

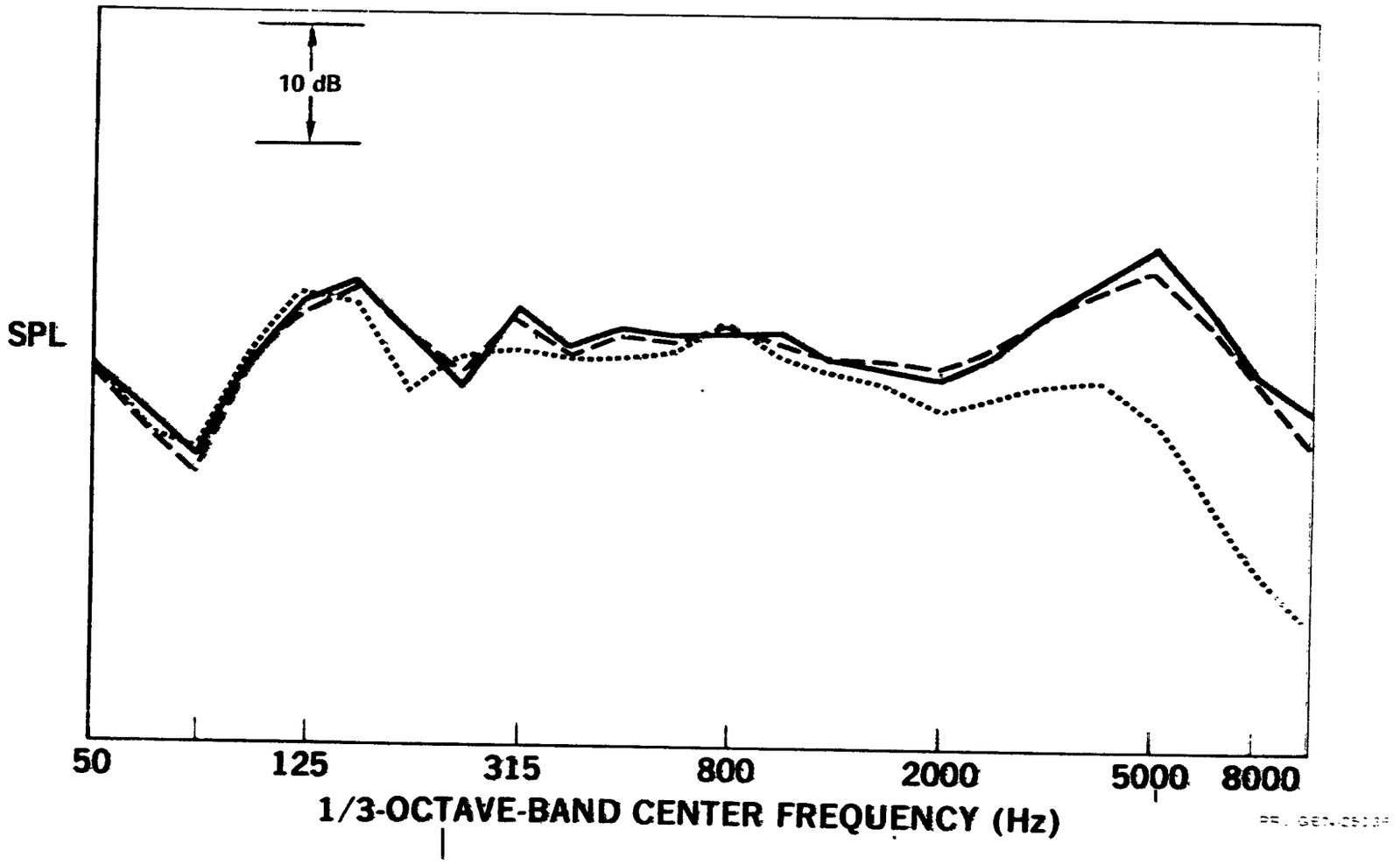

FIGURE 60. SPL SPECTRA MEASURED IN THE AFT QUADRANT FOR THE DC-10-10/CF6-6 AT APPROACH

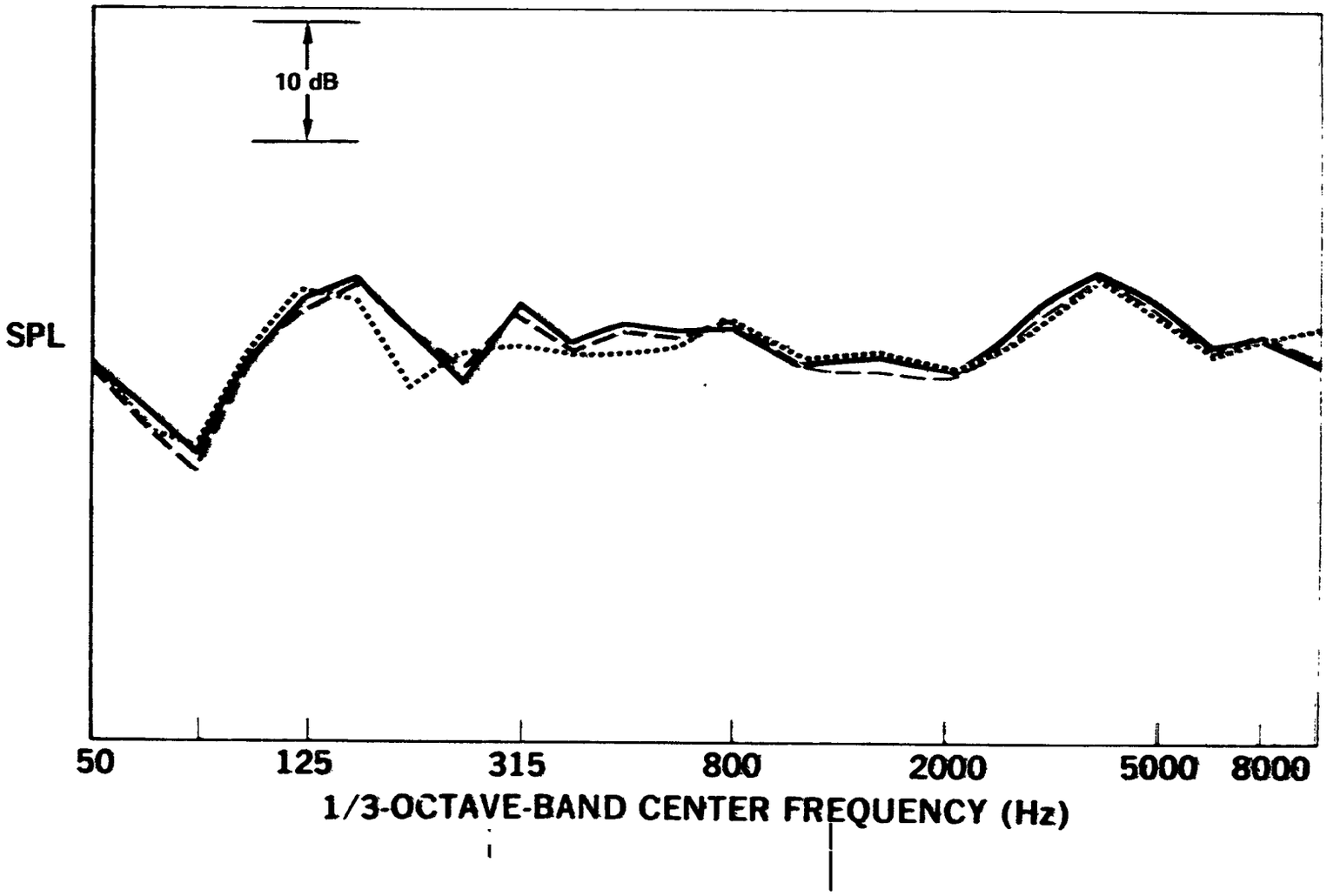

FIGURE 61. SPECTRAL COMPARISON BETWEEN DC-10-10 APPROACH TESTS AFTER LAYERED WEATHER CORRECTION

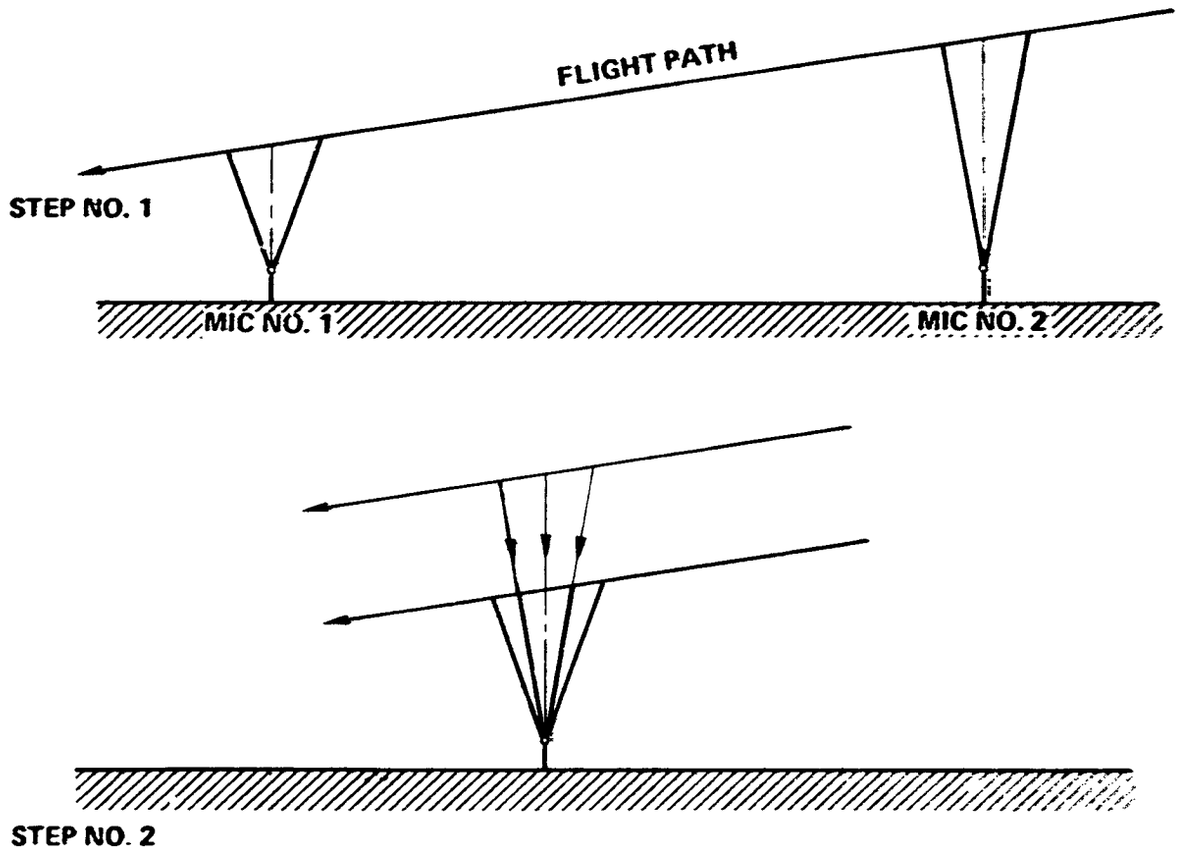

FIGURE 62. EXCESS ATTENUATION ANALYSIS APPROACH

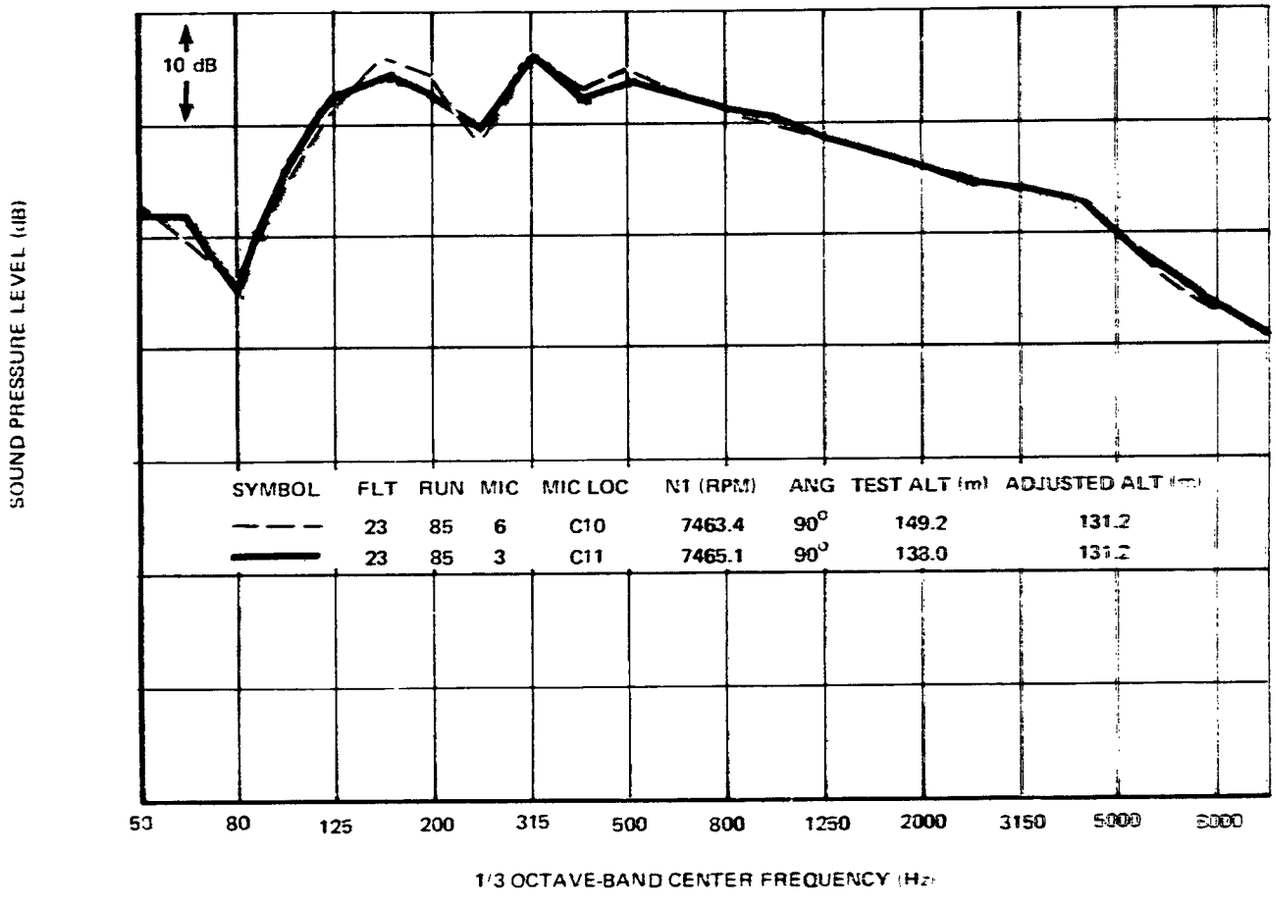

FIGURE 63. COMPARISON OF SPECTRA FROM DIFFERENT MICROPHONE LOCATIONS ADJUSTED TO THE SAME ALTITUDE – LEVEL FLIGHT

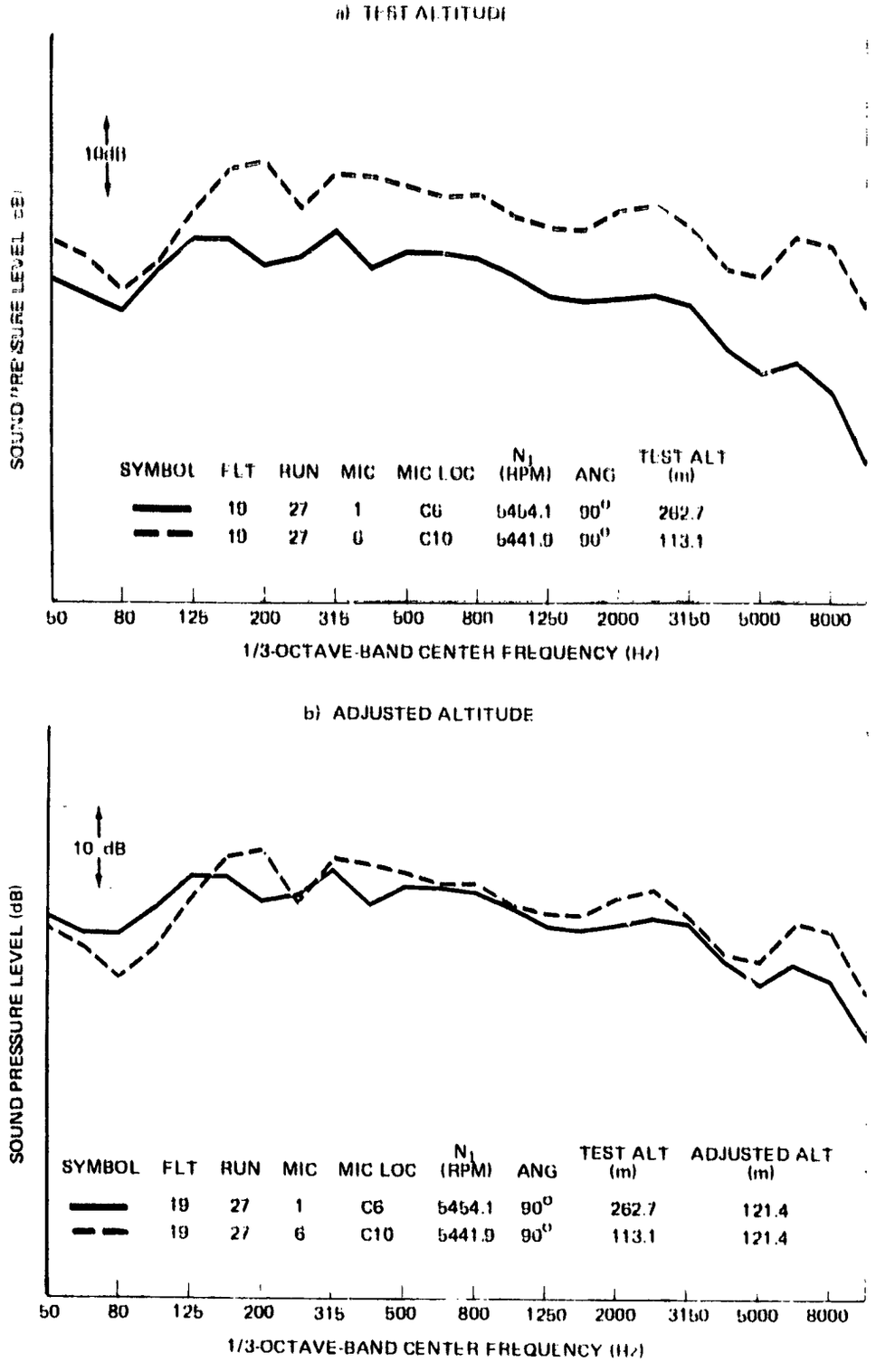

FIGURE 64. COMPARISON OF DC-9-30/JT8D-109 SPECTRA AT DIFFERENT MICROPHONE LOCATIONS ADJUSTED TO A COMMON APPROACH ALTITUDE

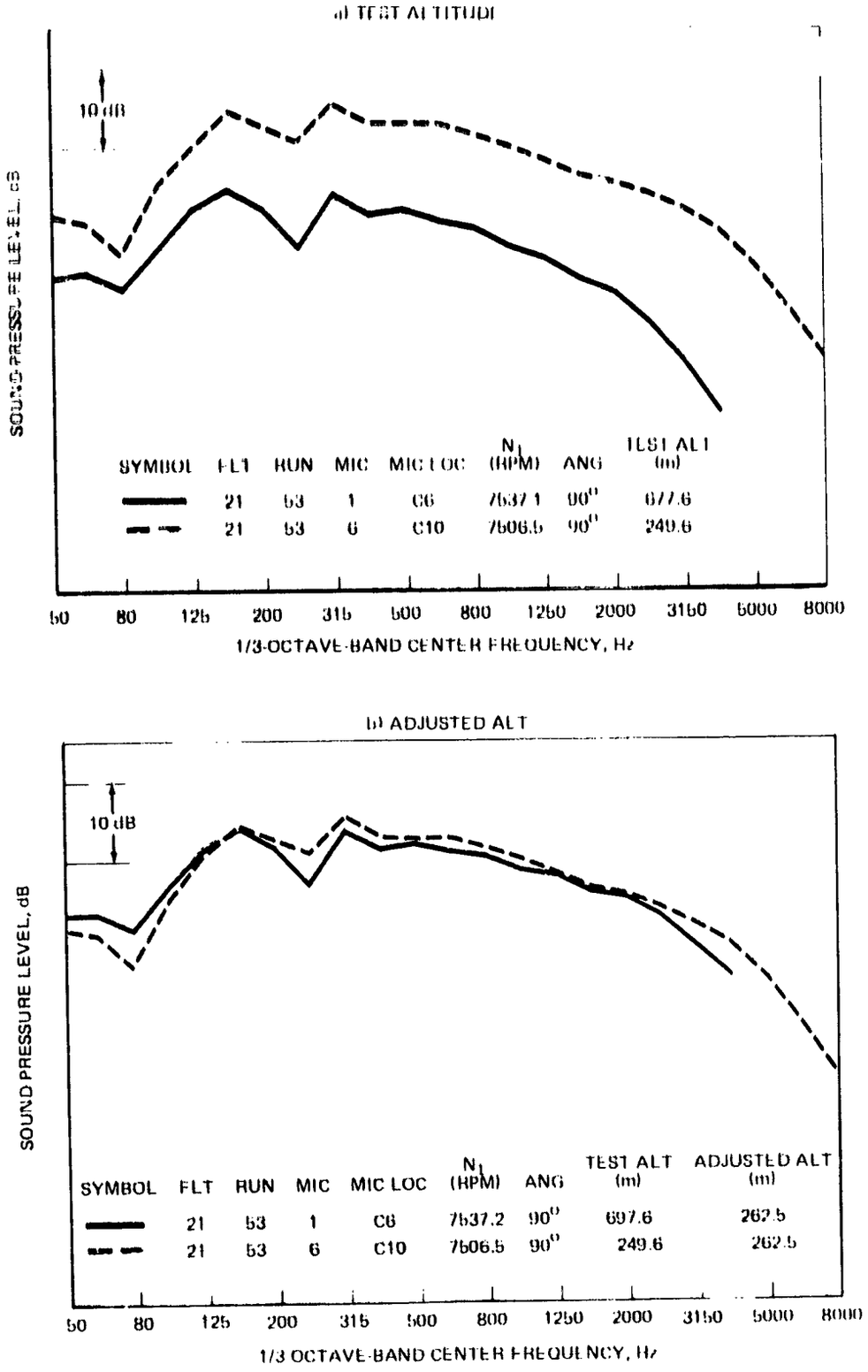

FIGURE 65. COMPARISON OF DC-9-30/JT8D-109 SPECTRA AT DIFFERENT MICROPHONE LOCATIONS ADJUSTED TO A COMMON TAKEOFF ALTITUDE

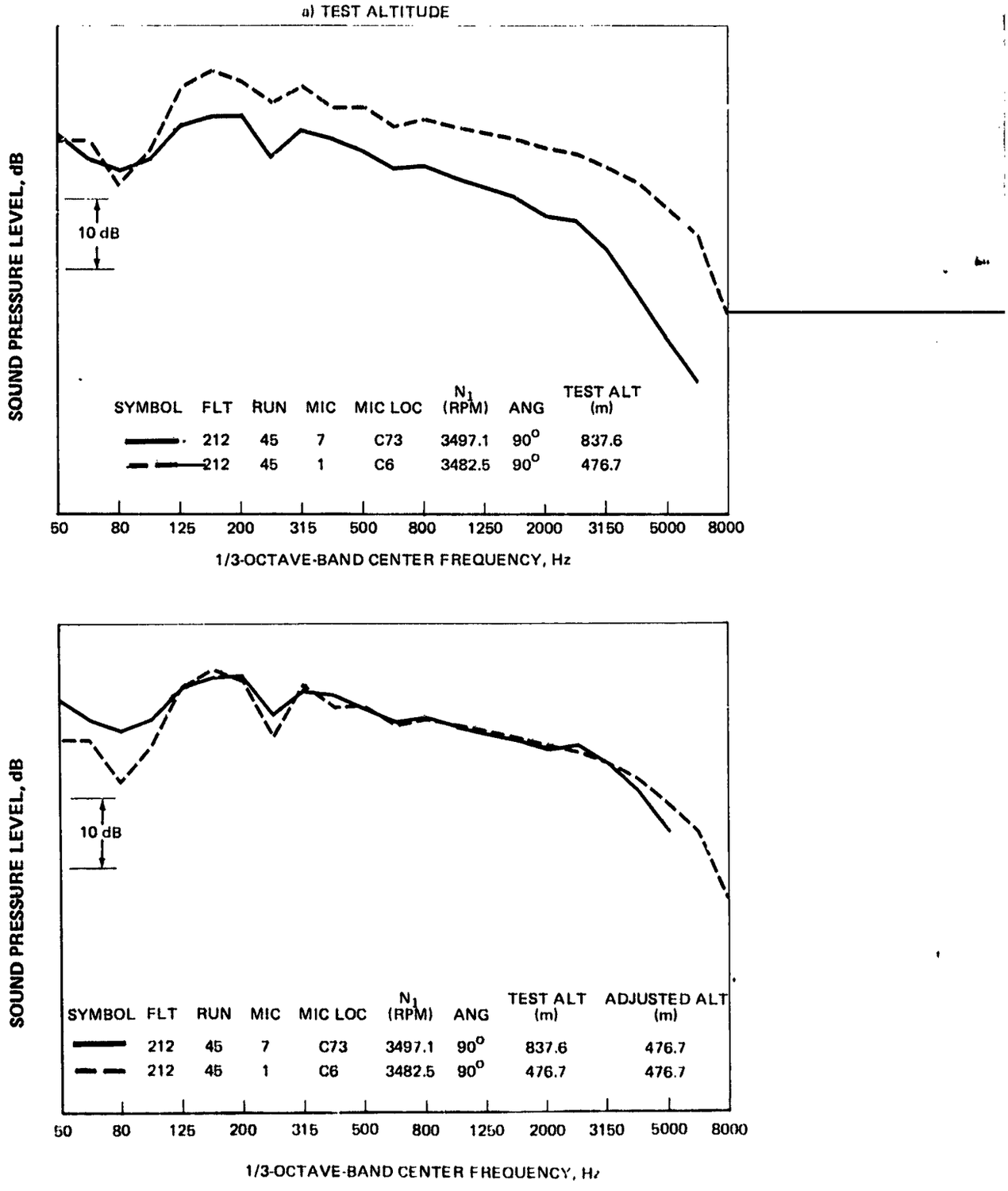

FIGURE 66. COMPARISON OF DC-10-40/JT9D-59A SPECTRA AT DIFFERENT MICROPHONE LOCATIONS ADJUSTED TO A COMMON TAKEOFF ALTITUDE

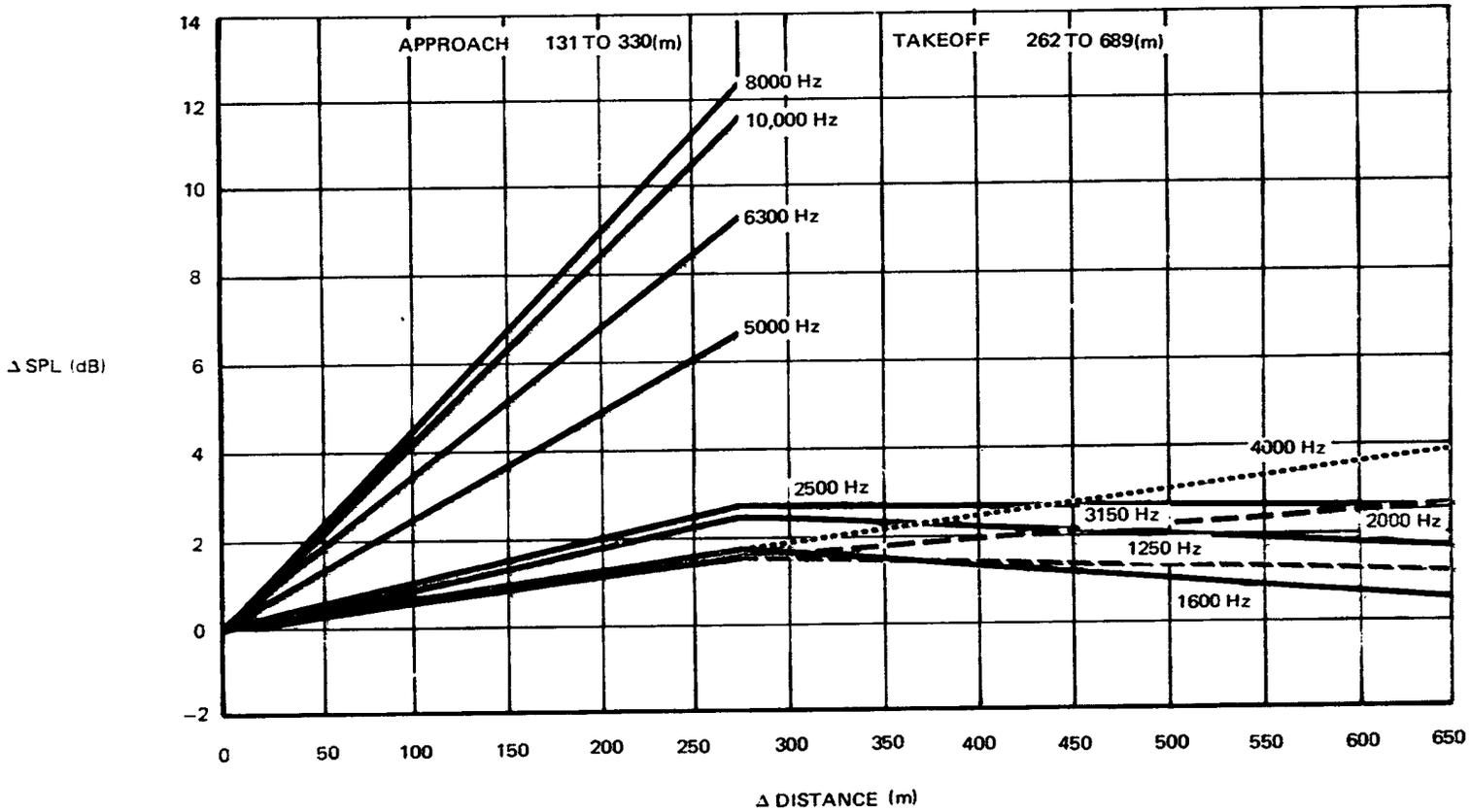

FIGURE 67. EFFECT OF ALTITUDE ON DC-9-30/JT8D-109 SPECTRA DATA MEASURED AT OVERHEAD

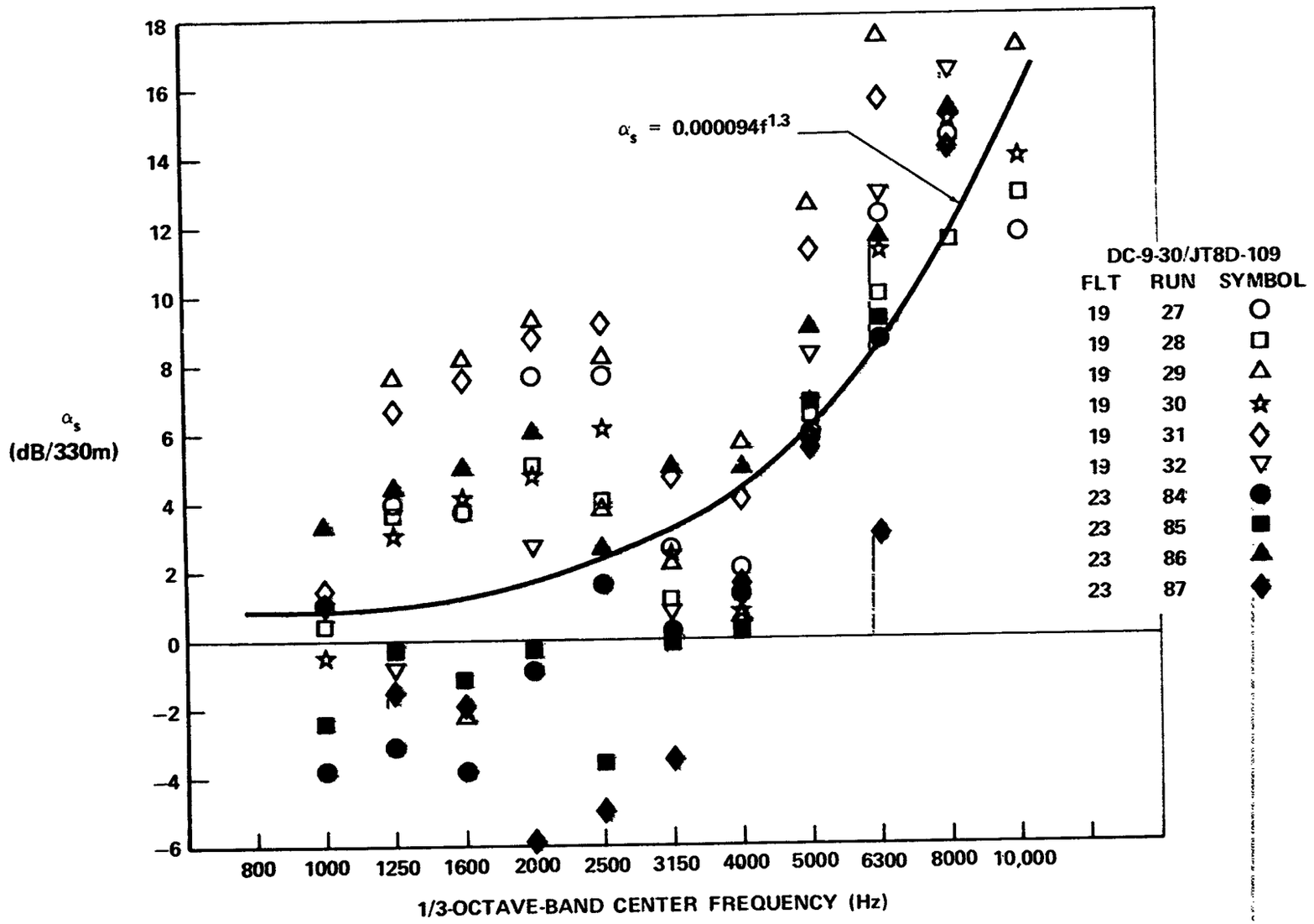

FIGURE 68. EXCESS-ATTENUATION COEFFICIENTS MEASURED AT OVERHEAD BETWEEN 100 AND 330(m)

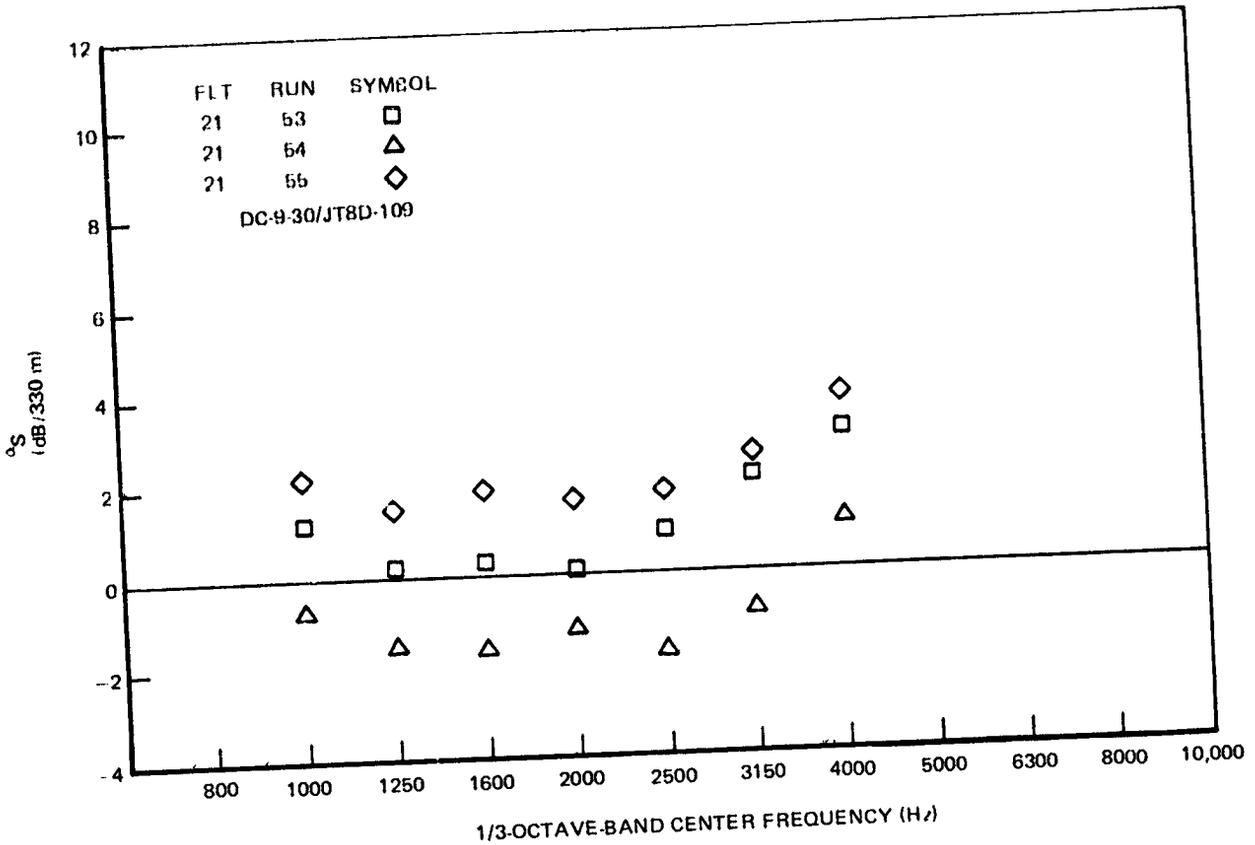

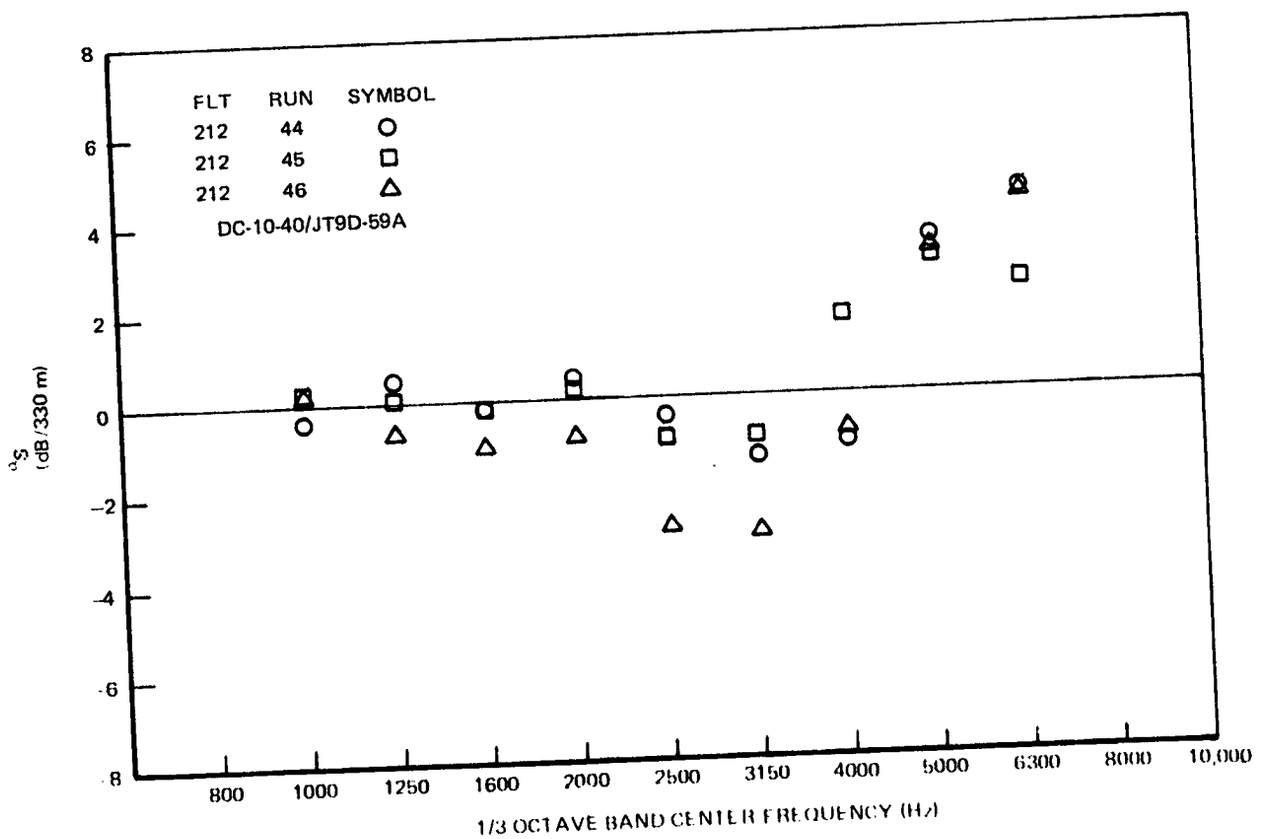

FIGURE 69. EXCESS-ATTENUATION COEFFICIENTS MEASURED AT OVERHEAD DURING TAKEOFF

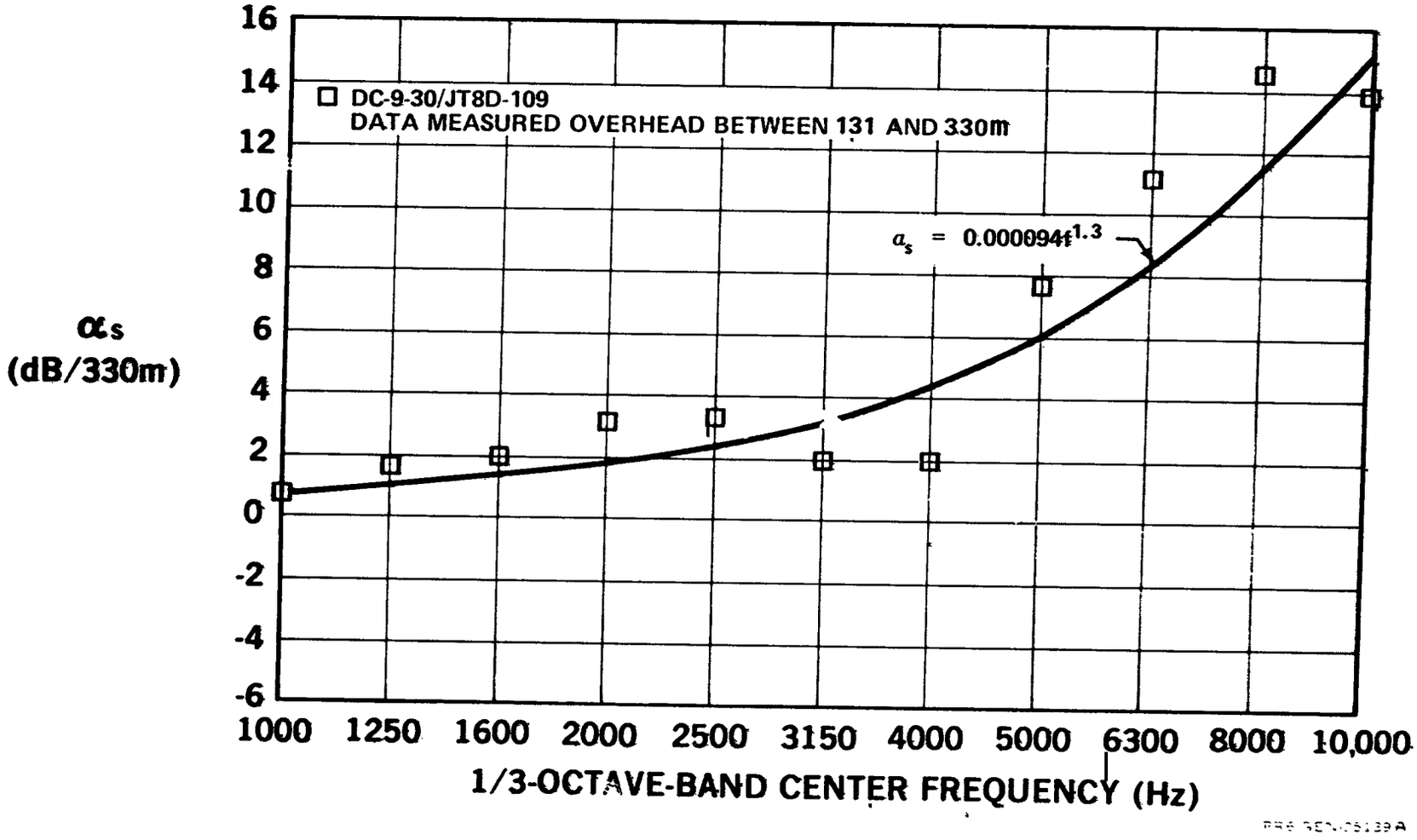

FIGURE 70. AVERAGED EXCESS-ATTENUATION COEFFICIENTS – APPROACH

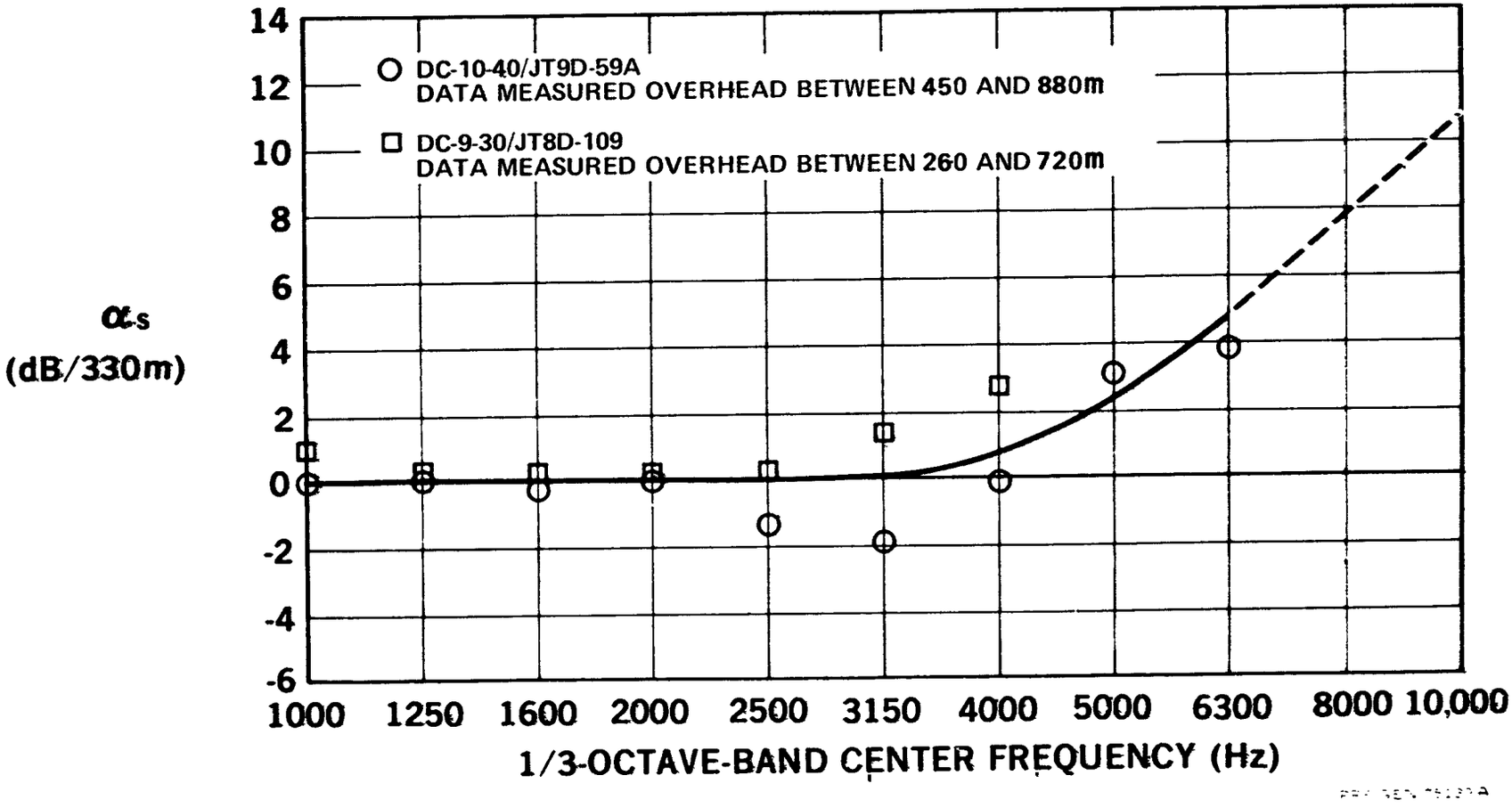

FIGURE 71. AVERAGED EXCESS-ATTENUATION COEFFICIENTS – TAKEOFF

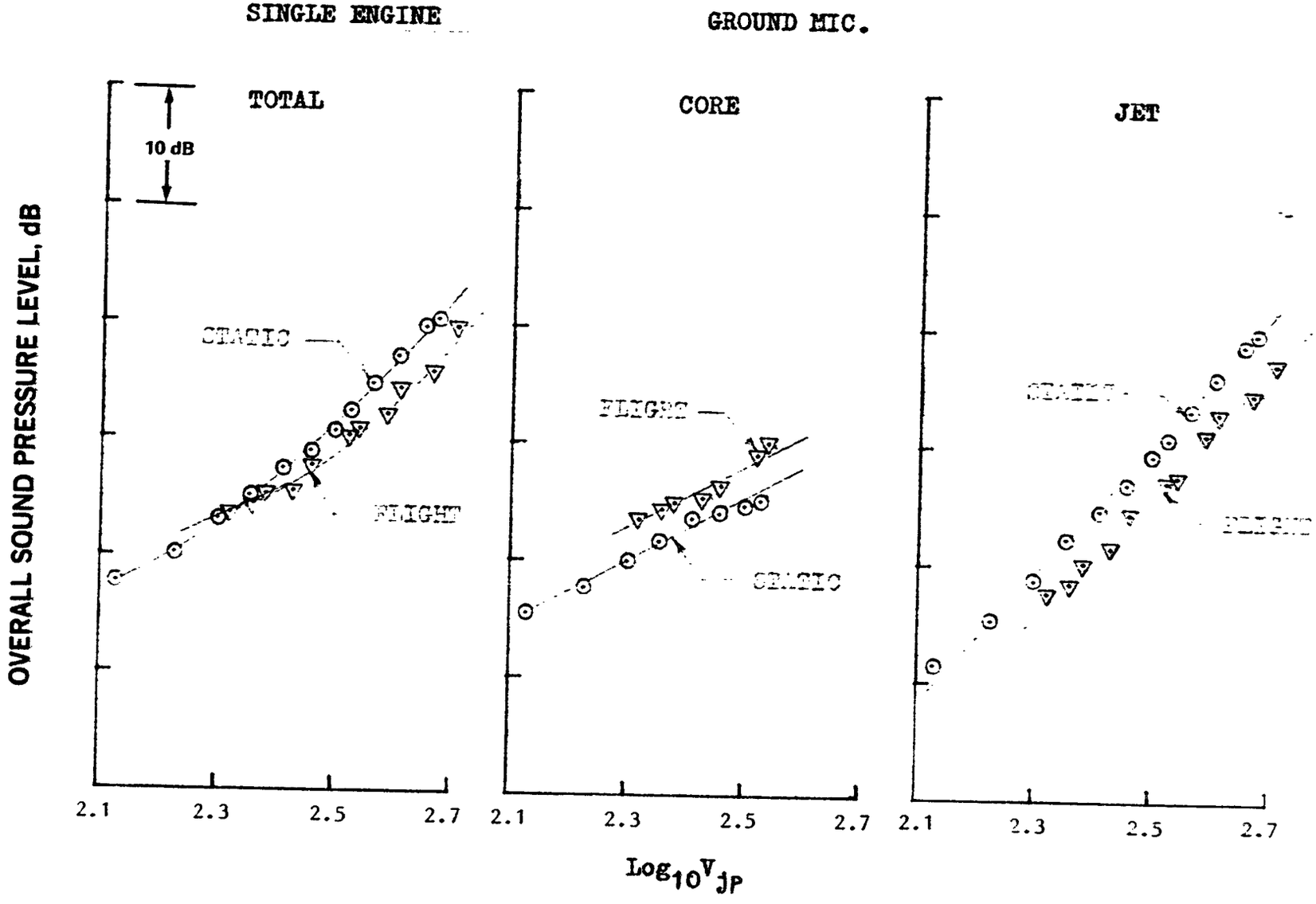

FIGURE 72. COMPARISON OF JT8D-109 TOTAL, JET, AND CORE NOISE SOURCE LEVELS GENERATED STATICALLY AND IN FLIGHT AT 45.7-METER RADIUS AND 50° FROM INLET CENTERLINE

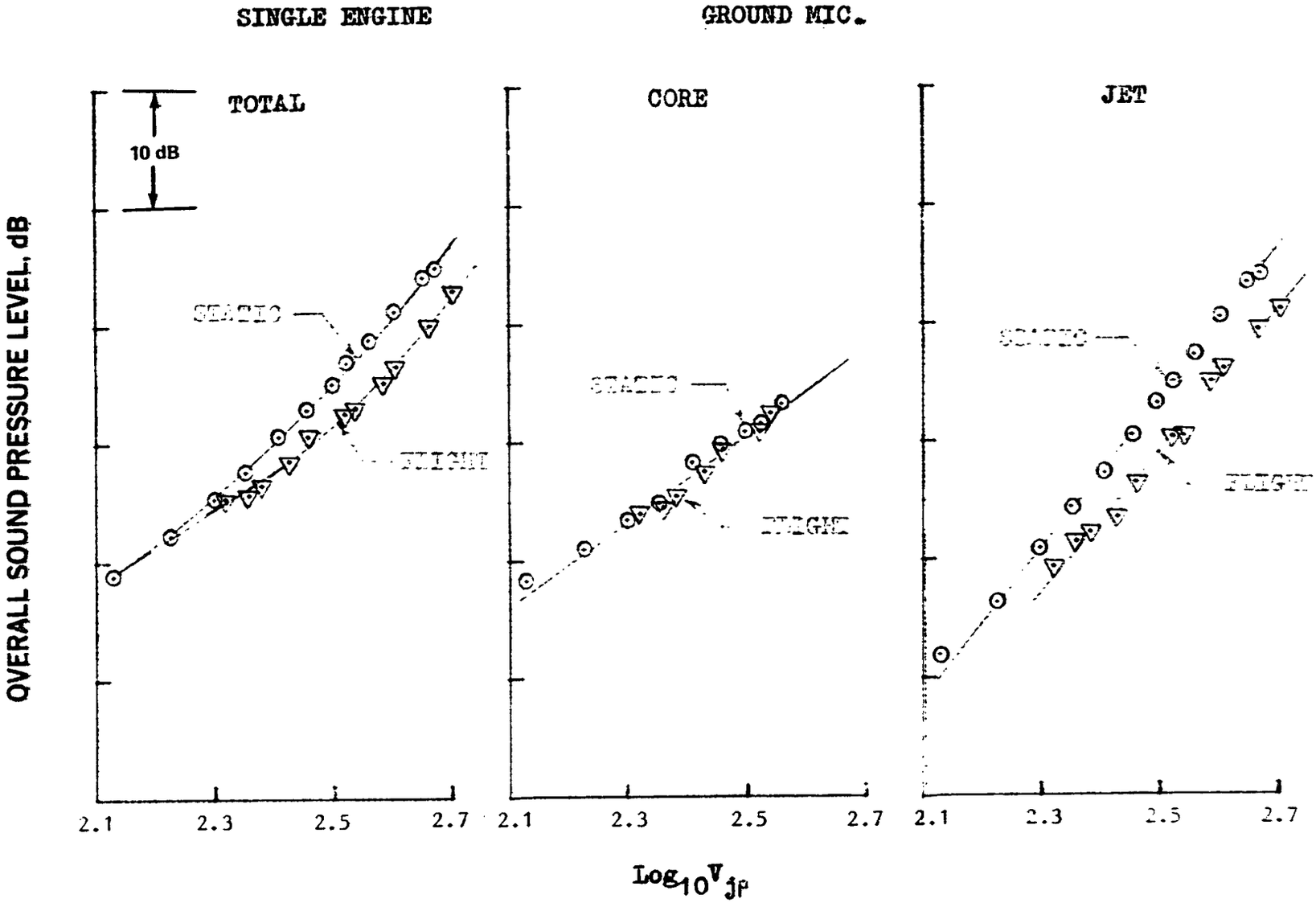

FIGURE 73. COMPARISON OF JT8D-109 TOTAL, JET, AND CORE NOISE SOURCE LEVELS GENERATED STATICALLY AND IN FLIGHT AT 45.7-METER RADIUS AND 90° FROM INLET CENTERLINE

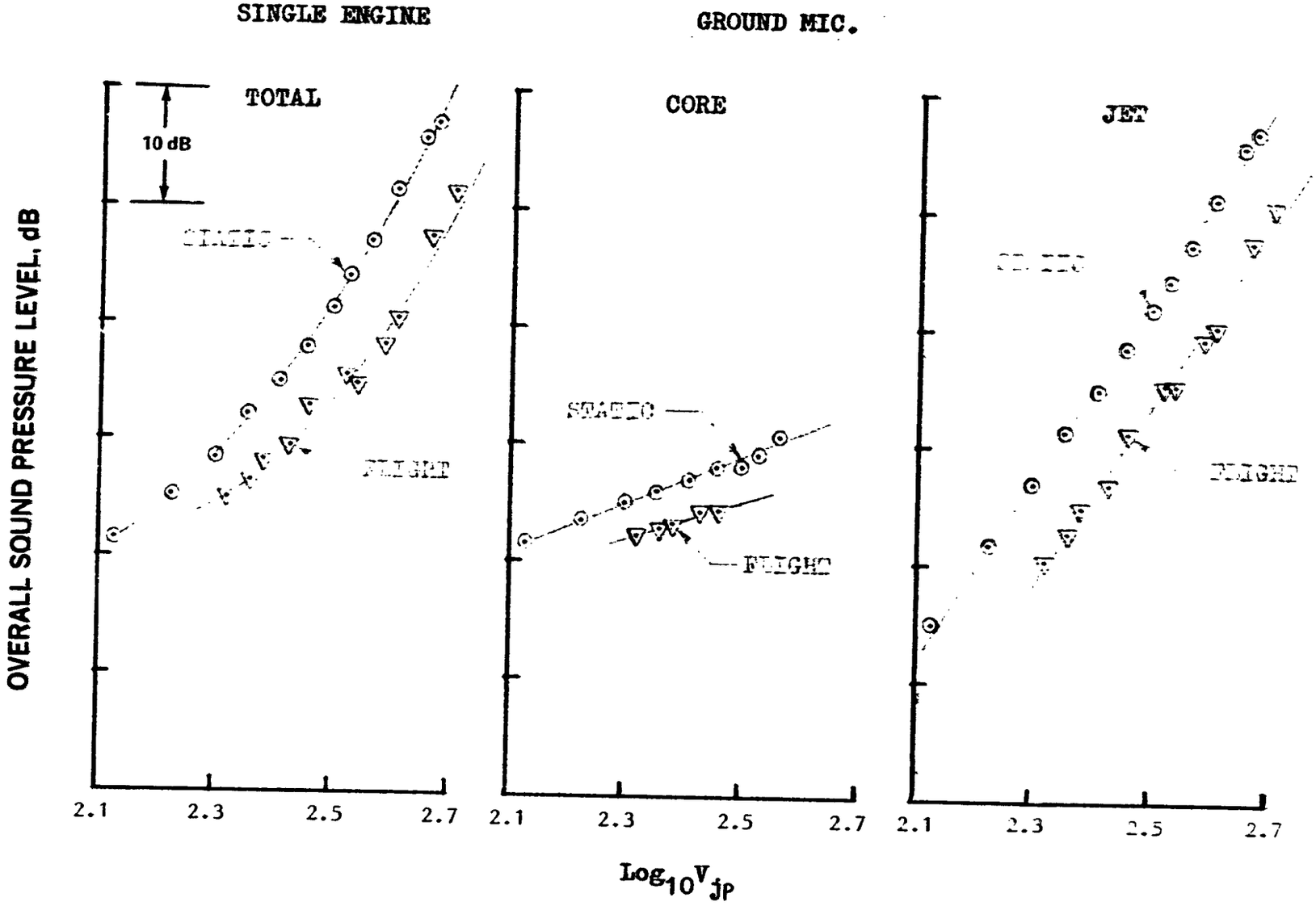

FIGURE 74. COMPARISON OF JT8D-109 TOTAL, JET, AND CORE NOISE SOURCE LEVELS GENERATED STATICALLY AND IN FLIGHT AT 45.7-METER RADIUS AND 140° FROM INLET CENTERLINE

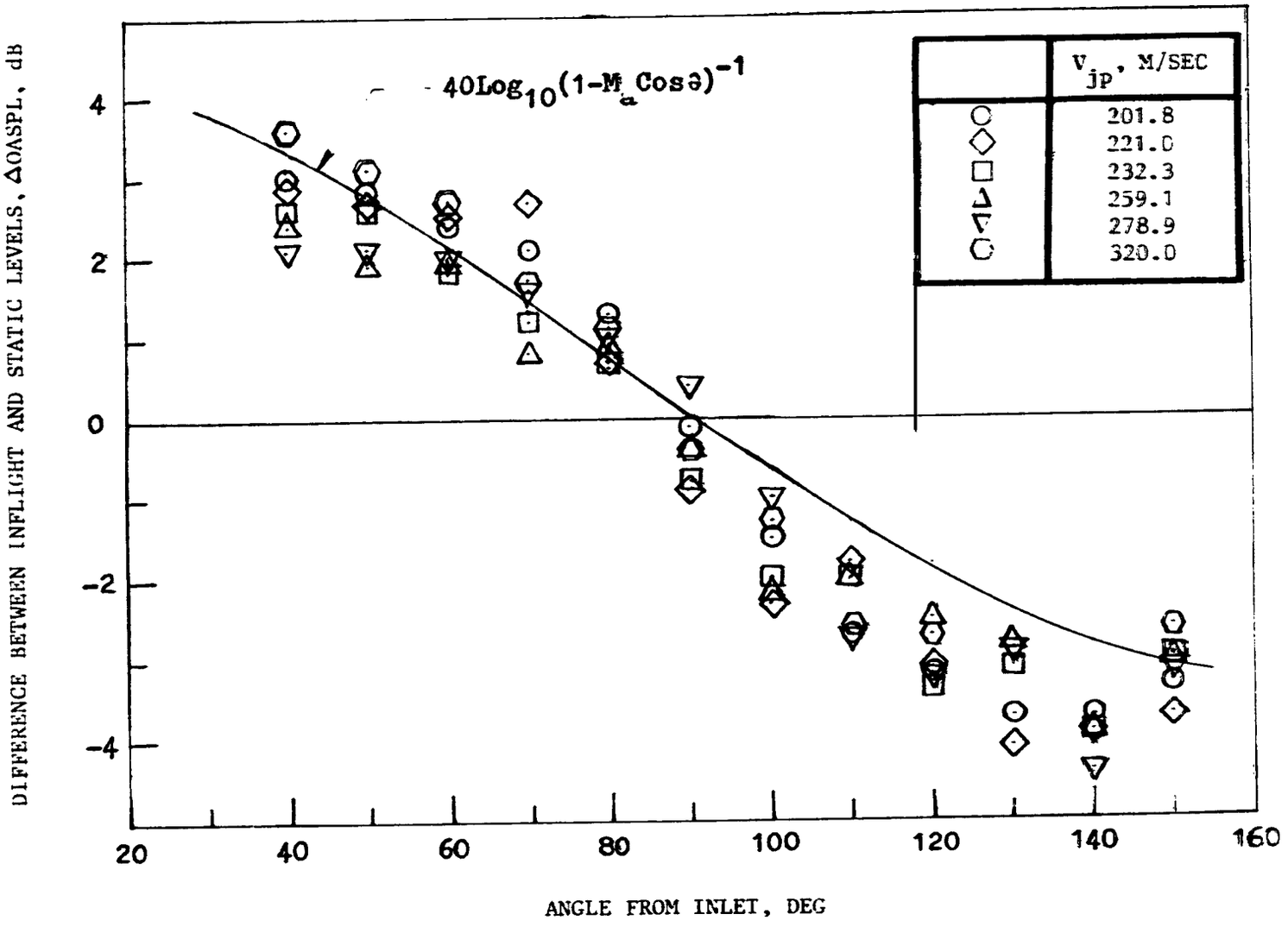

FIGURE 75. EFFECT OF CONVECTIVE AMPLIFICATION ON DC-9-30/JT8D-109 CORE-NOISE OVERALL SOUND PRESSURE LEVELS AT 76.2-M/SEC AIRCRAFT VELOCITY

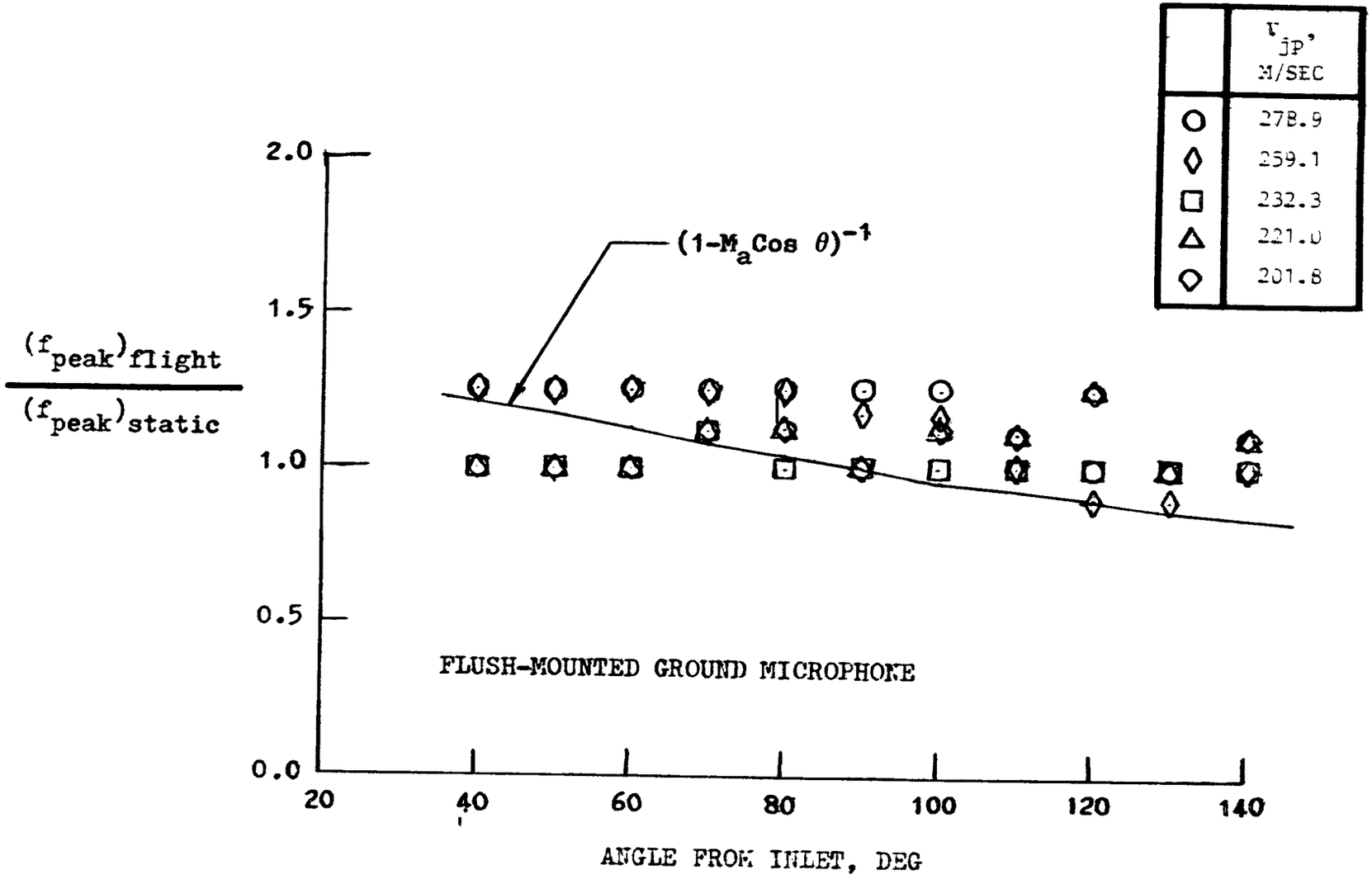

FIGURE 76. EFFECT OF FORWARD MOTION ON DC-9-30/JT8D-109 CORE-NOISE PEAK FREQUENCY AT 76.2-M/SEC AIRCRAFT VELOCITY

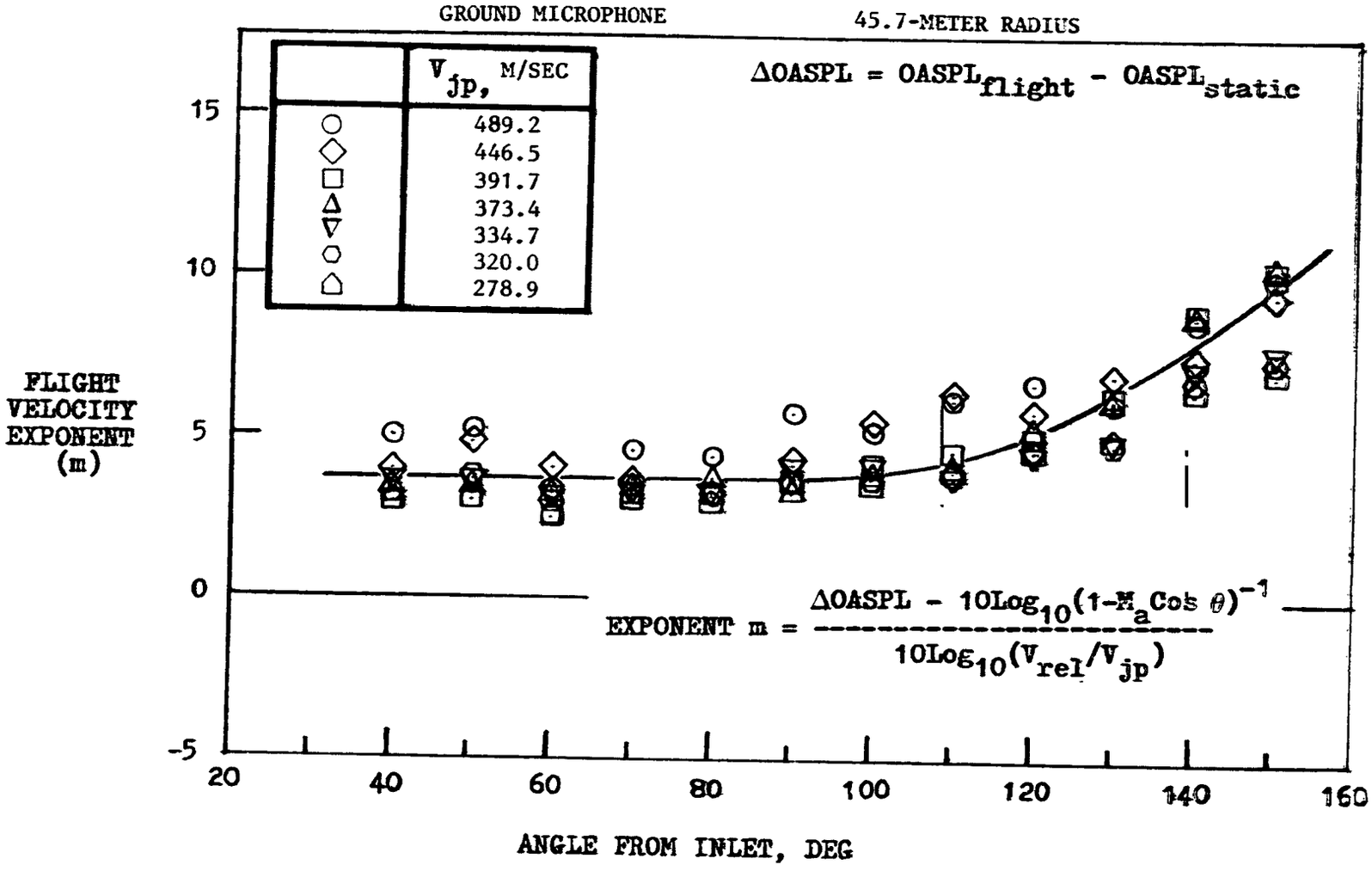

FIGURE 77. EFFECT OF CONVECTIVE AMPLIFICATION AND RELATIVE VELOCITY ON DC-9-30 JT8D-109 JET-NOISE FLIGHT VELOCITY EXPONENT

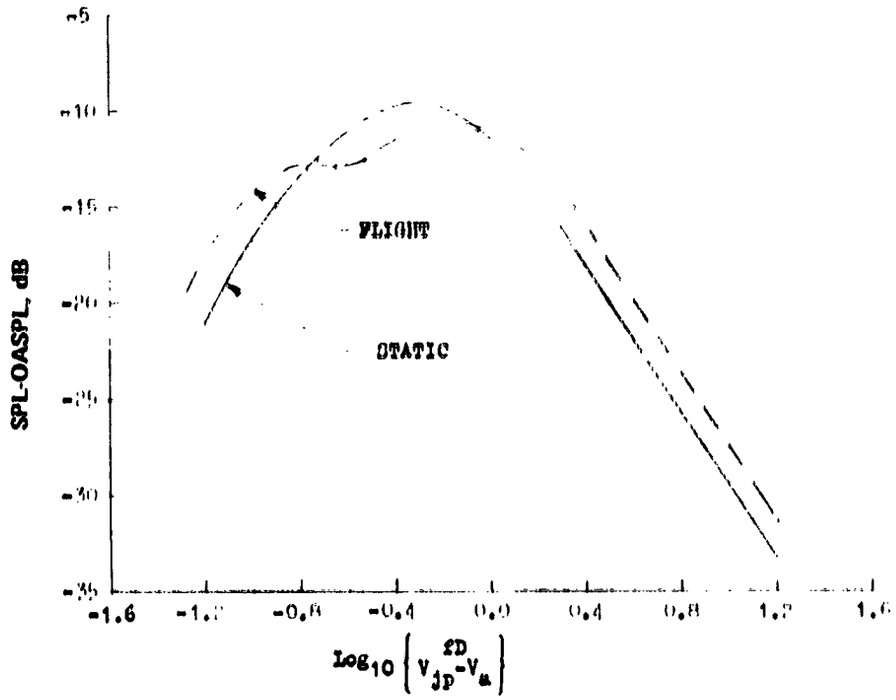

(a) 50° FROM INLET CENTERLINE

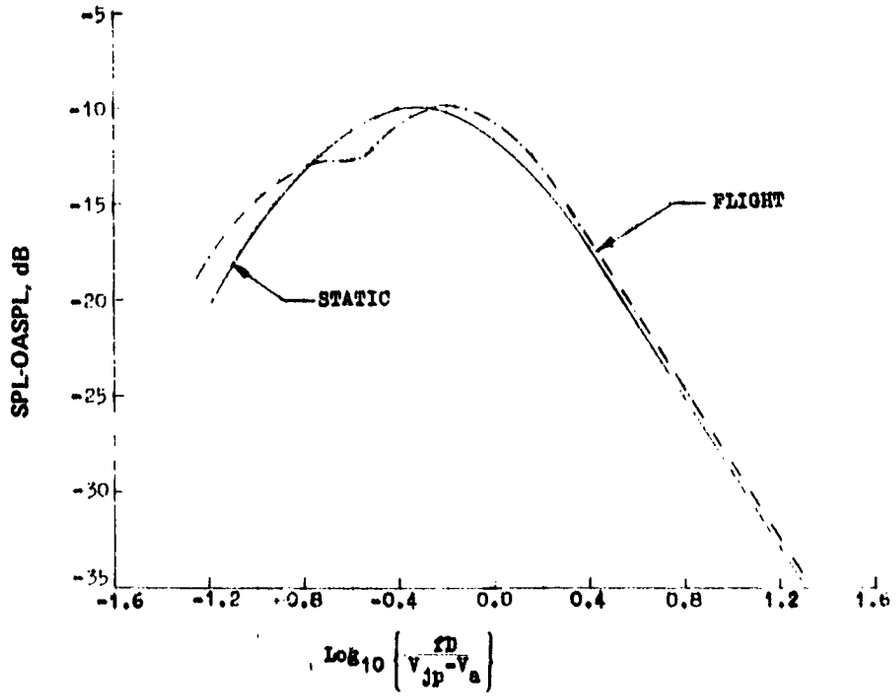

(b) 90° FROM INLET CENTERLINE

FIGURE 78. EFFECT OF FORWARD MOTION ON DC-9-30/JT8D-109 AVERAGE NORMALIZED JET-NOISE SPECTRA AT 45.7-METER RADIUS

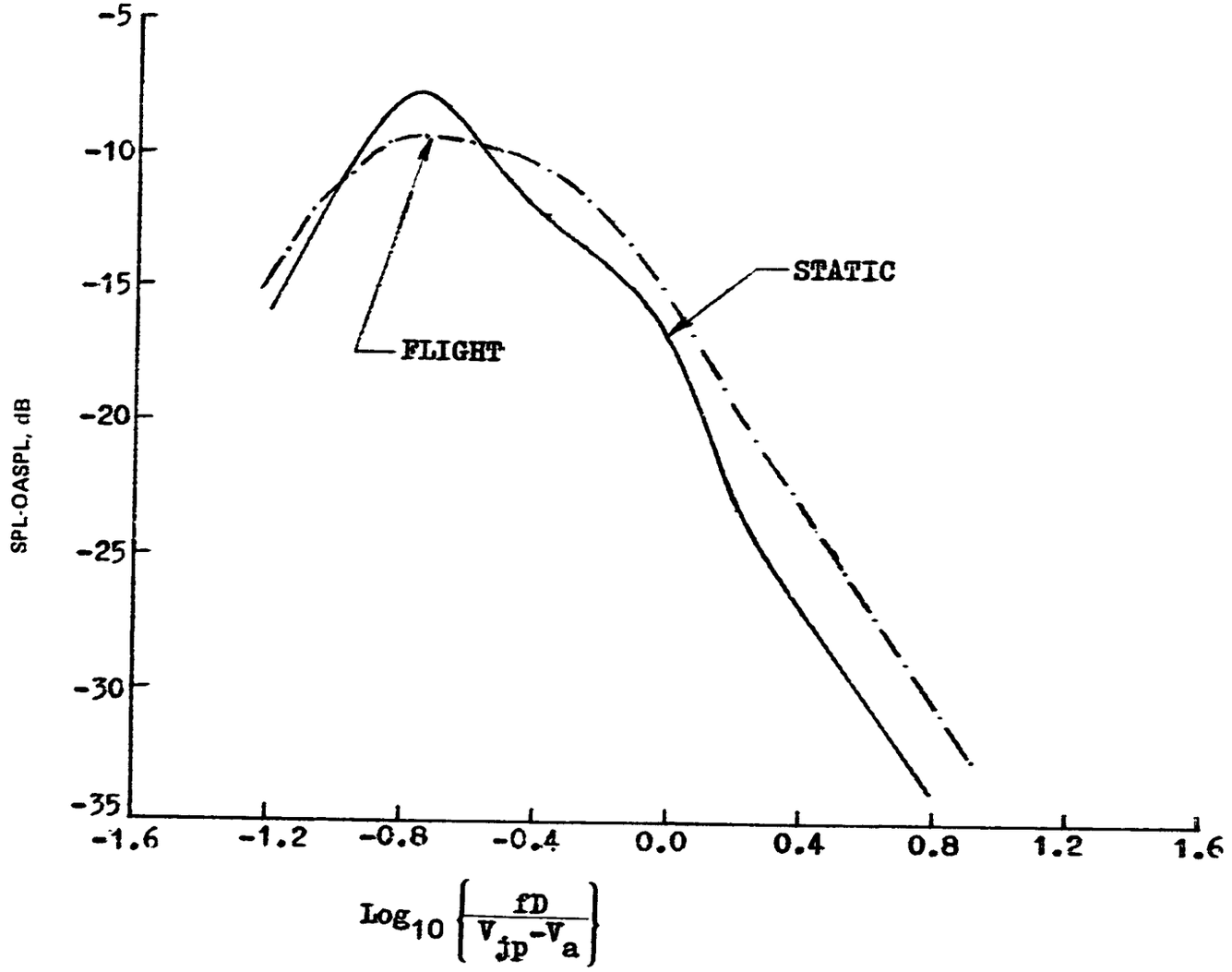

(c) 140° FROM INLET CENTERLINE

FIGURE 78. EFFECT OF FORWARD MOTION ON DC-9-30/JT8D-109 AVERAGE NORMALIZED JET-NOISE SPECTRA AT 45.7-METER RADIUS (CONTINUED)

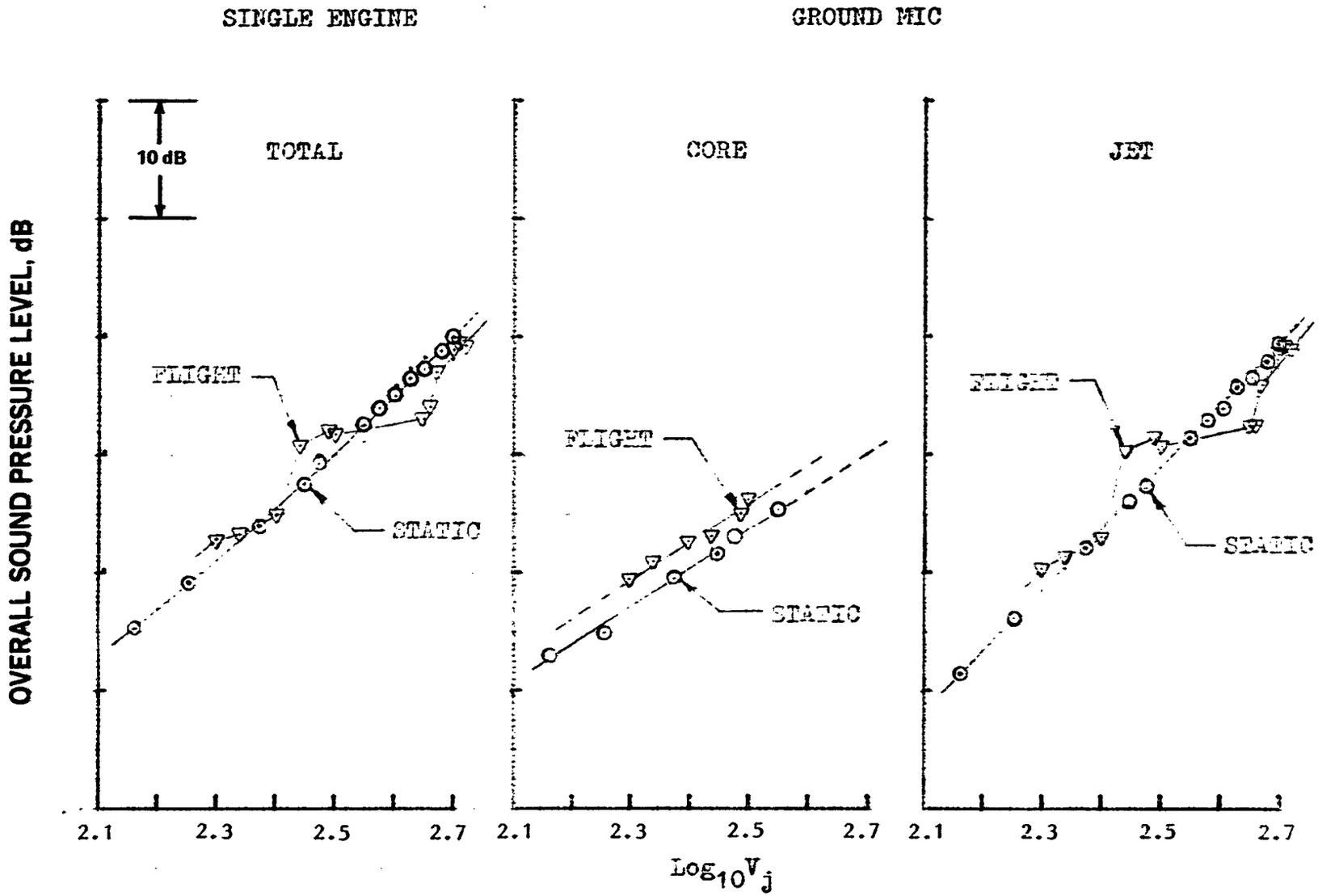

FIGURE 79. COMPARISON OF JT9D-59A TOTAL, JET, AND CORE NOISE SOURCE LEVELS GENERATED STATICALLY AND IN FLIGHT AT 45.7-METER RADIUS AND 50° FROM INLET CENTERLINE

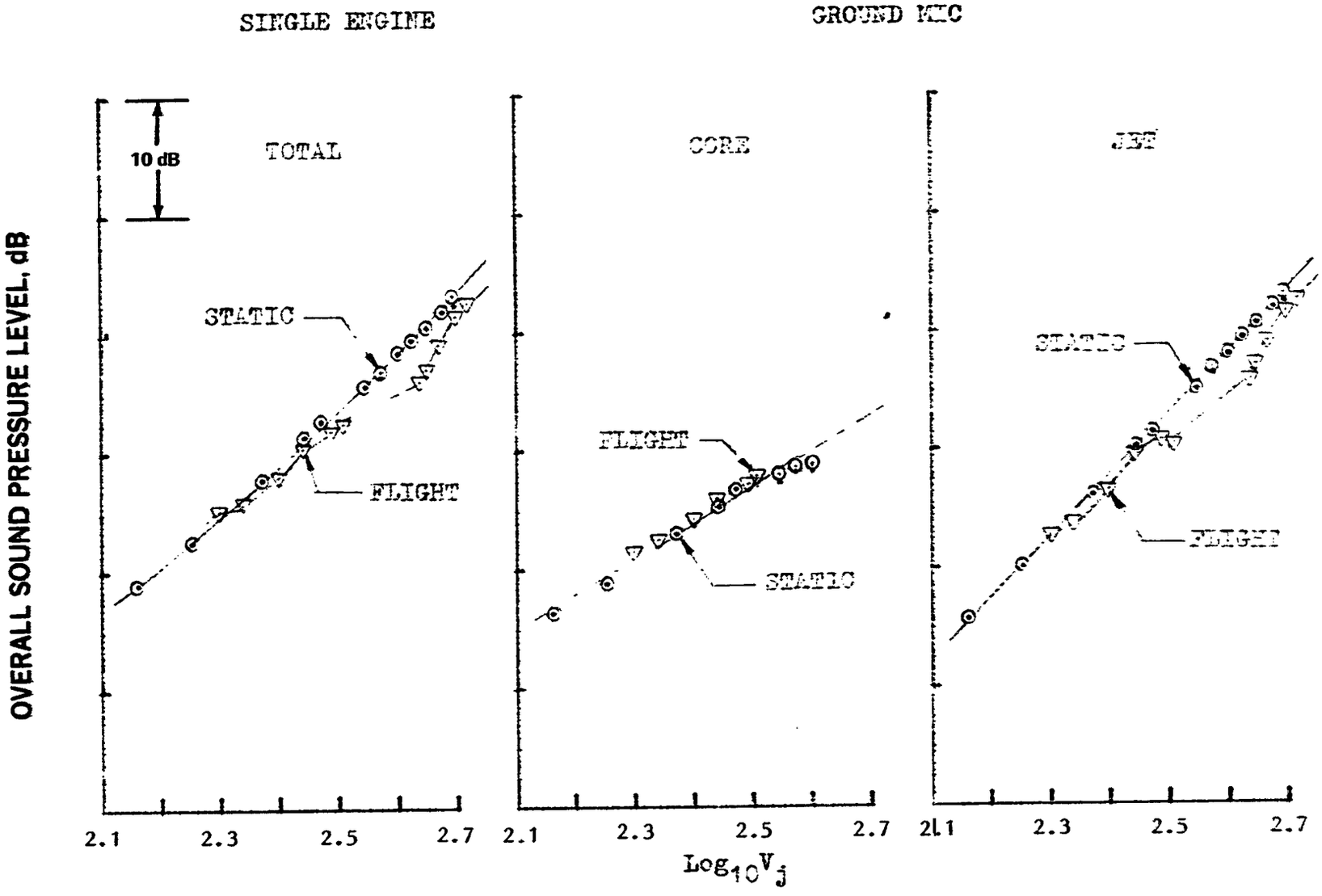

FIGURE 80 COMPARISON OF JT9D-59A TOTAL, JET, AND CORE NOISE SOURCE LEVELS GENERATED STATICALLY AND IN FLIGHT AT 45.7-METER RADIUS AND 90° FROM INLET CENTERLINE

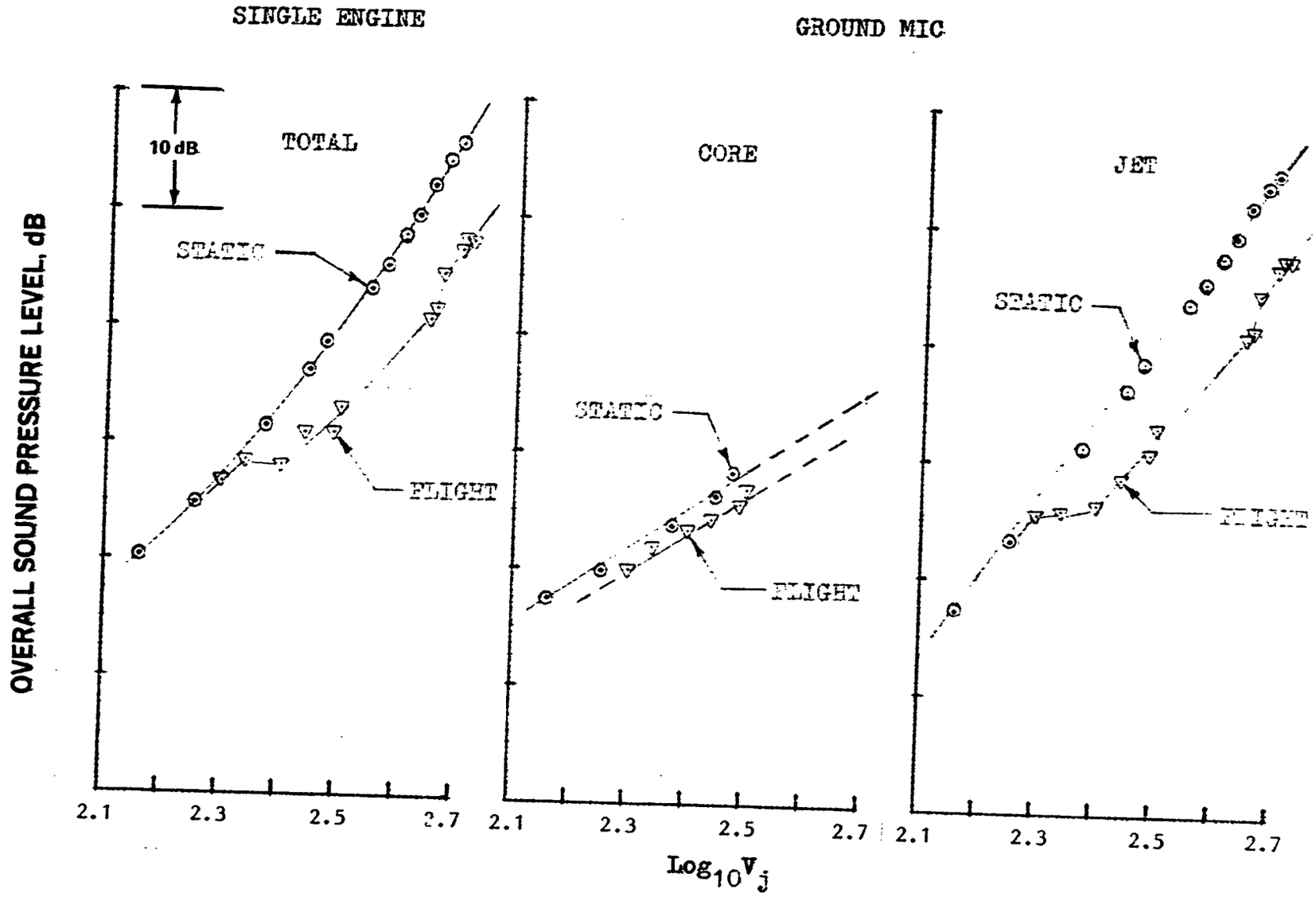

FIGURE 81. COMPARISION OF JT9D-59A TOTAL, JET, AND CORE NOISE SOURCE LEVELS GENERATED STATICALLY AND IN FLIGHT AT 45.7-METER RADIUS AND 140° FROM INLET CENTERLINE

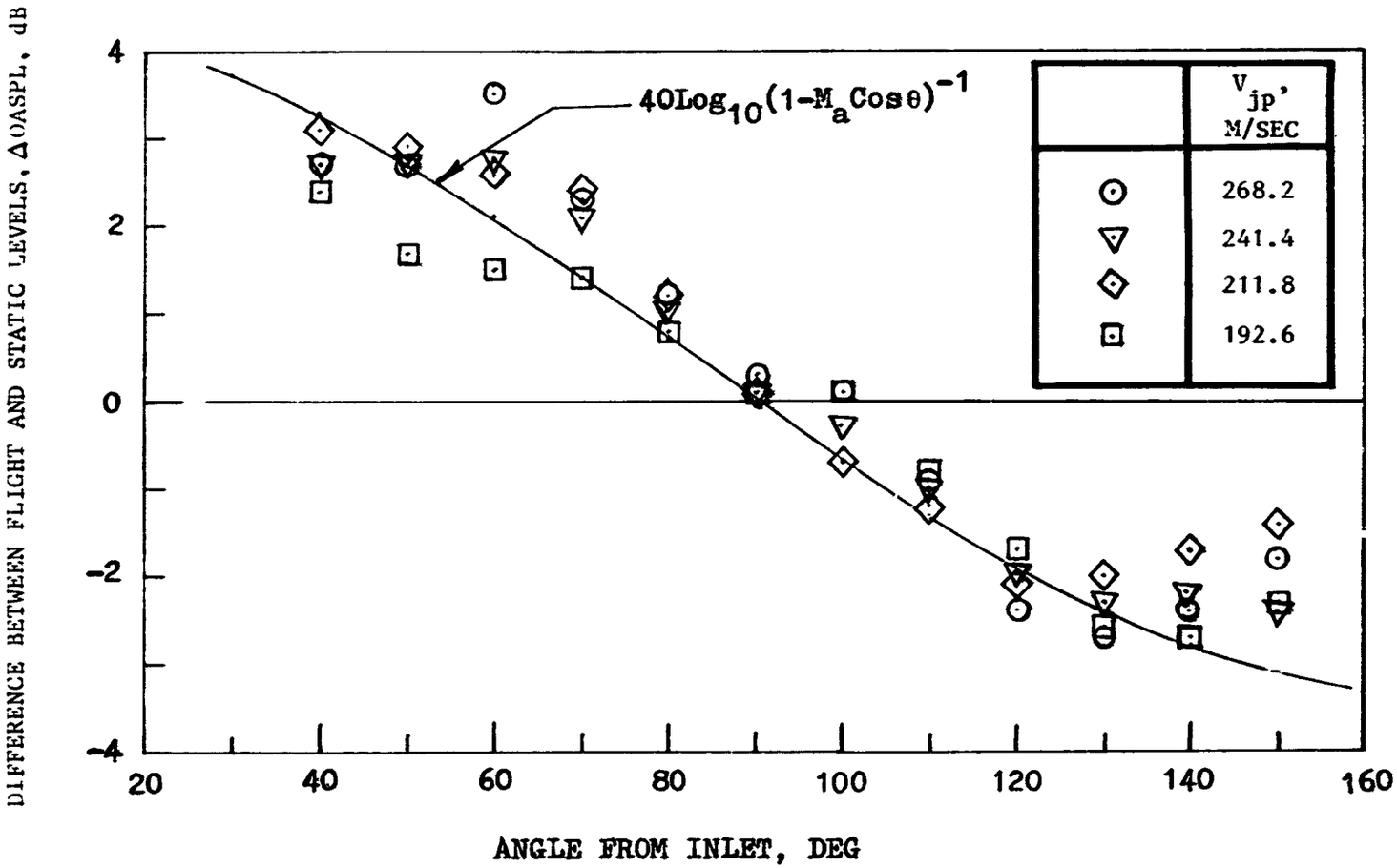

FIGURE 82. EFFECT OF CONVECTIVE AMPLIFICATION ON DC-10-40/JT9D-59A CORE-NOISE OVERALL SOUND PRESSURE LEVELS AT 76.2-M/SEC AIRCRAFT VELOCITY

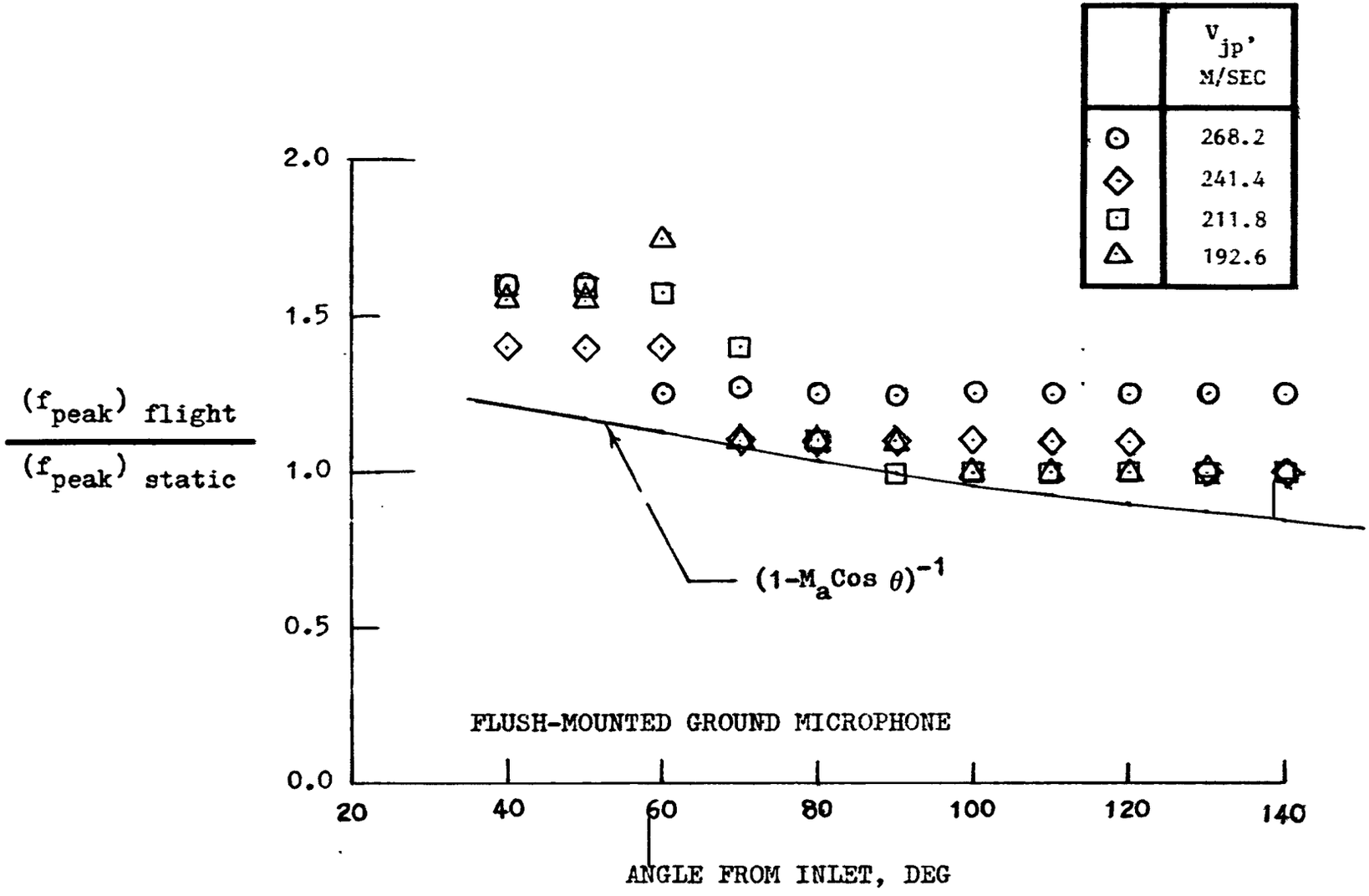

FIGURE 83. EFFECT OF FORWARD MOTION ON DC-10-40/JT9D-59A CORE-NOISE PEAK FREQUENCY AT 76.2-M/SEC AIRCRAFT VELOCITY

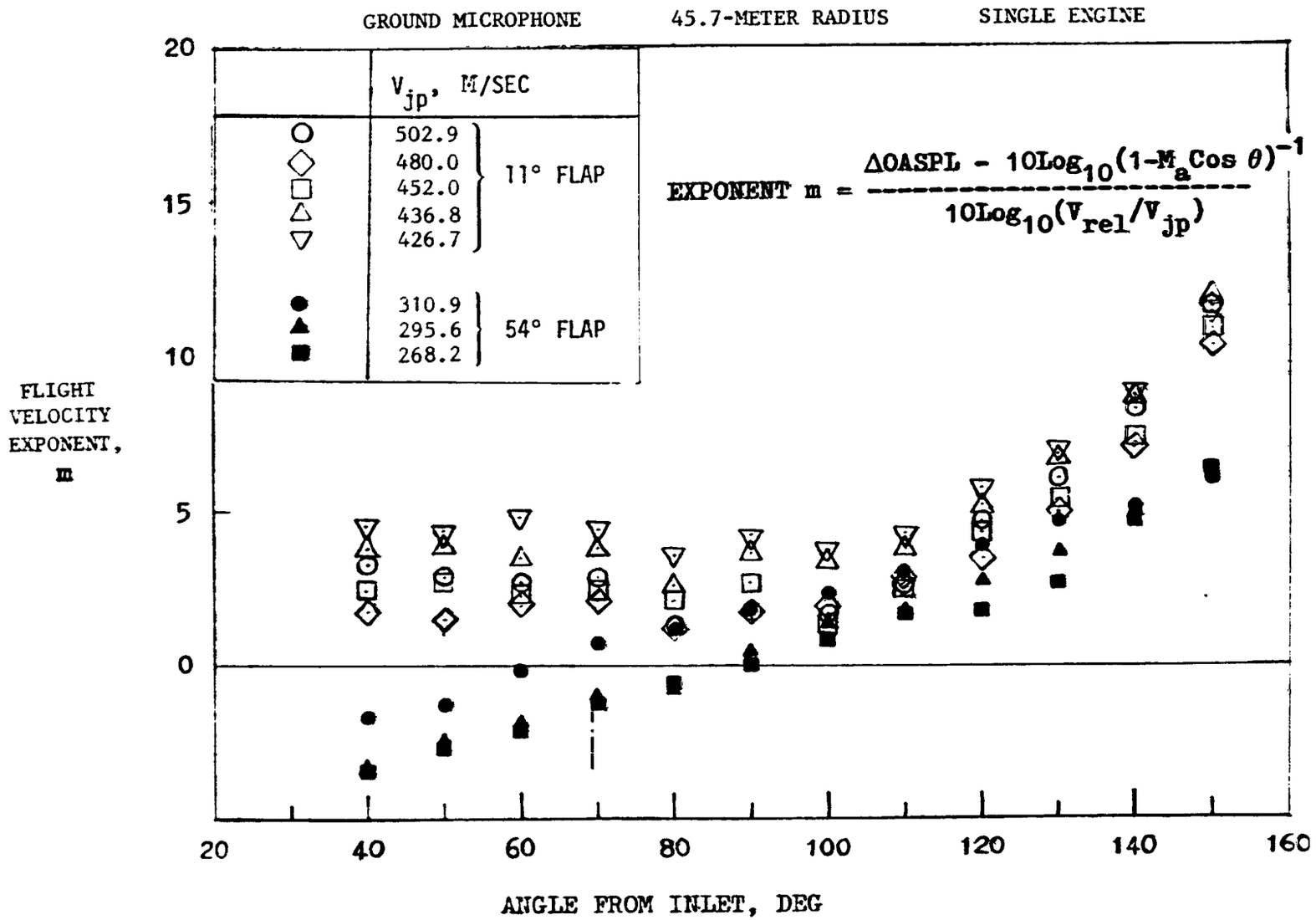

FIGURE 84. EFFECT OF CONVECTIVE AMPLIFICATION AND RELATIVE VELOCITY ON DC-10-40/JT9D-59A JET-NOISE FLIGHT VELOCITY EXPONENT

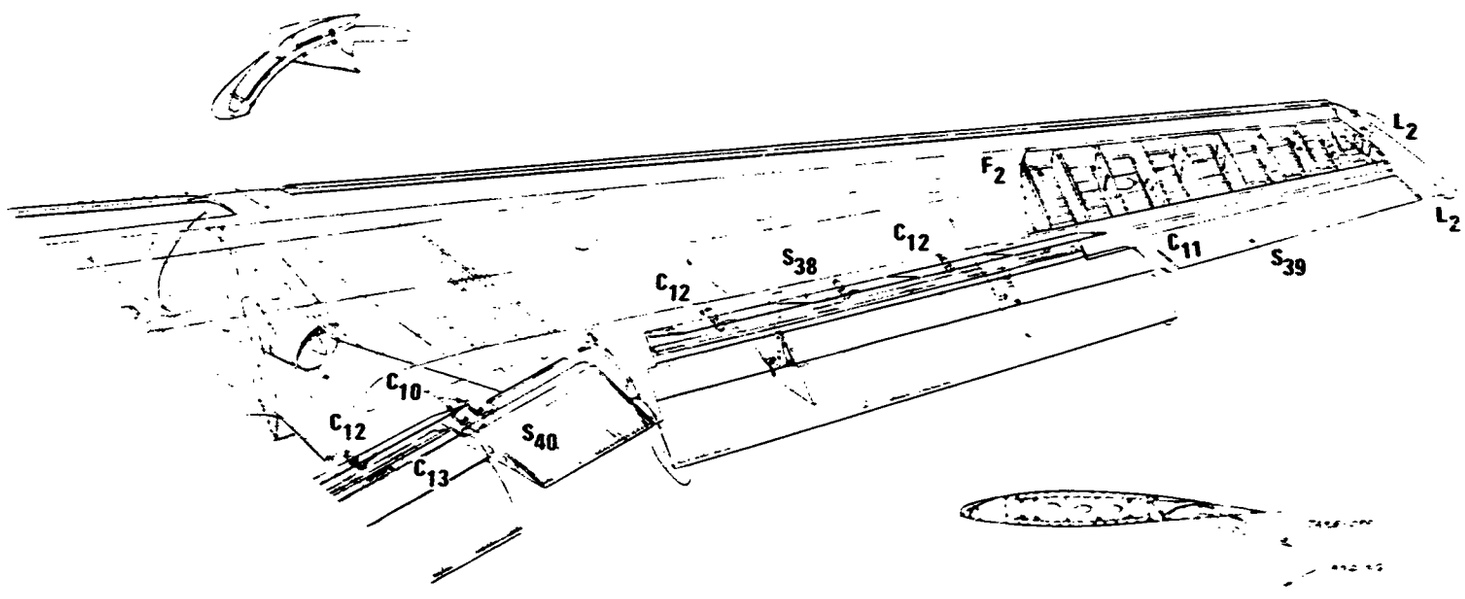

FIGURE 85. DC-10-40/JT9D-59A ENGINE NACELLE AND WING-FLAP SYSTEM FOR TAKEOFF AND APPROACH LANDING

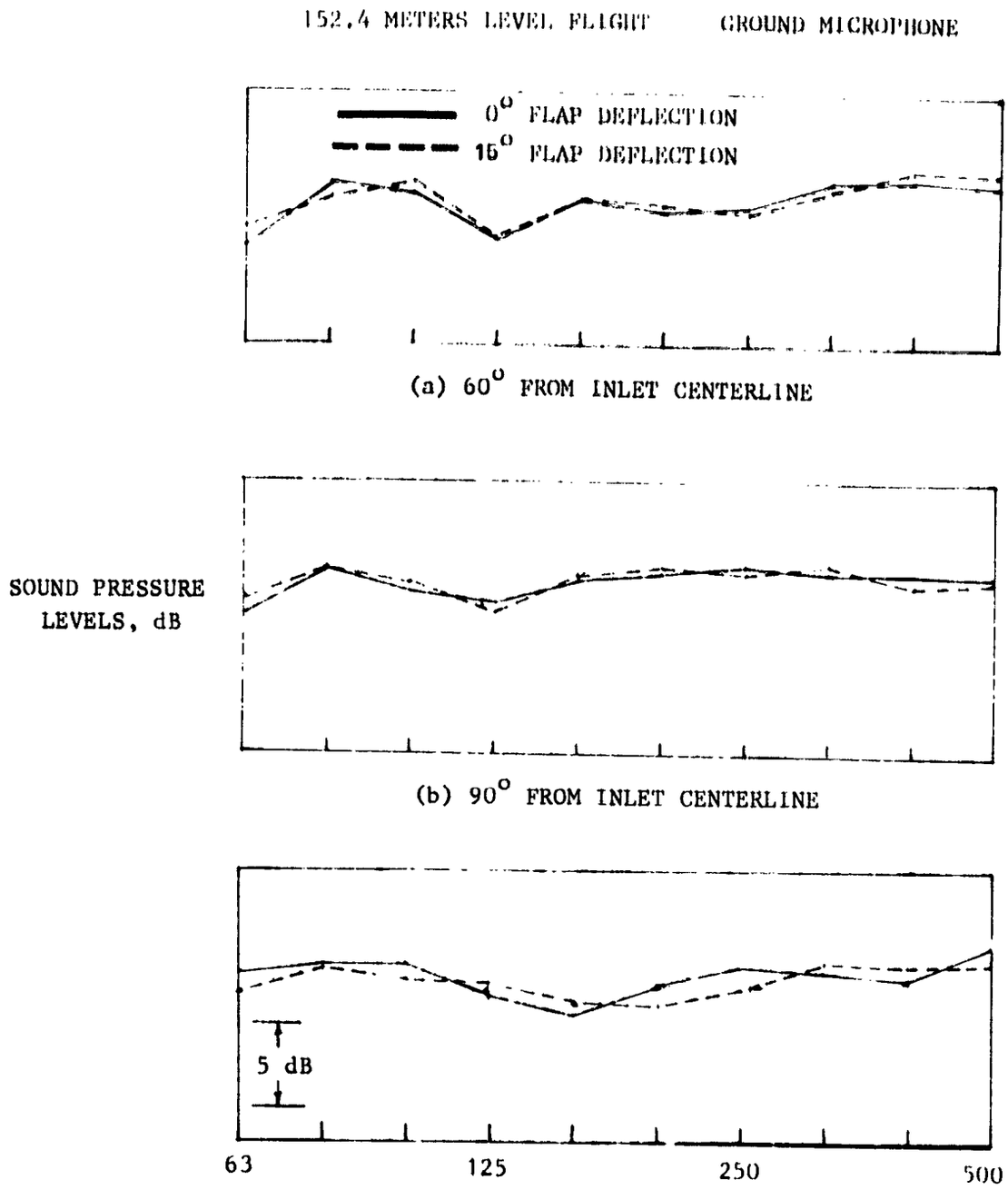

FIGURE 86. EFFECT OF FLAP SETTINGS ON DC-10-10/CF6-6D LOW-FREQUENCY FLYOVER NOISE V_{jp} = 198.1 M/SEC, V_a = 9.45 M/SEC (FLAP SETTINGS OF 0 AND 15 DEGREES)

152.4 METERS LEVEL FLIGHT GROUND MICROPHONE

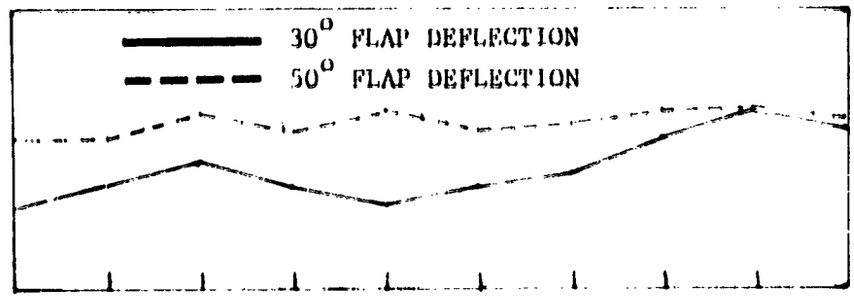

(a) 60° FROM INLET CENTERLINE

SOUND PRESSURE LEVELS

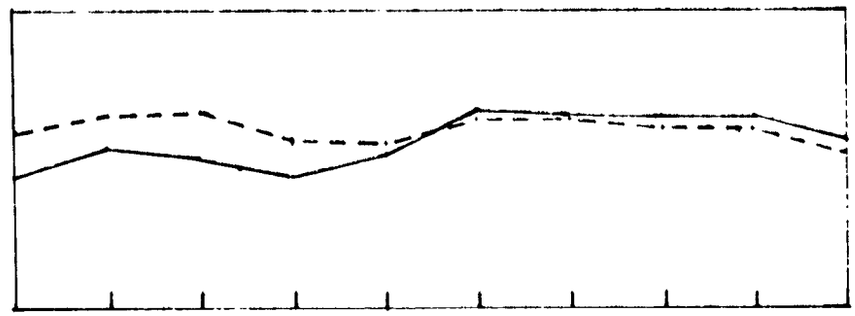

(b) 90° FROM INLET CENTERLINE

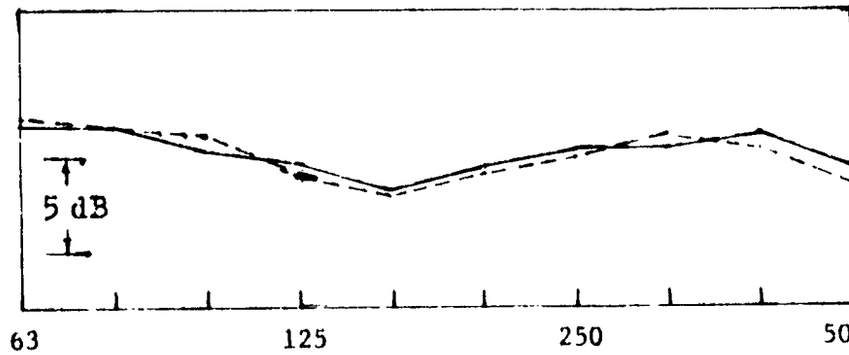

1/3-OCTAVE-BAND CENTER FREQUENCY, Hz

(c) 120° FROM INLET CENTERLINE

FIGURE 87. EFFECT OF FLAP SETTING ON DC-10-10/CF6-6D LOW-FREQUENCY FLYOVER NOISE. V_{jp} = 334.4 M/SEC, V_a = 94.5 M/SEC (FLAP SETTINGS OF 30 AND 50 DEGREES.

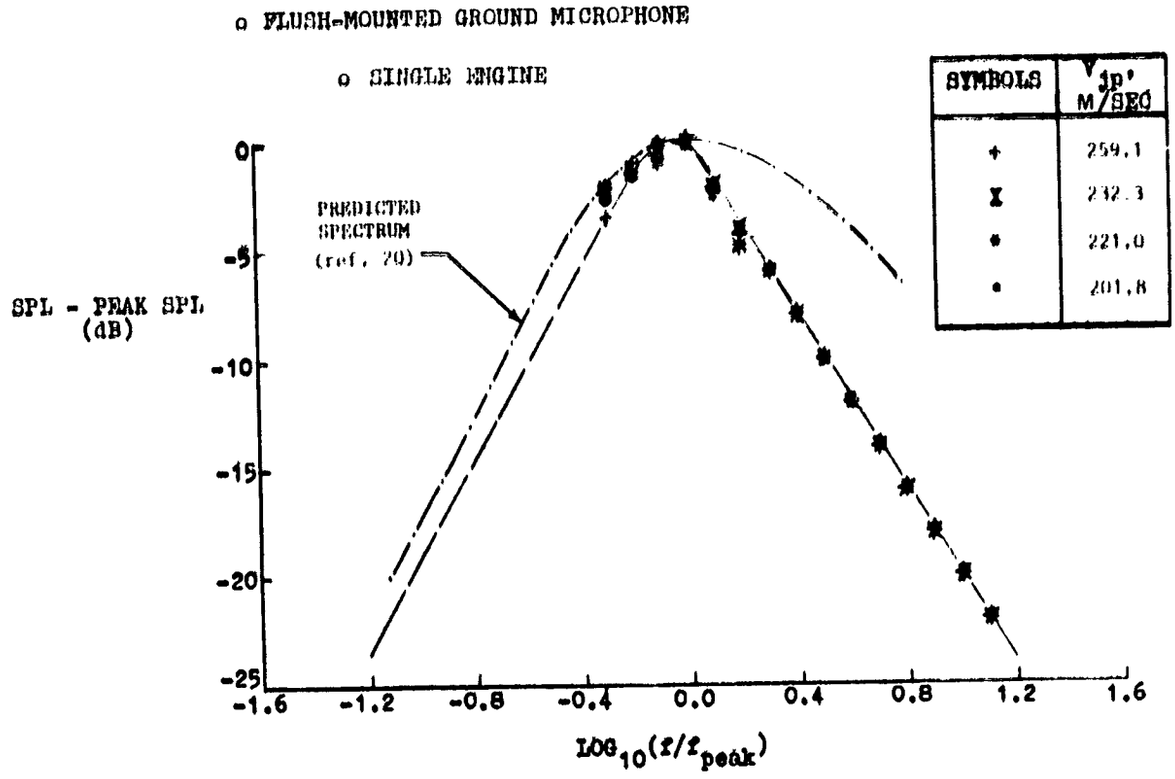

(a) DC-9-30/JT8D-109 CORE NOISE

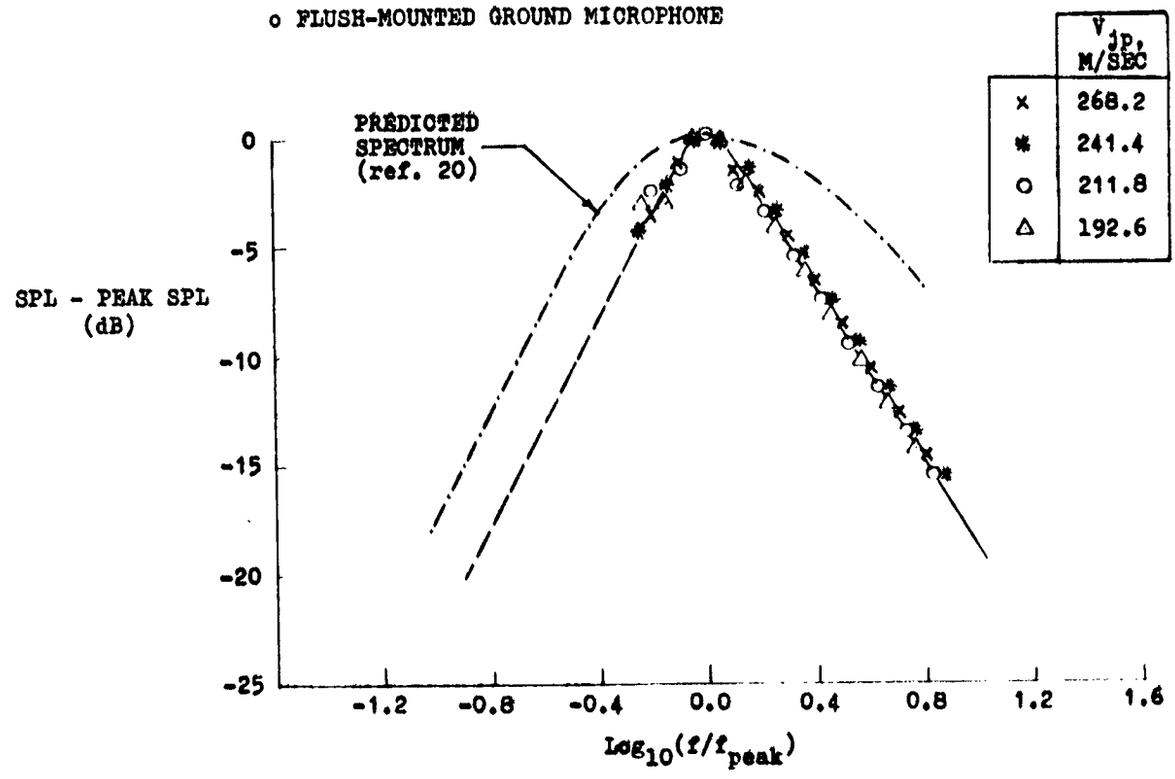

(b) DC-10-40/JT9D-59A CORE NOISE

FIGURE 88. COMPARISON OF MEASURED AND ANOPP PREDICTED CORE-NOISE SPECTRAL SHAPES FOR DC-9-30/JT8D-109 AND DC-10-40/JT9D-59A AT 45.7-METER RADIUS AND 76.2-M/SEC AIRCRAFT VELOCITY

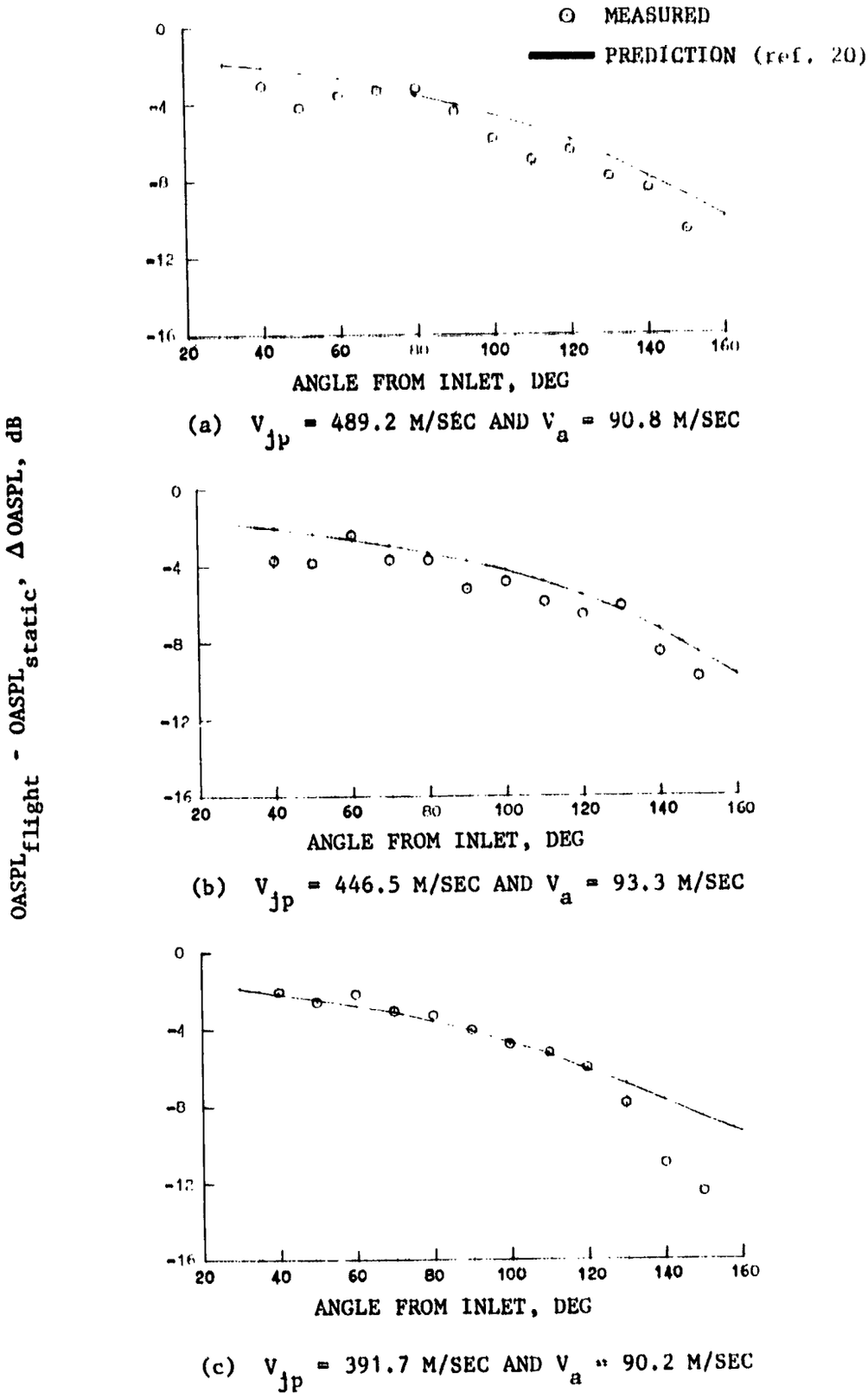

FIGURE 89. COMPARISON OF MEASURED AND ANOPP PREDICTED JET-NOISE REDUCTIONS FOR DC-9-30/JT8D-109 IN FLIGHT AT 45.7-METER RADIUS (CONTINUED)

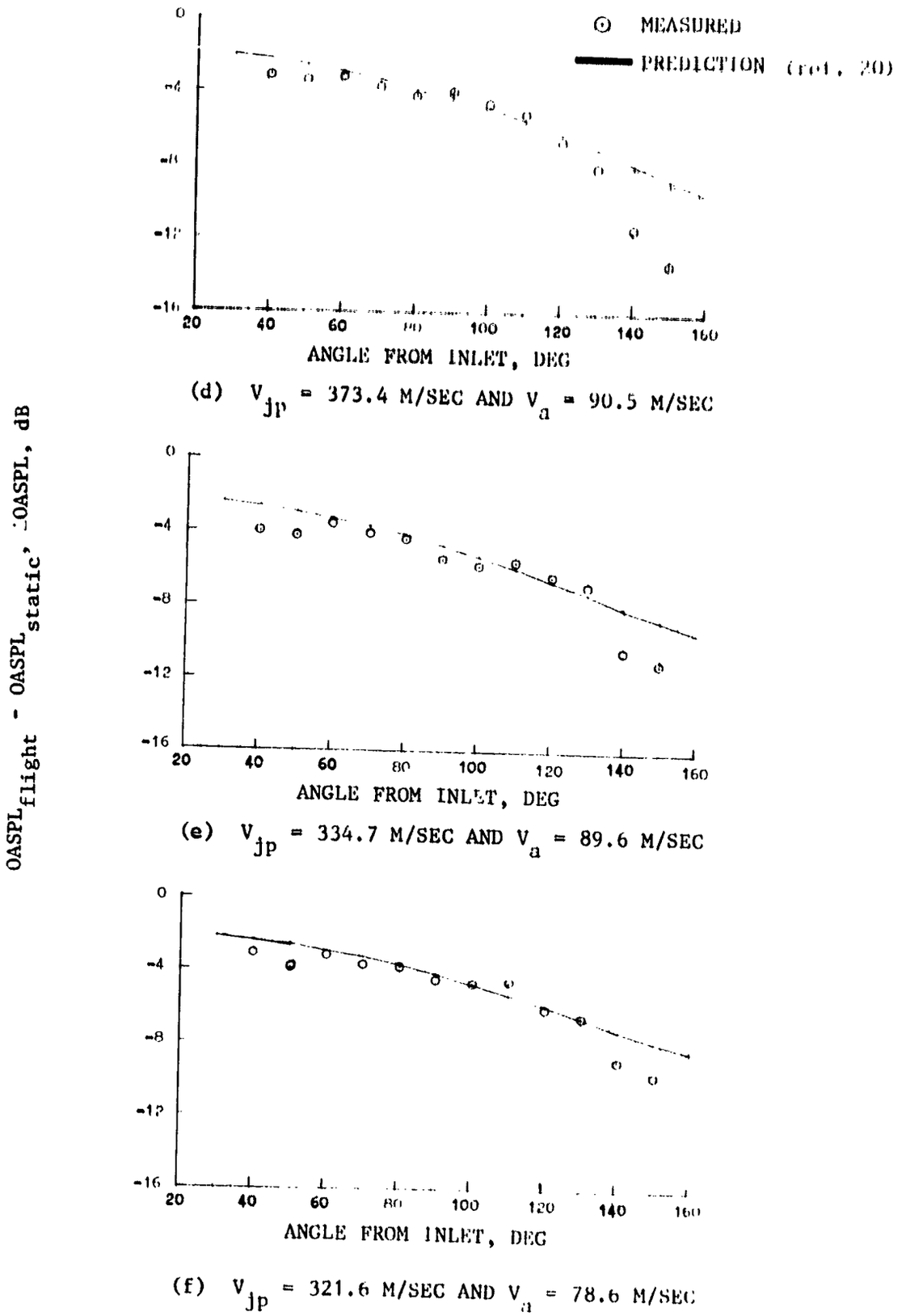

FIGURE 89. COMPARISON OF MEASURED AND ANOPP PREDICTED JET-NOISE REDUCTIONS FOR DC-9-30/JT8D-109 IN FLIGHT AT 45.7-METER RADIUS

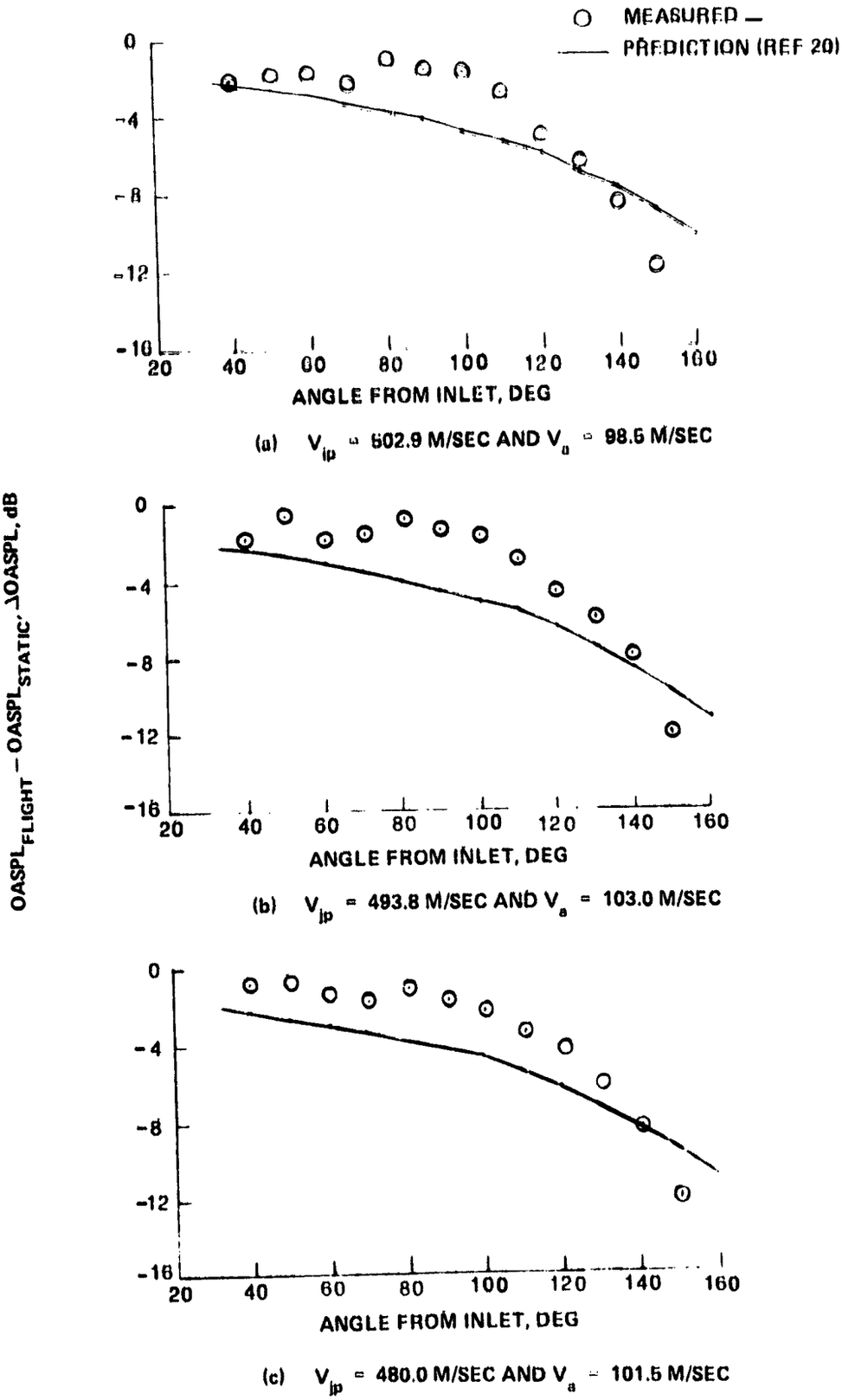

FIGURE 90. COMPARISON OF MEASURED AND ANOPP PREDICTED JET-NOISE REDUCTIONS FOR DC-10-40/JT9D-59A IN FLIGHT AT 45.7-METER RADIUS

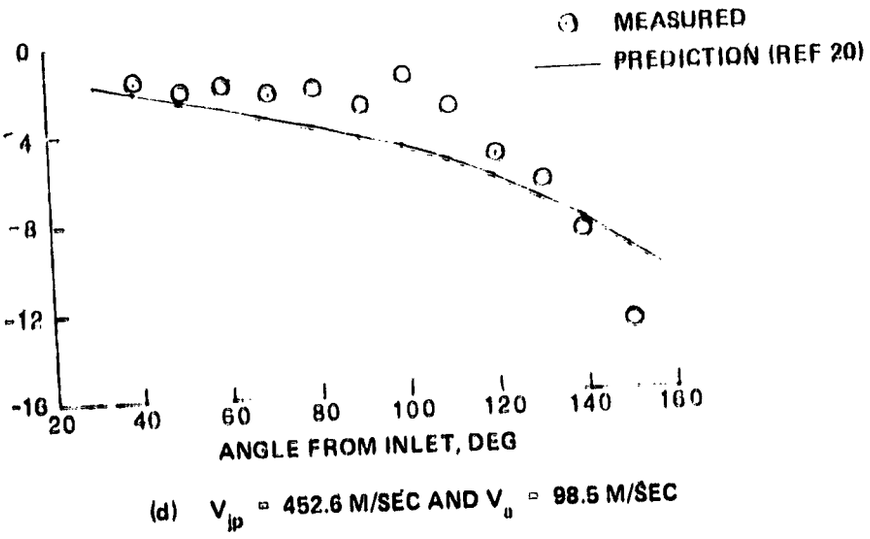

(d) V_{jp} = 452.6 M/SEC AND V_a = 98.5 M/SEC

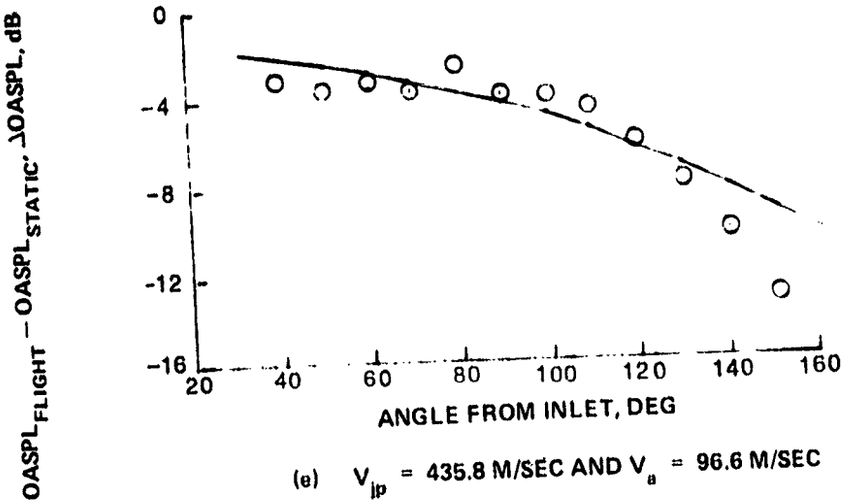

(e) V_{jp} = 435.8 M/SEC AND V_a = 96.6 M/SEC

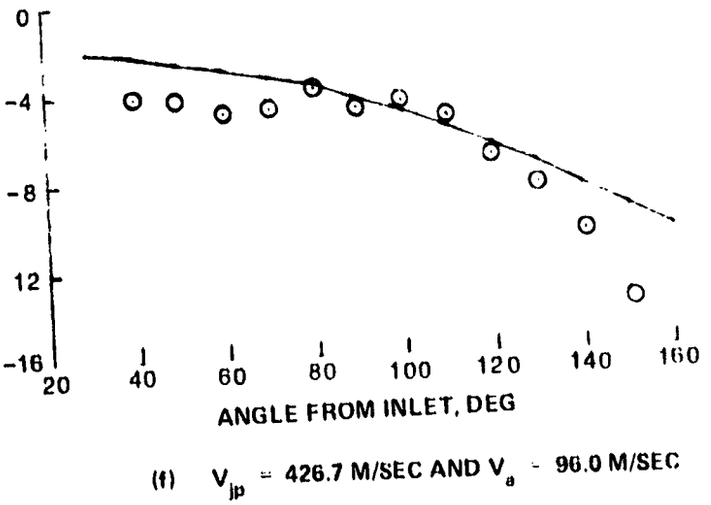

(f) V_{jp} = 426.7 M/SEC AND V_a = 96.0 M/SEC

FIGURE 90. COMPARISON OF MEASURED AND ANOPP PREDICTED JET-NOISE REDUCTIONS FOR DC-10-40/JT9D-59A IN FLIGHT AT 45.7-METER RADIUS (CONTINUED)

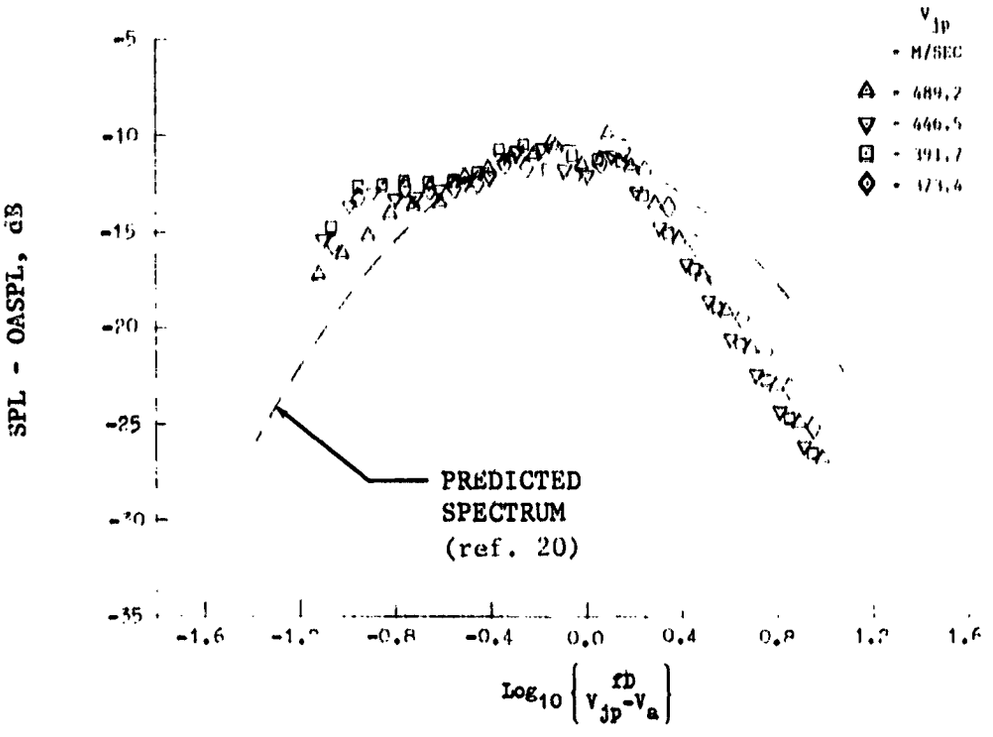

(a) 50° FROM INLET CENTERLINE

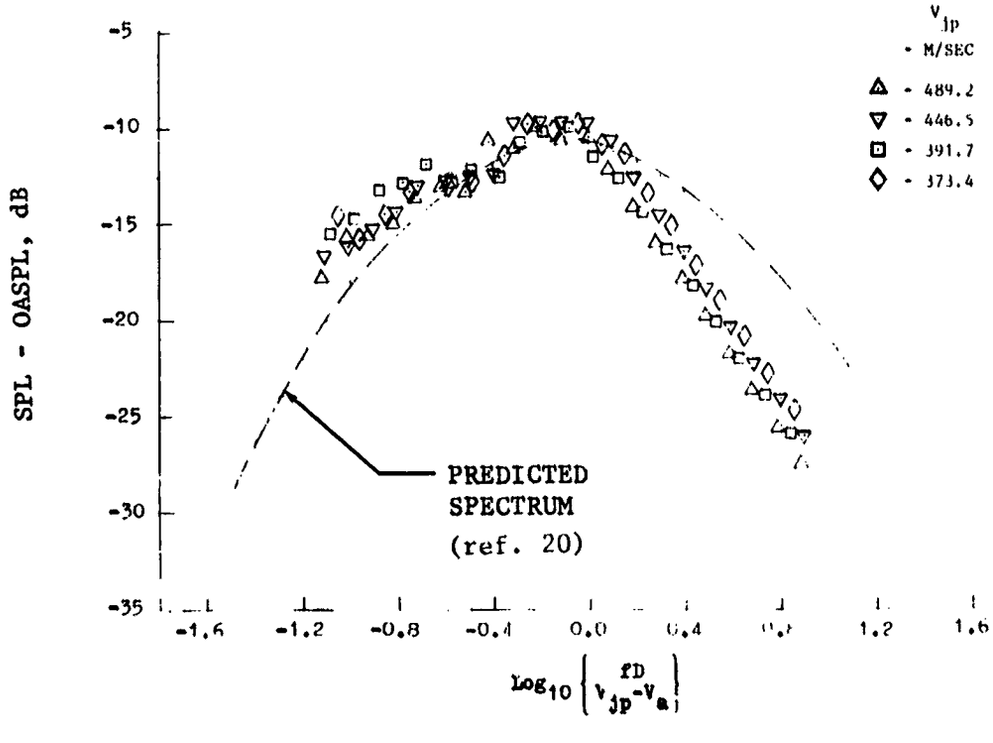

(b) 90° FROM INLET CENTERLINE

FIGURE 91. COMPARISONS OF MEASURED AND ANOPP PREDICTED JET-NOISE SPECTRAL SHAPES FOR DC-9-30/JT8D-109 AT 45.7-METER RADIUS (CONTINUED)

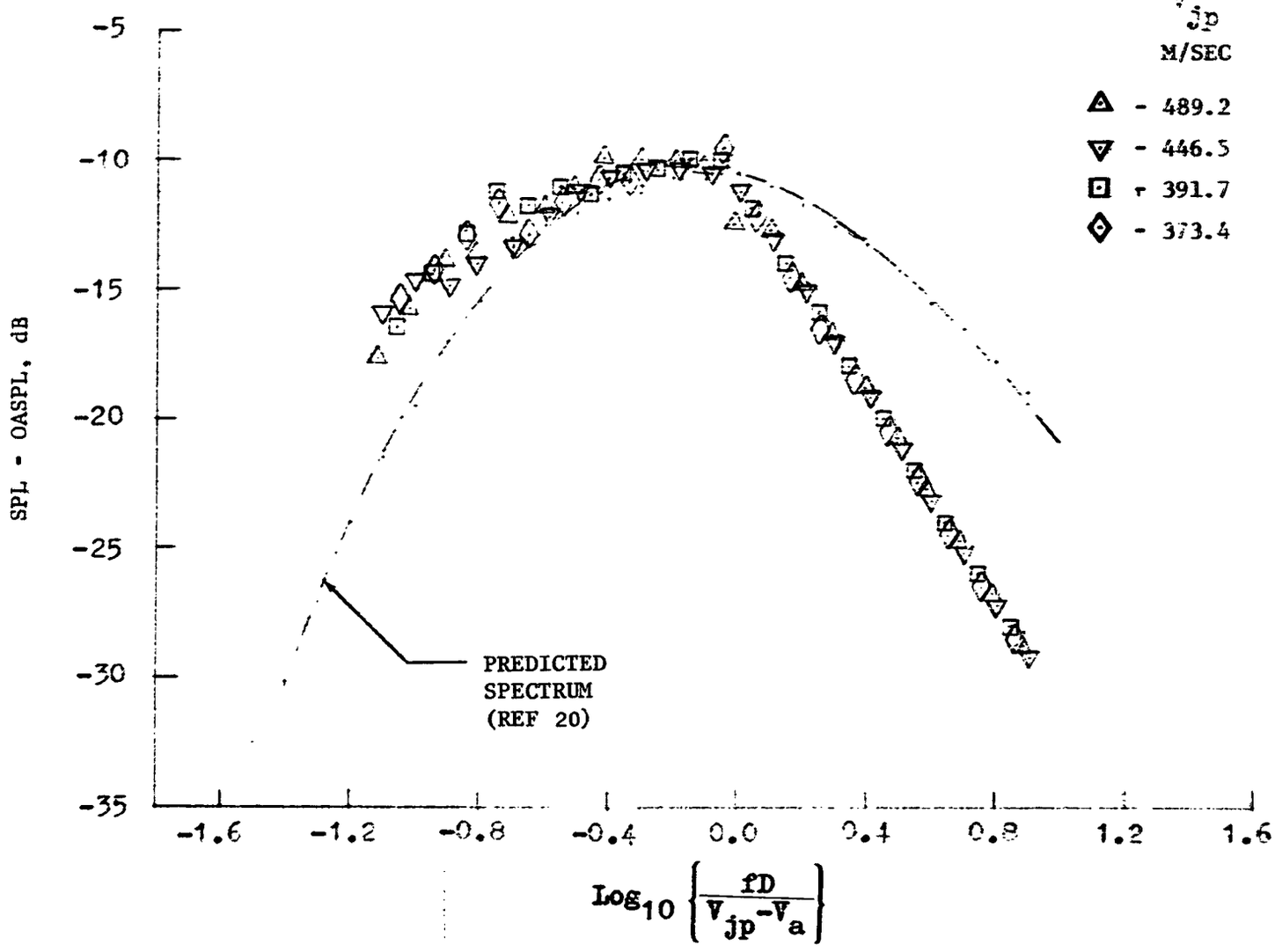

(c) 120° FROM INLET CENTERLINE

FIGURE 91. COMPARISONS OF MEASURED AND ANOPP PREDICTED JET-NOISE SPECTRAL SHAPES FOR DC-9-30/JT8D-109 AT 45.7-METER RADIUS.

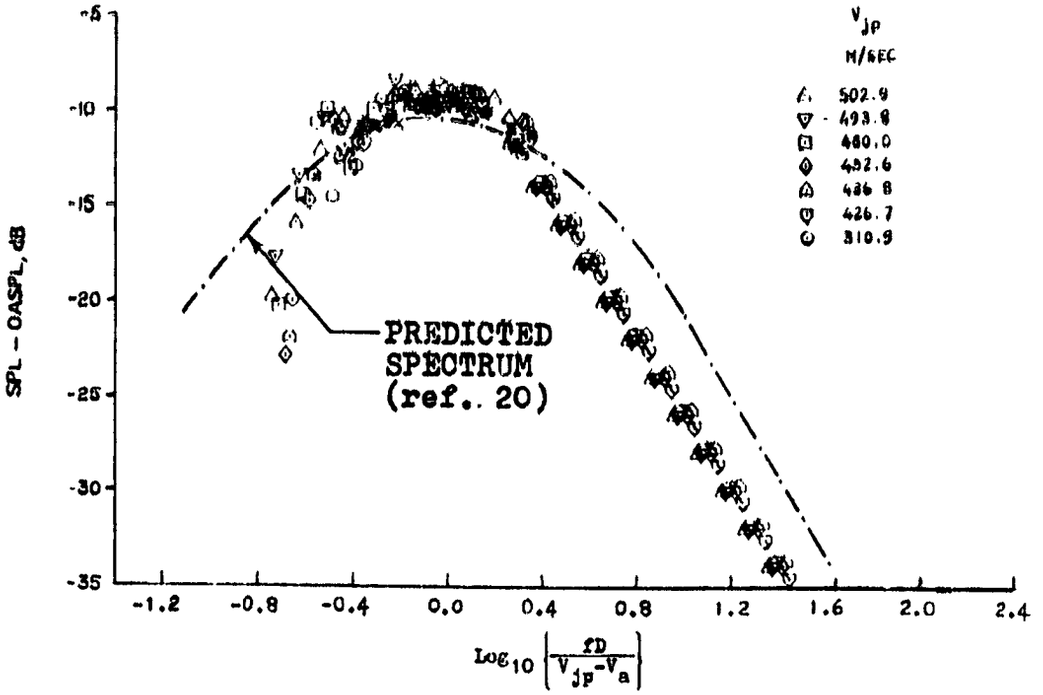

(a) 50° FROM INLET CENTERLINE

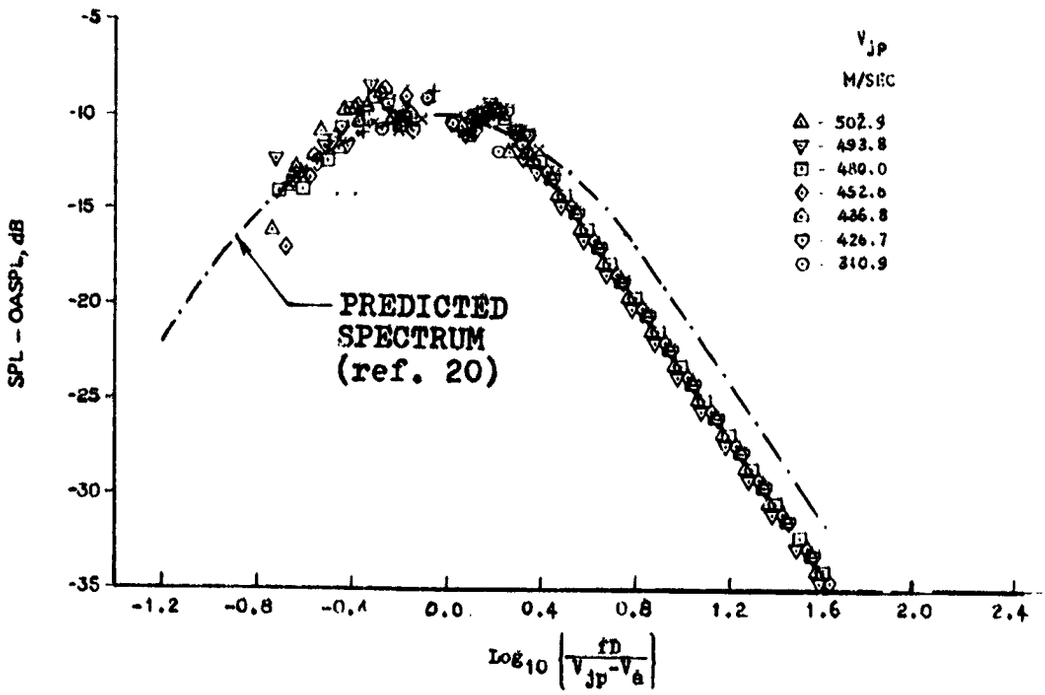

(b) 90° FROM INLET CENTERLINE

FIGURE 92. COMPARISON OF MEASURED AND ANOPP PREDICTED JET-NOISE SPECTRAL SHAPES FOR DC-10-40/JT9D-59A AT 45.7-METER RADIUS

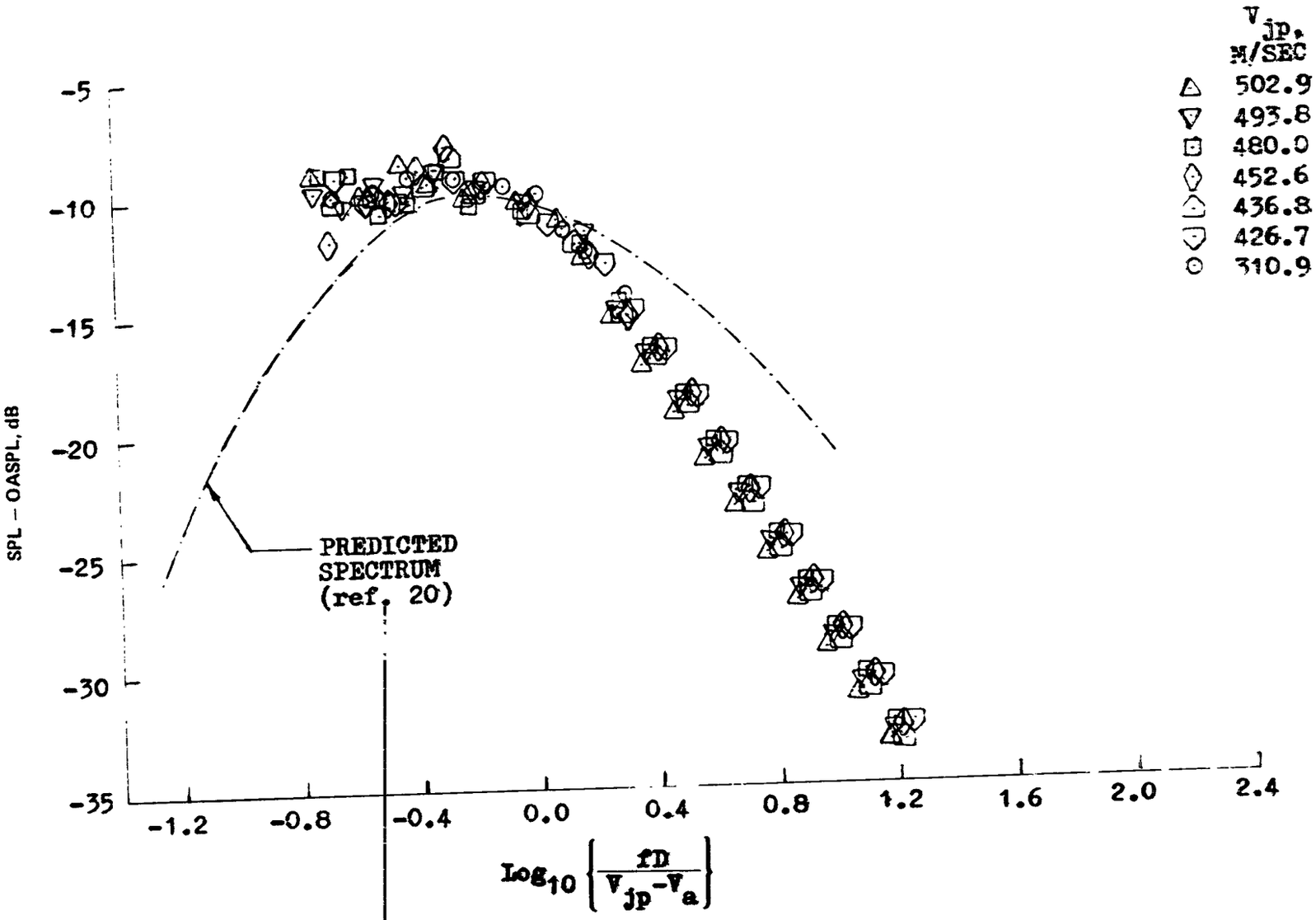

(c) 120 DEGREES FROM INLET CENTERLINE

FIGURE 92. COMPARISON OF MEASURED AND ANOPP PREDICTED JET-NOISE SPECTRAL SHAPES FOR DC-10-40/JT9D-59A AT 45.7-METER RADIUS

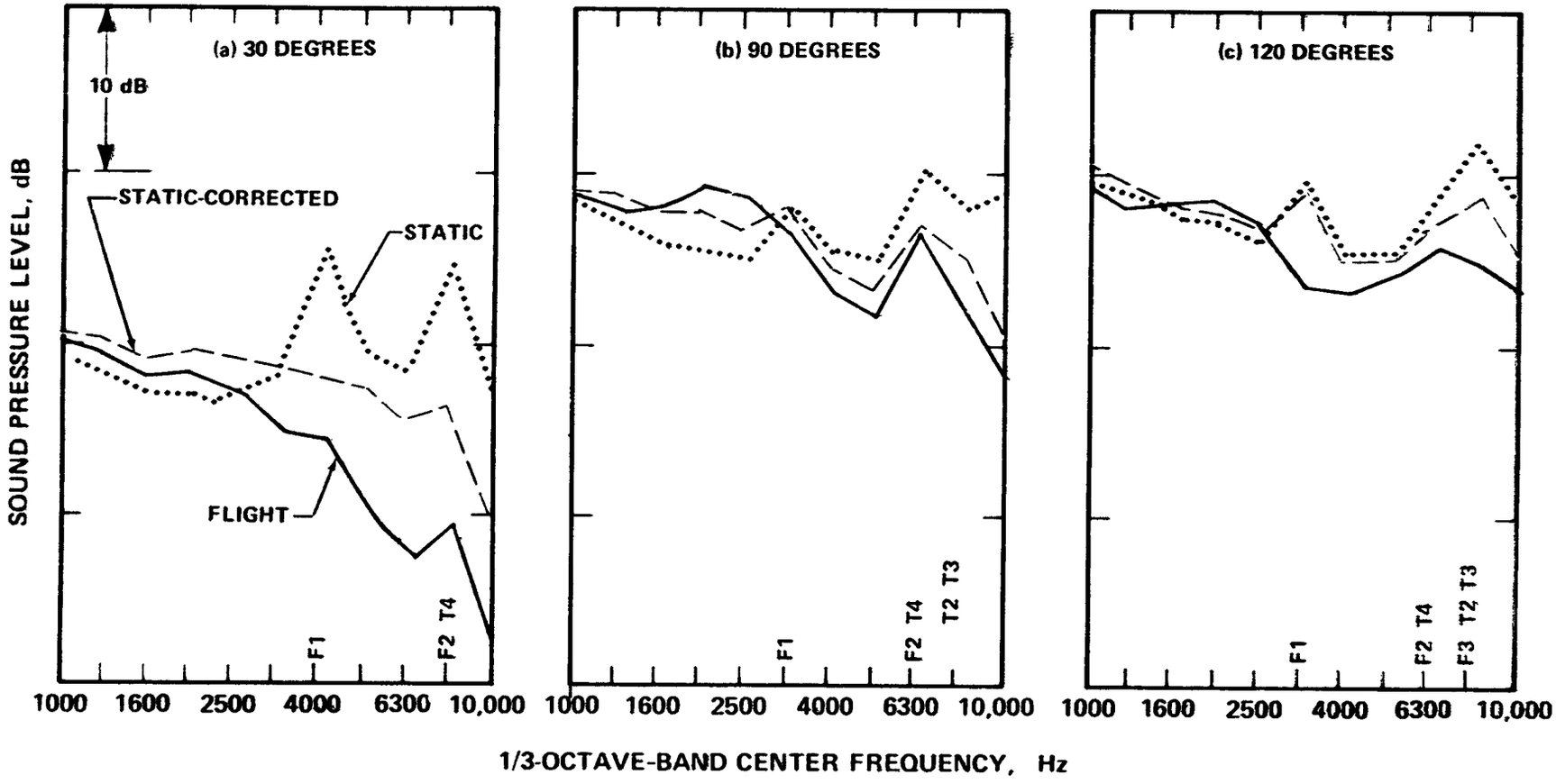

FIGURE 93. COMPARISON OF DC-9-30 FLIGHT AND JT8D-109 STATIC-PROJECTED SPL SPECTRA CORRECTED FOR ENGINE INSTALLATION EFFECTS DURING A 112.8-METER (370-FOOT) FLYOVER. CORRECTED FAN ROTOR SPEED = 5456 RPM

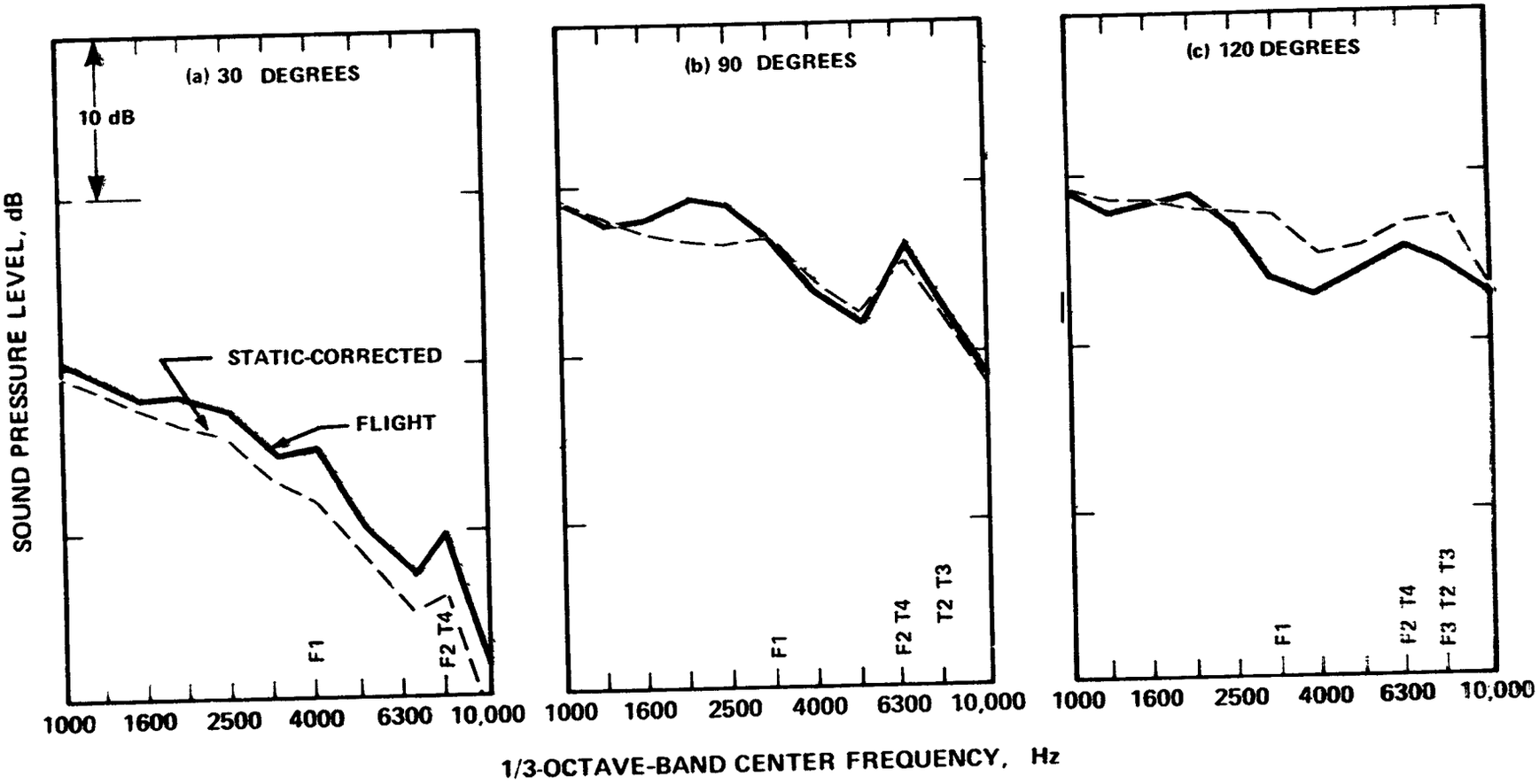

FIGURE 94. COMPARISON OF DC-9-30 FLIGHT AND JT8D-109 STATIC-PROJECTED SPL SPECTRA CORRECTED FOR INSTALLATION AND PROPAGATION EFFECTS DURING A 112.8-METER (370-FOOT) FLYOVER. CORRECTED FAN ROTOR SPEED = 5456.0 RPM

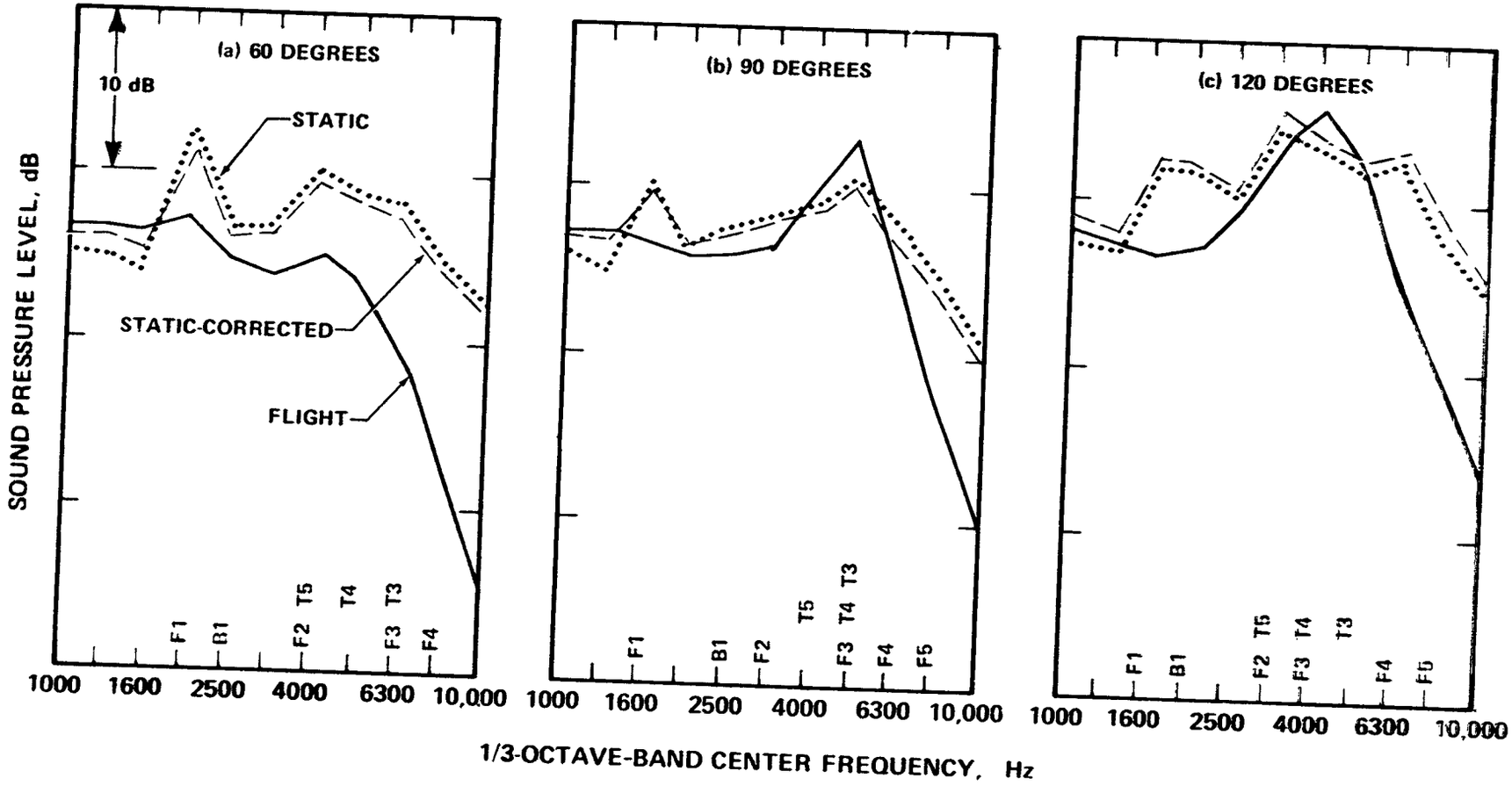

FIGURE 95. COMPARISON OF DC-10-10 FLIGHT AND CF6-6D STATIC-PROJECTED SPL SPECTRA CORRECTED FOR ENGINE INSTALLATION EFFECTS DURING A 152.4-METER (500-FOOT) LEVEL FLYOVER. CORRECTED FAN ROTOR SPEED = 2467.0 RPM

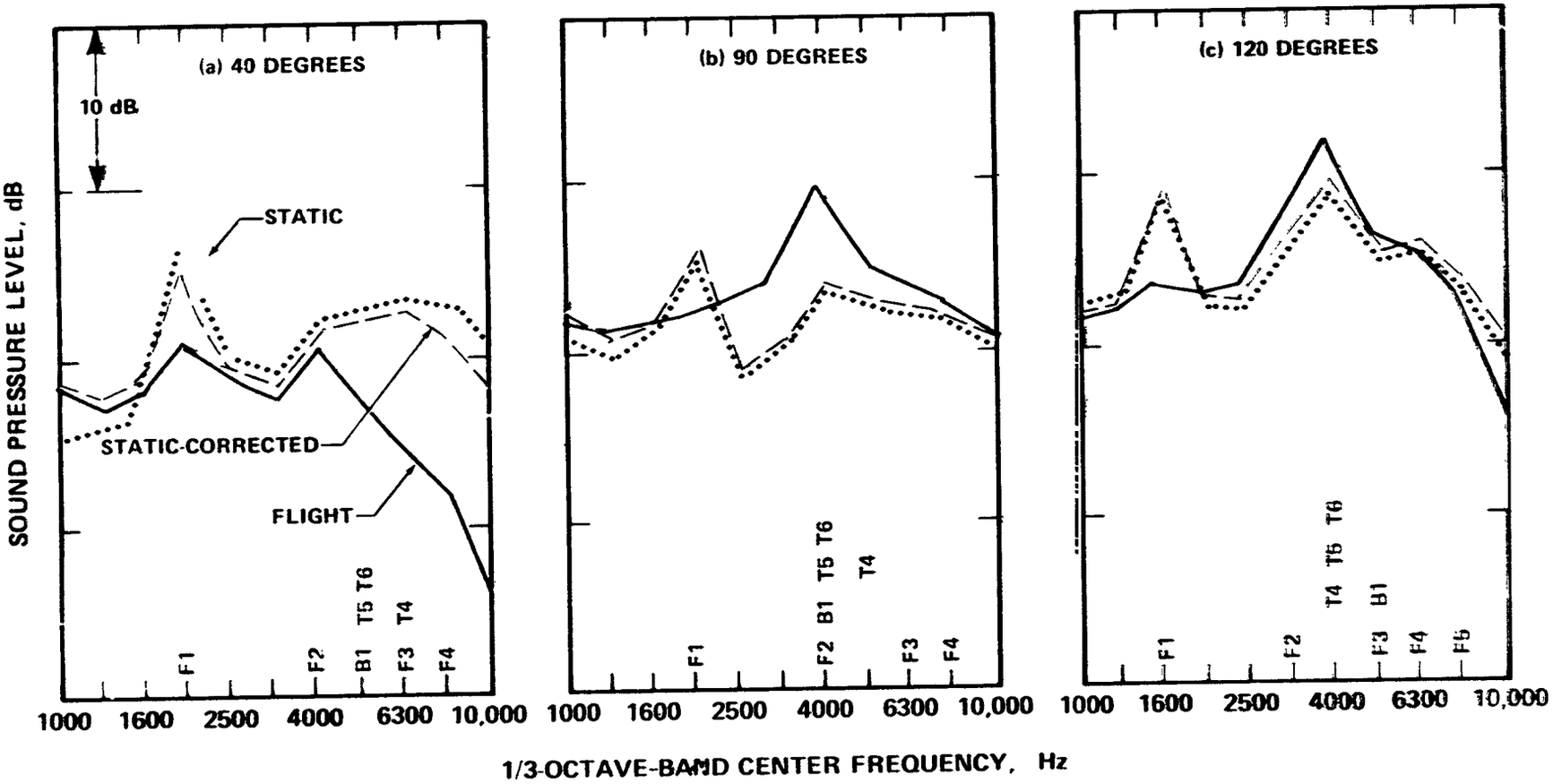

FIGURE 96. COMPARISON OF DC-10-40 FLIGHT AND JT9D-59A STATIC-PROJECTED SPL SPECTRA CORRECTED FOR ENGINE INSTALLATION EFFECTS DURING A 120.4-METER (395-FOOT) FLYOVER. CORRECTED FAN ROTOR SPEED = 2364.0 RPM

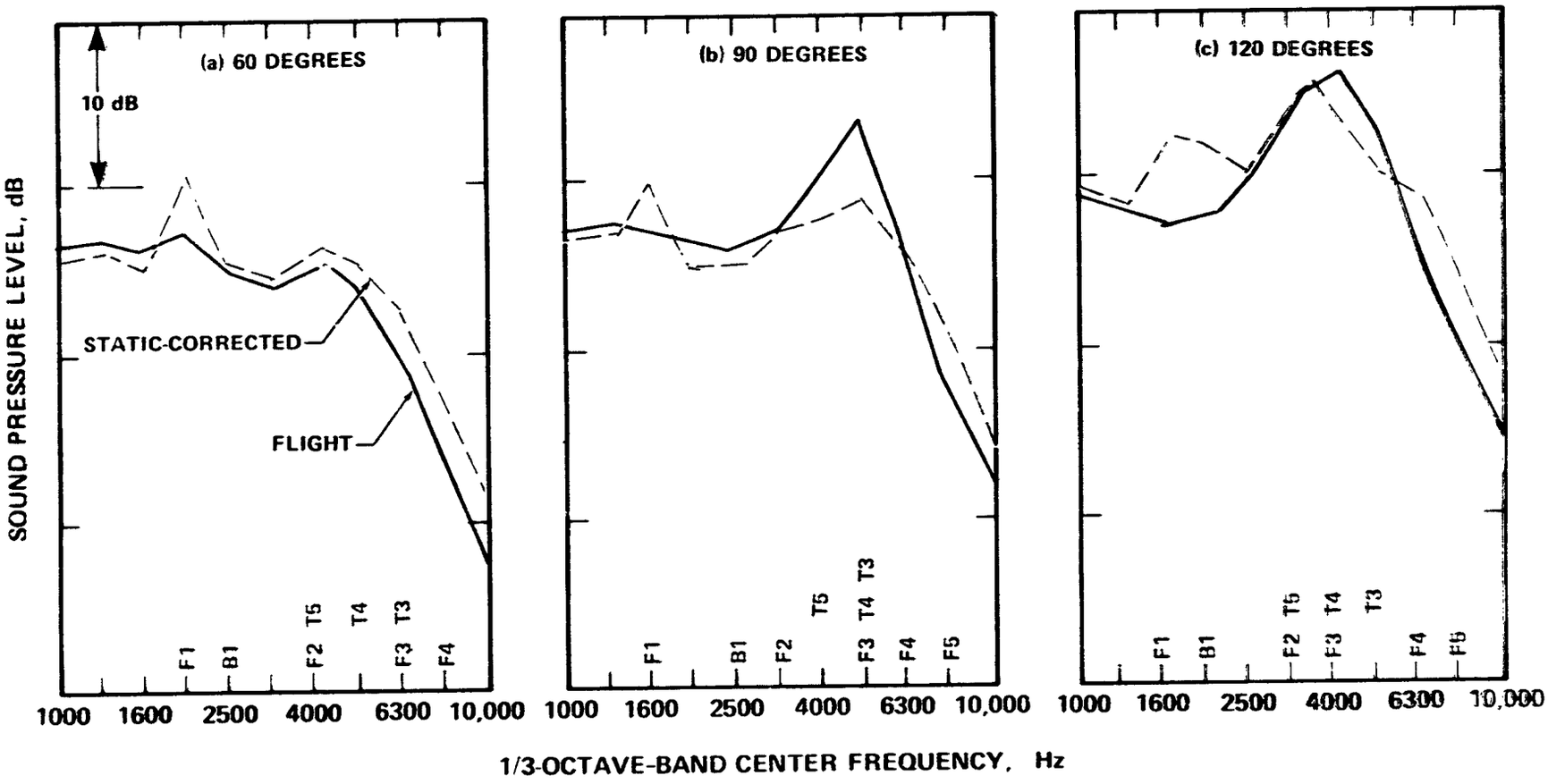

FIGURE 97. COMPARISON OF DC-10-10 FLIGHT AND CF6-6D STATIC-PROJECTED SPL SPECTRA CORRECTED FOR INSTALLATION AND PROPAGATION EFFECTS DURING A 152.4-METER (500-FOOT) LEVEL FLYOVER. CORRECTED FAN ROTOR SPEED = 2467.0 RPM.

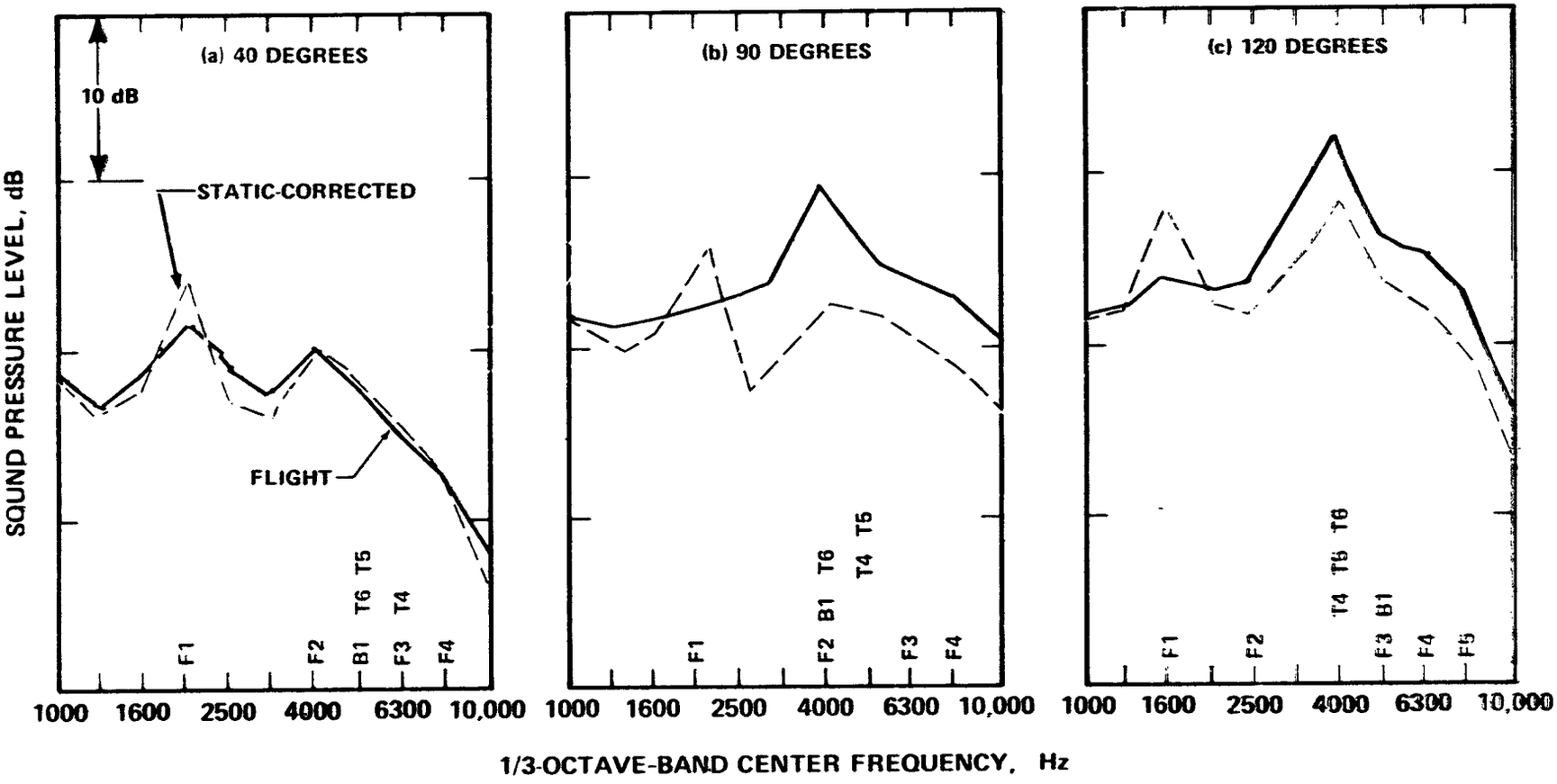

FIGURE 98. COMPARISON OF DC-10-40 FLIGHT AND JT9D-59A STATIC-PROJECTED SPL SPECTRA CORRECTED FOR INSTALLATION AND PROPAGATION EFFECTS DURING A 120.4-METER (395-FOOT) LEVEL FLYOVER. CORRECTED FAN ROTOR SPEED = 2364.0 RPM

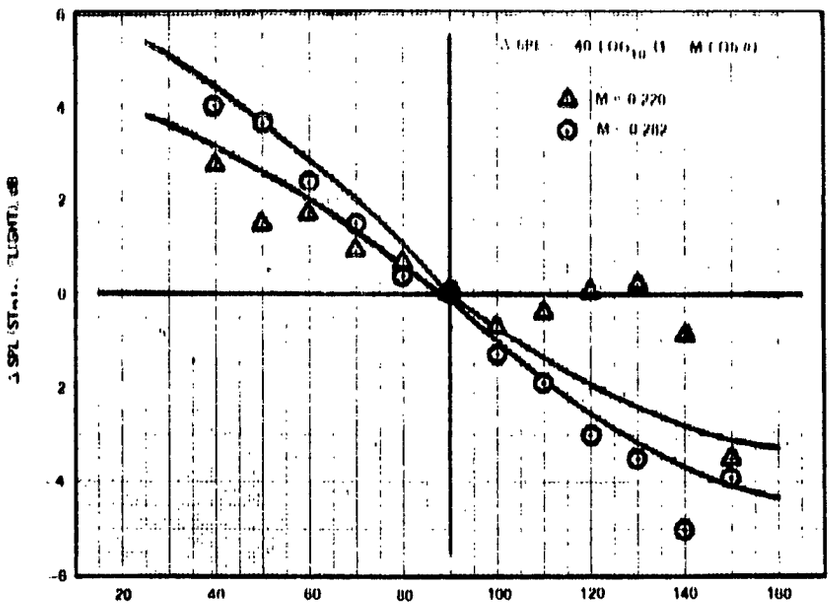

(a) DC-10-40/JT9D-59A

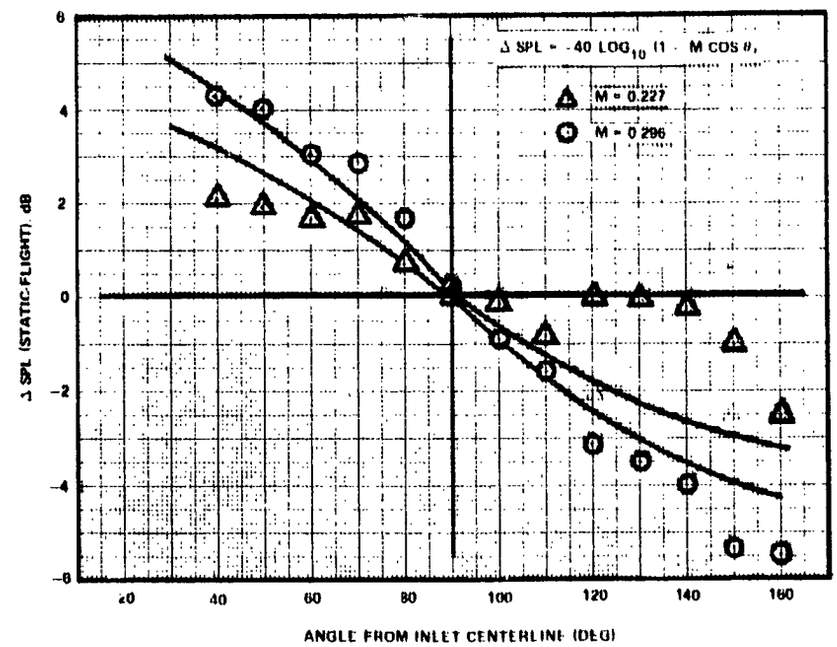

(b) DC-10-10/CF6-6D

FIGURE 99. COMPARISON OF THE EFFECTS OF FORWARD MOTION ON FAN BROADBAND NOISE LEVELS WITH PREDICTED EFFECTS OF CONVECTIVE AMPLIFICATION

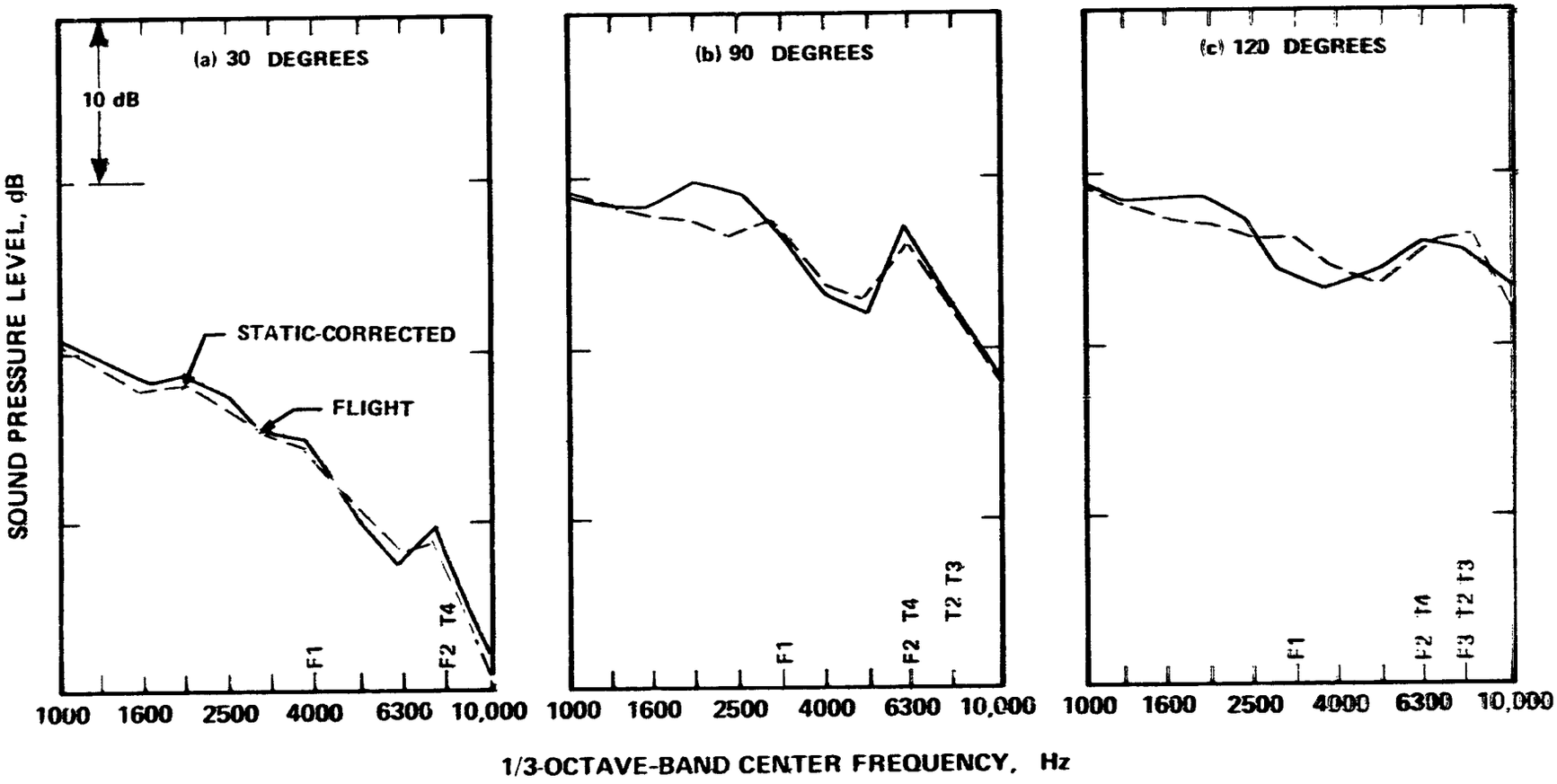

FIGURE 100. COMPARISON OF DC-9-30 FLIGHT AND JT8D-109 STATIC-PROJECTED SPL SPECTRA CORRECTED FOR INSTALLATION, PROPAGATION, AND CONVECTION EFFECTS DURING A 112.8-METER (370-FOOT) FLYOVER. CORRECTED FAN ROTOR SPEED = 5456.0 RPM

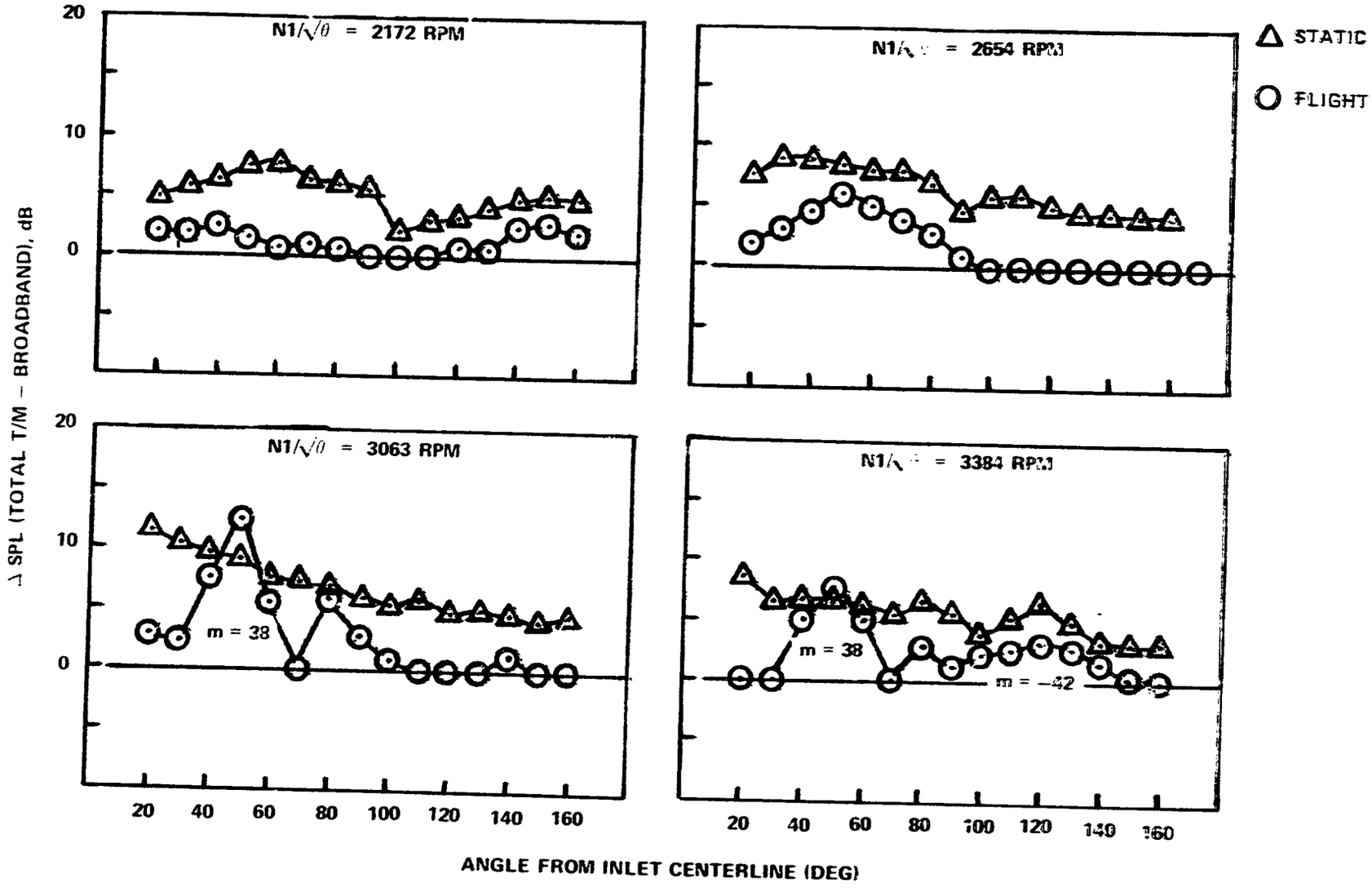

FIGURE 101. COMPARISON OF DC-10-10 FLIGHT AND CF6-6D STATIC-CORRECTED LEVELS OF THE FAN FUNDAMENTAL TONE

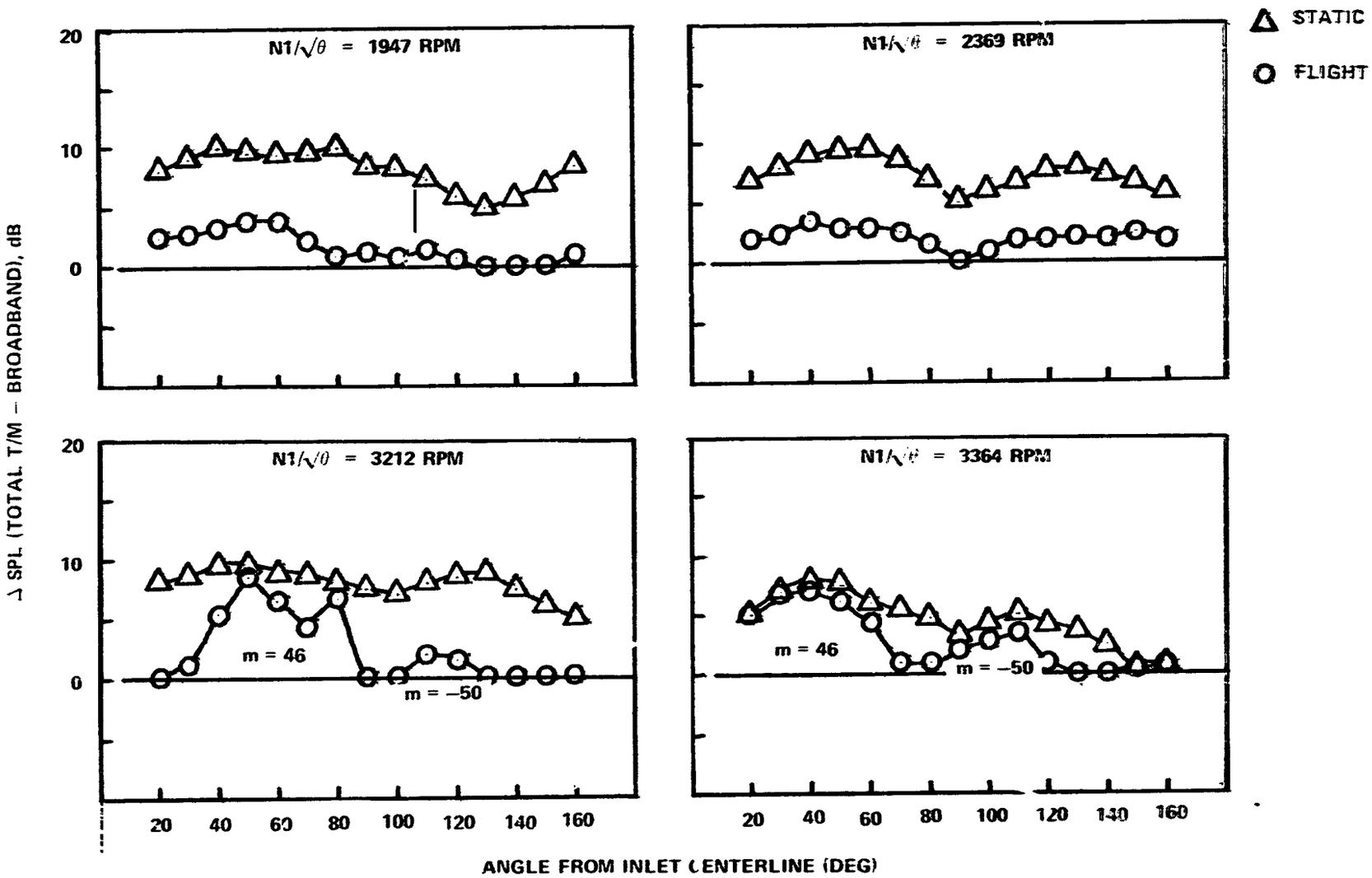

FIGURE 102. COMPARISON OF DC-10-40 FLIGHT AND JT9D-59A STATIC-CORRECTED LEVELS OF THE FAN FUNDAMENTAL TONE

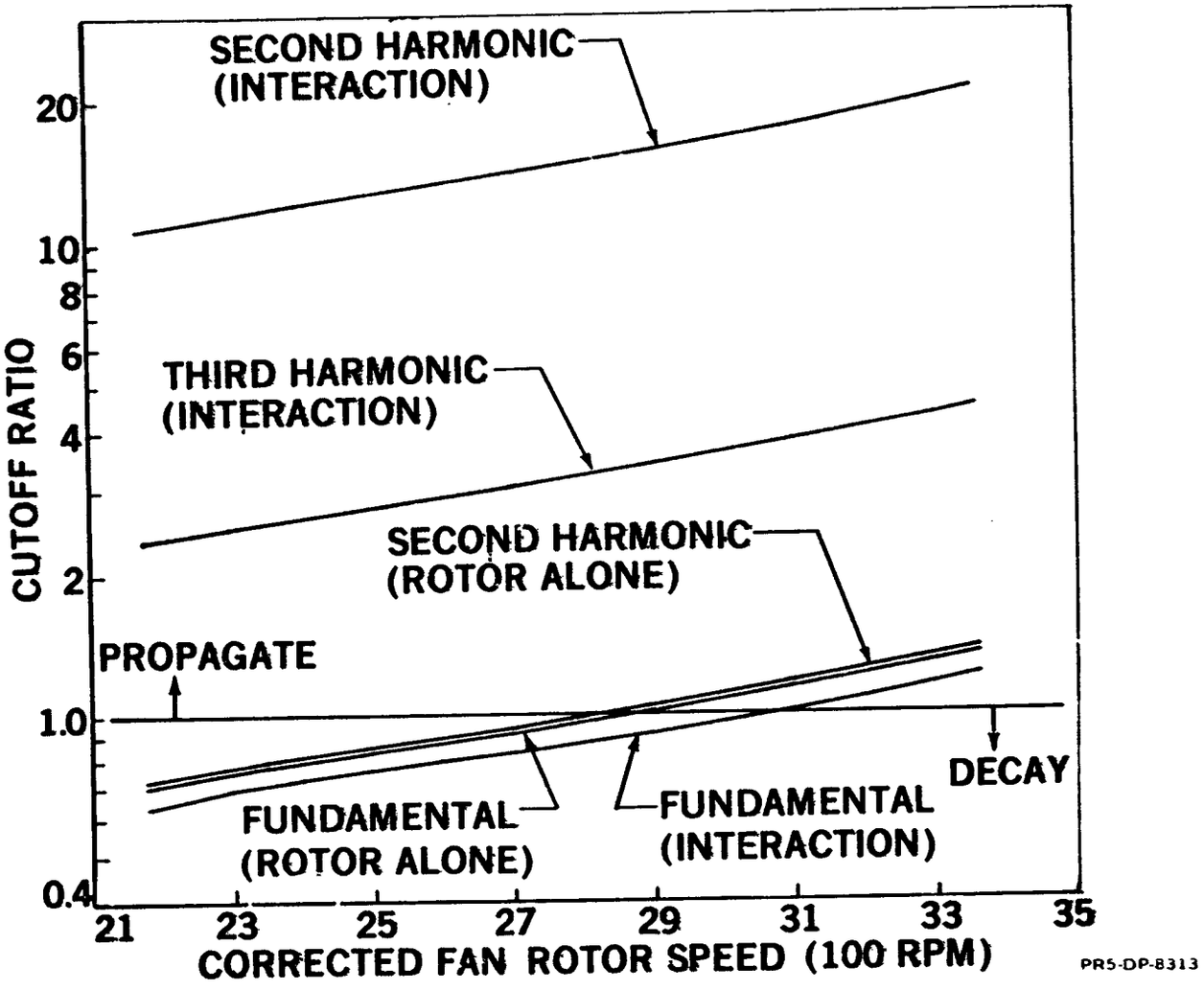

FIGURE 103. VARIATION OF CUTOFF RATIO WITH ROTOR SPEED FOR CF6-6D FAN TONES

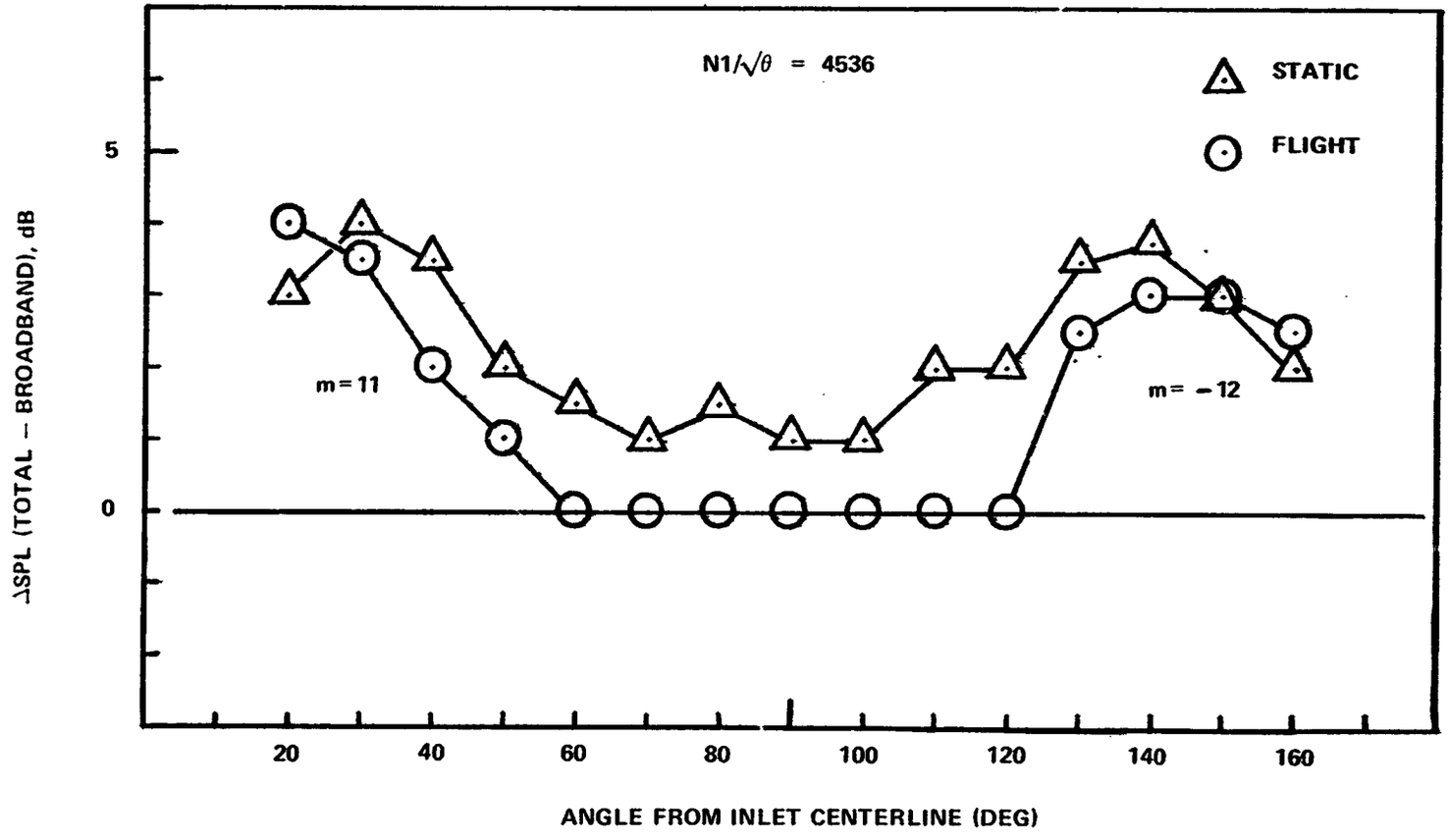

FIGURE 104. COMPARISON OF DC-9-30 FLIGHT AND JT8D-109 STATIC-CORRECTED LEVELS OF THE FAN FUNDAMENTAL TONE

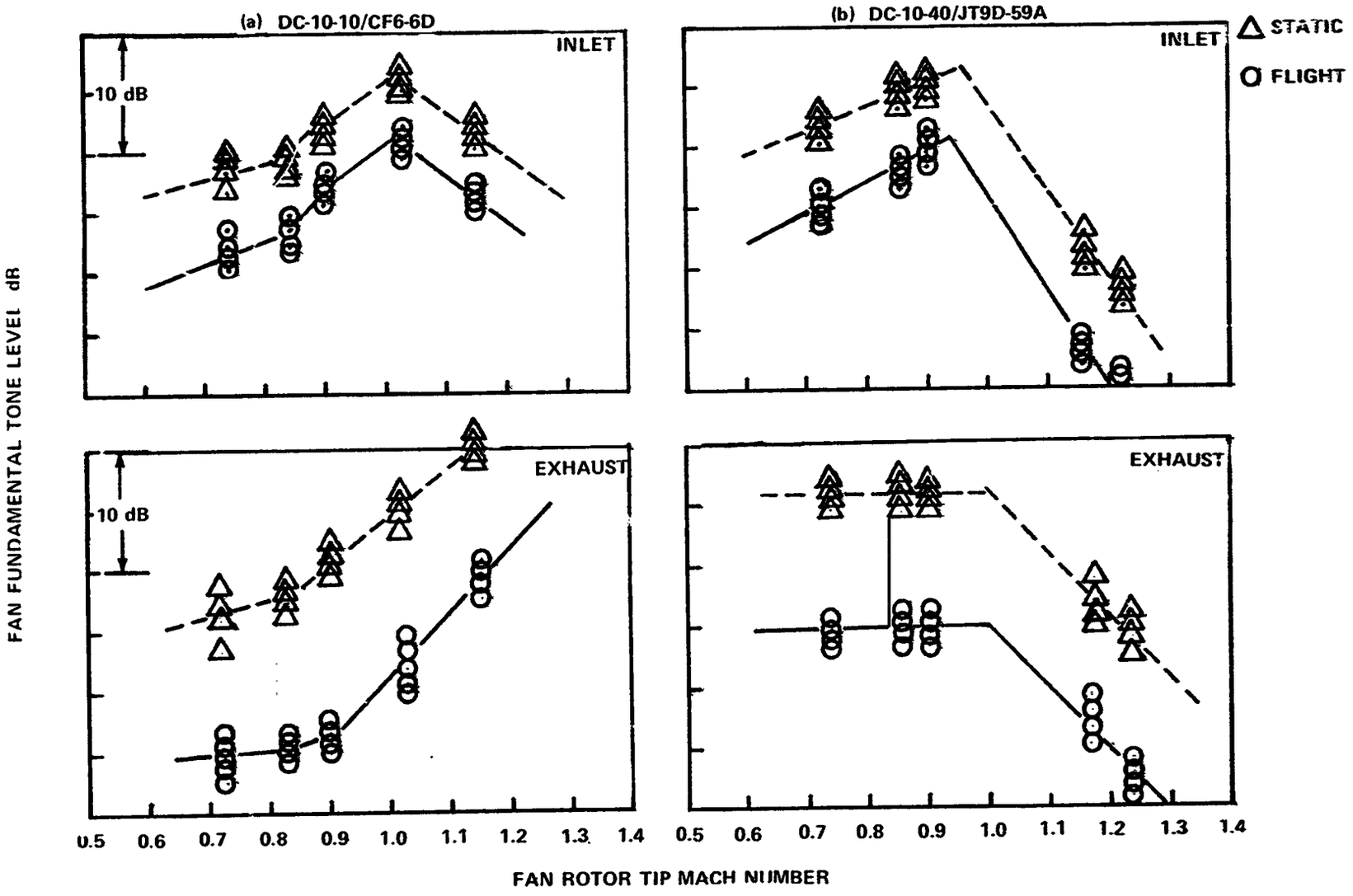

FIGURE 105. VARIATION IN THE FLYOVER AND STATIC-TURBULENCE-GENERATED LEVELS OF THE FAN FUNDAMENTAL TONE WITH FAN ROTOR TIP MACH NUMBER.

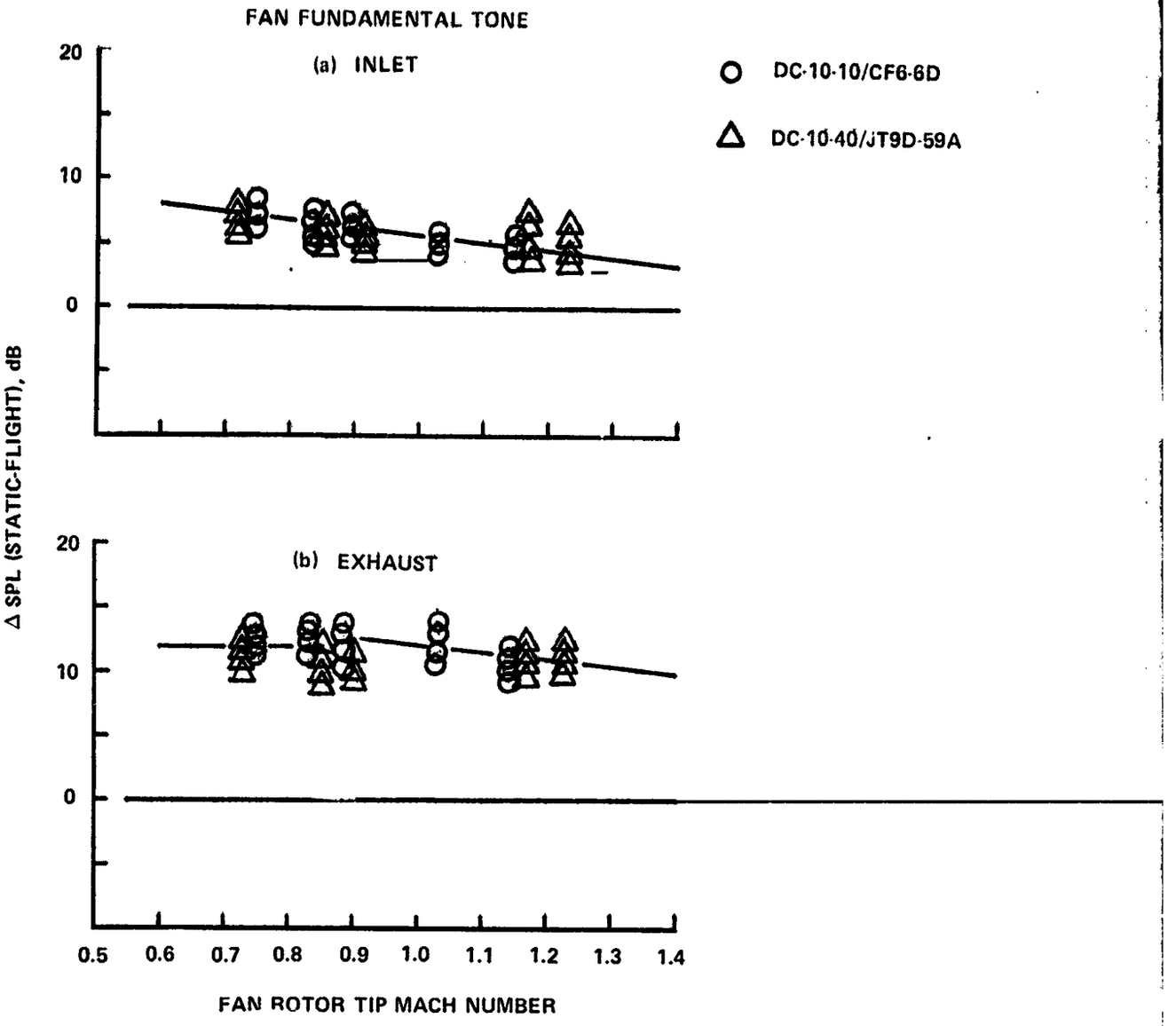

FIGURE 106. STATIC-TO-FLIGHT CORRECTION FOR THE EFFECTS OF NOISE GENERATION ON FAN FUNDAMENTAL TONE FOR DC-10-10/CF6-6D AND DC-10-40/JT9D-59A AIRPLANE CONFIGURATIONS

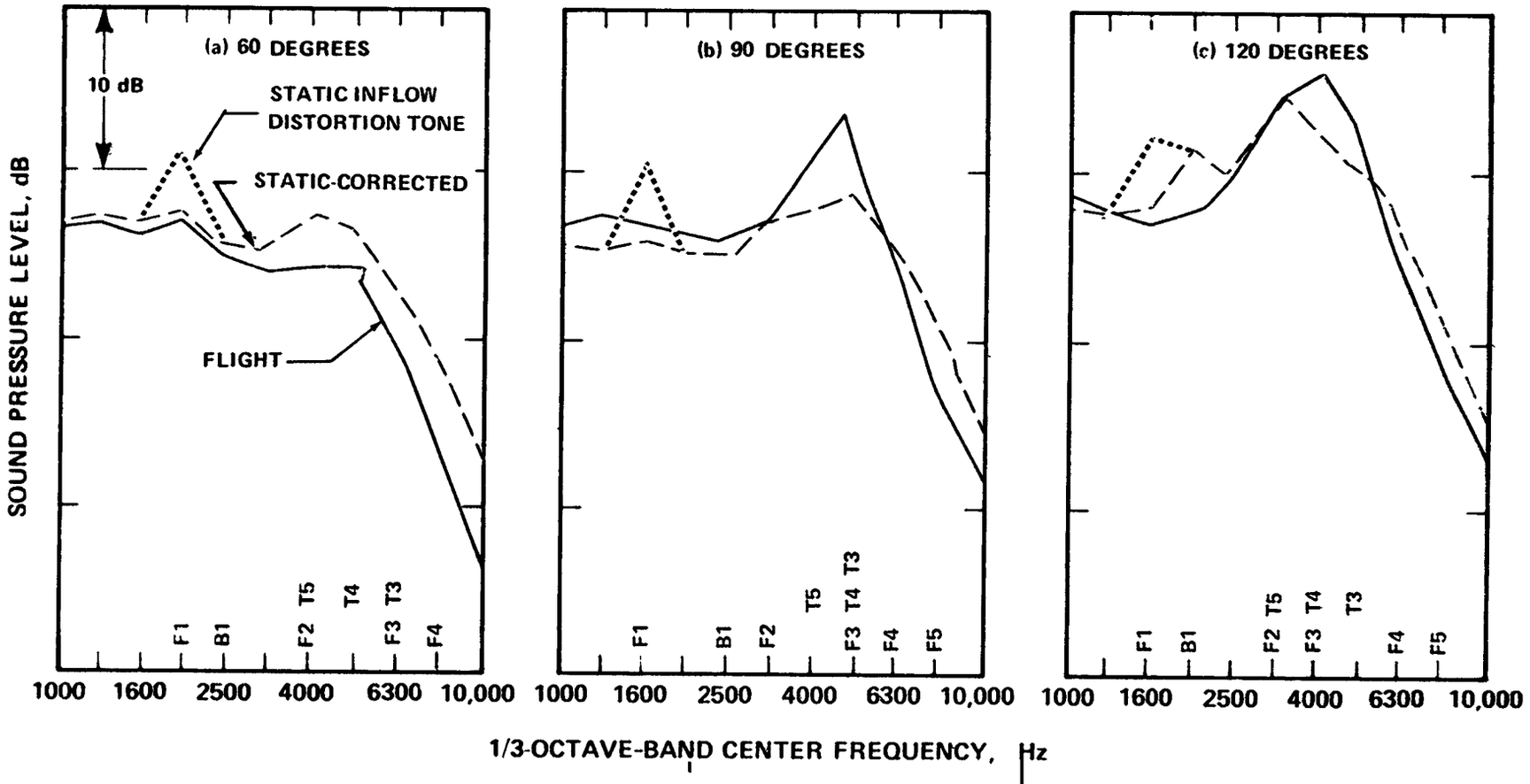

FIGURE 107. COMPARISON OF DC-10-10 FLIGHT AND CF6-6D STATIC-CORRECTED SPL SPECTRA CORRECTED FOR NOISE GENERATION ON THE FAN FUNDAMENTAL TONE AND CONVECTION DURING A 152.4-METER (500-FOOT) LEVEL FLYOVER. CORRECTED FAN ROTOR SPEED = 2467.0 RPM.

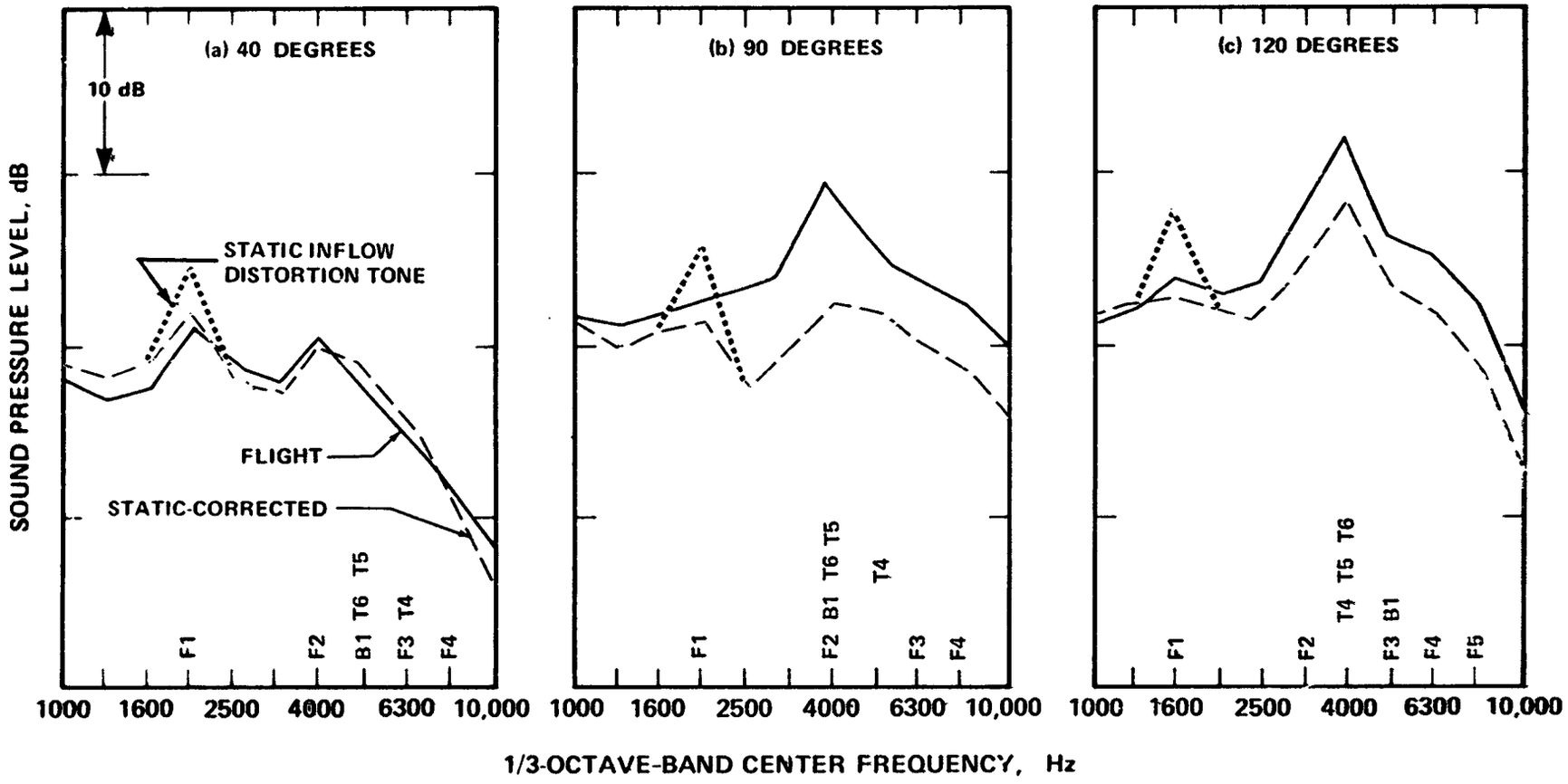

FIGURE 108. COMPARISON OF DC-10-40 FLIGHT AND JT9D-59A STATIC-CORRECTED SPL SPECTRA CORRECTED FOR NOISE GENERATION ON THE FAN FUNDAMENTAL TONE AND CONVECTION DURING A 120.4-METER (395-FOOT) FLYOVER. CORRECTED FAN ROTOR SPEED = 2364.0 RPM.

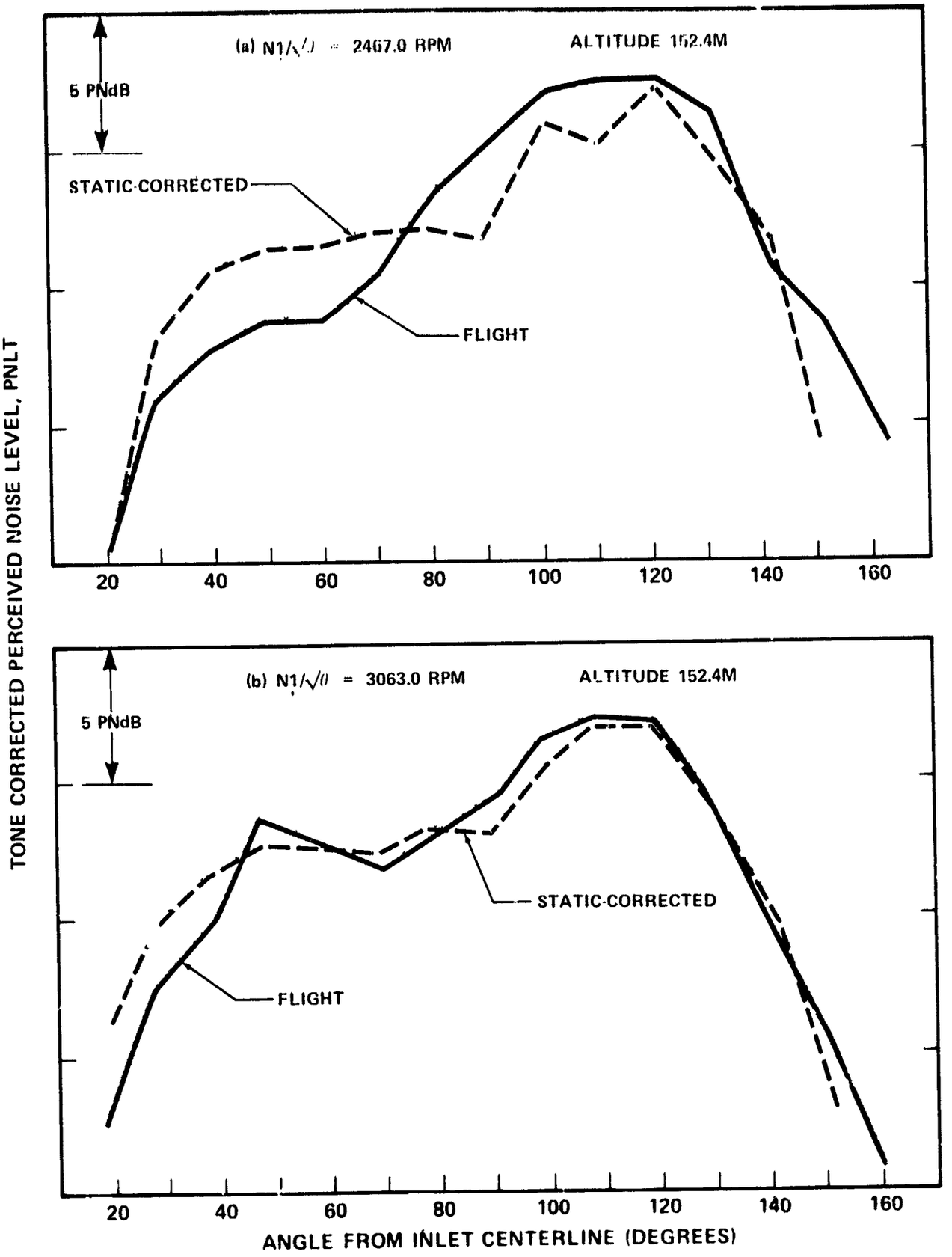

FIGURE 109. COMPARISON OF DC-10-10 FLIGHT AND CF6-6D STATIC-CORRECTED PNLT'S CORRECTED FOR THE EFFECTS OF FORWARD MOTION, PROPAGATION, AND ENGINE INSTALLATION.

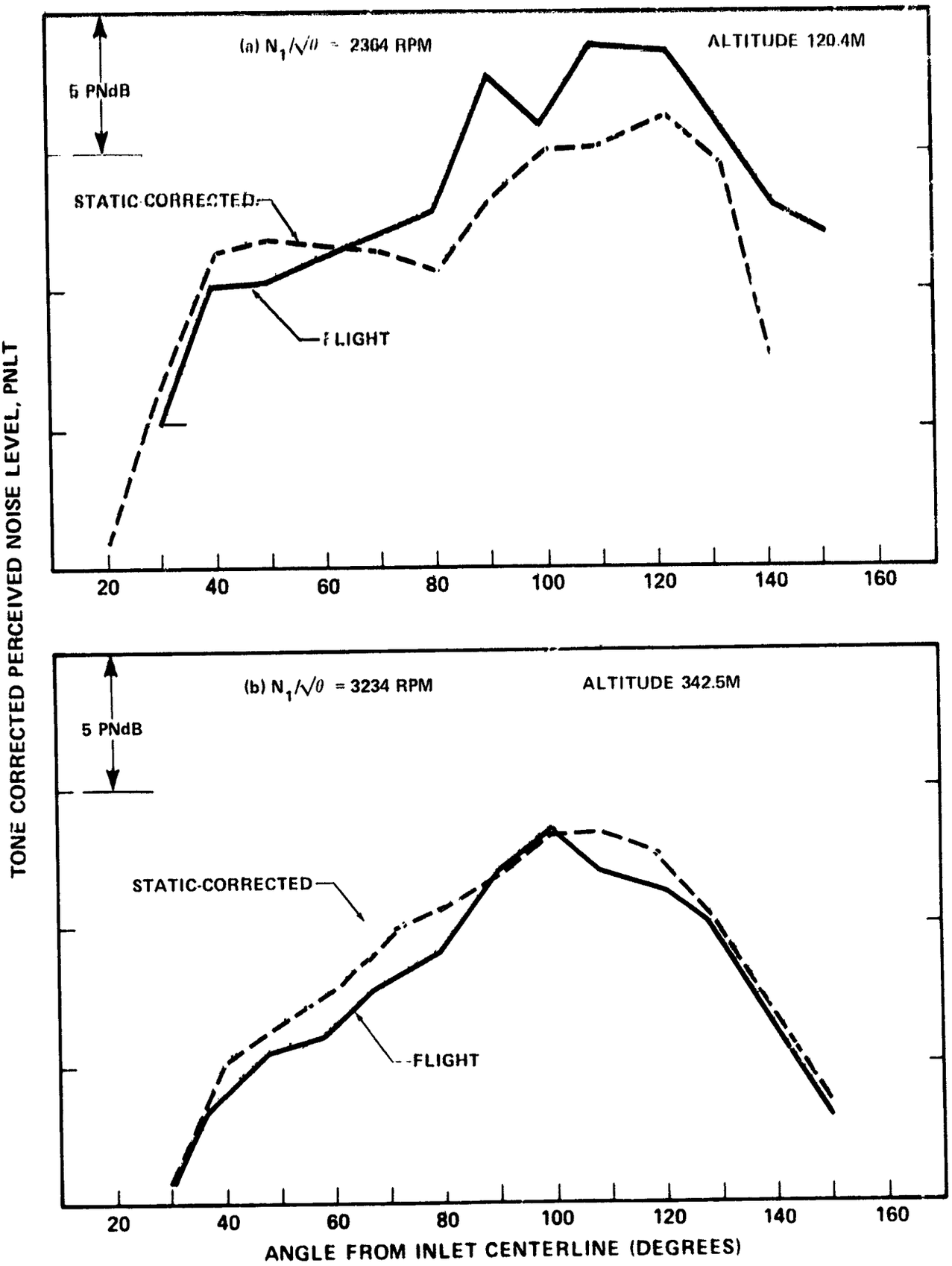

FIGURE 110. COMPARISON OF DC-10-40 FLIGHT AND JT9D-59A STATIC-CORRECTED PNLT'S CORRECTED FOR THE EFFECTS OF FORWARD MOTION, PROPAGATION, AND ENGINE INSTALLATION.

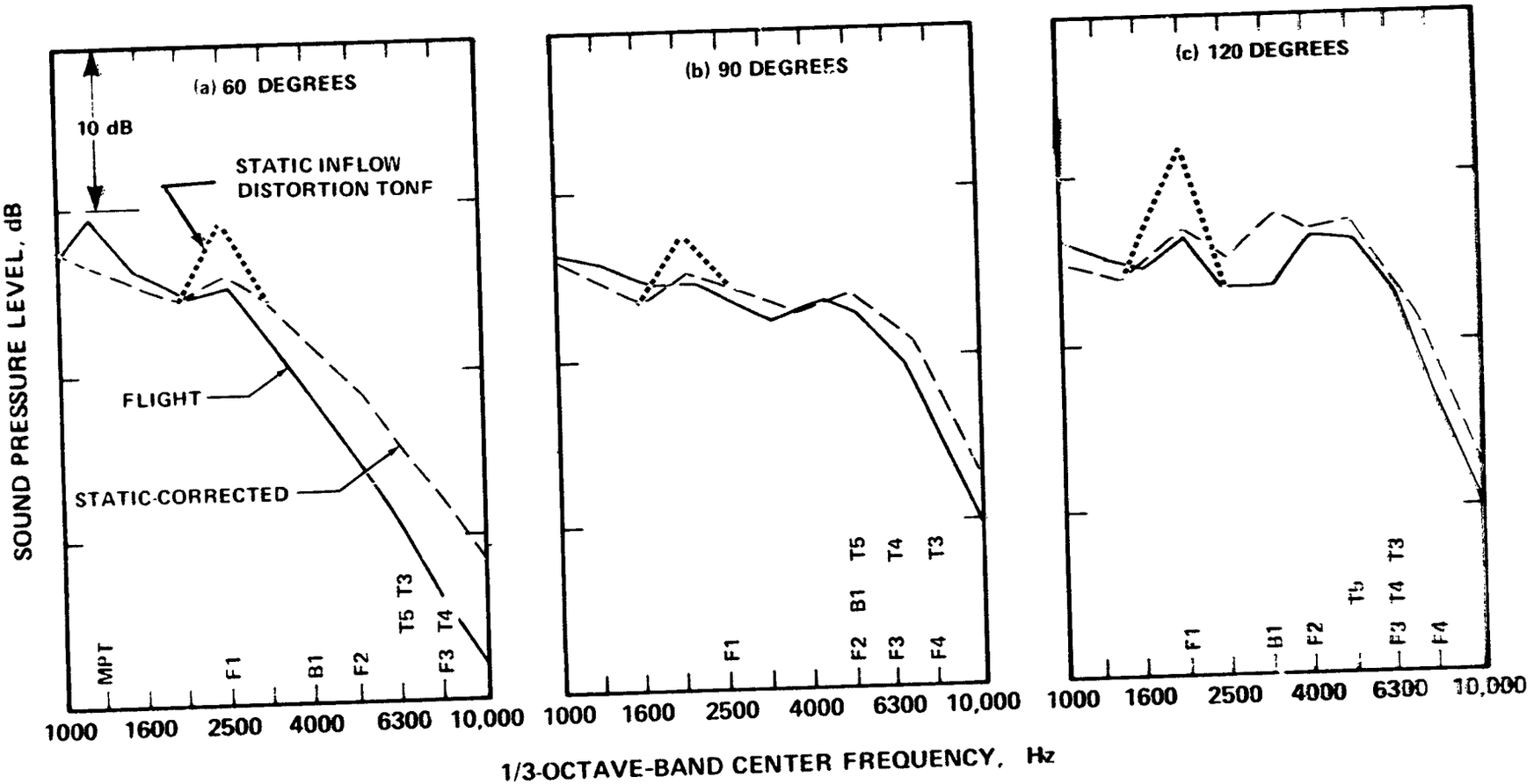

FIGURE 111. COMPARISON OF DC-10-10 FLIGHT AND CF6-6D STATIC-CORRECTED SPL SPECTRA CORRECTED FOR CONVECTION AND NOISE GENERATION ON THE FAN FUNDAMENTAL TONE DURING A 152.4-METER (500-FOOT) LEVEL FLYOVER. CORRECTED FAN ROTOR SPEED = 3063.0 RPM.

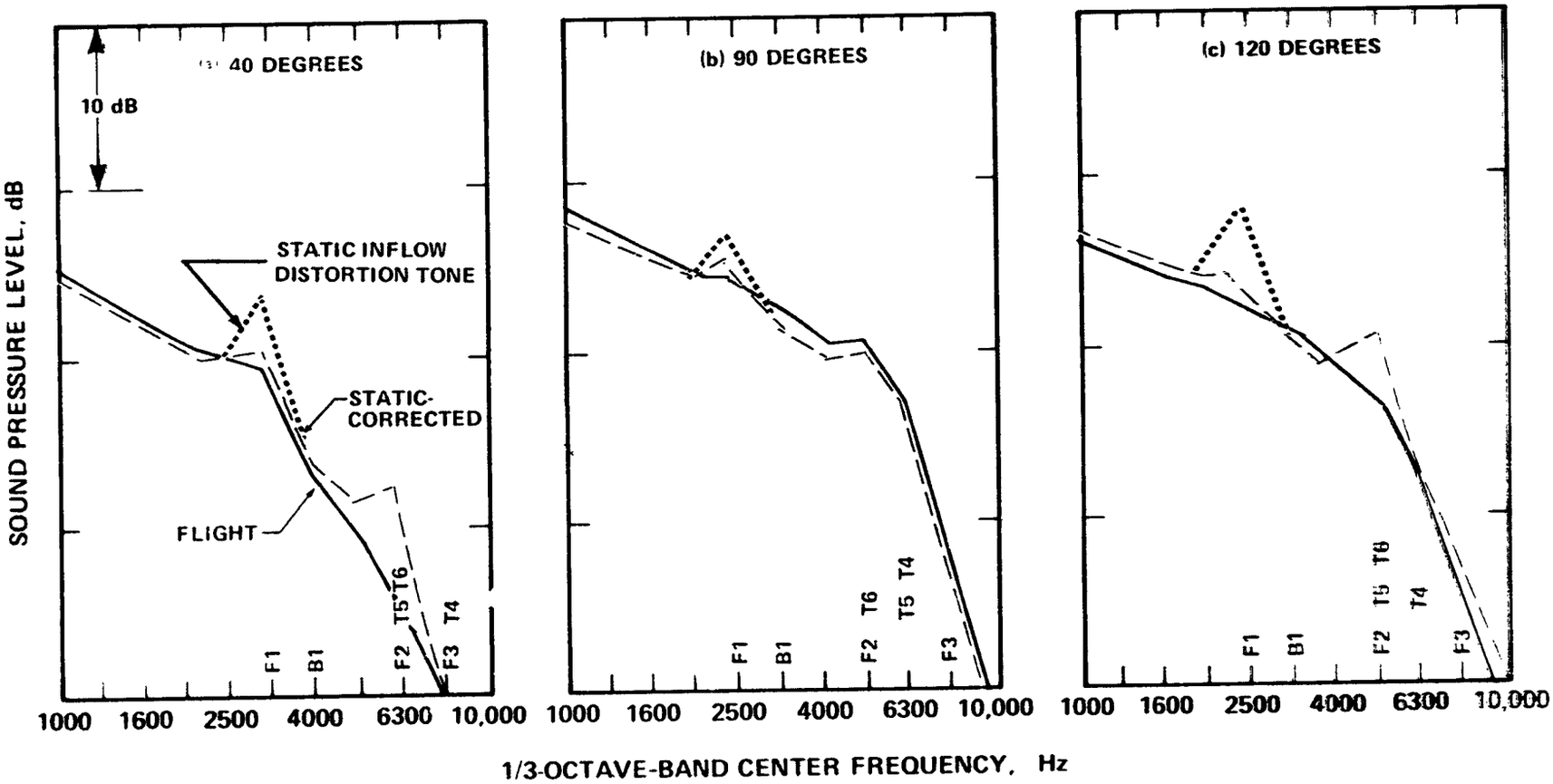

FIGURE 112 COMPARISON OF DC-10-40 FLIGHT AND JT9D-59A STATIC-CORRECTED SPL SPECTRA CORRECTED FOR CONVECTION AND NOISE GENERATION ON THE FAN FUNDAMENTAL TONE DURING A 120.4-METER (395-FOOT) FLYOVER. CORRECTED FAN ROTOR SPEED = 3234.0 RPM.

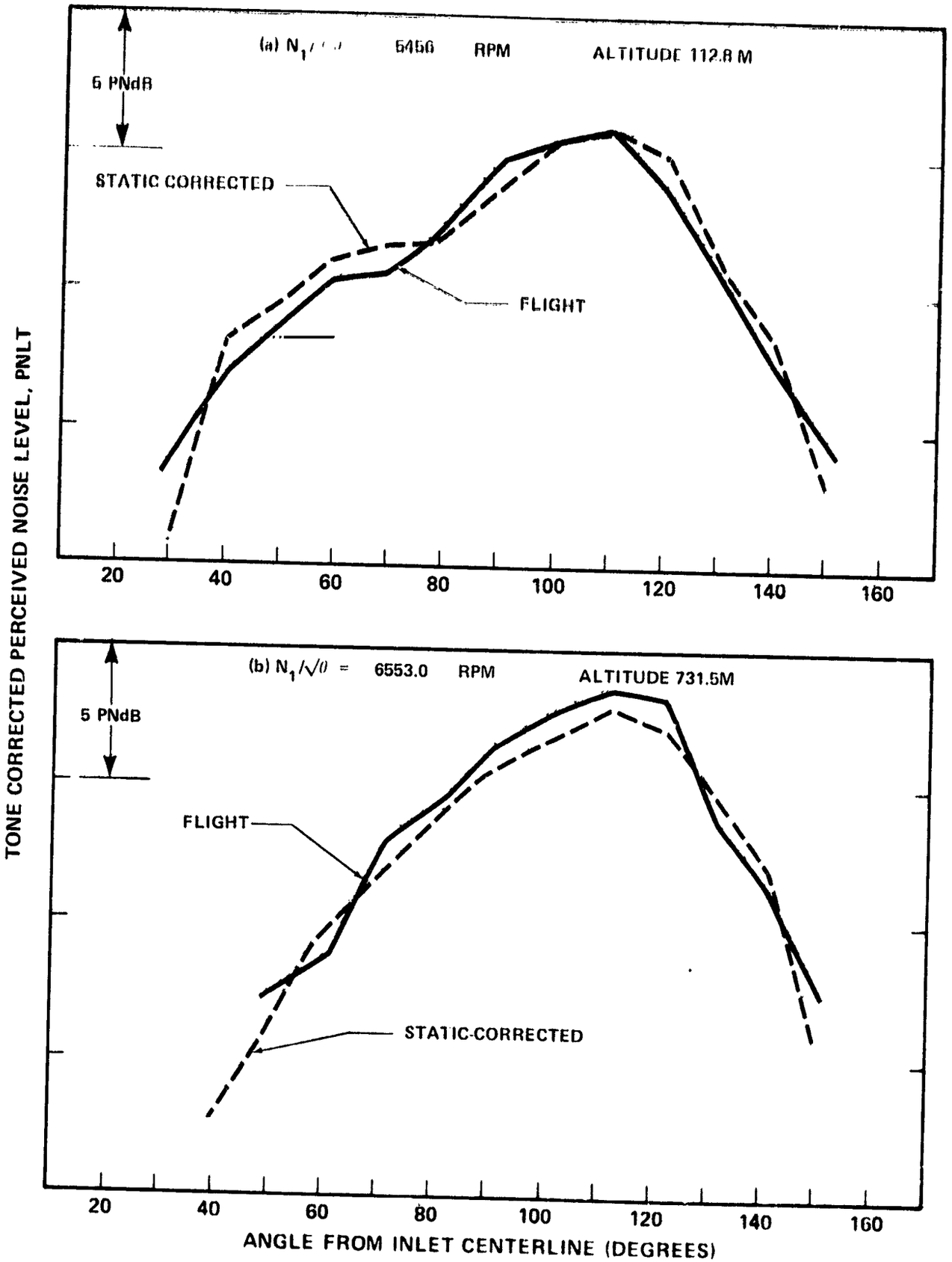

FIGURE 113. COMPARISON OF DC-9-30 FLIGHT AND JT8D-109 STATIC-PROJECTED SPL SPECTRA CORRECTED FOR INSTALLATION PROPAGATION AND CONVECTION EFFECTS DURING A 112.8-METER (370-FOOT) LEVEL FLYOVER. SPEED - 5456.0 RPM.

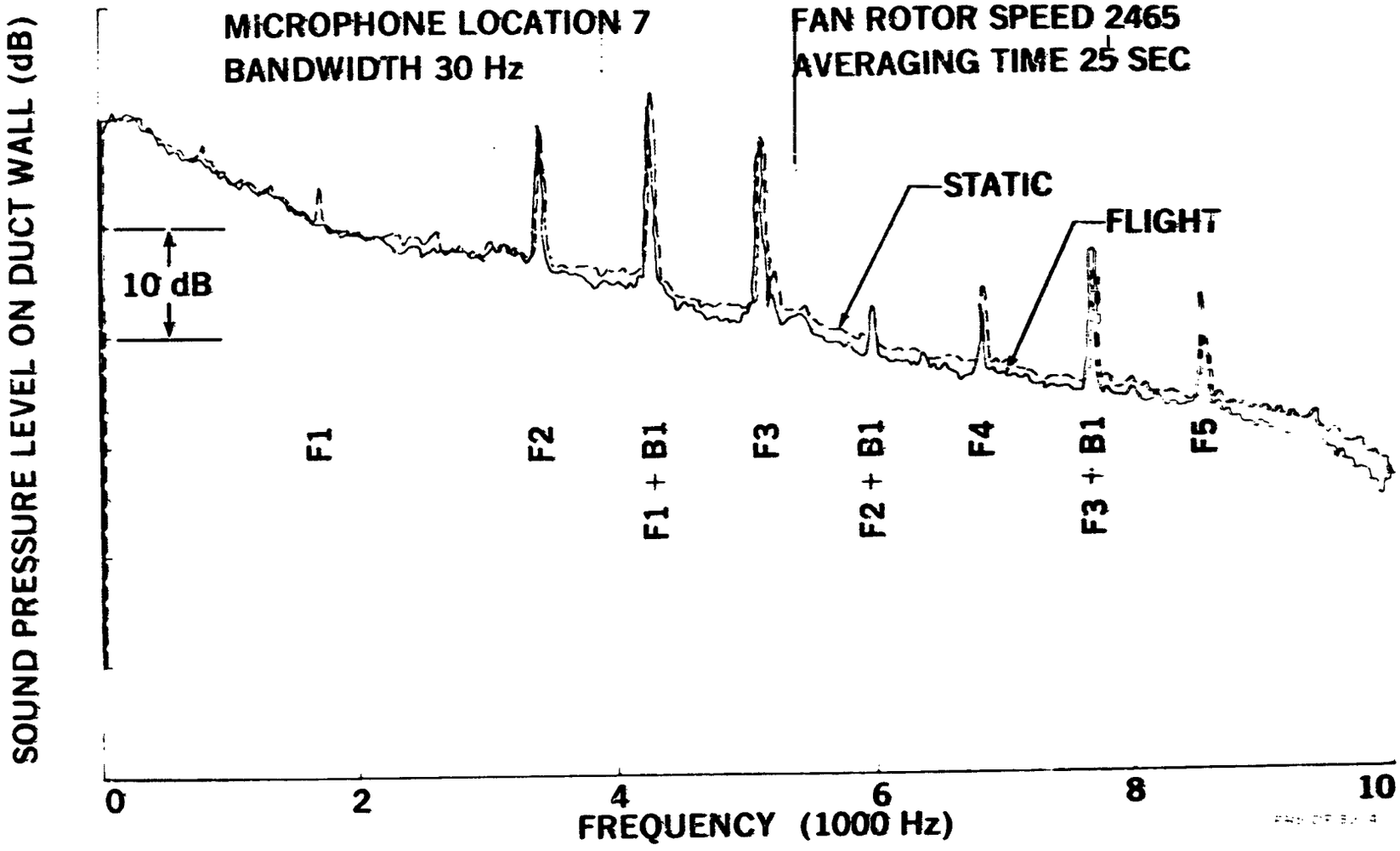

FIGURE 114. COMPARISON OF FLIGHT AND STATIC NARROW-BAND SPECTRA MEASURED ON THE FAN DISCHARGE WALL OF THE CF6-6D ENGINE

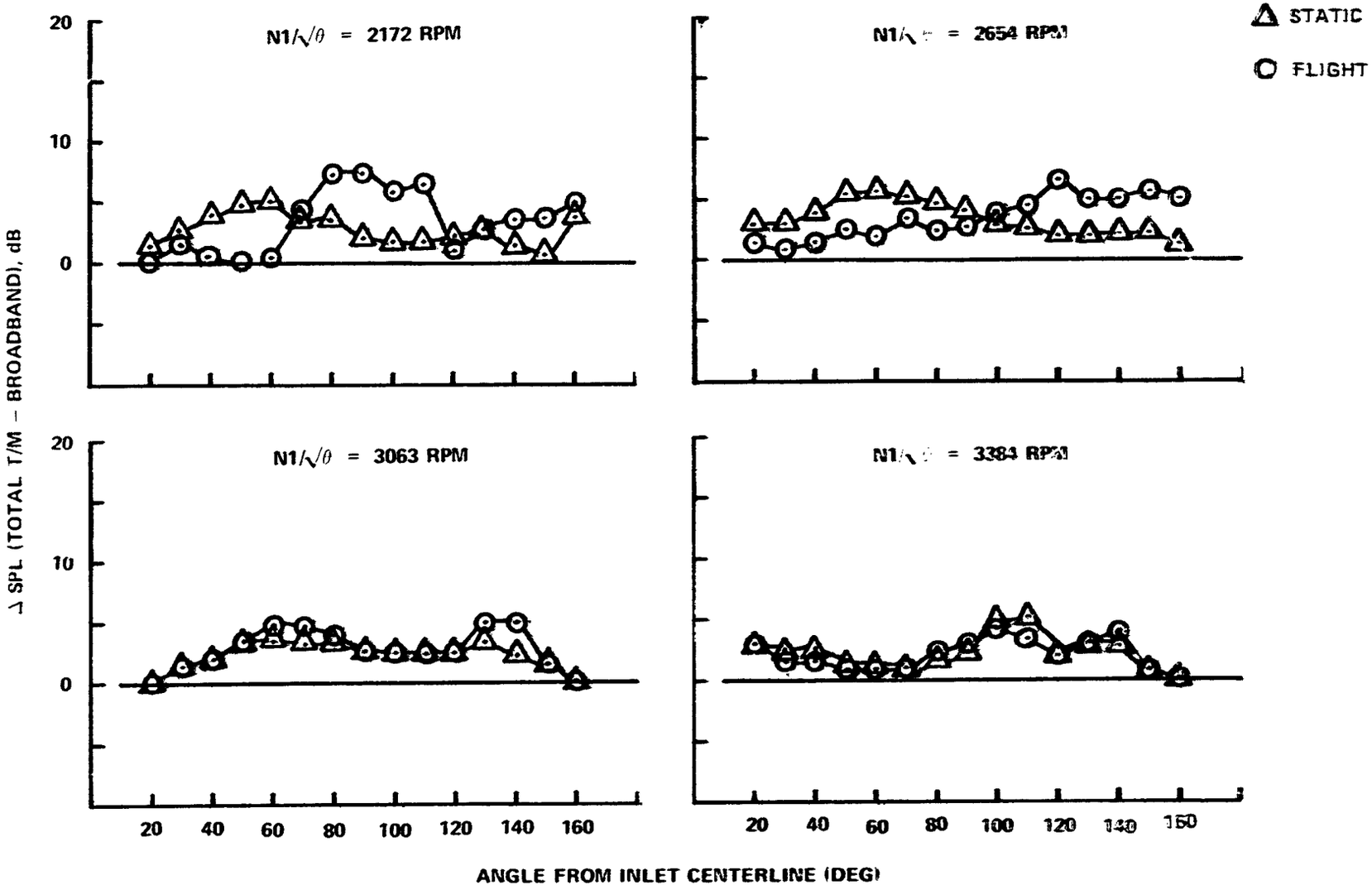

FIGURE 115. COMPARISON OF DC-10-10 FLIGHT AND CF6-6D STATIC-CORRECTED LEVELS OF THE FAN SECOND HARMONIC

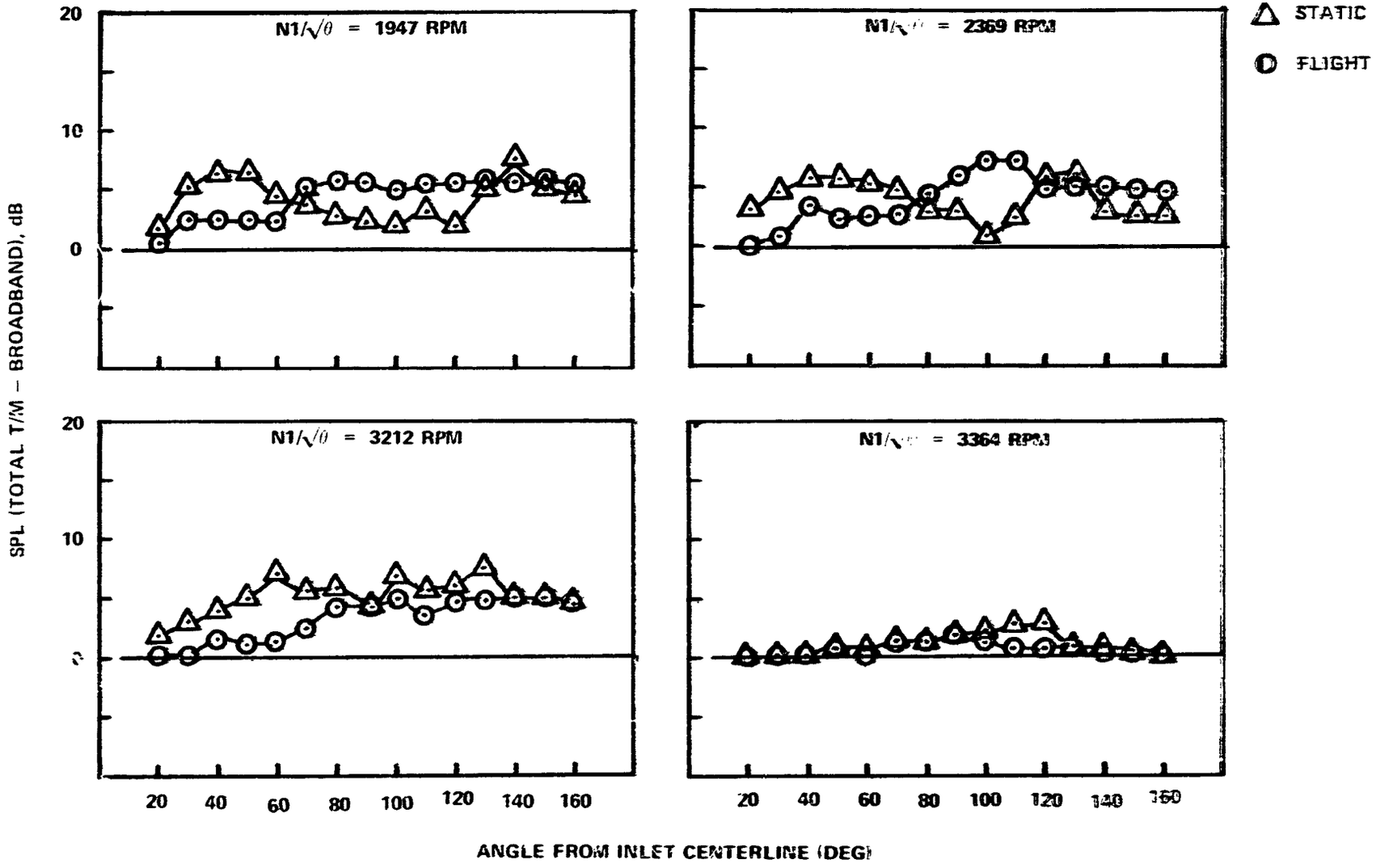

FIGURE 116. COMPARISON OF DC-10-40 FLIGHT AND JT9D-59A STATIC-CORRECTED LEVELS OF THE FAN THIRD HARMONIC